Highly sensitive sensors based on advanced materials for flexible and wearable electronic devices

A thesis submitted to

The University of Manchester

For the degree of

Doctor of Philosophy

In the Faculty of Science and Engineering

2021

Liming Chen

School of Engineering, Department of Electrical and Electronic Engineering

List of Contents

List of Figures*

List of Tables*

List of Abbreviations*

2D	Two dimensional
3D	There dimensional
LM	Liquid metal
XPS	X-ray photoelectron spectroscopy
XRD	X-ray diffraction
SEM	Scanning electron microscopy
EDS/EDX	Energy dispersive X-ray spectroscopy
XCT	X-ray computed tomography
GUI	Graphical user interface
PTFE	Polytetrafluoroethylene
PEO	Polyethylene oxide
PA6	Polyamide
TENG	Triboelectric nanogenerator
h-BN	Hexagonal boron nitride
PPy	Polypyrrole
MoS_2	Molybdenum disulfide
WHO	World Health Organization
COVID-19	Coronavirus disease 2019
OSAH	Obstructive sleep apnea hypopnea syndrome
PSG	Polysomnography monitor
SBS	poly(styrene-block-butadienstyrene)
PAN	Polyaniline
PDA	Polydopamine
REMS	Rapid eye movement sleep
eGaIn	Eutectic gallium−indium
AgNW	Silver nanowire
AgNP	Silver nanoparticles
CNT	Carbon nanotube
EM	Electromagnetic
LBP	Low back pain

CE	Contact electrification
PMMA	Poly(methyl methacrylate)
PDMS	Polydimethylsiloxane
LMNF	Liquid metal nanoparticles film
PU	polyurethane
PAMD	Polymer-assisted metal deposition
ELD	electroless deposition
PEDOT	poly(3,4-ethylenedioxythiophene)
PSS	poly(styrenesulfonate)
RH	relative humidity
XPS	X-ray Photoelectron Spectroscopy
NAP	Near Ambient Pressure
AFM	Atomic force microscopy
FTIR	Fourier-transform infrared spectroscopy
KPFM	Kelvin Probe Force Microscopy

Abstract

Flexible and wearable sensing technology is becoming increasingly important in personal healthcare and population health management. However, currently many wearable sensors are cumbersome, fragile and rigid, with obvious limitations, such as low sensitivity, slow response, low durability, and incompatibility with soft human skin surfaces. Advanced materials, such as graphene, hexagonal boron nitride (h-BN), MXene, metal nanoparticles (*e.g.,* gold, silver, copper and nickel), have shown great potential in wearable sensing applications due to their excellent electromechanical properties. However, there remain challenges to apply these sensing materials to real world wearable applications. (1) The physical interaction between sensing material and the substrate is weak, fail to be used for a long time; (2) The electrical signal analysis of the sensor is still in its infancy, and the relationship between electrical signals and external stimuli is not clear; (3) Most wearable sensors are passive and require a rigid input power supply; (4) A single sensor unit cannot simulate the real complex touch sense of the human skin, which requires a sensor array to achieve multipoint sensory and perception.

This thesis proposes several effective strategies to solve these problems. Firstly, efficient and low-cost surface modification strategies were used to form robust chemical interaction between the sensing materials and flexible substrates through hydrogen bonds, covalent bonds, and topological structures. The solid adhesion interconnection networks endow stable and durable sensing capabilities to the prepared sensors. The developed sensors were then applied to flexible and wearable electronic devices to monitor individuals' daily activities and health status in real-time, such as joint bending, speaking, running, watching TV, coughing, fever, runny and stuffy nose.

Secondly, interdisciplinary knowledge of materials science, electrical engineering, physics and chemistry is applied to promote signal output analysis. Taking the h-BN-based humidity sensor as an example, I successfully clarified the relationship between impedance output and

resistance & capacitance, and the relationship between resistance/capacitance and humidity changes. This showcases the interdisciplinary investigation (material science and electronic engineering) of a humidity sensor and its practical applications.

Thirdly, high-performance flexible triboelectric nanogenerators (TENGs) as flexible power sources are developed and integrated into a self-powered humidity sensor. The liquid metal nanoparticles film helps a typical TENG to greatly enhance contact surface, and thus increases the charge density by more than three times. The proposed charge excitation system offers a strong electric field, which causes the extra abundant positive/negative charge on tribo-surfaces due to quantum tunnelling effect, led to the maximum ~134-fold enhancement of output power density. Finally, a capacitive sensor array is constructed, by introducing TENG's structure to fabricating a self-powered sensor array.

In summary, the thesis made significant progress in developing highly sensitive and fast response wearable sensors.

University: The University of Manchester Degree: Doctor of Philosophy (PhD)

Candidate's name: Liming Chen Date: August 2021

Thesis title: Highly sensitive sensors based on advanced materials for flexible and wearable electronic devices

Declaration

No portion of the work referred to in the thesis has been submitted in support of an application for another degree or qualification of this or any other university or other institute of learning.

Copyright Statement

Acknowledgement

I'm very grateful to the University of Manchester for awarding me the Presidential Doctorate Scholarship, which covered my tuition and living cost. I am also thankful to the 2018 IEEE I&M Society Graduate Fellowship Award ($15,000) to support my research work.

I want to convey my heartfelt gratitude to my supervisor Dr. W. Yin and my co-supervisor Dr. X. Liu. Dr. Yin helped me to open the door of the electromagnetic sensing field. He helped and guided me patiently, offered encouragement whenever and wherever I need it, and supported and trusted me. He continued to supervise me to promote my research project systematically and strictly, and meanwhile gave me the freedom to innovate in my research. Dr. Liu provided me with the platform of advanced material-based sensor fabrication. He also showed me excellent guidance and advice in my research, especially in material preparation and characterization.

Besides my supervisors, I'd like to thank Prof. J. Luo in Zhejiang University, who helped me expand my skillset in the field of TENG.

I would like to express my gratitude to Dr. M. Lu, who gave me great help in various theoretical analysis parts of my research.

I also want to thank Prof. A. J. Peyton for his help and support on the research platform.

I would like to express my appreciation to all my colleagues Dr. M. Lu, Dr. Y. Xie, Dr. J. R. Salas Avila, Dr. R. Huang, Dr. Z. Chen, Dr. Q. Ran, Miss. L. Zhang, Mr. G. Hu, Mr. J. Li, Miss. X. Guan, Miss. X. Wang, Mr. Y. Wang, Mr. R. Xiao, Mr. Y. Huang and Mr. B. Shi, for their help in my research and establishing a comfortable and happy study environment.

I would like to thank all cooperators' help, Prof. C. Casiraghi and Dr. X. Song in the Department of Chemistry, Prof. L. Ren and Mr. H. Yang in the Department of Mechanical, Aerospace and Civil Engineering, Dr. G. Wei at the University of Salford, and Mr. Z. Yu at the University of Bolton. Thanks to Nanoplexus Ltd. to provide single/fewer layer MXene.

Finally, I'd like to thank my beloved family for their support and encouragement. I want to extend my appreciation to my boyfriend, Dr. K. Hu, for his love, accompany, care, help and support over six years.

List of Publications

1. **L. Chen**, M. Lu, X. Liu, W. Yin, *et. al.* Textile Based Capacitive Sensor for Physical Rehabilitation via Surface Topological Modification. ***ACS Nano*** 2020, 14, 8191. (*Included as Chapter 3*)

2. **L. Chen**, M. Lu, X. Liu, W. Yin, *et. al.* Whole System Design of a Wearable Magnetic Induction Sensor for Physical Rehabilitation. ***Adv. Intell. Syst.*** 2019, *1*, 1900037. (**Cover Paper**) (*Included as Chapter 4*)

3. **L. Chen**, X. Liu, W. Yin, *et. al.* Biofriendly, Regenerable, and Freestanding Emotional Monitor from Interfacial Ultrathin 2D PDA/AuNPs Crosslinking Film. ***ACS Appl. Mater. Interfaces*** 2019, *11*, 36259.

4. M. Lu, **L. Chen**, X. Meng, R. Huang, A. Peyton, W. Yin. Thickness measurement of metallic film based on a high-frequency feature of triple-coil electromagnetic eddy current sensor. ***IEEE Trans. Instrum. Meas.*** 2020, *70*, 1-8.

5. Z. Yu, H. Yang, N. Soin, **L. Chen**, J. Luo, et. al. Bismuth Oxyhalide based Photo-enhanced Triboelectric Nanogenerators. ***Nano Energy*** 2021, 106419.

6. Z. Qu, R. Dai, L. Wu, Y. An, **L. Chen**, W. Yin *et. al.* Continuous rotation of eccentric triboelectric nanosensor under low frequency periodic vibration. **Nano Energy** 2020, *76*, 105075.

7. C. Zhu, E. Chalmers, **L. Chen**, X. Liu. *et. al.* A Nature-Inspired, Flexible Substrate Strategy for Future Wearable Electronics. ***Small*** 2019, *15*, 1902440. (**Cover Paper**)

8. M. Lu, X. Meng, R. Huang, **L. Chen**, A. Peyton, W. Yin. Lift-off invariant inductance of steels in multi-frequency eddy-current testing. ***NDT E Int.*** 2021, *121*, 102458.

9. M. Lu, X. Meng, R. Huang, **L. Chen**, A. Peyton, W. Yin. A high-frequency phase feature for the measurement of magnetic permeability using eddy current sensor. ***NDT E Int.*** 2021, 121, 102458.

10. M. Lu, X. Meng, R. Huang, **L. Chen**, A. Peyton, W. Yin, Z. Qu. Thickness measurement of circular metallic film using single-frequency eddy current sensor. ***NDT E Int.*** 2021, *119*, 102420.

11. M. Lu, X. Meng, R. Huang, **L. Chen**, A. Peyton, W. Yin. Determination of Surface Crack Orientation Based on Thin-Skin Regime Using Triple-Coil Drive–Pickup Eddy-Current Sensor. ***IEEE Trans. Instrum. Meas.*** doi: 10.1109/TIM.2020.3044729.

12. M. Lu, X. Meng, R. Huang, **L. Chen**, A. Peyton, W. Yin. Inversion of Distance and Magnetic Permeability Based on Material-Independent and Liftoff Insensitive Algorithms Using Eddy Current Sensor. ***IEEE Trans. Instrum. Meas.*** doi: 10.1109/TIM.2020.3036099.

13. M. Lu, X. Meng, R. Huang, **L. Chen**, A. Peyton, W. Yin. Measuring lift-off distance and electromagnetic property of metal using dual-frequency linearity feature. ***IEEE Trans. Instrum. Meas.*** doi: 10.1109/TIM.2020.3029348.

14. M. Lu, X. Meng, R. Huang, **L. Chen**, A. Peyton, W. Yin. Liftoff tolerant pancake eddy-current sensor for the thickness and spacing measurement of nonmagnetic plates. ***IEEE Trans. Instrum. Meas.*** doi: 10.1109/TIM.2020.3033377.

15. M. Lu, X. Meng, **L. Chen**, W. Yin, *et. al.* Measurement of ferromagnetic slabs permeability based on a novel planar triple-coil sensor. ***IEEE Sens. J***. 2020, *20*, 2904.

16. Y. Xie, M. Lu, W. Yin, H. Xu, S. Zhu, J. Tang, **L. Chen**, *et. al.* Novel Wearable Sensors for Biomechanical Movement Monitoring Based on Electromagnetic Sensing Techniques. ***IEEE Sens. J.*** 2019, *20*, 1019.

Chapter 1 Introduction

This thesis investigates flexible and wearable sensors made by several advanced materials to fulfill the requirements of rapid response, high sensitivity, stability, durability and comfortability. Three different research topics were studied through a comprehensive interdisciplinary approach. The first concern is the preparation of advanced sensing materials, including 2D materials (h-BN, MoS_2, graphene and MXene) with ultrahigh sensitivity and polymer-assisted metal coatings (copper and nickel) to realize durable and washable abilities by constructing robust chemical interaction (*e.g.,* hydrogen bond, covalent bond and topological structure) between sensing layer and the substrates. Then, the as-prepared sensors were applied to real-time monitor individual's physiological and psychological activities, such as joints bending, running, speaking, abdominal respiration, nose respiration with typical symptoms of COVID-19 or flu (*e.g.,* cough, fever, runny and stuffy nose). In addition, the electrical signals for human health monitoring were carefully analyzed, combining the experimental and theoretical results, so that every signal output during practical application can be well explained.

1.1 Background

Wearable electronics have shown considerable potentials in a variety of applications,[1, 2] including robot intelligence,[3] biological recognition,[4] disease diagnosis,[5] and everyday health monitoring.[6, 7] Especially, disease prevention and diagnosis are a considerable challenge nowadays due to healthcare, professionals, technology and equipment. There are approximately 1 billion people with disabilities in the world (WHO 2011). WHO considers part of the reason for the increase in the global disability rate is the aging population and the increase in chronic health diseases. By 2030, chronic diseases will account for 69% of all deaths worldwide, such as cardiovascular disease, cancers, diabetes, mental disease and chronic respiratory disease.[8] (WHO 2005) The chronic patients require regular hospital visits for examinations, which is inconvenient and costly, and puts a lot of pressure on the hospital.

Examples of human disease that require wearable technology

Firstly, let's take Obstructive sleep apnea hypopnea syndrome (OSAH) as an example.[8] The OSAH may suddenly stop breathing. It is not a simple airway obstruction, but the upper airway collapse, which is very dangerous since it may cause different kinds of disease, such as hypertension, coronary heart diseases, diabetes, and cerebrovascular disease. The monitoring of OSAH is a practical approach to prevent these diseases. Polysomnography monitor (PSG) is the most crucial method to detect OSAH. However, the PSG should be monitored for at least 7 hours in a unique sleep breathing lab under the supervision of a professional. If the breathing process can be wearable monitored at home and the data emailed to the doctor for comments, it will be convenient, cost-effective, and relieve hospital stress.

Secondly, COVID-19, an infectious disease with over 5 million cases and 129,000 deaths, has caused severe hospital resource shortage and a growing negative impact on all sectors of the global economy.[9] The difficulty in obtaining healthcare is becoming increasingly critical. Therefore, it is vital to develop wearable devices with comfortable and cost-effective properties for disease diagnosis and prevention without the assistance of a hospital or healthcare center.

Thirdly, rehabilitation is an important way to prevent disease, beneficial to 2.41 billion patients in 2019.[10] For instance, Transcranial Magnetic Stimulation (TMS) is a successful state-of-the-art rehabilitation treatment for mental disease, such as schizophrenia, depression, sleep disorders. However, in many countries, rehabilitation is still under-resourced and has not been prioritized. While successful for patients, traditional rehabilitation procedures have drawbacks such as being time-consuming, arduous, and difficult to repeat. In many circumstances, one-on-one treatment is the only option. At the same time, many patients are not receiving timely and standardized rehabilitation care due to a severe shortage of professionals, and hence have missed the optimal time for treatment. Therefore, wearable electronics are highly desired to realize timely and continuous health monitoring during

rehabilitation training.

Current commercially bulk wearable devices generally are brittle and rigid, shown incompatibility with the soft human skin surface, and thus fail to record human health signals quantitatively.[11] While advances in flexible wearable electronic technology have aided the development of frequent and real-time human health monitoring in recent years. Flexible wearable sensors can detect and monitor various biological or mechanical stimuli from the human body, including pressure, tension, temperature, and humidity. However, most of studies only focus on developing new high-performance sensing materials.[12] Simply focusing on developing sensing materials in isolation hardly matches the enormous needs for practical wearable applications.

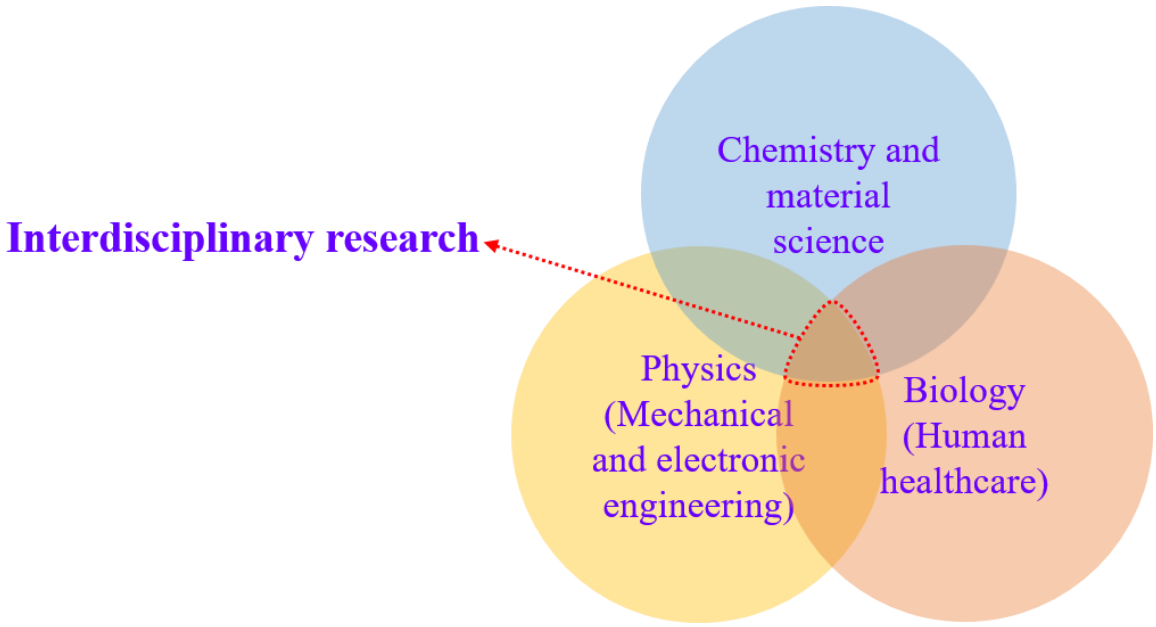

Figure 1.1 Interdisciplinary research of wearable electronics.

The investigation of wearable technology should be systematically considered through interdisciplinary knowledge (**Figure 1.1**). It combines chemistry and material science (material preparation), mechanical engineering (external stimuli), electronic engineering (signal acquisition and analysis) and human healthcare (research object). There are many questions to consider. First is chemistry foundation which is the most essential. How to

realize a material sensing capacity? Whether it is because of functional groups like hydrogen-bond, covalent bond, or the design of unique structures like aerogel or ultra-thin film? How to realize robust interaction with the substrate to realize stable and durable output? Then the knowledge about physics is necessary, such as electronic engineering to help acquire and analyze the signal output. How to link the material molecular changes or microstructure variables' effect with physical quantity changes? What kinds of mechanical deformation like pressure, shear, and torsion, or changes the conductivity, permittivity, or permeability? What is the exact relationship between the material variable and mechanical variable? And how it changes the electrical signal output? This is one of the most crucial parts of wearable electronics research besides material. Some information about biology is also vital since the research object is human. Does sensor mimic human sense? What kinds of disease can be detected, like hypertension, stroke, low pressure, OSAS, and Rapid eye movement sleep (REMS).

Human senses

To develop wearable sensors, we should comprehend human characteristics and learn from them. A genuine human with the five senses, smell, sight, hearing, taste, and touch, can teach us more about sensor sensation. The sensory organs that correspond to each sense convey data to the brain via the nervous system (**Figure 1.2**), to assist us in comprehending and perceiving the world around us.[13] As a result, we can sense pressure, tension, vibration, temperature, cold, warmth, pain, and chemical species from food, flowers, and other sources.

The skin is the body's biggest organ, with a surface area of roughly 2 m^2. It shields us from the elements, controls our body temperature and moisture, and gives us a sensation of touch for the outside world. The epidermis, dermis, and hypodermis layers of skin comprise a vast nerve network, which includes various sensory receptors. As a result, the human skin has a sensatory and perceptual ability.[13]

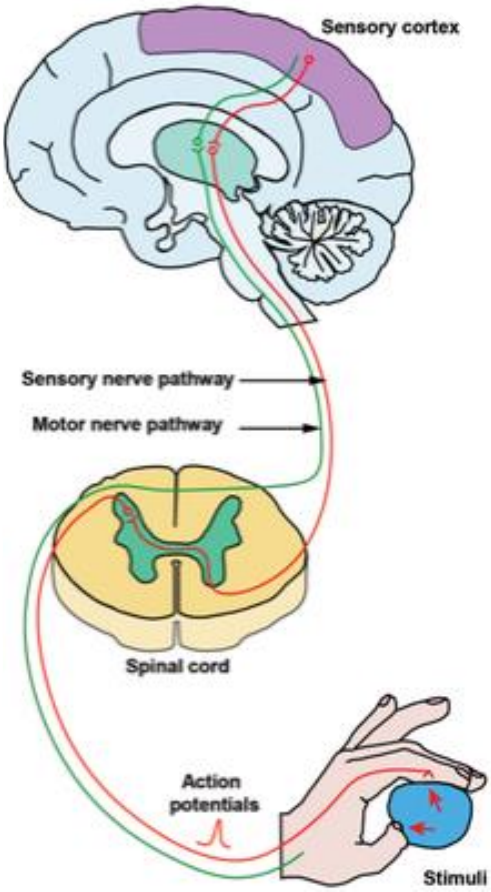

Figure 1.2 Sensory system in human.[13]

Artificial sensation and other functionalities have been achieved using flexible electronics to mimic human skin, which are impossible with traditional rigid electronics. Much effort has been put into developing wearable electronics, from materials preparation to sensor application, divided into the following four parts (**Figure 1.3**).[1, 14-22]

1) Design of sensing materials. It includes novel structural design of traditional sensing materials, such as gold, silver, carbon, *etc*., and novel materials, like new 2D materials, supramolecules, hydrogels, polymers, *etc*.. In this way, various essential properties (*e.g.,* self-healing, stretchability and robust interaction) can be realized.
2) Selection of detection mode, implantable or noninvasive, contact or non-contact. It depends on the health signal sources.
3) Sensing mechanism. When the material's conductivity is high and stable, it suits to construct a capacitance or inductance sensor. When the material resistance changes

significantly with external stimuli, it fits to serve as a resistance sensor.

4) System-level integration to expand more functions of the sensor, such as self-power, sensor array and wireless sensing system.

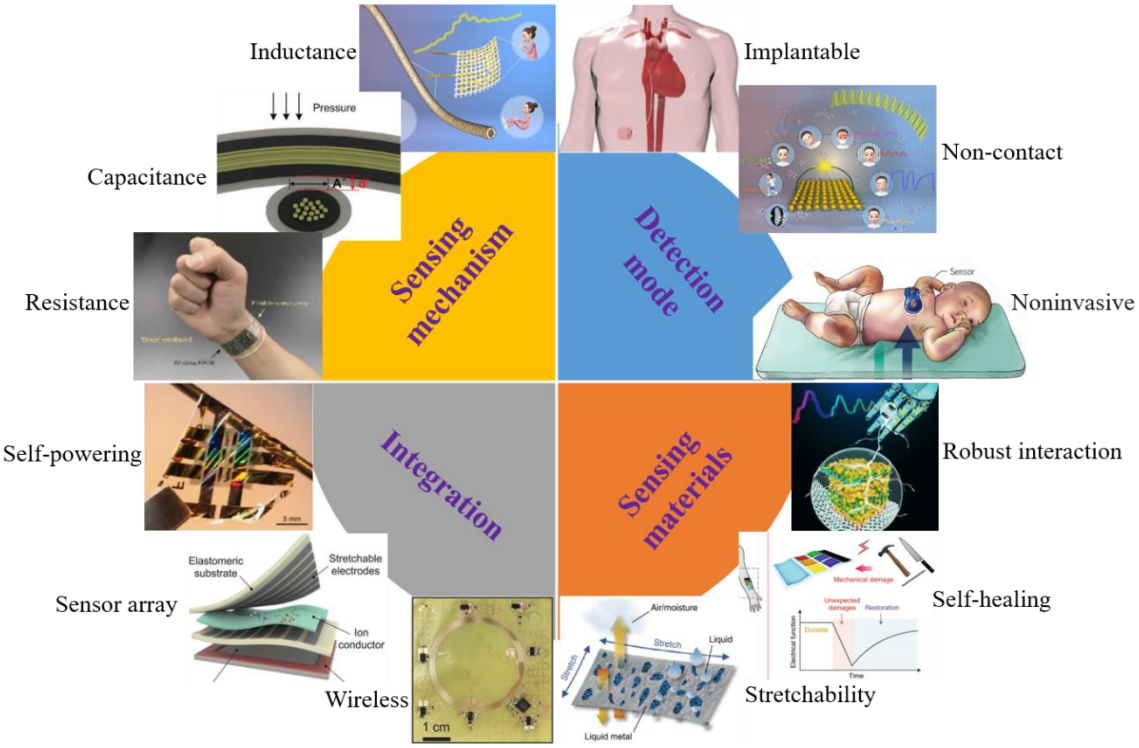

Figure 1.3 Comprehensive consideration of wearable sensors development from four aspects. [1, 14-22]

1.1.1 Sensing materials

The wearable sensor relies on advanced flexible sensing materials and optimized sensor device design to realize highly sensitive, reliable, and stable quantitative detection of wearable electronics. Materials science and chemistry have played a vital role in developing novel sensing materials, novel flexible substrates, and novel integration processes of the two.

Novel sensing materials

The novel sensing materials that researchers concern with are composed of two kinds. One is developing traditional materials with particular structure and characters, such as gold,

silver, copper, carbon nanotube film, *etc.*. The other is exploiting novel materials, like new 2D materials, supramolecules, hydrogels and other new polymers. Some typical sensing materials are listed in **Table 1.1**, containing 2D material such as graphene and MXene, metal material and polymer.

2D materials

2D materials show great potential in wearable sensing: their high surface-area-to-volume ratio provides high sensitivity; their ultra-thin thickness enables fast response and easy integration onto flexible substrates; the possibility to tune their surface properties with non-covalent functionalization allows to introduce tailored functional groups for fabrication of stable and printable water-based solution; and their superior electrical conductivity and mechanical strength for fabricating flexible electronics. 2D materials are frequently combined with polymers to make flexible wearable sensors. Therefore, the interaction between 2D materials and substrate should be considered for reliable and stable use in practical application. The conductivity of single-layer graphene can reach 10^8 S/cm due to its zero bandgap structure,[23, 24] but high quality single-layer graphene is difficult to mass-produce. Qu et. al. reported graphene-coated PU fibres to enhance the interaction between graphene and the textile substrate for wearable sensing application.[25, 26] However, practical application has been hampered by the low conductivity impacted by structural defects and the additive PU fibre. MXene ($Ti_3C_2T_x$) is metallic, shown a better conductivity (20000 S/cm) than other solution-processed materials, including graphene.[27-29] The hydrophilic groups (hydroxyl, oxygen-based groups) in T_x of MXene can form hydrogen bonding interaction with the cotton textile substrate without additives. Hence, MXene is an ideal candidate to construct textile-based capacitive sensor for wearable physical monitoring. On the other hand, for wearable chemical monitoring like breathing humidity monitoring, besides sensitivity, abilities including stability, reproducibility and fabrication costs are of fundamental importance. Therefore, these abilities of different 2D materials should be compared, such as h-BN, MoS_2, WS_2, in particular in comparison to graphene oxide. The strong cross-sensitivity issues such as any multiple changes in humidity, strain, temperature

should be concerned.

Conductive polymers

Conductive polymers (*e.g.,* PEDOT, PAN and PPy) have steadily gained attention owing to their excellent flexibility and transparency, but weak stability and low conductivity have impeded their practical applications.[30-32] Among them, the most conductive polymer, PEDOT (single crystal conductivity as high as 8797 S/cm), can achieve strong adhesion to flexible substrates by cross-linking PSS.[33-35] However, the conductivity of PEDOT is affected by the growth of its particular crystal phase and concentration of insulative PSS.[36] Its conductivity in the actual use cannot meet the demand.

Metals

As the most common conductive materials, metals, such as silver, aluminum, nickel and copper, are exceptionally conductive. However, most metal blocks are rigid, limiting their use in wearable electronics. Metals have amazing flexibility when reduced the size to the nanoscale, and can be combined with flexible substrates to make wearable electrodes. Grzybowki et al. proposed functionalized gold nanoparticles-based sensor, sensing various environmental changes, such as humidity, gas, and various metal cations.[37] However, the lack of interaction between substrates has influenced the stable and durable use of commercial conductive textiles and electrodes. Polymer-assisted metal deposition (PAMD) is an effective strategy to fabricate highly adhesive and conductive metal materials.[38-41] PAMD is made up of 3 steps: (1) polymer grafting (*e.g.,* polydopamine (PDA)); (2) palladium catalyst loading; (3) metal electroless deposition (ELD) process.[41] Unfortunately, the traditional PAMD process still exist some drawbacks, like the use of toxic solvent and the requirement of nitrogen protection.[42] A green, simple and low-cost method of PAMD is required for metal-base wearable electronics fabrication.

Beside of metal, metal oxides are also ideal candidates for wearable sensing application, due to their outstanding properties, such as high specific area, good biocompatibility, rapid

responsibility and durability.

Table 1.1 Material types for sensor fabrication.

Type	Material	Advantage	Disadvantage	Sensing mechanism
2D materials	Graphene, MXene, h-BN, MoS_2	Single atomic plane[43] (controllable thickness), printability,[44] stability and mechanical strength,[45] thermal & electrical conductivity[46]	Interaction between sensing layer and substrate [44]	Capacitance, resistance
Metals	Au, Pd, Ag, Cu, Al, Ni, Ga, GaIn	Conductivity	Flexibility, expensive and/or Oxidation	Capacitance, Inductance, resistance
Polymers	PAN, PPy, PEDOT:PSS, PDA, hydrogel	Flexibility, transparency, stretchability	Stability, conductivity	Capacitance, resistance

Interfacial assembly of sensing materials on flexible substrates

Assembly of advanced materials on flexible substrates is regarded as a fascinating way to control and enhance their mechanical and electrical properties for stable and durable use of wearable electronics.[47, 48] Interfacial assembly is considered as one of the most powerful approaches for preparation of functional structures, because structures adsorbed at two phase interface are highly mobile and can readily arrange into various equilibrium assemblies.[47, 48] And this assembly strategy is suitable to construct thin films of all kinds.[49-51] However, due to the relative weak physical interparticle interactions, the structures prepared by conventional interfacial assembly usually show low mechanical stability and is hard to transfer integrally onto other substrates, which limit their practical utilization. It remains a

great challenge to realize robust chemical interaction between sensing materials and the substrates for continuously recording signal from human daily activities, etc.

In addition, typical sensing materials have low sensitivity or/and responsiveness, limited their usage in wearable devices in the real-time physiological monitoring applications. Several efforts have made to construct ultrafast and sensitive sensors that can act as breath, heart or perspiration monitors, such as optimizing thickness of 2D graphene (15 nm),[52] introducing supramolecular polymer (nanofibres),[53] using transition metal dichalcogenides (*i.e.* WS_2 film), and polymer-nanoparticles composite films.[54, 55] However, the sensing mechanism is still unclear.

1.1.2 Detection mode

Wearable devices can be split into implanted sensors (in vitro) and noninvasive sensors (in vivo) based on detection methods. This thesis mainly focuses on the study of noninvasive sensors due to no pain and convenience. Another that is simpler, is we do not have to consider cytotoxicity/cell compatibility which could significantly limit the material pool. Gao *et. al.* summarized the noninvasive wearable sensors to monitor breath, sweat, saliva, blood, tears and other molecules in recent years.[56] Noninvasive sensors have contact and non-contact mode. It is determined by the biological signals to be detected.

1.1.2.1 Tactile sensor

The majority of wearable sensors are tactile sensors, which usually mimic the human sense of touch by direct contact with the soft skin surface to collect signals (*e.g.,* temperature, respiration and human motions). The tactile sensor contains capacitance sensor, inductance sensor and resistance sensor (most common), which are discussed in detail in the next section - sensing mechanism.

1.1.2.2 Non-contact sensor

Tactile sensors may cause cracks or damage to the sensing material and cannot be used for a long time. Some tactile sensors are uncomfortable for human skin and may cause anaphylactic reactions. Therefore, it is of great significance to explore non-contact sensitive materials that suits to detect individual gas molecules that spread from the body. Water is ideal for realizing a non-contact remote sensing signal source, because the water plays a significant role in most of the human body metabolism and physiological activities. The realization of the non-contact electronic devices requires sensing materials with ultrathin structure (high surface area volume ratio), able to fast absorb and desorb water molecules and record the dynamic signal of moisture change sensitively. My previous work about PDA/Au composite film-based humidity sensor is a successful example to long-term and non-contact monitor nose breathing moisture changes under different emotional states (**Figure 1.4**).[16]

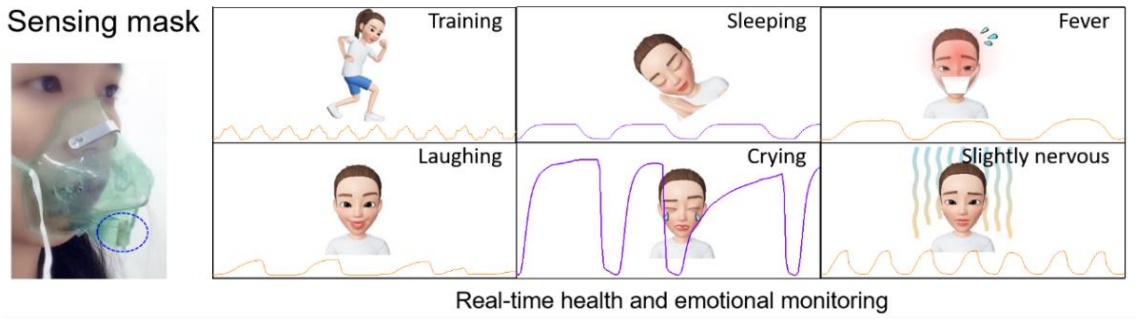

Figure 1.4 Respiratory sensor for emotional monitoring. [16]

1.1.3 Sensing mechanisms

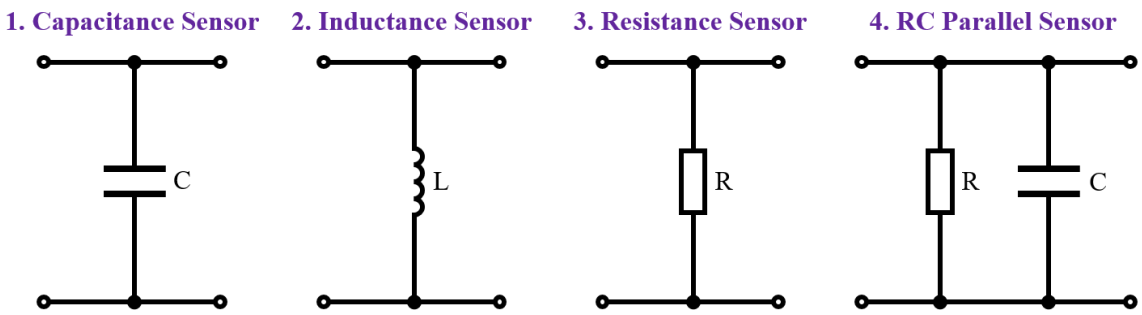

Figure 1.5 Sensor types classed based on the electrical signal outputs.

Wearable sensors can detect stimulus sources created by human physiological and psychological activities and generate electrical signals to collect information about human health states. They can be classed based on the electrical signals they generate, such as resistance, capacitance, inductance, RC parallel and other composite circuits sensors.

1.1.3.1 Capacitance sensor

A capacitive sensor is a device that convert the stimulus source into capacitance signals. The parallel-plate capacitor is one of the most common capacitors. The capacitance of the parallel-plate capacitor can be described as

$$C = \frac{\varepsilon S}{d} \tag{1.1}$$

where ε is permittivity between two plates, S is the active area of the plates and d is the distance between two plates.

External stimuli can create a change in ε, S or d, which results in a change in capacitance. As shown in **Figure 1.6A**, Atalay *et. al.* demonstrated microporous Polydimethylsiloxane (PDMS) dielectric layer enhanced the sensitivity to 121 × 10−4 kPa^{-1} by changes of ε and d.[57] You *et. al.* investigated the kinetics of ion relaxation in a deformable ion conductor and build an artificial multimodal ionic receptor by changes of ε or/and S, d (**Figure 1.6B**).[14] Lee *et. al.* described a SBS/AgNP-based fibre as a pressure sensor with high sensitivity (0.21 kPa^{-1}) by changes of S and d (**Figure 1.6C**).[22] Choi *et. al.* proposed a twistable and stretchable fibre-based capacitance sensor using buckled CNT with maximum 115.7% (stretching 200%) and 26% (twisting 270 turns/m) capacitance changes (**Figure 1.6D**).[58] Capacitive sensor is ideal for detecting minor deflection changes, due to fast response, rapid relaxation, great resolution and high sensitivity. Some properties of sensors from literatures were listed in **Table 1.2**. Electromagnetic interference, on the other hand, is the limitation of capacitance detection.

Table 1.2 A list of the properties of various capacitance sensors in the literature.

Ref.	Material	strategy	Detection mode	Sensitivity	Response time
[59]	AgNW	Screening printing	Contact	1.62 MPa^{-1} (~1.8 μm)	40 ms
[60]	eGaIn	Injection	Contact	Tunable	75 ms
[61]	Al	Hot embossing technique	Contact	1.15 mm	14 ms
[62]	Al and Ag	Sputtering technology	Contact		164 ms
[57]	Microporous silicone-conductive fabrics	Solid particle leaching method	Contact	121×10^{-4} kPa^{-1}	7 ms
[22]	SBS/AgNP	Coating	Contact	0.21 kPa^{-1}	40 ms
[58]	CNT		Contact	0.21 kPa^{-1}	
[63]	GO	Hummers method	Noncontact	472	10.5 s
[64]	GO		Noncontact	4.45×10^{4}	2.7 s
[64]	BP		Noncontact	5.08×10^{3}	4.7 s
[65]	MoS_2/SnO_2	Hydrothermal	Noncontact	12809 pF/%	5 s

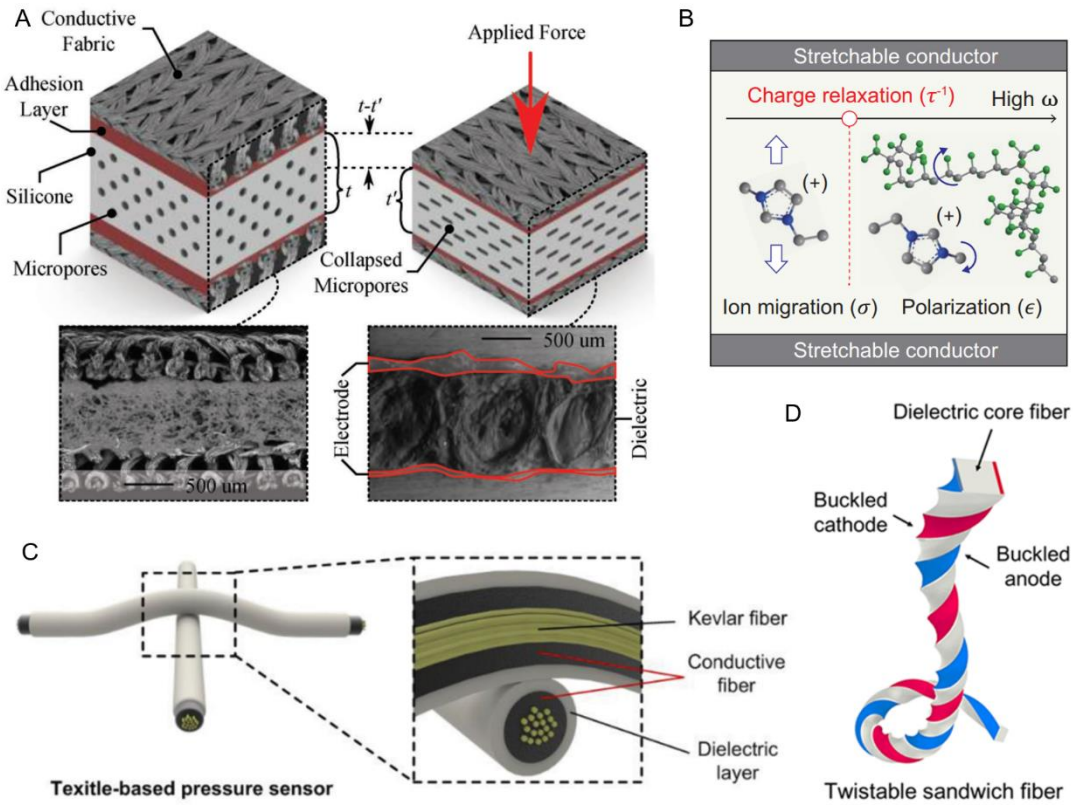

Figure 1.6 Enhancement of capacitance sensing capacity by introducing novel dielectric layer (A) a microporous silicone fabric,[57] (B) a deformable ion conductor structure, and creating new sensor structure[14] (C) SBS/AgNP composite fibre,[22] (D) sandwiched fibre using buckled CNT.[58]

1.1.3.2 Inductance sensor

EM technology is commonly employed in industries, and increasingly used as antenna for wireless sensing. Kim *et. al.* developed a sensor and antenna on a contact lens to detect tears' glucose concentration and intraocular pressure (**Figure 1.7A**).[66] Pan *et. al.* prepared wireless connectivity antenna using graphene inks by screen-printing technology for body temperature detection (**Figure 1.7B**).[67] However, the antenna is a short distance range wireless transmission, since the distance between the reading antenna and the sensor is short, within 10 mm.

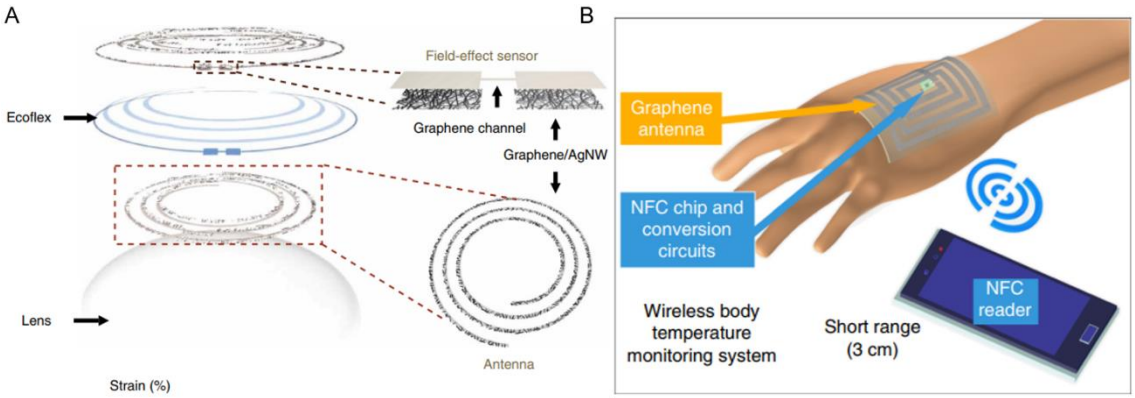

Figure 1.7 (A) A glucose and pressure sensing contact lens.[66] (B) Printed graphene-based wireless connectivity antenna.[67]

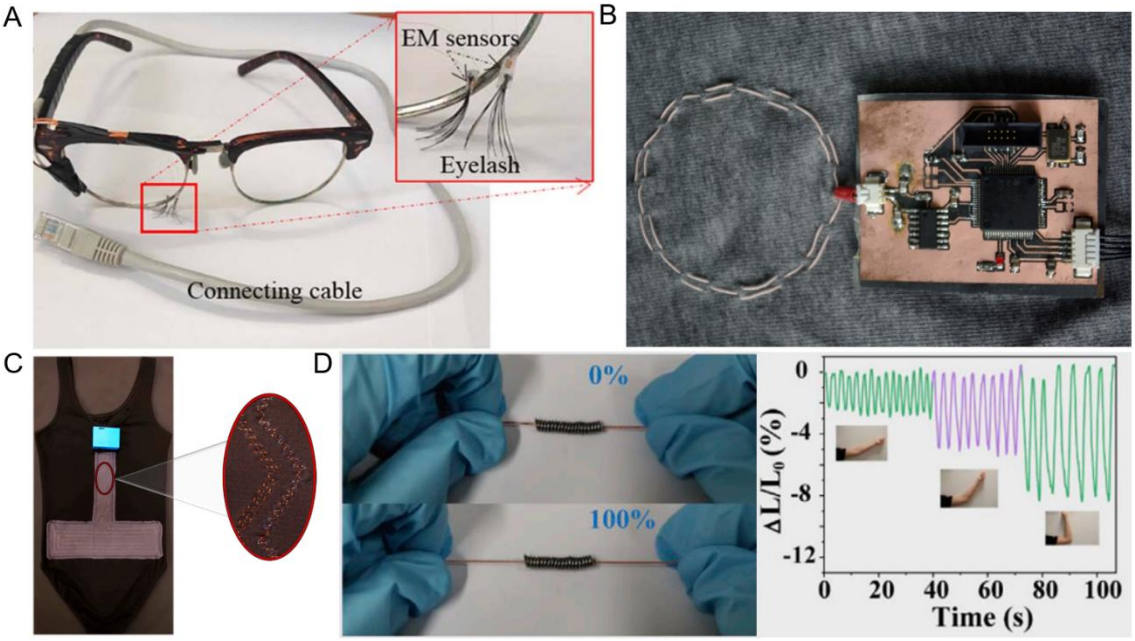

Figure 1.8 (A) EM sensor.[68] (B) Textile-integrated inductance sensor.[69] (C) Textile-based sensor for back posture monitoring.[70] (D) Retractable and stretchable inductance sensor.[71]

Besides, some inductance sensor has been developed to monitor human health. Xie *et. al.* suggested an effective EM sensor for monitoring eye blinking and other biomechanical motions (**Figure 1.8A**).[68] Teichmann *et. al.* prepared a textile-integrated inductance sensor to monitor respiration and pulse (**Figure 1.8B**).[69] Patino *et. al.* proposed a textile-based sensor to monitor back posture for preventing LBP (**Figure 1.8C**).[70] Wu *et. al.* reported a

retractable and stretchable inductance sensor to monitor different human motions with 0.4 mH/% sensitivity and <0.1 s response time (**Figure 1.8D**).[71] The flexibility and comfortability should be improved in the development of inductance sensor.

1.1.3.3 Resistive sensor

Resistive sensor is a series of functional sensor receiving and transferring input signals (IS) into resistance (R) output. The sensitivity (S) could be defined as the equation,

$$S = \frac{\Delta R}{(R_0 * \Delta IS)}, \Delta R = R - R_0, \Delta IS = IS - IS_0 \quad (1.2)$$

where IS_0 is the intensity of initial input signal and R_0 is the corresponding resistance of the sensor, while IS and R are the intensity of specified signals and the corresponding resistance. Sensors capable of responding to pressure, strain, moisture, volatile organic compounds (VOC), temperature, and light have tremendously developed in the last decades. Different sensors from the electroactive materials employ for specific applications as follows.

(1) Pressure and strain sensor

Wearable pressure[72-74] and strain[75-77] sensor could precisely monitor human motion of pulse, joint bending, and even nuance of facial expression, demonstrating its prospective application in personal physical and mental health care. Due to characteristics of elasticity and stretch, the sensor could be conformally connected on the human-device interface, enhancing the signal, and reducing the noise. He *et. al.* fabricated a high-performance pressure sensor based on the sensing film of graphene and patterned elastic substrate, which could reveal subtle arterial pulse signal information even with the interference of strenuous exercise (**Figure 1.9A and 1.9B**).[78] The initial resistance of the sensor consists of the contact resistance between the electrode and the sensing film, and the inherent resistance of the film. With external force applied, the patterned elastic deformed evidently and the contact resistance therefore decreased dramatically, leading to the corresponding electrical signal output. Textile-based sensor was further developed in the virtue of its outstanding wearability. Zhang *et. al.* proposed a pressure sensor with textile being coated by carbon nanotube (CNT)

inks (**Figure 1.9C**), carrying a high sensibility over 140 kP^{-1} and applicable to detecting a variety of human motions. Stretchable textiles are involved in as well.[79] Yang *et. al.* prepared a stretchable sensor by dip-coating the textile with graphene oxide ink and demonstrated its application in subtle facial expression (**Figure 1.9D**).[80] Elastomer and hydrogel make themselves representative of stretchability as the substrate of a strain sensor. Liang *et. al.* partly embedded the conductive CNTs into the polydimethylsiloxane (PDMS) film on the air-water interface (**Figure 1.9E**).[81] With external strain applied on the film, the conductive path among CNTs would reduce and result in an increase of resistance. Different to the stretchable elastomer-based strain sensor, conductivity of hydrogel could be empowered by cations and anions.[82] As shown in **Figure 1.9F**, potassium iodide (KI) was dissolved into the hydrogel or organohydrogel, the resistance of which increased with the increased tensile strength.[83] Additional functions, such as transparence, self-healing and bio-degradability, could be realized by selecting and designing the electroactive materials and substrate.

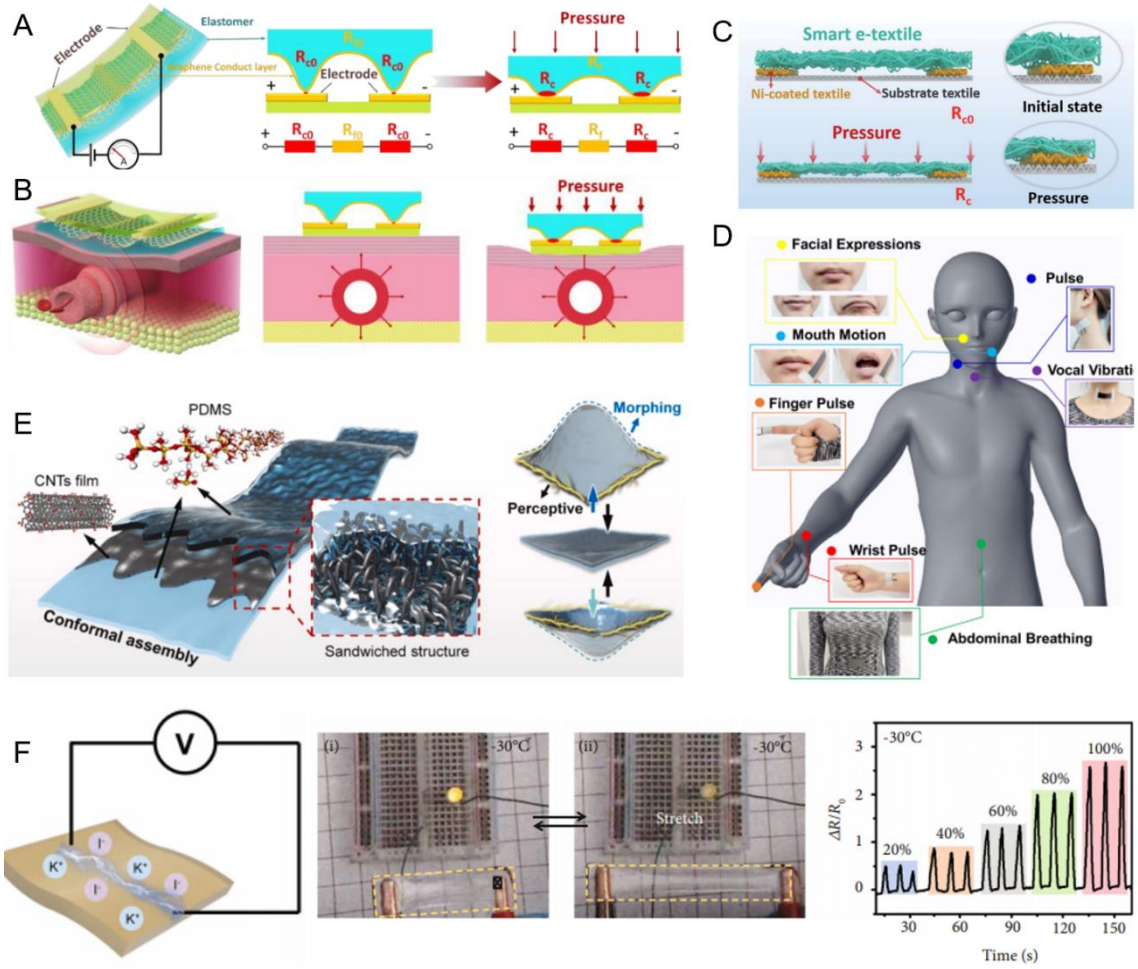

Figure 1.9 Mechanism of a pressure sensor based on elastomer (A, B)[78] film and textile (C).[79] (D) A stretchable textile sensor applied in human motion monitoring.[80] (E) Stretchable sensors based on CNTs conductive network embedded in elastomer[81] or (F) ion conductive path involved in hydrogel. [83]

(2) Chemical sensor

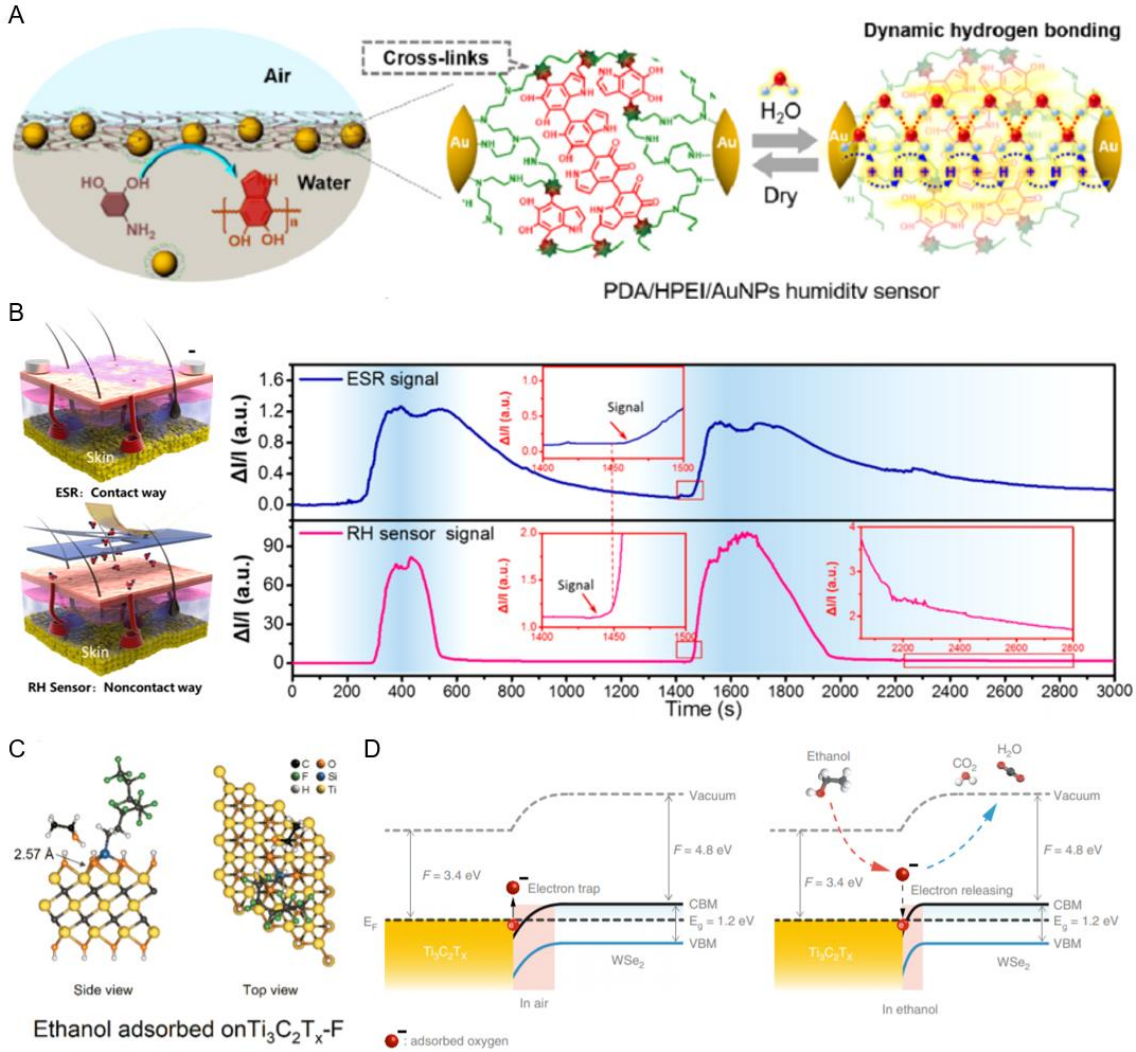

Figure 1.10 (A) Schema of the structure of an Au nanoparticle based moisture sensor and it detecting mechanism.[16] (B) The moisture sensibility of a contact and non-contact sensor.[84] Detecting mechanism of metallic conductive MXene film (C)[85] and MXene/WSe_2 hydride (D).[86]

Human body metabolism includes a series processes of water and other volatile gases transferring through the upper respiratory system and the skin. Recognizing those gas molecules in concentration and variety at real time would provide important health information of the detected subjects. Wearable moisture and volatile organic compounds (VOC) sensor therefore come on the stage.[87] Gas detecting includes three processes: gas absorption, interaction of gas molecular and sensing active center, and gas desorption. Chen

et. al. employed the Au nanoparticles into a self-assembled film with high specific area and then modified the film with hyperbranched polyethyleneimine (HPEI) and PDA (**Figure 1.10A**).[16] Such a hybrid film could rapid response to the water molecular due to the formation of dynamic hydrogen bonds among abundant amino and hydroxyl of HPEI and PDA. Electrical channels between AuNPs were then constructed through the hydrogen bonds, which would release the charge carriers of proton and hydronium ion, and finally result in resistance change. The moisture sensor could therefore work under non-contact mode, empowering itself with accuracy and reliability, while a sensor of contact mode may output unreliable signal with unproper operating process. Sensor working under non-contact mode may perform better. He *et. al.* prepared a non-contact PDA/Graphene-based moisture sensor and contrasted it to a contact sensor for epidermis moisture detecting (**Figure 1.10B**).[84] The sensor of non-contact behaves in a higher signal-noise rate.

Sensors for other specific volatile gases, such as NH_3,[88] H_2S,[89] etc. are developed as well. Different to the classical hydrogen-bond mechanism abovementioned, sensors based on metallically conductive 2D MXene of Ti_3C_2Tx behaves in another principle. On a MXene film, the adsorption of either electron-accepting or electron-donating gas hinders the charge-carrier-transport channel and decreases the number of charge carriers, result in increased resistance (**Figure 1.10C**).[85] Chen et. al. hybridized MXene with transition metal dichalcogenides to construct a n-type heterostructure, which performs an outstanding sensitivity in moisture sensing. As shown in **Figure 1.10D**, the partially occupied Fermi level takes effect of catalysis.[86] The electrons flow from the conductive MXene are trapped by the oxygen species from the fresh air (turns into O_2^- or O^-), resulting in a depletion layer. Then, with oxygen-VOCs being absorbed (such as ethanol), it could be oxidized into CO_2 and H_2O and the trapped electrons are then turns back to the MXene. The formation and reduction of depletion layer reflect a distinguish change in resistance of the hybrid film.

(3) Temperature and optical sensor

Physiological reactions always follow with heat energy release, therefore body temperature

monitoring at real time could unveil diseases of early stage, such as fever, flu, heat stroke and even tumor. Conductive materials respond to temperature in nature, behaving in positive (*e.g.,* metal conductor) or negative (*e.g.,* metallic oxide semi-conductors) temperature correlation. As for the metal conductor,[90] directional shift move of electrons is reduced by the increased temperature, while more electrons are excited to the conductive bands of semiconductor at higher temperature.[91] Nanomaterials involved in wearable temperature sensor could behave in either positive[92] or negative[93] correlation, which depend on its composition to polymer substrates or matrixes. Photo-resistive sensor (or in another words, photo detector) are generally based on semiconductor, carriers of electrons and holes are sensitive to ambient specific lights with various wavelengths.[94, 95]

1.1.4 Integration

Despite the fact that wearable sensing has made significant progress in recent years, some crucial milestones have yet to be achieved, including sensing system integration, flexible power supply for the wearable electronics and wireless transmission for data processing.

1.1.4.1 Integrated sensing system

Highly-integrated electronics build the intelligence for our daily life, such as the cellphone at your hand now. The integration of wearable electronics aroused tremendous interests among researchers. Two approaches the previous works could be sorted into, empowering a single device with multi-functions,[96-98] or collecting numerous electronics into one piece of high-performance module.[1, 99, 100] As for the first approach, Lei *et. al.* designed a dual-function sensor, responding to both pressure and temperature.[101] While the two sensibilities are of cross effect. Bae *et. al.* then proposed a sensor, capable of independently outputting pressure and temperature change at the same time (**Figure 1.11A**).[102] Self-powered sensor based on triboelectric nanogenerator (TENG), as a matter of fact, is an integration of powering and sensing functions.[103]

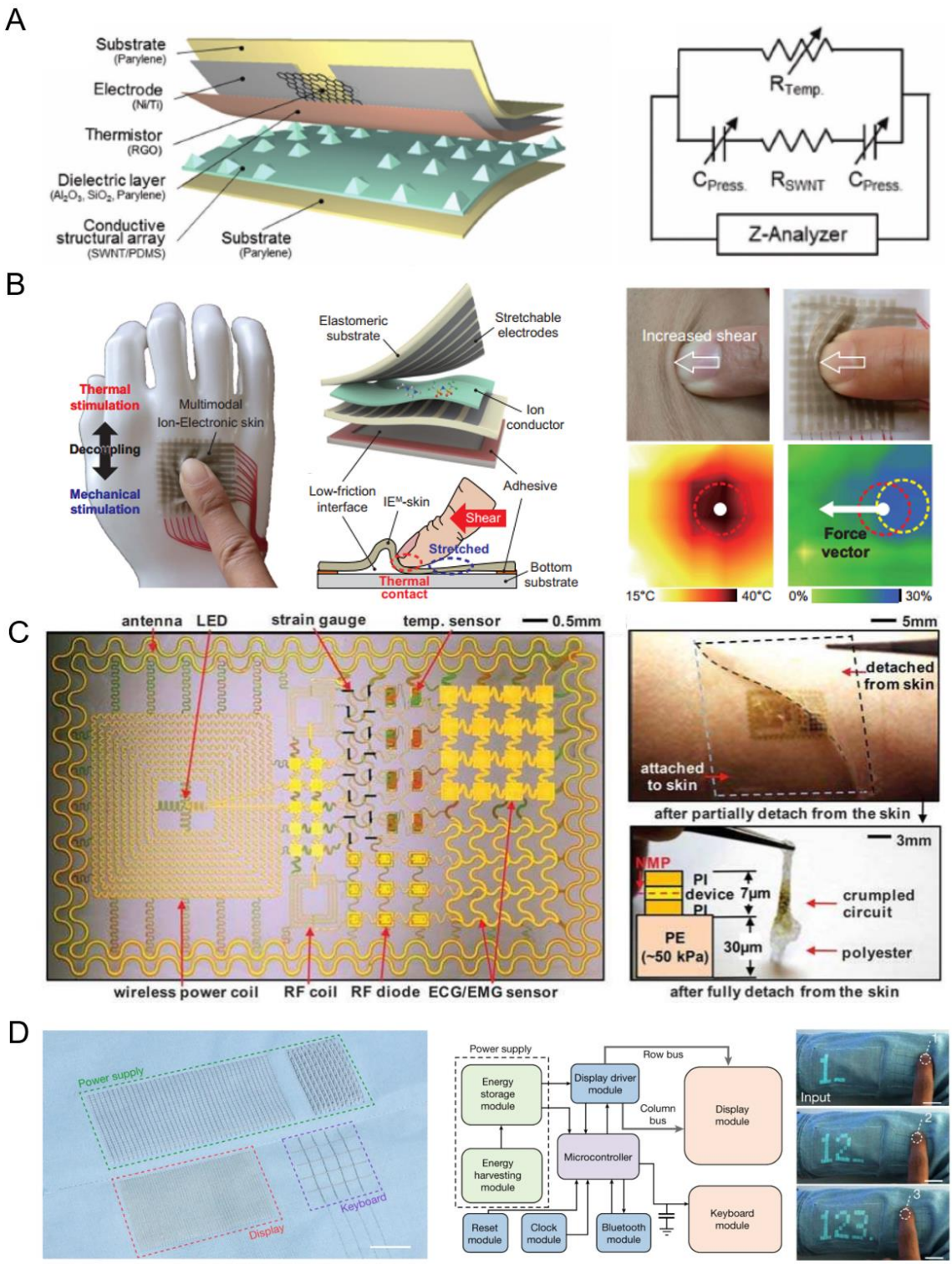

Figure 1.11 (A) a pressure and temperature independently-responding sensor.[102] (B) A sensing array for electronic skin.[14] (C) A highly integrated sensing system with various electronic elements.[99] (D) A flexible all-textile display.[104]

The other approach provides more capacitance changes to explore. Various wearable sensing systems have been exploited and applied in the field of human-machine interaction. Sensor array is a collection of close-set sensors on a specific plane, which provides spatial distribution of external stimulus. You *et. al.* designed a stretchable receptor with temperature and strain measuring modes.[14] The interactive interface of the electronic film would showcase the motion trajectory and temperature of applied fingers (**Figure 1.11B**). Collections of various elements are conducted as well. Kim *et. al.* constructed an epidemic electronics system for physiological signal detecting with various elements rationally distributed on a piece of stretchable elastomer film.[99] Electrophysiological, strain, temperature sensors, transistor and solar cell are included (**Figure 1.11C**). Different to the integration with high proportion of traditional rigid devices at the early stage, Shi *et. al.* integrated an all-textile display consisting of a main display, a keyboard and a power supply (**Figure 1.11D**).[104]

1.1.4.2 Self-powered system

The rapid advancement of wearable electronics and the growing demand for multifuctions of wearables (*e.g.,* sensing, integrating and processing) have prompted the development of effective and long-term power sources. For powering wearable electronics, the power supply must be flexible to fit the contours of the skin for comfortable wear. However, current rigid and heavy batteries limit the ability of flexible electronics to create smaller, thinner designs and comfortable use.

A new type of energy device called TENG based on advanced materials is developed to transfer surrounding mechanical energies to electrical energy, which is sustainable. Moving two strips of dielectric material, which hold opposing charges on their surfaces due to CE,[105] together or apart causes a pulse of current to flow. The current can be drawn off using electrodes and therefore mechanical movements are converted into electricity. **Figure 1.12** displayed an example of the published triboelectric series.[106] A material closer top in contact with a material closer bottom will charge positively, and vice-versa. TENG offers unique

advantages such as light weight, flexibility (made of polymers such as PA6, PEO, PDMS, PTFE, *etc.*), and scalability as it can be made by low-cost manufacturing techniques. This is in contrast with the conventional big, heavy electromagnetic generators that are made up of turbines, magnets and metal coils. More fundamentally, slow motions and oscillations in random directions, such as water waves, winds and human motions, that otherwise would be wasted can be perfectly used by TENG.

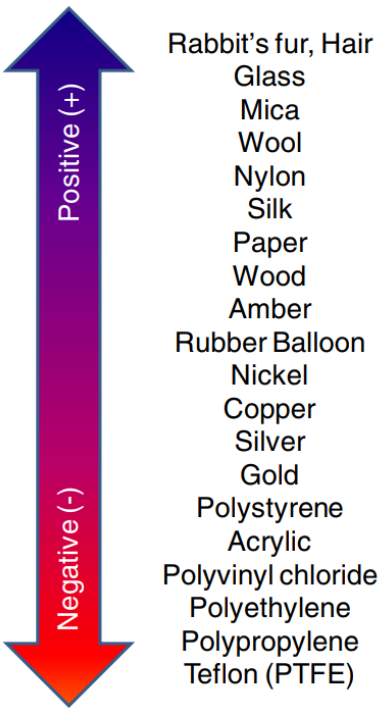

Figure 1.12 Triboelectric series.[106]

The amount of electricity generated at this stage is still small, but the TENG has shown its potential for wearable electronics. To fully exploit the potential of TENG, fundamental understanding of Contact electrification (CE) in dielectric materials is critical. Based on the mechanism research of TENG, I can optimize the TENG with the best electric performance for self-powered sensing system. Wang et al. demonstrated the CE mechanism in TENG and proposed an electron cloud-potential well model (**Figure 1.13**).[107-110] The charge transfers when the distance between two atoms from different dielectric materials is shorter than the bonding length (D). However, only parts of atoms from two surfaces, called active area, are close to D due to the roughness of solid materials and mismatch between the two surfaces, especially to the microscopic level. In this thesis, I have provided two universal methods to

enhance the active area to optimize TENG and developed self-powered sensors.

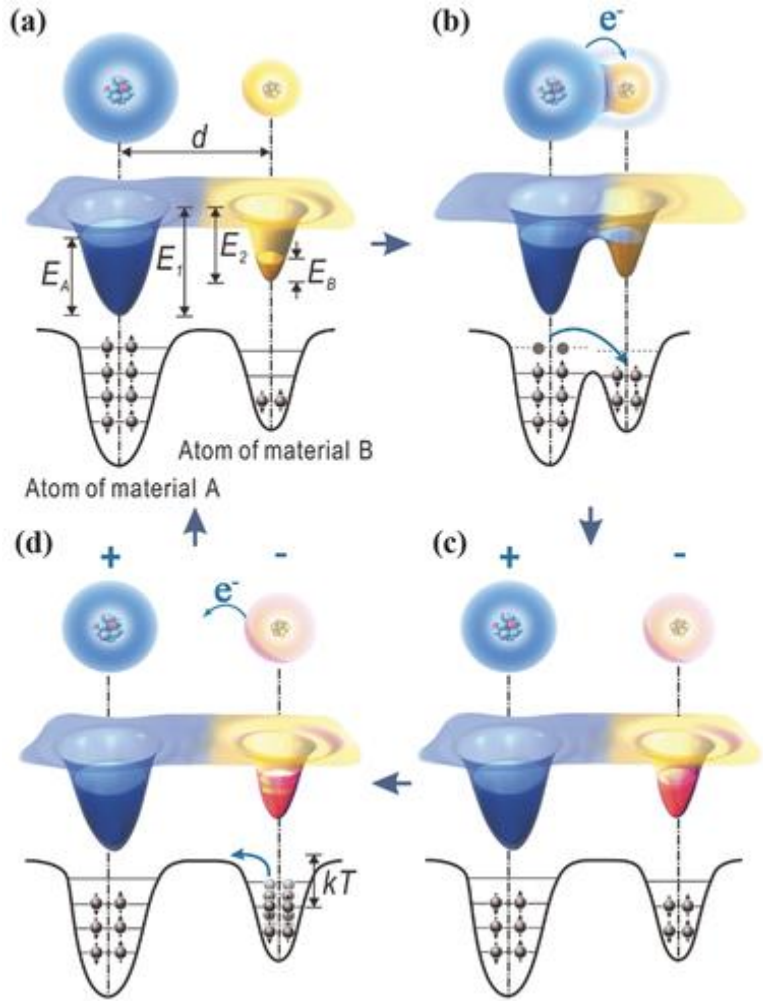

Figure 1.13 CE mechanism based on electron cloud-potential well model.[107-110]

1.1.4.3 Wireless sensing system

Generally, in sensor development, the test platform is an expensive instrument, such as an electrochemical workstation, impedance analyzer and electrometer. Ordinary people can't buy such a costly device to test their health in practice. Sensor testing is best conducted directly with a mobile or computer without any other special testing equipment. Therefore, it is vital to transmit the sensor signal to the mobile APP or computer software in Bluetooth or antenna, and read the electrical signal quantitatively and in real-time in the shape of a curve. **Figure 1.14** demonstrates a typical schematic of a wireless sensor to collect human daily activities (*e.g.,* respiratory, body movement) for human health monitoring, and the wireless transmission system can transfer the collected data to a remote center.[111]

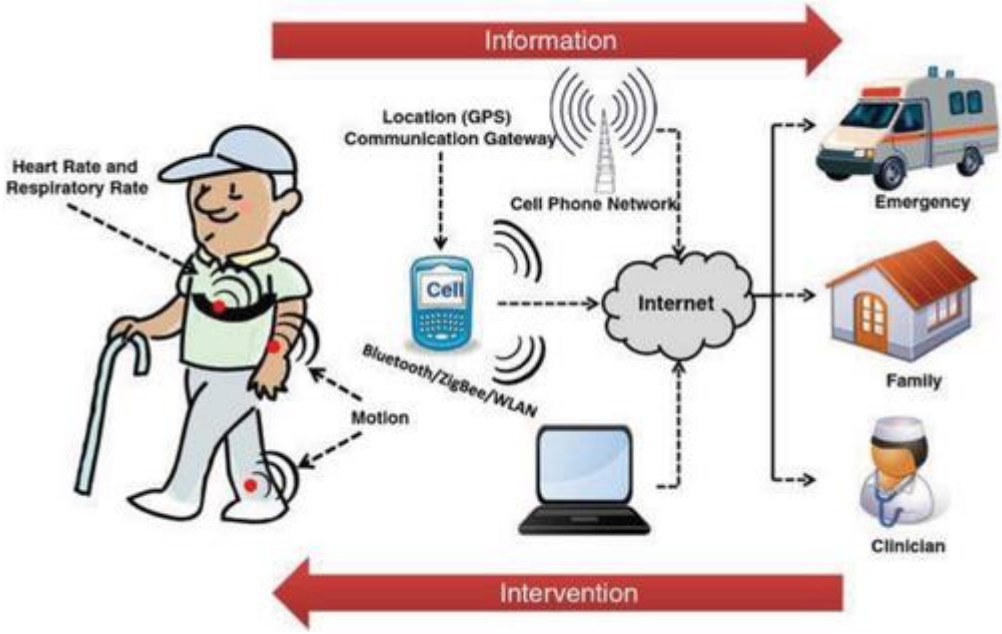

Figure 1.14 Wireless wearable sensors for physiological monitoring.[111]

Besides above-mentioned challenges, like poor sensor fabrication that affect sensor's performance, signal acquisition and analysis should be taken into account for developing wearable technology. Although great progress has been made in signal acquisition, the realization of perception within systems, that is, sensing signal processing, is still in its infancy, due to the lack of multi-disciplinary knowledge. Actually, many sensors fail to apply in real complex situations, since changes in electrical signals (resistance, capacitance or inductance) caused by changes in materials (conductivity, permittivity, permeability or deformation) induced by external stimuli (temperature, humidity or mechanical stimuli) are not clear from signal analysis.

These challenges should be resolved through multidisciplinary knowledge, hardware realization for system integration, novel sensing material preparation to improve sensor performance and then sensor integration for wearable application with more functions.

1.2 Research Objectives

The exploitation and development of advanced sensing materials is the premise of further research on their functionalization and application. In addition, the product structure design, manufacturing methods, sensing modes, performance measurements and practical

applications all need to be considered comprehensively. This thesis places an emphasis on the interdisciplinary research, including designing advanced sensing materials, optimizing sensor structure, acquiring and analyzing electrical signals, developing practical wearable applications and expanding sensor functions to wireless, sensor array and self-powered sensing system. Before further research into wearable sensors, it is necessary first to prepare the sensing materials with high sensitivity, stability, fast response and durability in a low-cost strategy. Furthermore, the sensor's incredible flexibility allows it to conform to human skin, which improves detection accuracy and wearable comfortability. Besides, electrical signals are analyzed carefully to clarify the relationship between electrical signals and external stimuli signals. In this way, it is clear that the external stimuli cause changes in the electrical signal (type and amount), to achieve reliable quantitative detection. In addition, to adapt to more practical applications, I expand sensor functions including wireless, sensor array and self-powered sensing system.

The following are the thesis's objectives:

1) To produce advanced materials, including metal nanostructures (copper-coated textile, nickel-coated textile and LM), 2D materials (h-BN and MXene) and polymers (PDA, PMMA, PEO, PA6, *etc.*)
2) To optimize sensor assembly process to achieve highly sensitive, stable, durable and reliable performance.
3) To apply the developed sensors to real-time monitor different human health status and activities, such as joints bending, running, speaking, blinking and breathing with cough, fever, runny and stuffy nose.
4) To realize reliable quantitative detection, careful analysis of change in electrical signal output produced by the source of the human signal is performed. It also provides good guidance for others who are studying the implications of electrical sensing signal output.
5) To mass-produce low-cost sensors with more useful functions: to introduce a TENG-based flexible power supply to improve the comfort and convenient use of wearable electronics; to design self-powered sensor array to achieve multi-point detection; to construct wireless sensor system to simplify the detection platform using an APP.

6) To contribute to low-cost population-wide self-monitoring of health status. The ultimate significance of this thesis is to improve quality of life and societal well-being: personal and customized healthcare monitoring could reduce disease and deaths as well as providing economic benefits.

1.3 Thesis Outline

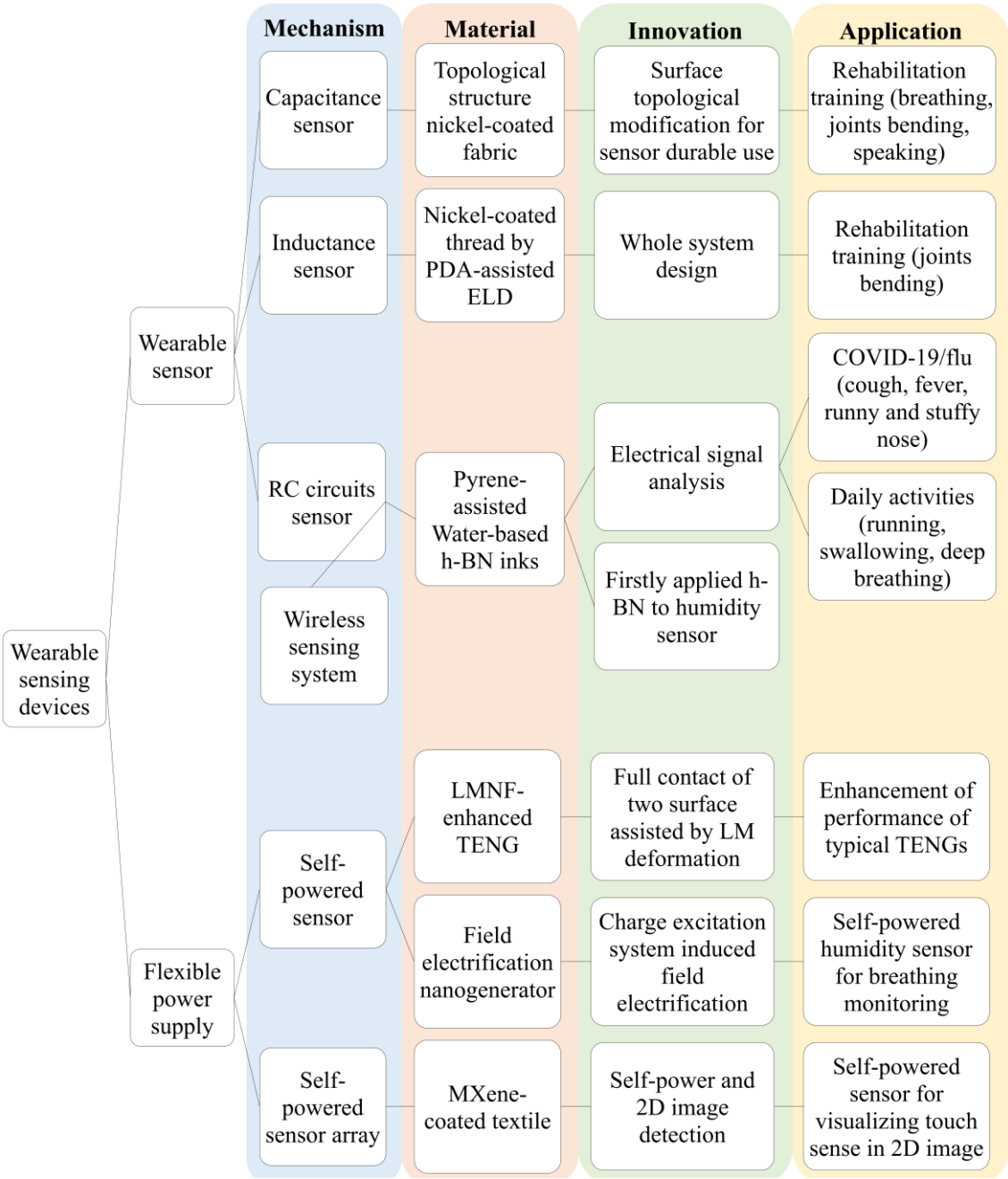

Figure 1.15 Outline of the thesis.

There are eight chapters in this thesis, as shown in **Figure 1.15**. **Chapter 1** provides an overview introduction of wearable sensor research. The research findings are summarized in the **Chapter 2**. In **Chapters 3 to 7**, the research results are offered in the form of scientific journals in detail. The fundamental relationship between chapters depicted in **Figure 1.9**. The conclusions as well as future work are discussed in **Chapter 8**.

References

[1] W. Gao, S. Emaminejad, H. Y. Y. Nyein, S. Challa, K. Chen, A. Peck, H. M. Fahad, H. Ota, H. Shiraki, D. Kiriya, D. H. Lien, G. A. Brooks, R. W. Davis, A. Javey, *Nature* **2016**, *529*, 509.

[2] Y. Cai, J. Shen, Z. Dai, X. Zang, Q. Dong, G. Guan, L. J. Li, W. Huang, X. Dong, *Adv. Mater.* **2017**, *29*, 1606411.

[3] T. Bu, T. Xiao, Z. Yang, G. Liu, X. Fu, J. Nie, T. Guo, Y. Pang, J. Zhao, F. Xi, C. Zhang, Z. L. Wang, *Adv. Mater.* **2018**, *30*, e1800066.

[4] T. Q. Trung, L. T. Duy, S. Ramasundaram, N.-E. Lee, *Nano Res.* **2017**, *10*, 2021.

[5] D. J. Wile, R. Ranawaya, Z. H. Kiss, *J. Neurosci. Methods* **2014**, *230*, 1.

[6] L. Q. Tao, K. N. Zhang, H. Tian, Y. Liu, D. Y. Wang, Y. Q. Chen, Y. Yang, T. L. Ren, *ACS nano* **2017**.

[7] H. Yan, L. Zhang, P. Yu, L. Mao, *Anal. Chem.* **2017**, *89*, 996.

[8] B. Samb, N. Desai, S. Nishtar, S. Mendis, H. Bekedam, A. Wright, J. Hsu, A. Martiniuk, F. Celletti, K. Patel, F. Adshead, M. McKee, T. Evans, A. Alwan, C. Etienne, *The Lancet* **2010**, *376*, 1785.

[9] I. Ali, S. Ali, *Disaster Med. Public Health Prep.* **2020**, 1.

[10] A. Cieza, K. Causey, K. Kamenov, S. W. Hanson, S. Chatterji, T. Vos, *The Lancet* **2020**, *396*, 2006.

[11] H. Joh, S. W. Lee, M. Seong, W. S. Lee, S. J. Oh, *Small* **2017**, *13*.

[12] Y. Liu, K. He, G. Chen, W. R. Leow, X. Chen, *Chem. Rev.* **2017**, *117*, 12893.

[13] M. Wang, Y. Luo, T. Wang, C. Wan, L. Pan, S. Pan, K. He, A. Neo, X. Chen, *Adv. Mater.* **2021**, *33*, e2003014.

[14]I. You, D. G. Mackanic, N. Matsuhisa, J. Kang, J. Kwon, L. Beker, J. Mun, W. Suh, T. Y. Kim, J. B.-H. Tok, *Science* **2020**, *370*, 961.

[15]R. Guinsburg, *Science* **2019**, *363*, 924.

[16]L. Chen, Y. Huang, L. Song, W. Yin, L. Hou, X. Liu, T. Chen, *ACS Appl. Mater. Interfaces* **2019**, *11*, 36259.

[17]W. Lu, W. Bai, H. Zhang, C. Xu, A. M. Chiarelli, A. Vázquez-Guardado, Z. Xie, H. Shen, K. Nandoliya, H. Zhao, *Sci. Adv.* **2021**, *7*, eabe0579.

[18]Z. Ma, Q. Huang, Q. Xu, Q. Zhuang, X. Zhao, Y. Yang, H. Qiu, Z. Yang, C. Wang, Y. Chai, Z. Zheng, *Nat. Mater.* **2021**, 20, 859.

[19]J. Kang, J. B. H. Tok, Z. Bao, *Nat. Electron.* **2019**, *2*, 144.

[20]S. Park, S. W. Heo, W. Lee, D. Inoue, Z. Jiang, K. Yu, H. Jinno, D. Hashizume, M. Sekino, T. Yokota, K. Fukuda, K. Tajima, T. Someya, *Nature* **2018**, *561*, 516.

[21]X. Yu, Z. Xie, Y. Yu, J. Lee, A. Vazquez-Guardado, H. Luan, J. Ruban, X. Ning, A. Akhtar, D. Li, B. Ji, Y. Liu, R. Sun, J. Cao, Q. Huo, Y. Zhong, C. Lee, S. Kim, P. Gutruf, C. Zhang, Y. Xue, Q. Guo, A. Chempakasseril, P. Tian, W. Lu, J. Jeong, Y. Yu, J. Cornman, C. Tan, B. Kim, K. Lee, X. Feng, Y. Huang, J. A. Rogers, *Nature* **2019**, *575*, 473.

[22]J. Lee, H. Kwon, J. Seo, S. Shin, J. H. Koo, C. Pang, S. Son, J. H. Kim, Y. H. Jang, D. E. Kim, T. Lee, *Adv. Mater.* **2015**, *27*, 2433.

[23]M.-S. Cao, X.-X. Wang, W.-Q. Cao, J. Yuan, *J. Mater. Chem. C* **2015**, *3*, 6589.

[24]D. R. Cooper, B. D'Anjou, N. Ghattamaneni, B. Harack, M. Hilke, A. Horth, N. Majlis, M. Massicotte, L. Vandsburger, E. Whiteway, V. Yu, *ISRN Condens. Matter Phys.* **2012**, *2012*, 1.

[25]F. Sun, M. Tian, X. Sun, T. Xu, X. Liu, S. Zhu, X. Zhang, L. Qu, *Nano Lett.* **2019**, *19*, 6592.

[26]X. Hu, M. Tian, T. Xu, X. Sun, B. Sun, C. Sun, X. Liu, X. Zhang, L. Qu, *ACS Nano* **2020**, *14*, 559.

[27]T. S. Mathis, K. Maleski, A. Goad, A. Sarycheva, M. Anayee, A. C. Foucher, K. Hantanasirisakul, C. E. Shuck, E. A. Stach, Y. Gogotsi, *ACS Nano* **2021**, *15*, 6420.

[28]B. Anasori, M. R. Lukatskaya, Y. Gogotsi, *Nat. Rev. Mater.* **2017**, *2*, 16098.

[29] A. Lipatov, A. Goad, M. J. Loes, N. S. Vorobeva, J. Abourahma, Y. Gogotsi, A. Sinitskii, *Matter* **2021**, *4*, 1413.

[30] M. Z. Seyedin, J. M. Razal, P. C. Innis, G. G. Wallace, *Adv. Funct. Mater.* **2014**, *24*, 2957.

[31] Y. Guo, M. T. Otley, M. Li, X. Zhang, S. K. Sinha, G. M. Treich, G. A. Sotzing, *ACS Appl. Mater. Interfaces* **2016**, *8*, 26998.

[32] S. Seyedin, P. Zhang, M. Naebe, S. Qin, J. Chen, X. Wang, J. M. Razal, *Mater. Horiz.* **2019**, *6*, 219.

[33] B. Cho, K. S. Park, J. Baek, H. S. Oh, Y. E. Koo Lee, M. M. Sung, *Nano Lett.* **2014**, *14*, 3321.

[34] X. Wang, X. Zhang, L. Sun, D. Lee, S. Lee, M. Wang, J. Zhao, Y. Shao-Horn, M. Dincă, T. Palacios, *Sci. Adv.* **2018**, *4*, eaat5780.

[35] B. J. Worfolk, S. C. Andrews, S. Park, J. Reinspach, N. Liu, M. F. Toney, S. C. Mannsfeld, Z. Bao, *Proc. Natl. Acad. Sci. U. S. A.* **2015**, *112*, 14138.

[36] H.-W. Chen, C. Li, *Chin. J. Polym. Sci.* **2019**, *38*, 435.

[37] Y. Yan, S. C. Warren, P. Fuller, B. A. Grzybowski, *Nat. Nanotechnol.* **2016**, *11*, 603.

[38] L. Chen, M. Lu, H. Yang, J. R. Salas Avila, B. Shi, L. Ren, G. Wei, X. Liu, W. Yin, *ACS Nano* **2020**, *14*, 8191.

[39] L. Chen, M. Lu, Y. Wang, Y. Huang, S. Zhu, J. Tang, C. Zhu, X. Liu, W. Yin, *Adv. Intell. Syst.* **2019**, *1*, 1900037.

[40] Y. Yu, X. Xiao, Y. Zhang, K. Li, C. Yan, X. Wei, L. Chen, H. Zhen, H. Zhou, S. Zhang, Z. Zheng, *Adv. Mater.* **2016**, *28*, 4926.

[41] P. Li, Y. Zhang, Z. Zheng, *Adv. Mater.* **2019**, *31*, e1902987.

[42] X. Wang, C. Yan, H. Hu, X. Zhou, R. Guo, X. Liu, Z. Xie, Z. Huang, Z. Zheng, *Chem. Asian J.* **2014**, *9*, 2170.

[43] A. K. Geim, *Science* **2009**, *324*, 1530.

[44] S. Afroj, S. Tan, A. M. Abdelkader, K. S. Novoselov, N. Karim, *Adv. Funct. Mater.* **2020**, *30*, 2000293.

[45] K. S. Novoselov, V. I. Fal'ko, L. Colombo, P. R. Gellert, M. G. Schwab, K. Kim, *Nature*

2012, *490*, 192.

[46]B. Fang, D. Chang, Z. Xu, C. Gao, *Adv. Mater.* **2020**, *32*, e1902664.

[47]H. Duan, D. Wang, D. G. Kurth, H. Mohwald, *Angew. Chem. Int. Ed. Engl.* **2004**, *43*, 5639.

[48]L. Hu, M. Chen, X. Fang, L. Wu, *Chem. Soc. Rev.* **2012**, *41*, 1350.

[49]H. Xia, D. Wang, *Adv. Mater.* **2008**, *20*, 4253.

[50]Yong Kyun Park, Sang Hoon Yoo, S. Park., *Langmuir* **2008**, *24*, 4370.

[51]Yong Kyun Park, S. Park., *Chem. Mater.* **2008**, *20*, 2388.

[52]S. Borini, R. White, D. Wei, M. Astley, S. Haque, E. Spigone, N. Harris, J. Kivioja, T. Ryhanen, *ACS nano* **2013**, *7*, 11166.

[53]U. Mogera, A. A. Sagade, S. J. George, G. U. Kulkarni, *Sci. Rep.* **2014**, *4*, 4103.

[54]H. Guo, C. Lan, Z. Zhou, P. Sun, D. Wei, C. Li, *Nanoscale* **2017**, *9*, 6246.

[55]J. Lee, S. Mulmi, V. Thangadurai, S. S. Park, *ACS Appl. Mater. Interfaces* **2015**, *7*, 15506.

[56]Y. Yang, W. Gao, *Chem. Soc. Rev.* **2019**, *48*, 1465.

[57]S. Yao, Y. Zhu, *Nanoscale* **2014**, *6*, 2345.

[58]L. Yu, Y. Feng, S. O. M. T. S. D, L. Yao, R. H. Soon, J. C. Yeo, C. T. Lim, *ACS Appl. Mater. Interfaces* **2019**, *11*, 33347.

[59]A. Sadeghi, A. Mondini, M. Totaro, B. Mazzolai, L. Beccai, *Adv. Eng. Mater.* **2019**, *21*, 1900886.

[60]O. Atalay, A. Atalay, J. Gafford, H. Wang, R. Wood, C. Walsh, *Adv. Mater. Technol.* **2017**, *2*, 1700081.

[61]O. Atalay, A. Atalay, J. Gafford, C. Walsh, *Adv. Mater. Technol.* **2018**, *3*, 1700237.

[62]C. Choi, J. M. Lee, S. H. Kim, S. J. Kim, J. Di, R. H. Baughman, *Nano Lett.* **2016**, *16*, 7677.

[63]H. Bi, K. Yin, X. Xie, J. Ji, S. Wan, L. Sun, M. Terrones, M. S. Dresselhaus, *Sci. Rep.* **2013**, *3*, 2714.

[64]P. He, J. R. Brent, H. Ding, J. Yang, D. J. Lewis, P. O'Brien, B. Derby, *Nanoscale* **2018**, *10*, 5599.

[65]D. Zhang, Y. Sun, P. Li, Y. Zhang, *ACS Appl. Mater. Interfaces* **2016**, *8*, 14142.

[66]J. Kim, M. Kim, M. S. Lee, K. Kim, S. Ji, Y. T. Kim, J. Park, K. Na, K. H. Bae, H. Kyun Kim, F. Bien, C. Young Lee, J. U. Park, *Nat. Commun.* **2017**, *8*, 14997.

[67]K. Pan, Y. Fan, T. Leng, J. Li, Z. Xin, J. Zhang, L. Hao, J. Gallop, K. S. Novoselov, Z. Hu, *Nat. Commun.* **2018**, *9*, 5197.

[68]Y. Xie, Z. Qu, M. Lu, W. Yin, H. Xu, S. Zhu, J. Tang, L. Chen, Q. Ran, Y. Zhang, *IEEE Sens. J.* **2020**, *20*, 1019.

[69]D. Teichmann, A. Kuhn, S. Leonhardt, M. Walter, *Sensors (Basel)* **2014**, *14*, 1039.

[70]A. Garcia Patino, M. Khoshnam, C. Menon, *Sensors (Basel)* **2020**, *20*.

[71]R. Wu, L. Ma, S. Liu, A. B. Patil, C. Hou, Y. Zhang, W. Zhang, R. Yu, W. Yu, W. Guo, X. Y. Liu, *Mater. Today Phys.* **2020**, *15*, 100243.

[72]M. Liu, X. Pu, C. Jiang, T. Liu, X. Huang, L. Chen, C. Du, J. Sun, W. Hu, Z. L. Wang, *Adv. Mater.* **2017**, *29*, 1703700.

[73]M. Jian, K. Xia, Q. Wang, Z. Yin, H. Wang, C. Wang, H. Xie, M. Zhang, Y. Zhang, *Adv. Funct. Mater.* **2017**, *27*, 1606066.

[74]C.-L. Choong, M.-B. Shim, B.-S. Lee, S. Jeon, D.-S. Ko, T.-H. Kang, J. Bae, S. H. Lee, K.-E. Byun, J. Im, Y. J. Jeong, C. E. Park, J.-J. Park, U.-I. Chung, *Adv. Mater.* **2014**, *26*, 3451.

[75]T. Yamada, Y. Hayamizu, Y. Yamamoto, Y. Yomogida, A. Izadi-Najafabadi, D. N. Futaba, K. Hata, *Nat. Nanotechnol.* **2011**, *6*, 296.

[76]L. Shaoting, Y. Hyunwoo, Z. Teng, P. G. Alberto, K. Hyunwoo, Y. Cunjiang, Z. Xuanhe, *Adv. Mater.* **2016**, *28*, 4497.

[77]J. J. Park, W. J. Hyun, S. C. Mun, Y. T. Park, O. O. Park, *ACS Appl. Mater. Interfaces* **2015**, *7*, 6317.

[78]J. He, P. Xiao, W. Lu, J. Shi, L. Zhang, Y. Liang, C. Pan, S.-W. Kuo, T. Chen, *Nano Energy* **2019**, *59*, 422.

[79]L. Zhang, J. He, Y. Liao, X. Zeng, N. Qiu, Y. Liang, P. Xiao, T. Chen, *J. Mater. Chem. A* **2019**, *7*, 26631.

[80]Z. Yang, Y. Pang, X. L. Han, Y. Yang, J. Ling, M. Jian, Y. Zhang, Y. Yang, T. L. Ren, *ACS Nano* **2018**.

[81]Y. Liang, P. Xiao, F. Ni, L. Zhang, T. Zhang, S. Wang, W. Zhou, W. Lu, S.-W. Kuo, T.

Chen, *Nano Energy* **2021**, *81*, 105617.

[82]C. H. Yang, Z. G. Suo, *Nat. Rev. Mater* **2018**, *3*, 125.

[83]Y. Jian, B. Wu, X. Le, Y. Liang, Y. Zhang, D. Zhang, L. Zhang, W. Lu, J. Zhang, T. Chen, *Research (Wash D C)* **2019**, *2019*, 2384347.

[84]F. Yin, W. Yue, Y. Li, S. Gao, C. Zhang, H. Kan, H. Niu, W. Wang, Y. Guo, *Carbon* **2021**, *180*, 274.

[85]J. He, P. Xiao, J. Shi, Y. Liang, W. Lu, Y. Chen, W. Wang, P. Théato, S.-W. Kuo, T. Chen, *Chem. Mater.* **2018**, *30*, 4343.

[86]S. W. Lee, H. G. Jung, J. W. Jang, D. Park, D. Lee, I. Kim, Y. Kim, D. Y. Cheong, K. S. Hwang, G. Lee, D. S. Yoon, *Sens. Actuators B Chem.* **2021**, *345*, 130361.

[87]A. D. Ugale, G. G. Umarji, S. H. Jung, N. G. Deshpande, W. Lee, H. K. Cho, J. B. Yoo, *Sensors Actuators B: Chem.* **2020**, *308*, 127690.

[88]W. Y. Chen, S. N. Lai, C. C. Yen, X. Jiang, D. Peroulis, L. A. Stanciu, *ACS Nano* **2020**, *14*, 11490.

[89]W. Y. Chen, X. Jiang, S. N. Lai, D. Peroulis, L. Stanciu, *Nat. Commun.* **2020**, *11*, 1302.

[90]R. C. Webb, A. P. Bonifas, A. Behnaz, Y. Zhang, K. J. Yu, H. Cheng, M. Shi, Z. Bian, Z. Liu, Y. S. Kim, W. H. Yeo, J. S. Park, J. Song, Y. Li, Y. Huang, A. M. Gorbach, J. A. Rogers, *Nat. Mater.* **2013**, *12*, 938.

[91]K. Sim, Z. Rao, Z. Zou, F. Ershad, J. Lei, A. Thukral, J. Chen, Q.-A. Huang, J. Xiao, C. Yu, *Sci. Adv.* **2019**, *5*, eaav9653.

[92]J. Yang, D. Wei, L. Tang, X. Song, W. Luo, J. Chu, T. Gao, H. Shi, C. Du, *RSC Adv.* **2015**, *5*, 25609.

[93]G. Landi, H.-C. Neitzert, *ACS Appl. Electron. Mater.* **2021**, *3*, 2790.

[94]D. H. Kim, J. Viventi, J. J. Amsden, J. Xiao, L. Vigeland, Y. S. Kim, J. A. Blanco, B. Panilaitis, E. S. Frechette, D. Contreras, D. L. Kaplan, F. G. Omenetto, Y. Huang, K. C. Hwang, M. R. Zakin, B. Litt, J. A. Rogers, *Nat. Mater.* **2010**, *9*, 511.

[95]P. C. Y. Chow, T. Someya, *Adv. Mater.* **2020**, *32*, e1902045.

[96]C. Wang, K. Xia, M. Zhang, M. Jian, Y. Zhang, *ACS Appl. Mater. Interfaces* **2017**, *9*, 39484.

[97]J.-C. Zhang, C. Pan, Y.-F. Zhu, L.-Z. Zhao, H.-W. He, X. Liu, J. Qiu, *Adv. Mater.* **2018**, *30*, 1804644.

[98]Z. Lou, S. Chen, L. Wang, R. Shi, L. Li, K. Jiang, D. Chen, G. Shen, *Nano Energy* **2017**, *38*, 28.

[99]D. H. Kim, N. Lu, R. Ma, Y. S. Kim, R. H. Kim, S. Wang, J. Wu, S. M. Won, H. Tao, A. Islam, K. J. Yu, T. I. Kim, R. Chowdhury, M. Ying, L. Xu, M. Li, H. J. Chung, H. Keum, M. McCormick, P. Liu, Y. W. Zhang, F. G. Omenetto, Y. Huang, T. Coleman, J. A. Rogers, *Science* **2011**, *333*, 838.

[100] I. You, D. G. Mackanic, N. Matsuhisa, J. Kang, J. Kwon, L. Beker, J. Mun, W. Suh, T. Y. Kim, J. B.-H. Tok, Z. Bao, U. Jeong, *Science* **2020**, *370*, 961.

[101] Z. Lei, Q. Wang, P. Wu, *Mater. Horiz.* **2017**, *4*, 694.

[102] G. Y. Bae, J. T. Han, G. Lee, S. Lee, S. W. Kim, S. Park, J. Kwon, S. Jung, K. Cho, *Adv. Mater.* **2018**, *30*, 1803388.

[103] T. Chen, Q. Shi, M. Zhu, T. He, L. Sun, L. Yang, C. Lee, *ACS Nano* **2018**, *12*, 11561.

[104] X. Shi, Y. Zuo, P. Zhai, J. Shen, Y. Yang, Z. Gao, M. Liao, J. Wu, J. Wang, X. Xu, Q. Tong, B. Zhang, B. Wang, X. Sun, L. Zhang, Q. Pei, D. Jin, P. Chen, H. Peng, *Nature* **2021**, *591*, 240.

[105] H. Baytekin, A. Patashinski, M. Branicki, B. Baytekin, S. Soh, B. A. Grzybowski, *Science* **2011**, *333*, 308.

[106] D. J. Lacks, R. Mohan Sankaran, *J. Phys. D: Appl. Phys.* **2011**, *44*, 453001.

[107] A. C. Wang, B. Zhang, C. Xu, H. Zou, Z. Lin, Z. L. Wang, *Adv. Funct. Mater.* **2020**, *30*, 1909384.

[108] S. Lin, L. Xu, L. Zhu, X. Chen, Z. L. Wang, *Adv. Mater.* **2019**, *31*, e1901418.

[109] C. Xu, Y. Zi, A. C. Wang, H. Zou, Y. Dai, X. He, P. Wang, Y. C. Wang, P. Feng, D. Li, Z. L. Wang, *Adv. Mater.* **2018**, *30*, e1706790.

[110] X. Li, J. Tao, X. Wang, J. Zhu, C. Pan, Z. L. Wang, *Adv. Energy Mater.* **2018**, *8*., 1800705.

[111] S. Patel, H. Park, P. Bonato, L. Chan, M. Rodgers, *J. neuroeng. rehabilitation* **2012**, *9*, 1.

Chapter 2 Summary of Papers

This thesis first constructed the metal nanostructures (*e.g.,* nickel, copper and LM) and 2D materials (*e.g.,* graphene, BN, MoS_2 and MXene) and other sensing materials. Different sensing materials can be precisely synthesized by chemical modification and functionalized to achieve various functions. Using the high performance sensors with their flexibility, high sensitivity, stability, and rapid responsiveness, I designed wearable sensors to observe and record the signals of different human physiological activities, such as joints bending, running, speaking, blinking, and breathing with cough, fever, runny and stuffy nose. Particularly, the electrical signals are analyzed through experimental and theoretical results. More importantly, combining these sensors with integrated circuits can enable wireless sensors and sensor arrays, enabling wearable sensors to be practical. In addition, conductive materials including nickel, copper, LM and MXene are combined with different polymers (*e.g.,* PMMA, PEO, PA6, PTFE, PDMS, etc.) to help self-powered sensing technology and applications in human healthcare.

Scientific publications in the chapters of this thesis are displayed in **Table 2.1**.

Table 2.1 The publications and manuscripts in the chapters of this thesis

Chapter	Publications
3	Textile-based capacitive sensor for physical rehabilitation via surface topological modification **L. Chen**, M. Lu, X. Liu, W. Yin, *et. al.* ***ACS Nano*** 2020, 14, 8191.
4	Whole system design of a wearable magnetic induction sensor for physical rehabilitation **L. Chen**, M. Lu, X. Liu, W. Yin, *et. al.* ***Adv. Intell. Syst.*** 2019, *1*, 1900037. (**Cover Paper**)
5	Wireless Humidity Sensors with Enhanched Stability and Sensitivity made with Water-based Hexagonal Boron Nitride Inks **L. Chen**, X. Song, M. Lu, W. Yin, C. Casiraghi, *et. al.* ***To be submitted***
6.1	High Charge Density Triboelectric Nanogenerators based on Liquid Metal Nanoparticles Assembled Films **L. Chen**, M. Lu, J. Luo, X. Liu, W. Yin, *et. al.* ***To be submitted***
6.2	A novel high performance nanogenerator - field electrification nanogenerator **L. Chen**, Y. Xie, M. Lu, J. Luo, X. Liu, W. Yin, *et. al.* ***To be submitted***
7	Self-powered Sensor Array using MXene-coated textile for Visualizing Touch Sense in 2D Image **L. Chen**, M. Lu, Z. Chen, W. Yin, *et. al.* ***To be submitted***

2.1 Summary of Contribution

Chapter 3

1) Presenting a novel topological modification method for producing textile-based wearable sensors with high efficiency.
2) This strategy realizes a conformal coating strong adhesion and high conductivity to cotton textile. The robust adhesion is attributed by the designed covalent and hydrogen-bonded entangled molecular topological structures. The thickness of the continual

coating is ~500 nm, realizing high conductivity. The metal growth mechanism was characterized via microscopy during ELD process.

3) The conductive textile was used as electrodes to fabricate capacitance sensor. The capacitive signal varied with the electrode motions (distance and angle) was analyzed by experiment results and theoretical simulations.
4) The prepared textile-based capacitive sensor shows outstanding stability (thousands of bending cycles) and durability (five washing cycles) for monitoring physical rehabilitation training, including abdominal breathing, speaking, swallowing, blinking and joint motions.

Chapter 4

1) Developing a proof-of-concept whole system design of an inductance sensor for monitoring joints bending activities.
2) A highly conductive thread is prepared by a PDA-assisted ELD process to realize robust chemical interaction (stable & durable).
3) Besides sensing material preparation, sensor assembly optimization, sensing signals acquisition, theoretical analysis and final sensor performance characterization are comprehensively considered.
4) During rehabilitation exercises, the inductance sensor exhibits a 6-fold inductance change in response to joint bending motions.

Chapter 5

1) We prepared a water-based h-BN via ultrasonic exfoliation technology, and firstly used h-BN as a wireless humidity sensor for monitoring nose breathing with typical symptoms of COVID-19 and flu.
2) Experimental result shows a decrease of resistance over six orders of magnitude and an increase of capacitance from 5% to 100% in the relative humidity (RH) range.
3) The detailed electronics signal analysis by modelling with RC parallel circuit is studied to determine how resistance and capacitance change the impedance (real and imaginary

parts) with the RH.

4) Using two parameters (*i.e.* imaginary and real parts) enable us to reach high sensitivity to the whole range of RH, and identify characteristics signals from breathing associated to different individuals and different activities (*e.g.,* watching video, reading, running, deep breathing and swallowing) and common symptoms of COVID-19 and flu, including coughing, fever, runny and stuffy nose.
5) Construction of wireless sensing system.

Chapter 6

Demonstrating two methods to enhance TENG performance as a flexible power supply.

6.1

1) First is to use LMNF-based TENG to achieve a full contact of two surfaces, and thus increase the charge density by more than three times.
2) LMNPs film is assembled at the water-air interface via Marangoni effect and Capillary force, and transferred to a solid surface to realize full contact between the two different surfaces assisted by deformation of LMNPs.
3) Agreement of experimental and theoretical results.
4) This work shows a universal strategy to improve the performance of different TENGs through a full contact between the two surfaces, with great prospects.
5) The electrical output, including voltage and charge density, in this work are quite higher compared with relative LM-based TENG.

6.2

1) Second is the design of self-powered Field Electrification Nanogenerator (FENG) consisting of a charge excitation system, an energy management module and a typical dielectric-dielectric nanogenerator, to realize the maximum electrification between two tribo-layers.
2) The proposed charge excitation system can supply a strong electric field, which causes

the extra abundant positive/negative charge on tribo-surfaces due to quantum tunneling effect, led to the maximum ~134-fold enhancement of output power density.

3) Study of the mechanism of the FENG electrical outputs enhancement via electrostatic potential (ESP) and surface potential distributions
4) Using the FENG as a flexible and sustainable power unit, a self-powered humidity sensor was designed as a novel design concept to passively monitor human health in real-time.

Chapter 7

1) A novel 2D material, MXene, was used to fabricate conductive fabric with stripes pattern as a self-powered capacitive sensor array for visualizing human touch sense in 2D image.
2) The system consists of a customized multi-channel EM instrument, a LabVIEW-based GUI and an innovative material MXene-coated textile.
3) The 64-bit conformal sensor array with capacitive sensing function can realize real-time, multipoint and quantitative detection, and intuitively visualize touch perception in 2D imaging.
4) A TENG structure was designed on the sensor array, to construct self-powered sensor array.
5) The findings should make an important contribution to the development of haptic devices, intelligent prostheses and intelligent robots.

2.2 Chapter 3: "Textile-Based Capacitive Sensor for Physical Rehabilitation via Surface Topological Modification" (*ACS Nano* 2020, *14*, 8191.)

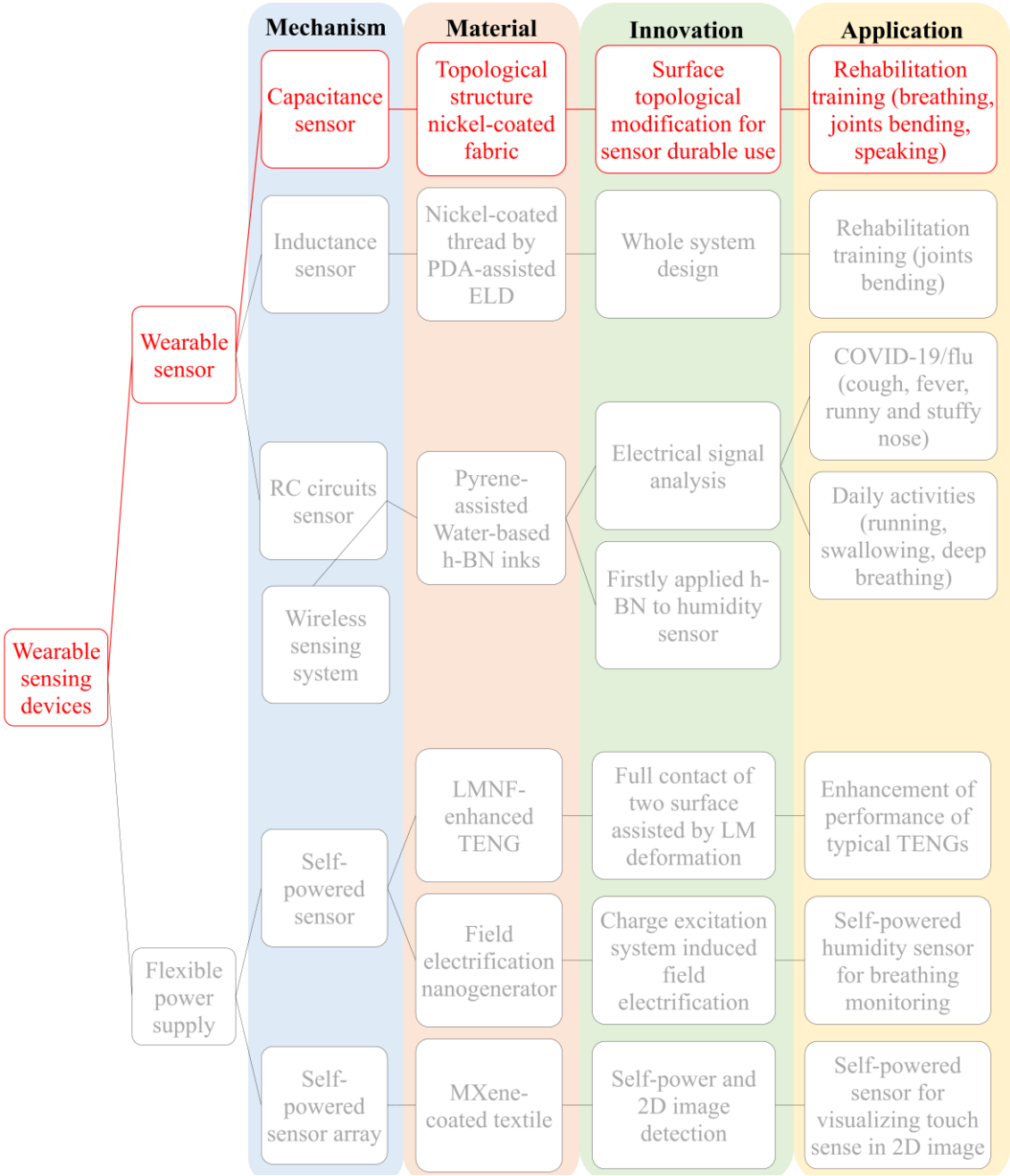

Figure 2.1 Outline of Chapter 3 in the thesis.

Wearable technologies are gaining popularity, particularly for continuous monitoring of diverse human health states. Current rigid sensors, on the other hand, have clear limitations, such as low durability and poor comfort. Here, a novel topological modification method is proposed for producing textile-based wearable sensors with high efficiency. This strategy realizes a conformal coating strong adhesion and high conductivity to cotton textile. The robust adhesion is attributed by the designed covalent and hydrogen-bonded entangled molecular topological structures. The thickness of the continual coating is ~500 nm, realizing high conductivity. The metal growth mechanism was characterized via microscopy during ELD process. The conductive textile was used as electrodes to fabricate capacitance sensor. The capacitive signal varied with the electrode motions (distance and angle) was analyzed by experiment results and theoretical simulations. The prepared textile-based capacitive sensor shows outstanding stability (thousands of bending cycles) and durability (five washing cycles) for monitoring physical rehabilitation training, including abdominal breathing, speaking, swallowing, blinking and joint motions.

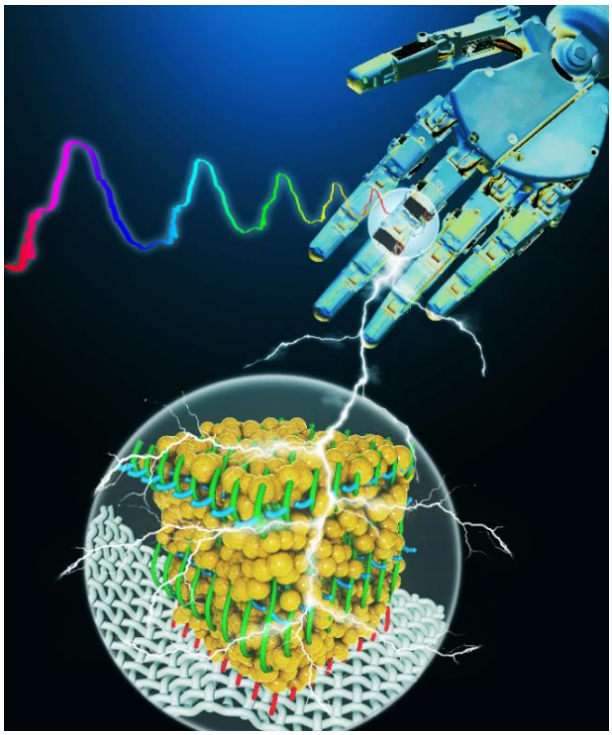

Figure 2.2 Graphical abstract of Chapter 3.

2.3 Chapter 4: "Whole System Design of a Wearable Magnetic Induction Sensor for Physical Rehabilitation" (*Adv. Intell. Syst.* 2019, 1, 1900037.)

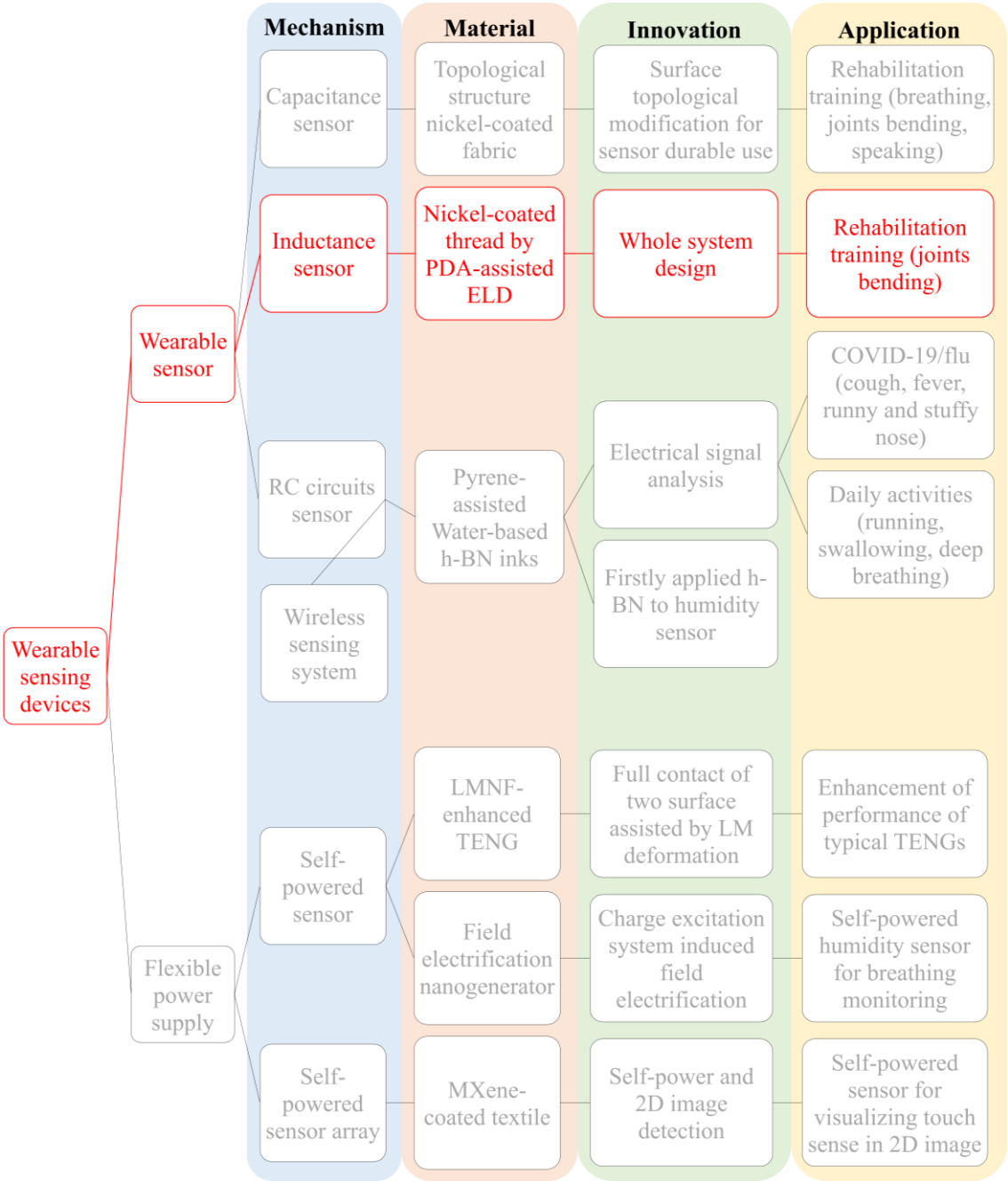

Figure 2.3 Outline of Chapter 4 in the thesis.

Wearable sensor technologies are gaining popularity as a means of continuously monitoring human health. It takes a lot of effort to produce advanced materials with great performance (*e.g.,* high sensitivity and responsiveness). However, isolated study of sensing materials is unlikely to meet significant demands for practically wearable applications. A proof-of-concept whole system design of an inductance sensor is developed for monitoring joints bending activities. A high conductive thread is prepared by a modified ELD process assisted by PDA. Besides sensing material preparation, sensor assembly optimization, sensing signals acquisition, theoretical analysis and final sensor performance characterization are comprehensively considered. During rehabilitation exercises, the inductance sensor exhibits a 6-fold inductance change in response to joint bending. This integrated design method introduces a new concept: a whole sensing system design, for wearable applications.

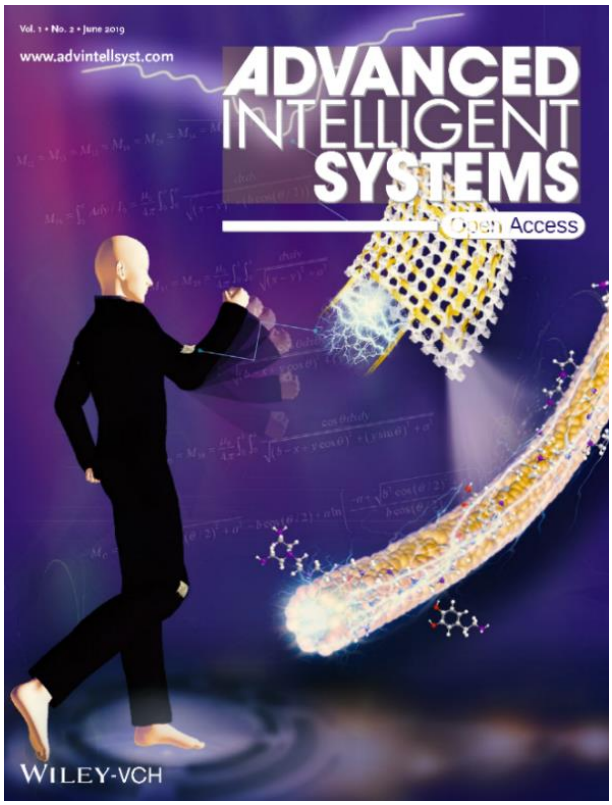

Figure 2.4 Graphical abstract of Chapter 4.

2.4 Chapter 5: "Wireless Humidity Sensors with Enhanched Stability and sensitivity made with Water-based Hexagonal Boron Nitride Inks" (To be submitted)

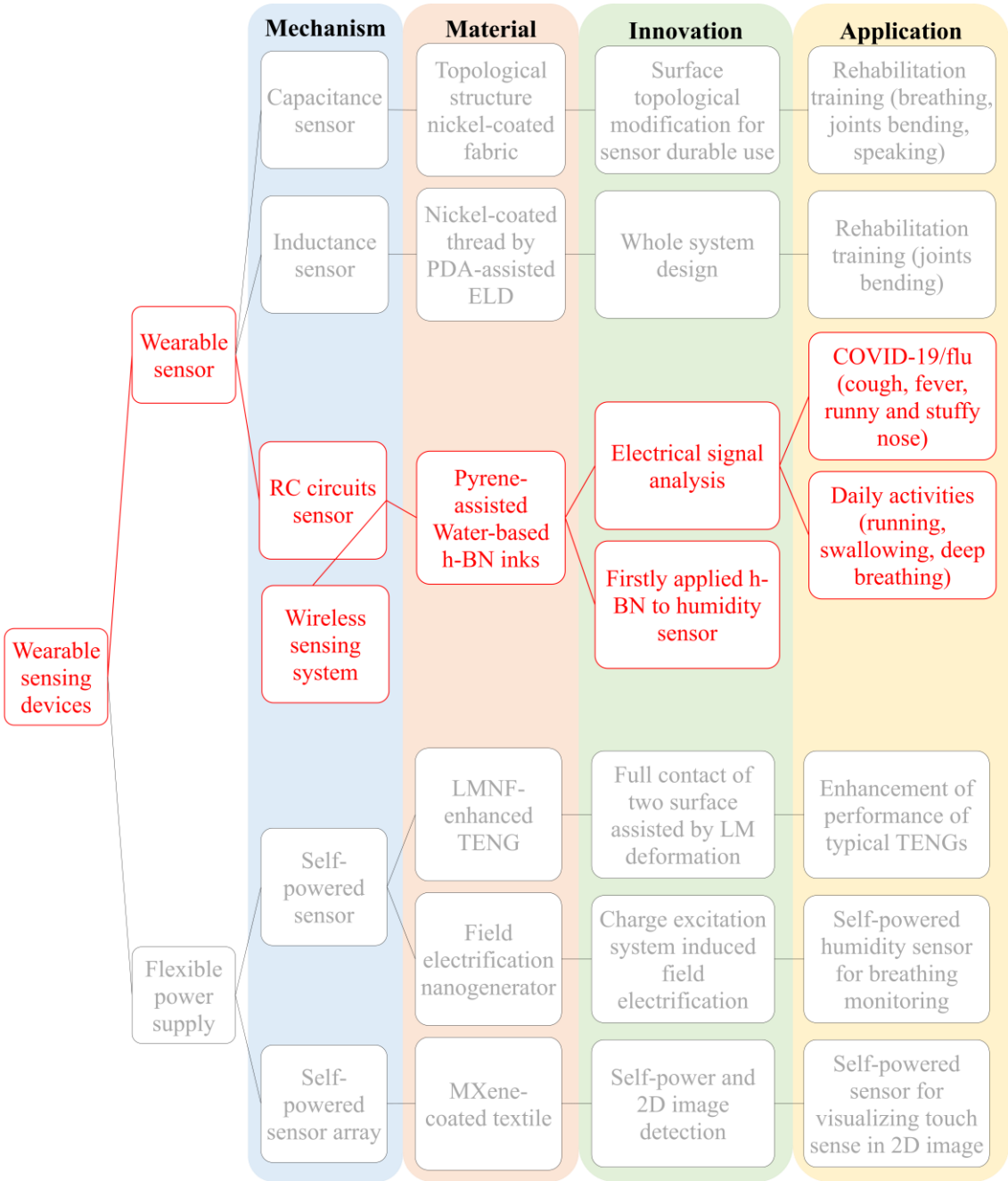

Figure 2.5 Outline of Chapter 5 in the thesis.

Hexagonal boron nitride (h-BN), a new generation of two-dimensional (2D) material has been recognized by its excellent stability under high temperature, high pressure and corrosive environment. However, the application of h-BN is still very limited. Here, I prepared hydrophilic h-BN via ultrasonic exfoliation technology and opened a new door to the application of h-BN in humidity sensing. Reversible dynamic process of hydrogen bond (H-O-S) formation and cleavage endows a decrease of resistance over six orders of magnitude and an increase of capacitance from 5% to 100% in the relative humidity (RH) range. Based on the effective sensor, a wearable respiration monitoring system with a user-friendly and portable wireless transmission module were constructed to record signals of different individuals and daily activities (*e.g.*, watching video, reading, running, deep breathing and swallowing) in real time. More importantly, the breathing sensor is successfully used to monitor several common symptoms of COVID-19 and flu, including cough, fever, runny and stuffy nose caused shortness of breath or difficulty breathing. The successful sensing system will accelerate the development of the next generation 2D material like h-BN in the field of long-term, real-time and non-contact wireless human health monitoring.

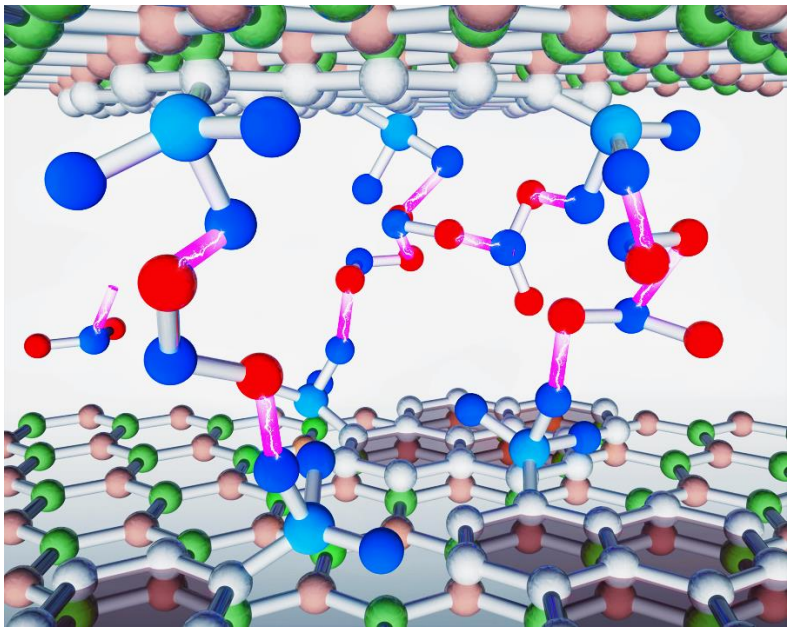

Figure 2.6 Graphical abstract of Chapter 5.

2.5 Chapter 6.1: "High Charge Density Triboelectric Nano-generators based on Liquid Metal Nano-particles Assembled Films" (To be submitted)

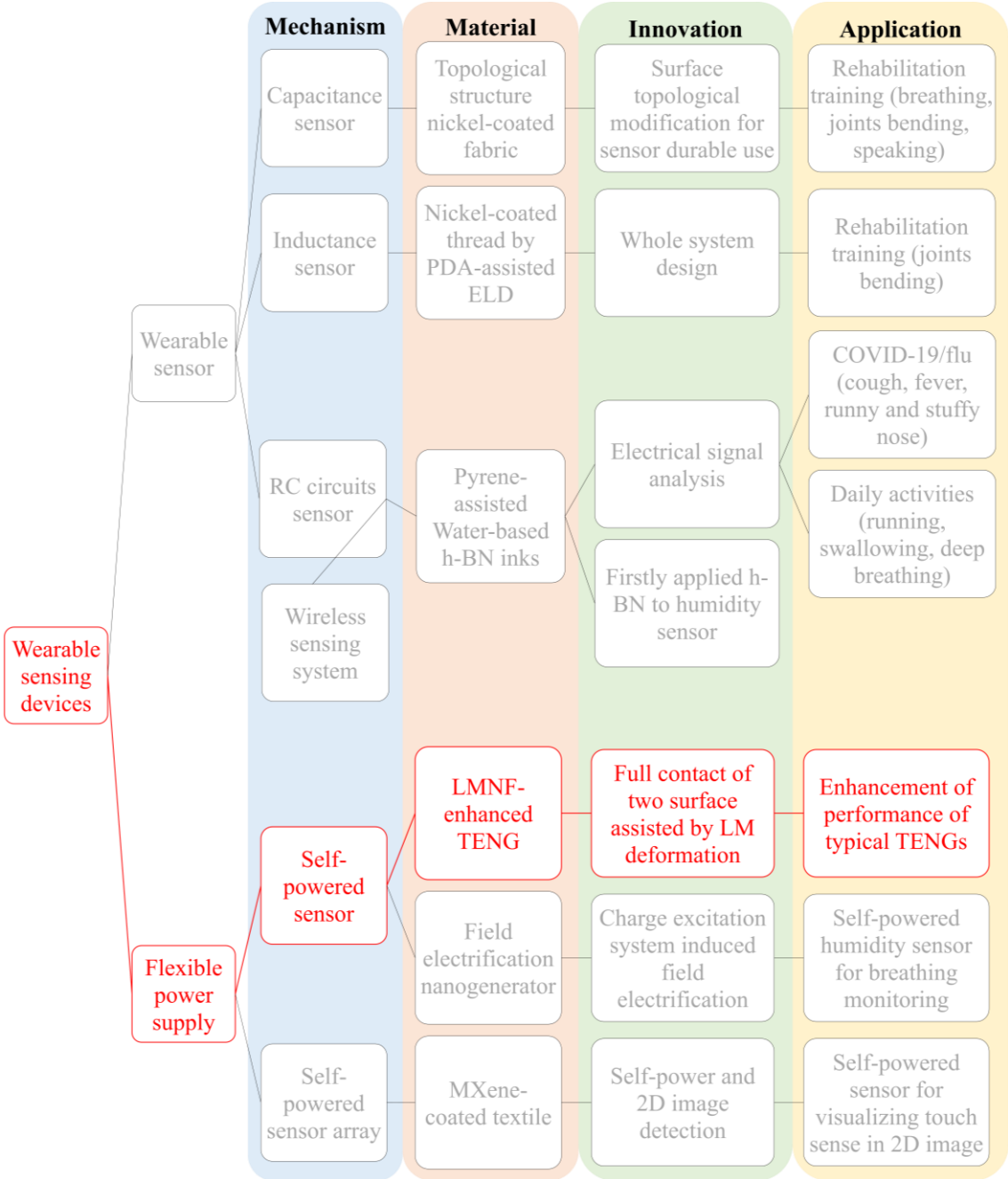

Figure 2.7 Outline of Chapter 6.1 in the thesis.

Coupled with contact electrification (CE) and electrostatic induction, triboelectric nanogenerators (TENGs) can harvest mechanical energy from the surrounding environment and convert it into electricity, hence are excellent candidates as a sustainable and mobile power source. CE occurs when the interatomic distance is shorter than the bonding length, however, only a small fraction of atoms from two solid surfaces can occur CE due to the roughness and mismatch natures of solid surfaces, which greatly limits the TENG performance. Here, liquid metal nanoparticles (LMNPs) film is assembled at the water-air interface via Marangoni effect and Capillary force, and transferred to a solid surface to realize full contact between the two different surfaces assisted by deformation of LMNPs, thereby increasing the charge density by more than three times. This work shows a universal strategy to improve the performance of different TENGs through full contact between the two surfaces, with great prospects.

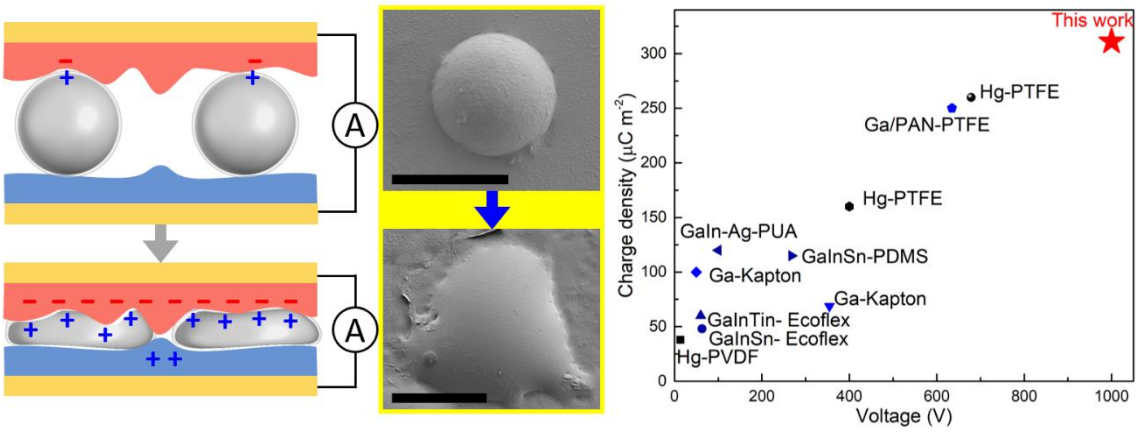

Figure 2.8 Graphical abstract of Chapter 6.1.

2.6 Chapter 6.2: "A Novel High Performance Nanogenerator - Field Electrification Nanogenerator" (To be submitted)

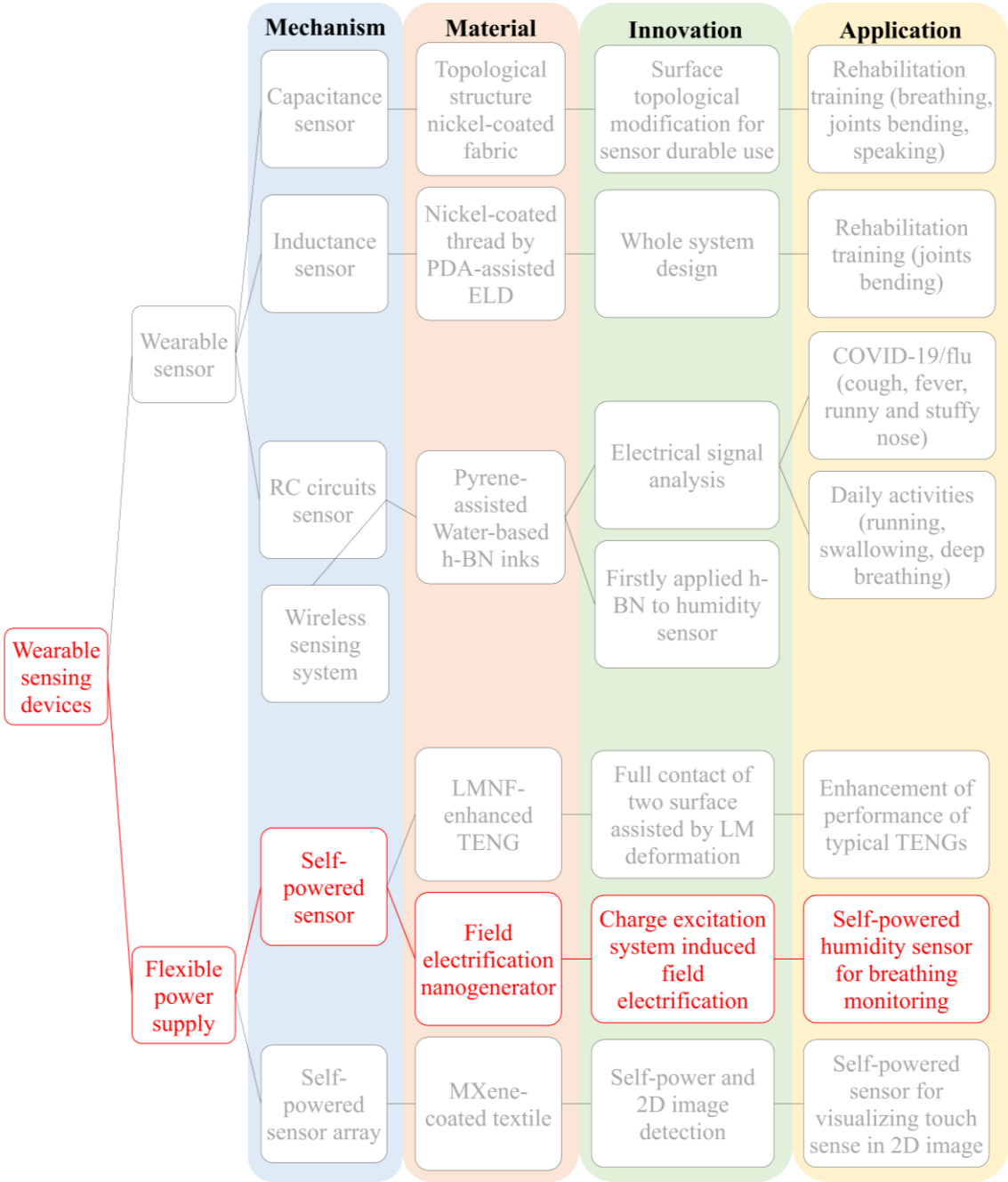

Figure 2.9 Outline of Chapter 6.2 in the thesis.

Triboelectric Nanogenerators (TENGs) can convert mechanical energy into electricity to serve as a sustainable and mobile power source for smart electronics. However, the output performance of conventional TENG is limited by low charge density, since only a small portion of atoms from two solid tribo-layers can be brought into contact electrification. Here, a self-powered Field Electrification Nanogenerator (FENG) is proposed, consisting of a charge excitation system, an energy management module and a typical dielectric-dielectric nanogenerator, to realize the maximum electrification between two tribo-layers. The proposed charge excitation system can supply a strong electric field, which causes the extra abundant positive/negative charge on tribo-surfaces due to quantum tunneling effect, and leads to the maximum ~134-fold enhancement of output power density. Using the FENG as a sustainable power unit, a self-powered humidity sensor was designed as a novel design concept to passively monitor human health in real-time.

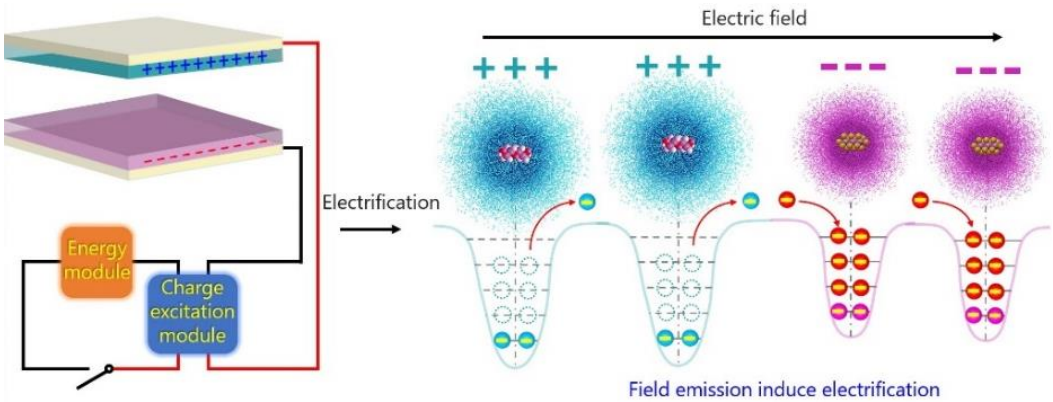

Figure 2.10 Graphical abstract of Chapter 6.2.

2.7 Chapter 7: "MXene-Coated Textile-based Self-Powered Sensor Array for Visualizing Touch Sense in 2D Image" (To be submitted)

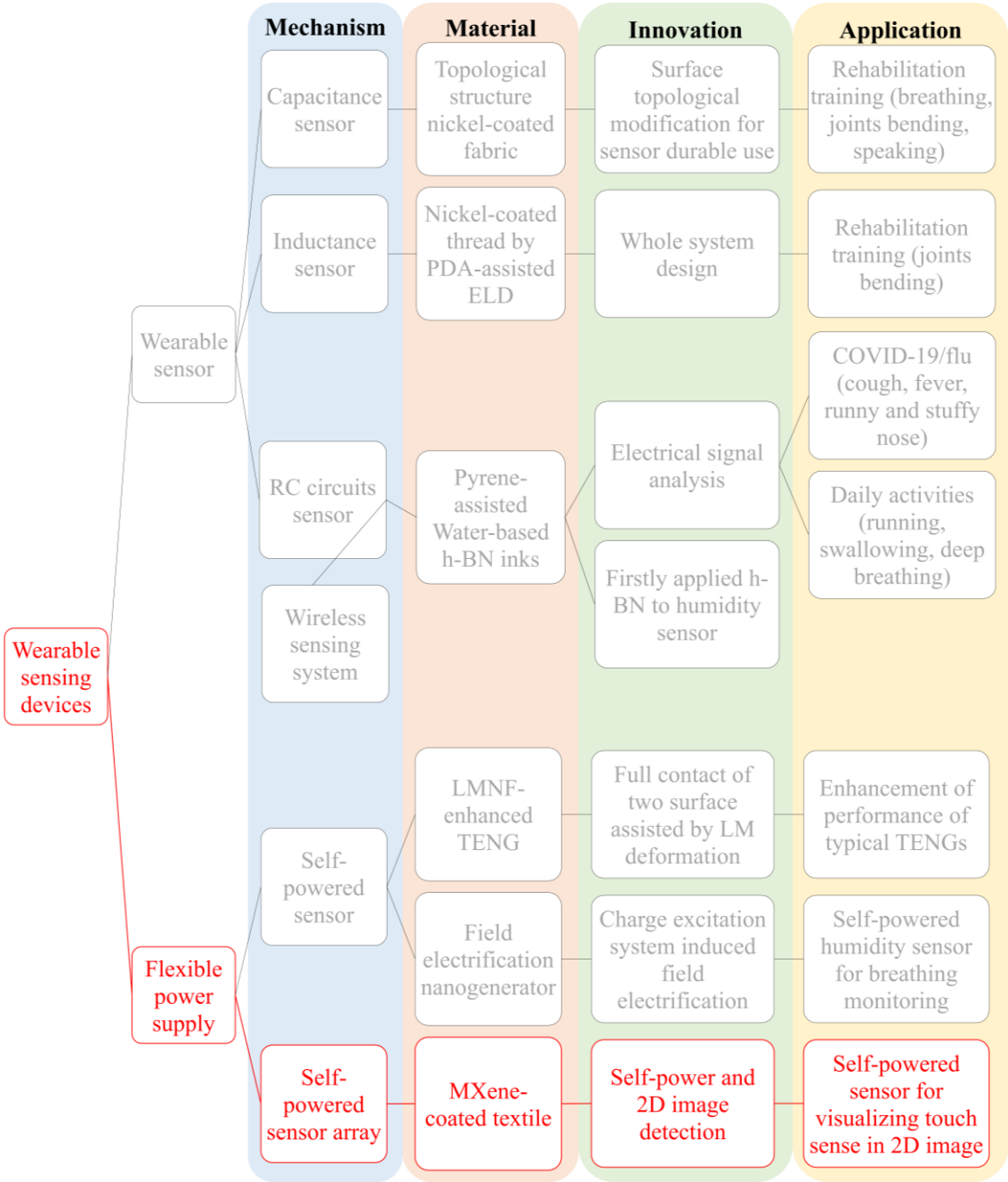

Figure 2.11 Outline of Chapter 7 in the thesis.

Human skin has different tactile receptors, which can sense the intensity of external stimuli at various locations. I propose a flexible multi-channel sensing system that can imitate tactile receptors to study the source and intensity of stimulus information. The system consists of a customized multi-channel EM instrument, a LabVIEW-based GUI and an innovative material MXene-coated textile. The 64-bit conformal sensor array with capacitive sensing function can realize real-time, multipoint and quantitative detection, and intuitively visualize touch perception in 2D imaging. Moreover, a TENG structure was designed on the sensor array, to construct self-powered sensor array. The findings should make an important contribution to the development of haptic devices, intelligent prostheses and intelligent robots.

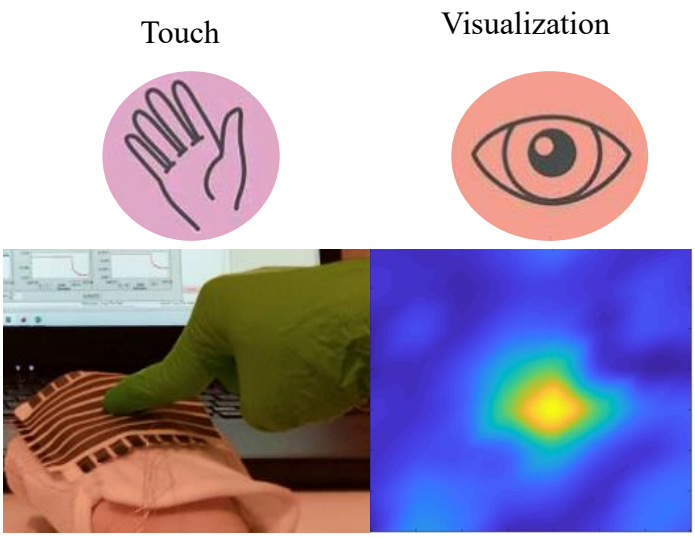

Figure 2.12 Graphical abstract of Chapter 7.

Chapter 3 Textile-Based Capacitive Sensor for Physical Rehabilitation via Surface Topological Modification

Abstract

Wearable sensor technologies, especially continuous monitoring of various human health conditions, are attracting increasing attention. However, current rigid sensors present obvious drawbacks, like lower durability and poor comfort. Here, a strategy is proposed to efficiently yield wearable sensors using cotton fabric as an essential component, and conductive materials conformally coat onto the cotton fibres, leading to a highly electrically conductive interconnecting network. To improve the conductivity and durability of conductive coatings, a topographical modification approach is developed with genus-3 and genus-5 structures, and topological genus structures enable cage metallic-seeds on the surface of substrates. A textile-based capacitive sensor with flexible, comfortable, and durable properties has been demonstrated. High sensitivity and convenience of signal collection have been achieved by the excellent electrical conductivity of this sensor. Based on results of in-deep investigation on capacitance, effects of distance and angles between two conductive fabrics contribute to the capacitive sensitivity. In addition, the textile-based capacitive sensor has successfully been used for real-time monitoring human breathing, speaking, blinking and joint motions during physical rehabilitation exercises.

3.1 Introduction

Comfortable and lightweight characters enable textile-based electronic devices to be used in a wider range of applications, compared to conventional heavy and cumbersome electronic devices.[1, 2, 3, 4] Particularly, this kind of electronic devices can be simply integrated into wearable formats (*e.g.*, clothing) and then provide real-time health monitoring continuously instead of expensive large equipment in a hospital or health center. In fact, as the global population ages, a growing number of elders are suffering from chronic health problems and declining functionality, which poses intensive stress on the healthcare system.[5] This textile-based wearable sensor can collect individual dynamic health signals to diagnose health conditions, which effectively release the burden of hospitalization.

There are various flexible and stretchable electrodes, made from carbon materials, conductive polymers and metal-based electronics, which could be used as conductive materials.[2, 6, 7] Carbon materials, including carbon nanotube (CNT) and graphene, have been used as flexible electronics with reliable and stable properties. The previous works, taken as an example, have shown graphene coating on the surface of polyurethane (PU) fibres to realize real-time wearable sensation.[8, 9] However, complicated processing, cytotoxicity, and the high-cost have limited the mass-production and practical applications. Conductive polymers, such as poly(3,4-ethylenedioxythiophene):poly(styrenesulfonate) (PEDOT:PSS) and polypyrrole (PPy), have gradually attracted attention due to their excellent flexible properties, while limitations in processing, stability and conductivity have still prevented their widespread uses.[2, 10, 11] Metals (*e.g.*, silver, aluminum, nickel and copper), as the most common conductive material, exhibit excellent ductility and outstanding conductivity. Nevertheless, the bulk metals are rigid, which limits the application in wearable electronics. When the metal coating is reduced to the micrometer/nanometer scale, it has excellent flexibility and can be combined with fibres to form a flexible conductive fabric or electrode,[12, 13, 14] which dominates the majority of market. However, due to the lack of adhesion between substrates and metal coatings, the durability of the commercialized conductive fabrics and electrodes should be improved.

Until now, several efforts have developed to fabricate textile-based electronic devices, such as atomic layer deposition,[15] physical vapor deposition,[16] electrodeposition,[17] chemical solution process,[12] and polymer-assisted metal deposition (PAMD).[18, 19, 20, 21] PAMD consists of three steps (**Figure 3.1A**), polymer grafting, catalyst loading into polymer network and electroless deposition (ELD) of metal nanoparticles.[22] It has received the most attention contributed by manufacturing conductive textiles in a user-friendly and money-saving way. Unfortunately, some drawbacks still exist in the conventional PAMD process.[23] Toxic solvent like toluene is frequently used in surface-initiated radical polymerization, which is undesirable in wearable textiles.[24, 25] Traditional surface-initiated radical polymerization offers low yields and requires nitrogen protection. Very recently, dopamine[14, 20] and tannic acid[18] were introduced to the surface-grafted polymer layer, which is environment-friendly and mass-producible. However, the process of oxypolymerization is time-consuming and difficult to control. The weak hydrogen bonds between the substrate and the surface-grafted linear polymer (**Figure 3.2A**) may cause the polymer in some regions to fall off. Thus, a controllable chemical reaction process with robust interaction bonds is highly desired.

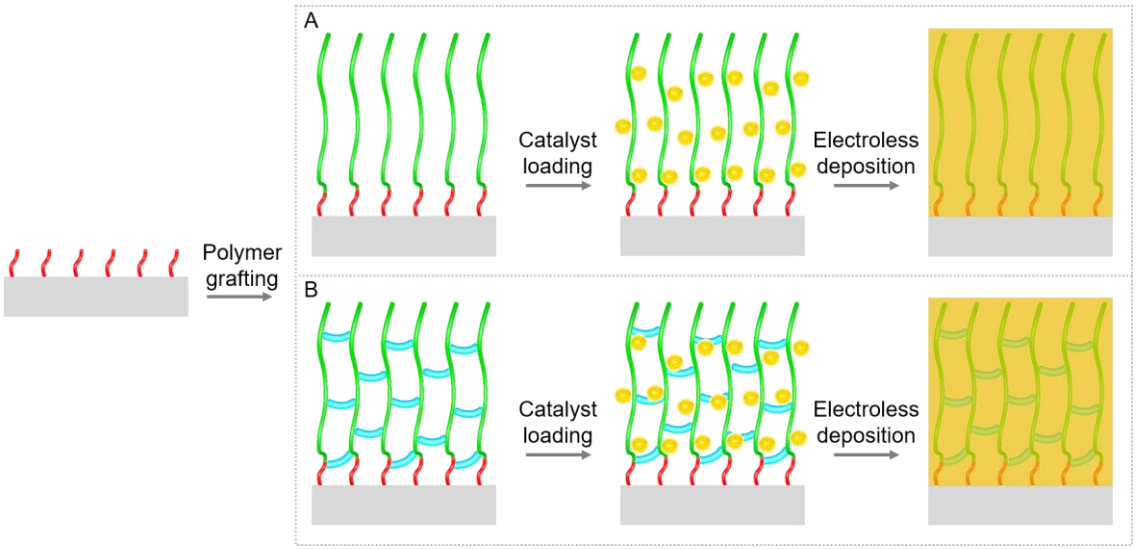

Figure 3.1 Schematic illustration of the PAMD fabrication, (A) traditional surface-grafted polymer, (B) topologies adhesion of polymer network in this work.

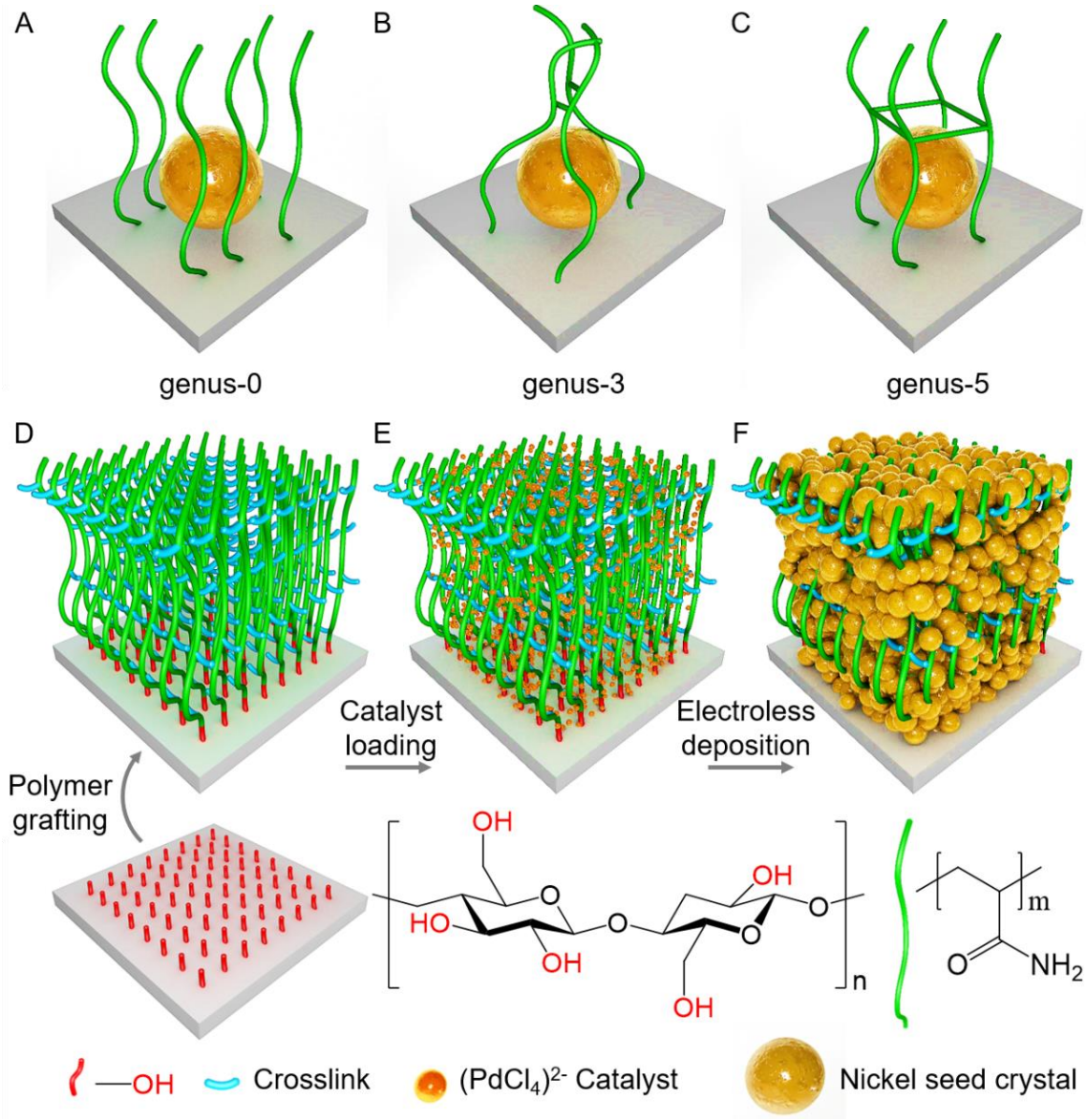

Figure 3.2 Genus-0 (A), genus-3 (B) and genus-5 (C) surface to cage catalyst-based nickel seed crystal, and schematic illustration of the PAMD fabrication via surface nanotechnology, involved three steps (D) topologies entangled grafting of polymer networks across the gaps and surfaces of cotton fibres, (E) immobilization of catalysts in the polymer networks, (F) and subsequent ELD of nickel nanoparticles at the catalytic active sites to form a nickel nanoparticle film on the surface of cotton fibres.

Herein, the ‘das Geschlecht (genus)’ of the surface from mathematic is proposed to develop a universal strategy in surface modification, and to understand the relationship of surface topology and performances. Mathematician Riemann studied the topology of surfaces, and

Clebsch considered surfaces from a more algebraic geometric viewpoint, called p 'das Geschlecht (genus)' of the surface to show invariant determines the surface.[26] In traditional materials surface modification, there are no any topographical interactions between coatings and substrates (genus-0, **Figure 3.2A**). In this work, a topographical modification is developed to improve the surface adhesion force of coating. Genus-3 (**Figure 3.2B**) and genus-5 surface (**Figure 3.2C**), inspired by a common synthesis method of the hydrogel structure, were introduced by topographical modification of crosslinked polymers (**Figure 3.2C and 3.3**). Catalyst-based nickel seed crystals are caged by the genus-3 and genus-5 structures (**Figure 3.2D and 3.2F**), to upsurge the density of seed crystals on the surface of modified substrates, and to increase the conductivity in the following deposition process.[27, 28, 29] Benefitted from topological adhesion, the robust chemical network enables the subsequent electroless deposited nickel nanoparticles to coat onto the cotton fabric (**Figure 3.1B**). The obtained conductive fabric can act as a capacitive sensor with high sensitivity. I used the capacitive sensor to investigate the fundamental properties of capacitance change level monitoring. As a proof of concept, it was applied for real-time monitoring of individual respiration, speaking and joint motions during physical rehabilitation exercises.

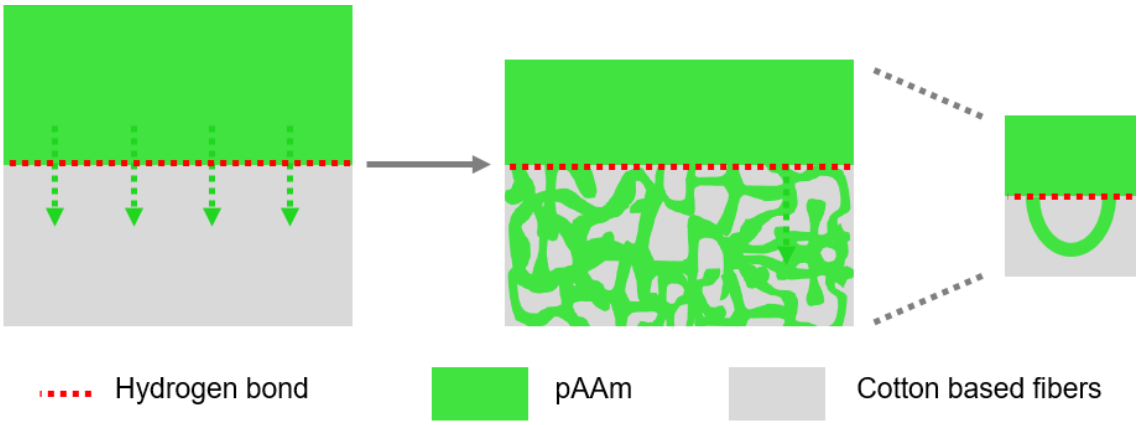

Figure 3.3 Macroscopic topologies of pAAm adhesion into cotton fibres, (1) thread-hole topology formed between the pAAm and the fibres, (2) bond topology through hydrogen bond formed between amine groups of the pAAm and hydroxyl groups of the fibres.

3.2 Experimental Section

Materials and Instrumentation. Ammonium tetrachloropalladate(II) [$(NH_4)_2PdCl_4$], nickel sulfate hexahydrate ($NiSO_4$ $6H_2O$), acrylamide (AAm) N,N'-methylene bis(acrylamide) (BIS), potassium persulfate (KPS) and all other chemicals were purchased from Sigma-Aldrich. All textile substrates were obtained from the Dye House at the University of Manchester. Scanning electron microscopy (SEM) was performed at a ZEISS Ultra-55 instrument. X-ray diffraction (XRD) data were collected using a Bruker D8 Discover (A25) theta-theta diffractometer (660 mm diameter) with a LynxEye 1D Strip detector in Bragg-Brentano geometry employing Cobalt Point/Line Focus X-ray tube with Iron kβ absorber (0.02 mm; Kβ = 1.62079 Angstrom) producing Kα radiation (Kα1 = 1.78897 Angstrom, Kα2 = 1.79285 Angstrom, Kα ratio 0.5, Kαav = 1.79026 Angstrom). Fourier transform infrared (FTIR) spectra were recorded with a Nicolet NEXUS 670 FTIR spectrometer with a liquid nitrogen cooled high-sensitivity mercury cadmium telluride (MCT) detector.

Polymer modification of cotton fabric. Firstly, cotton fabric was immersed into AAm monomer aqueous solution with 10 g/L AAm, 0.4 g/L BIS and 0.4 g/L KPS at 60 ℃ heating for 6h. After the thermally induced radical polymerization, the poly (acrylamide) (pAAm) was chemically cross-linked with cellulose on the surface of the cotton fabric.

Palladium catalyst coated fibre/fabrics. The pAAm-based fibre/fabrics were washed with deionized (DI) water and hydrochloric acid (pH = 3~5) to protonate the amino groups, and immersed into an $(NH_4)_2PdCl_4$ aqueous solution (10×10^{-3} M) under dark condition for 2 h, followed by rinsing with water to remove the excess catalyst inks.

Nickel-coated fibre/fabrics. Nickel-coated fibre/fabrics preparation is an improvement on our previous reports.[20] The nickel electroless plating was performed in an ELD bath containing a 1:1 volumetric proportion of nickel-to-reductant stocks at room temperature. A nickel stock solution consisting of 20 g/L lactic acid, 40 g/L sodium citrate and 80 g/L $NiSO_4$ $6H_2O$

was prepared in advance. A fresh reductant solution containing 10 g/L dimethylamine borane in DI water was prepared separately. After mixing, the solution was adjusted with sodium hydroxide to keep the pH value at 8 to 10. The as-prepared nickel-coated fibre/fabrics were washed with water and dried in the oven for future use.

Copper-coated fibre/fabrics. The copper electroless plating was performed in an ELD bath containing a 30:1 volumetric proportion of copper-to-reductant stocks at room temperature. A copper stock solution consisting of 13 g/L sodium hydroxide, 30 g/L potassium sodium tartrate and 15 g/L copper sulfate pentahydrate was prepared in advance. 1 mL butyraldehyde was added to 30 mL copper stock solution and the mixture was left to stand for the night. Then, 10 mL fresh sodium borohydride (2 mg/L) in ice water was prepared to accelerate the copper reduction process. The as-prepared copper-coated fibre/fabrics were washed with water and dried at room temperature for future use.

Sensor Description. 3 sizes of conductive fabrics were used, (1) 13 mm ×37 mm for breathing activities, swallow and sounds monitoring, (2) 3 mm ×30 mm for blink and head movements monitoring, and (3) 7 mm ×16 mm for finger joint activity monitoring. For breathing detection, a fabric was integrated into tights and another one was fixed on the inside of a belt. For other motion detection, two conductive fabrics with the same size were integrated into different parts of the tights.

MCR-Hand Description. In this work, a robotic hand combining linkage and tendon driven system was designed according to the size and geometry of a real hand, named MCR-Hand. This hand (about 21cm) has 4 jointed fingers and 2-split palms. All joints of the MCR-Hand were driven by built-in 18 servomotors. All servos, wires and actuators were inside of the palm. Ordinary gloves could be worn by the robotic hand to make it match more closely to the human hand. So the sensor for the MCR-Hand joints, motion monitoring could be assembled into normal gloves, which is user-friendly.

Capacitance Data Acquisition. The Zurich Instruments MFIA Impedance Analyzer was used to carry out the electrical signals. A four-terminal configuration was used to interface the capacitive sensor with the impedance analyzer. The excitation frequency to carry out the capacitive measurements was fixed at 20 and 200 kHz due to its good signal-to-noise ratio (SNR). Therefore, the measurement is almost real-time since the response time is 50 and 5 us. The amplitude of voltage was fixed at 1 V. All experiments were performed at room temperature (298 K).

The relationship between the sensor impedance and its capacitance is described as

$$Z = \frac{1}{j\omega C} \tag{3.1}$$

where the real part of the impedance Z is probe resistance R, and imaginary part ωC represents reactance.

Generally, R can be neglected. After obtaining impedance results, real part C values are defined as

$$C = \frac{1}{\omega Z_{imag}} \tag{3.2}$$

For a certain constant frequency (f), part ω is a fixed parameter,

$$\omega = 2\pi f \tag{3.3}$$

where Z_{imag} is the impedance imaginary part of the impedance measured by the sensor connected with the Zurich Instruments MFIA Impedance Analyzer.

Therefore, different C values could be measured for the detection of human motions.

3.3 Results and Discussion

3.3.1 Characterization of conductive fibres

The microscopic morphologies of fabric composites were characterized by SEM. AAm uniformly crosslinking with the cotton surface was supported by no obvious morphology difference between the pristine cotton fabric and AAm-crosslinking fabric (**Figure 3.4A and 3.4B).** Nickel nanoparticles densely aggregate on the fabric surface (**Figure 3.4C**). Genus is used to describe an orientable surface, which can be defined in terms of the Euler character-

istic χ, *via* the relationship $\chi = 2 - 2g$ for closed surfaces. It is clear in **Figure 3.4A**, the surface grafted polymer brushes are no inter-connection between each other, so that the genus number of the closed surface is 0. And in **Figure 3.4B** and **3.4C**, the linked caged structures is developed, which can capture catalysts and metallic seeds *via* several closed surfaces, according to genus 3 and 5. The closed surfaces formed cage could tether more catalysts and metallic seeds on the surface of substrates, leading to a higher density of metallic deposition, as well as higher conductivity.

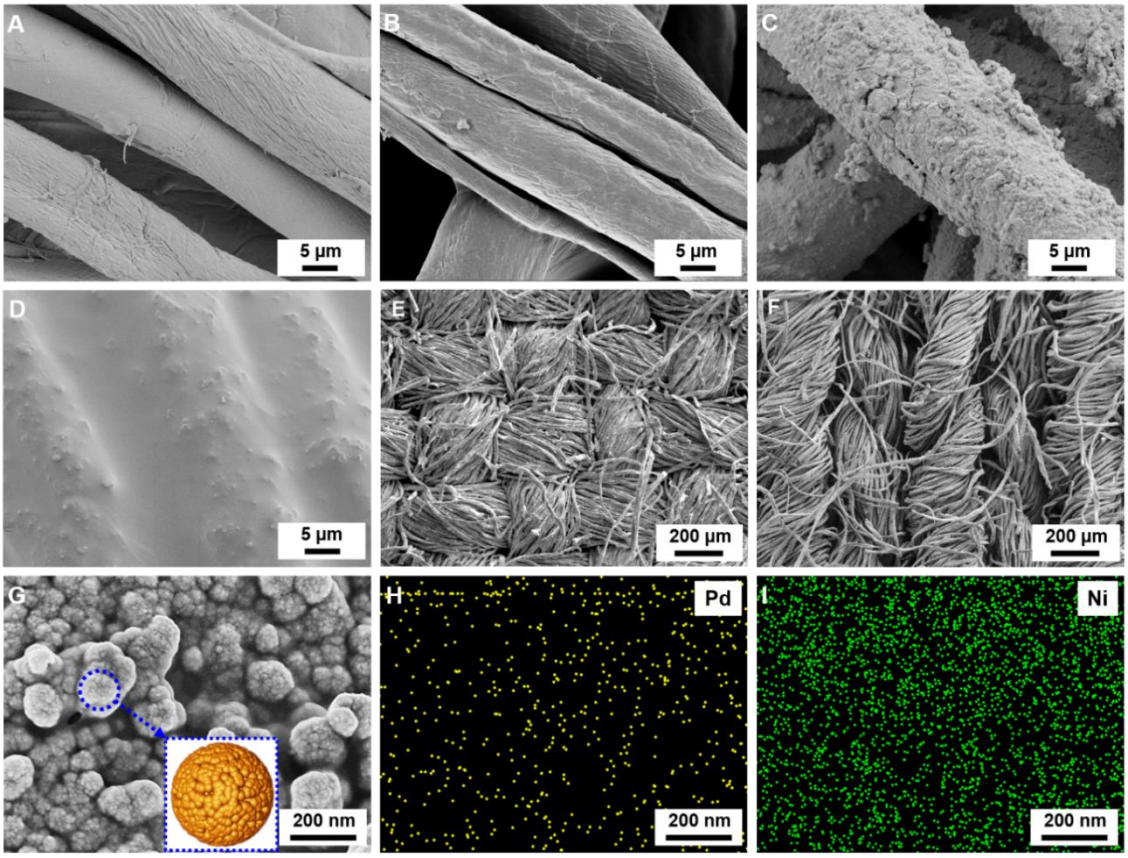

Figure 3.4 Representative SEM images of the as-prepared nickel-coated conductive fabrics, (A) pristine cotton fabric, (B) AAm-based fabric, (C) nickel-coated fabric via ELD, (D) PDMS-protected conductive fabric, (E) woven fabric (F, G) knitted fabric at low and high magnifications, respectively. The inset is the proposed microstructure of nickel nanoparticles on the fibre surface. The EDS mapping images for (H) palladium and (I) nickel.

The as-prepared nickel-coated conductive fabric was protected using PDMS to prevent nickel particles from falling off (**Figure 3.4D**). **Figure 3.4E and 3.4F** representative SEM

images of as-prepared nickel-coated woven and knitted fabrics with an approximate diameter yarn of about 200μm. Every yarn contains many fibres. The enlarged regions of fibres in **Figure 3.4G** suggested that the uniform and dense nickel nanoparticles (~100 nm) self-assemble into a continuously conductive film and aggregate on every fibre unit of the fabric composites. Importantly, the densely structured nickel nano-spheres consisting of many very fine small nanoparticles (~10 nm) were formed. This area was further analyzed by EDS mapping to confirm the element distribution. Due to the main component of cellulose from fabric materials and polyacrylamide (pAAm) cross-linked network, carbon and oxygen were detected in the mapping images (**Figure 3.5**). The nitrogen element from pAAm could also be clearly observed in **Figure 3.5**, forming various ionic bonds with chloropalladium anions. Here, Palladium and subsequent catalytic preparation of nickel were well distributed throughout the whole area (**Figure 3.4H and 3.4I**). Since the extremely dense aggregation of nickel nanoparticles, the most nickel content and the densest distribution were demonstrated in the mapping images, compared with other elements.

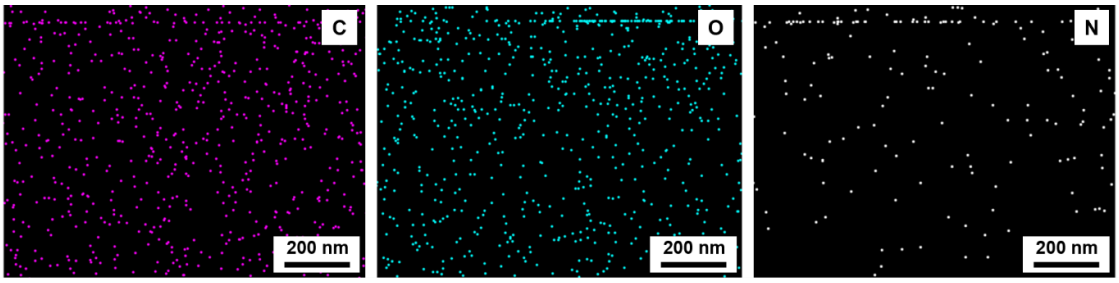

Figure 3.5 EDS mapping images for carbon, oxygen and nitrogen.

Fourier transform infrared spectroscopy (FTIR) was further used to confirm the success of the grafting process (**Figure 3.6A**). The pAAm absorption peaks are located at 1660 cm^{-1} (N-H) and 1314 cm^{-1} (C-N). It is a strong proof that the pAAm has cross-linked with cellulose in the fabric. These amine groups protonated under acidic conditions and provided effective ionic bonds with chloropalladium anions catalyst for subsequent ELD process of nickel/copper nanoparticles to realize the high conductivity of the fibres. The presence of nitrogen species was confirmed by the N 1s X-ray photoelectron spectroscopy (XPS) spectrum of the Pd-based fabric as shown in **Figure 3.7**. The XPS Pd 3d spectrum in **Figure**

3.6B displays a double feature with peaks located at 336.4 eV and 341.7 eV, which is attributed to the Pd (II) $3d_{5/2}$ and $3d_{3/2}$ signals of Pd (II) species, respectively. The Pd (II) ion peaks are relatively narrow and symmetrical, indicating only one chemical state of Pd (II) existing in Pd-based fabric. Then, the nickel-coated cotton fabrics and copper-coated cotton fabrics were stored for two days and characterized by X-ray diffraction (XRD) spectrum. **Figure 3.6C** shows that the 2θ peak at 44.9 degrees corresponds to the (111) crystal planes of nickel. **Figure 3.6D** demonstrates that the peaks at 43.5 and 50.6 degrees belong to the (111) and (200) crystal planes of copper, while the peak at 33.6 degrees attribute to the (111) crystal planes of copper peroxide. These results suggest that copper is easily oxidized, while nickel-coated fabric shows great air stability. For better comparison, I extracted the XRD spectrum (10-40 degrees) from **Figure 3.6C** (nickel-coated cotton fibre) and **Figure 3.6D** (copper-coated cotton fibre), as shown in **Figure 3.8**. According to the literature, these peaks reveal the presence of cellulose crystallite in cotton fibres.[30]

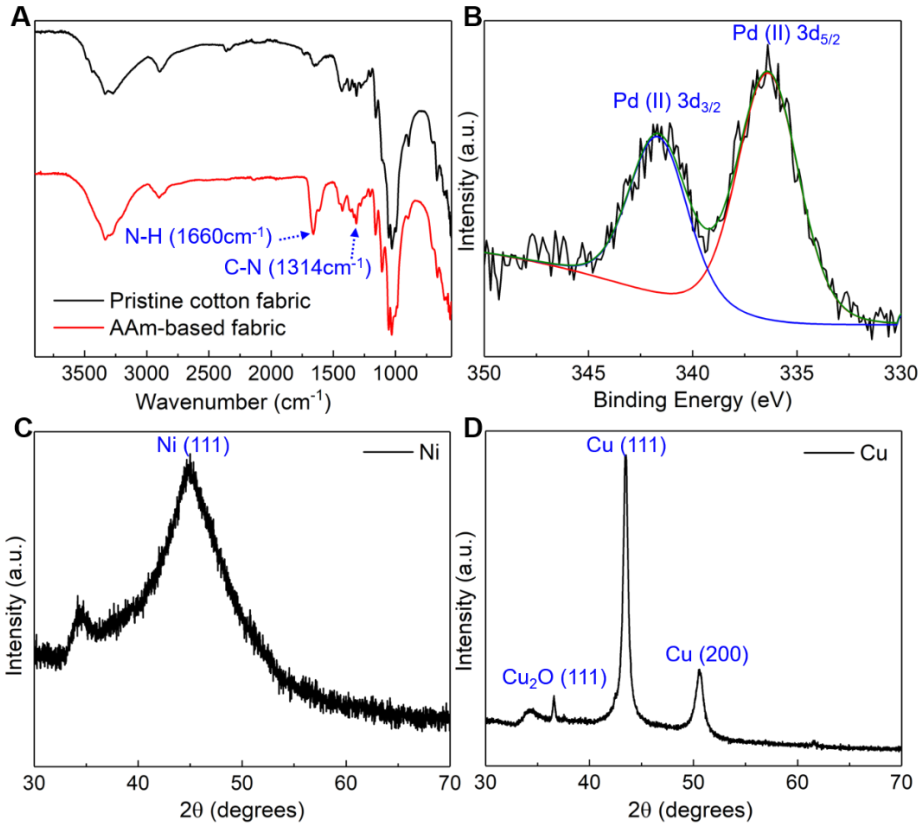

Figure 3.6 (A) FTIR spectrum of pristine cotton (black) and pAAm-modified cotton fabric (red). (B) The XPS Pd 3d spectrum of Pd-based fabric. XRD spectrum of (C) nickel-coated fabric and (D) copper-coated fabric stored in air for 2 days.

Moisture absorption is the main property of comfort in textiles. Cotton fabric has been attractive to people due to its outstanding absorption properties for invisible perspiration.[31, 32] To study the effect of nickel coating on the comfort performance of cotton textile, I measured the moisture regain of cotton fabric before and after nickel coating. The result indicates that the cotton after nickel coating remains 80% of its moisture absorption capacity, which is still higher than most of the synthetic fibres. Therefore, I believe that the nickel-coated cotton fabric can still maintain the comfort of raw cotton.

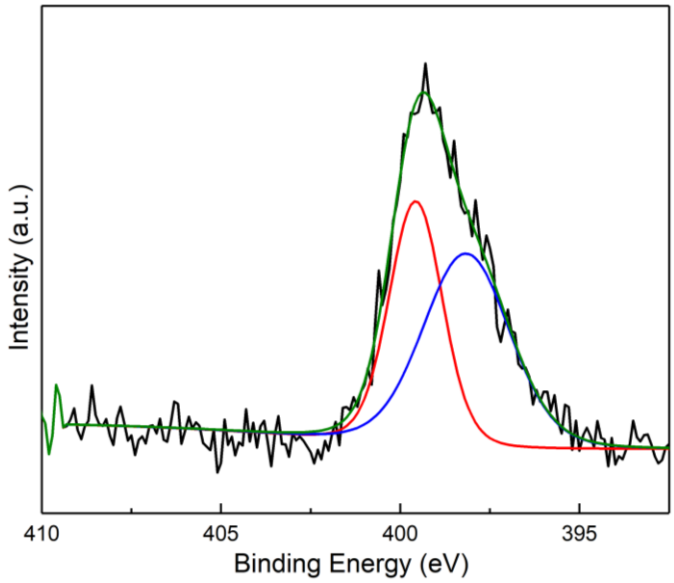

Figure 3.7 The XPS N 1S spectrum of Pd-based fabric.

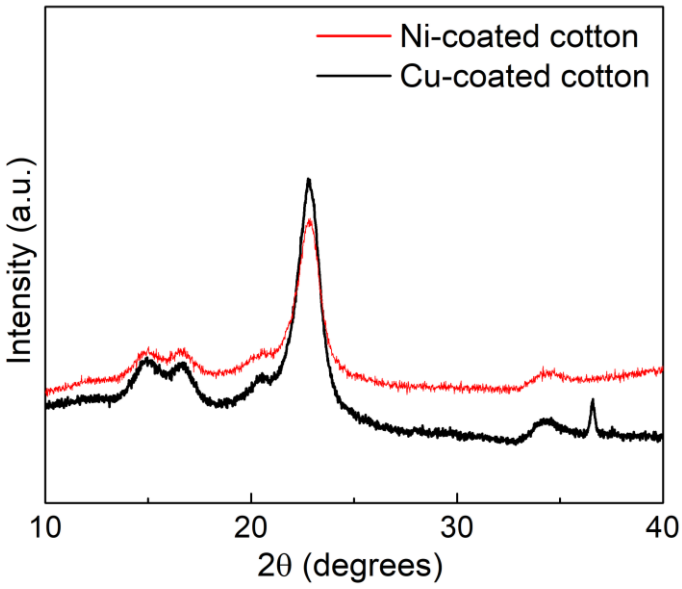

Figure 3.8 XRD spectrum (10-40 degrees) of (red line) nickel-coated fabric and (black line) copper-coated fabric.

3.3.2 Growth mechanism of nickel nanoparticles

Although ELD technology has been developed for a long time, the metal growth mechanism *via* PAMD strategy is still unclear. Here, a series of samples at different ELD process times were measured by SEM. As shown in **Figure 3.2F**, catalyst-based nickel seed crystals are caged by crosslinked polymers, to upsurge the density of seed crystals on the surface of modified substrates, and to increase the conductivity in the following deposition process. The nickel seed crystals keep growing to larger nickel particles in the ELD bath, and the final state of nickel coating on the surface of the substrate (**Figure 3.9**) indicates a continual film assembled from many particles. The growth process of nickel particles is shown in **Figure 3.10**.

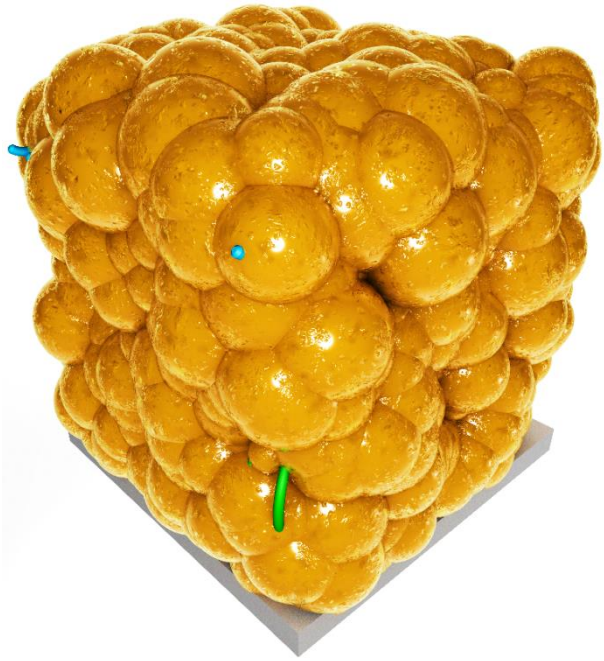

Figure 3.9 The final state of nickel nanoparticle on the surface of cotton fibres after ELD process.

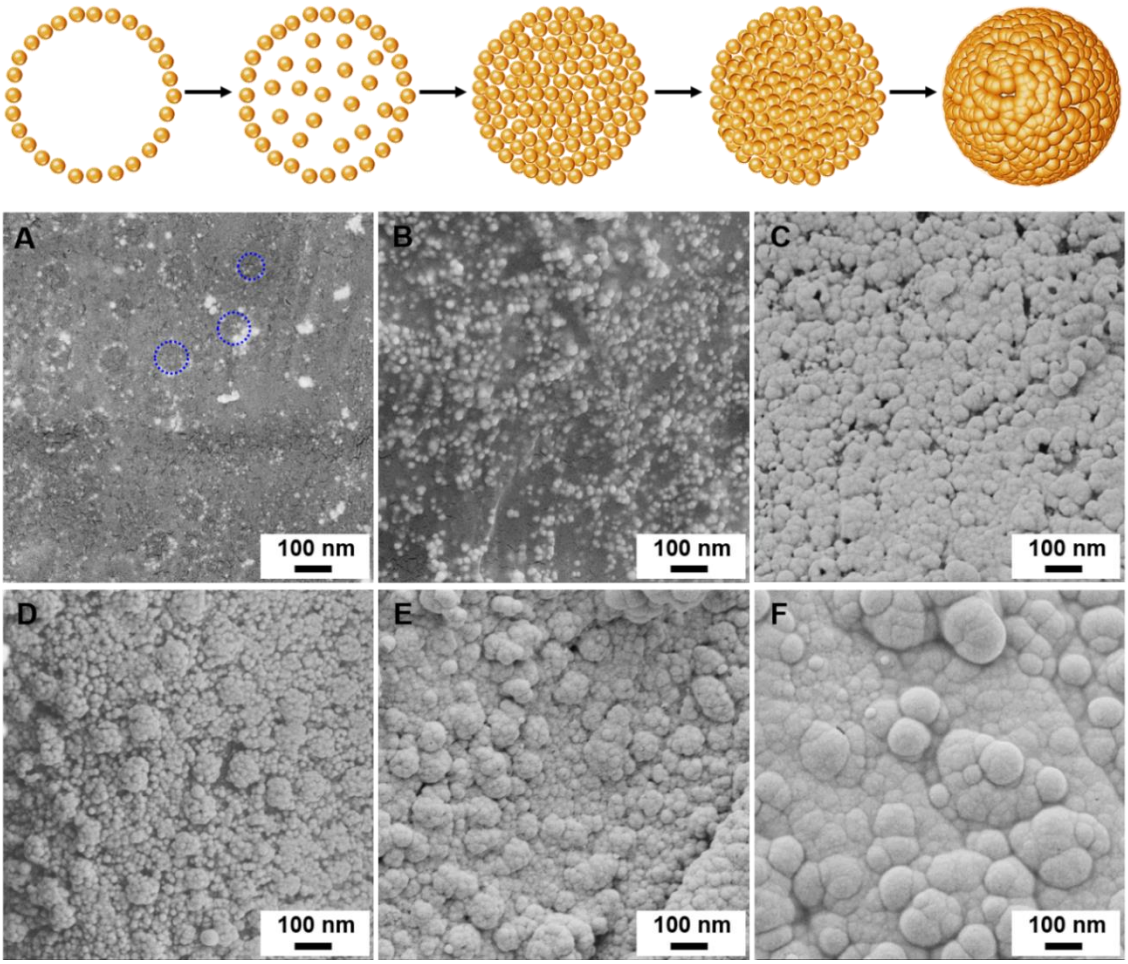

Figure 3.10 Representative SEM images of the nickel-coated conductive fabrics prepared at different ELD times, (A) 5 min ELD, (B) 10 min ELD, (C) 20 min ELD, (D) 30 min ELD, (E) 40 min ELD, (F) 60 min ELD.

Based on the classical nucleation theory,[33, 34] a thermodynamic system tends to minimize its Gibbs free energy, causing many small particles to form a spherical shape and accumulate into a circle after 5 min ELD (**Figure 3.10A** and **Figure 3.11**). According to the literature,[35] the polymers form a sparse and strong network with a mesh size on the order of 10 nm. The diameter of the initially formed nickel seed crystal is 10 nm approximately, which is consistent with the SEM result in **Figure 3.10A**. In this stage, the nickel particles are not continuous, and the resistance is tens of megaohms. Fast reduction induces a rapid growth of new particles in other reaction sites to form uniformly dispersed nickel seed crystals on the surface of catalyst-based cotton fabric (**Figure 3.10B**). Consequently, many small particles occur, and some of them break through the cage to form bigger particles after 10 min ELD

and the resistance is in kilo euro level. **Figure 3.10C** shows an aggregation of the primary particles into a dense nickel nanoparticle film after around 20 min ELD with hundreds of ohms of resistance. Then several large nickel nanoparticles (~100 nm) were grown by aggregating many small particles on the film surface (**Figure 3.10D**, 30 min ELD with tens of ohms of resistance) and many growth events lead to an increasing number of large particles (**Figure 3.10E**). Finally, all large nanoparticles aggregate into extremely dense nickel nanoparticles film with around 500 nm thickness (**Figure 3.10F and Figure 3.12**) and the final maximum resistance can reach around 3 ohms/cm.

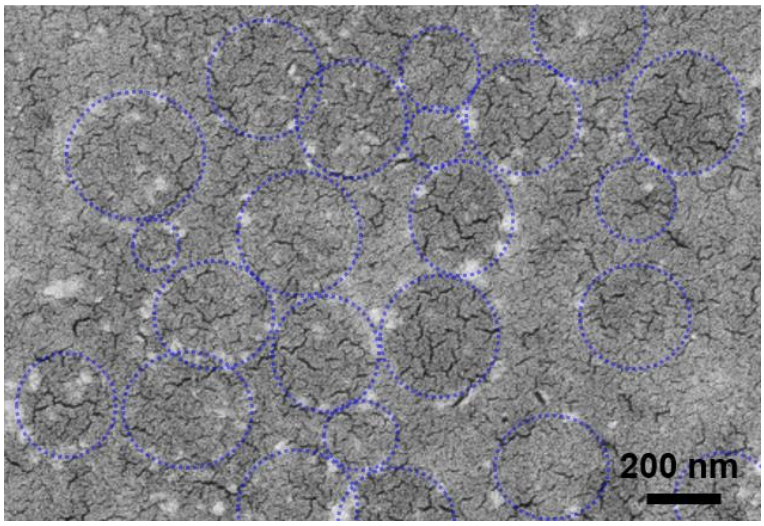

Figure 3.11 Representative SEM image of the nickel-coated conductive fabrics prepared by 5 min ELD.

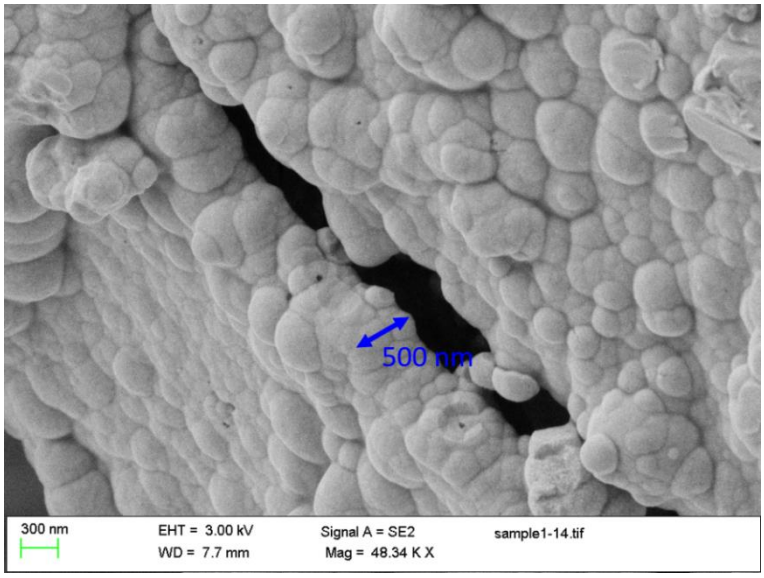

Figure 3.12 Representative SEM images of the obtained nickel-coated conductive fabrics.

3.3.3 Fundamental properties of capacitance sensor

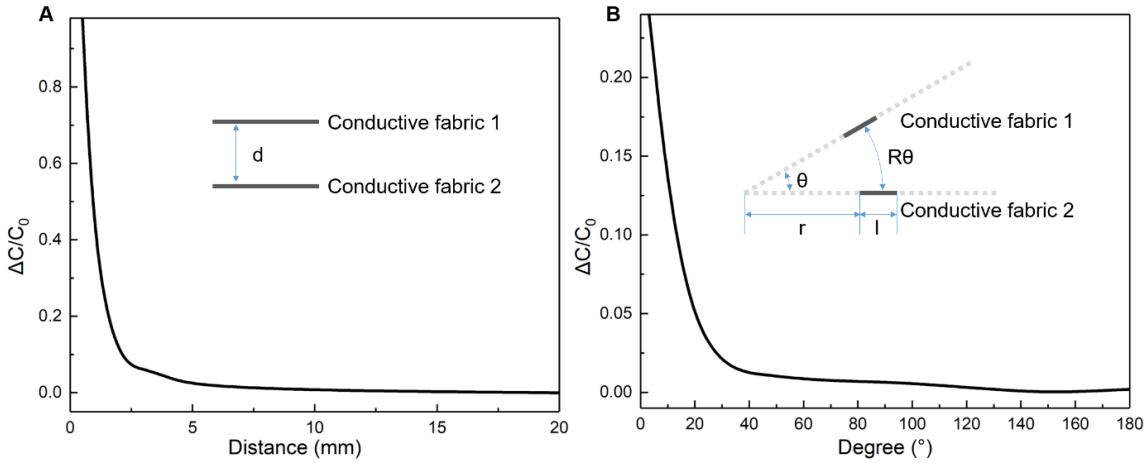

Figure 3.13 Capacitance change as functions of (A) distance and (B) bending angle for conductive fabrics-based sensor. The inset is the schematic diagram of parallel and non-parallel plate capacitors, respectively. Two nickel-coated fabrics with the same size were prepared. The size is 13×37 mm, and the dotted line from conductive fabric to bending center for degree test was set as 40 mm.

To understand the standalone effect of distance on the capacitive sensitivity of the proposed sensor, the relative capacitance change ($\Delta C/C_0$) was measured according to different distances (0-20 mm) between two as-prepared conductive fabrics. The ΔC and C_0 represent capacitance change and its baseline, respectively. As shown in **Figure 3.13A**, the capacitance is inversely proportional to the distance between the two conductive fabrics. A programmable C scan stage from Newmark systems Inc. USA, according to a previous report,[36] were operated to control the micro distance between 0-2 mm. The drive X-axis with 0.019 mm resolution controlled by an Arduino-based controller board from a host PC was used to control the distance from 0 to 20 mm, and the data interval is 0.5 mm. The electrode area (S) is constant, and as the distance between the two conductive fabrics (the inset of **Figure 3.13A**) monotonously decreases, the capacitance of the sensor (C) gradually increases, which is described as

$$C = \frac{\varepsilon S}{d} \tag{3.4}$$

where ε represents vacuum permittivity (8.85E-12 F/m), S represents the area of overlap of the two electrodes (13 mm × 37 mm) and d represents the distance between the two conductive fabrics.

To verify the reliability of the experimental result in **Figure 3.13A**, an analytical capacitance for different distances was carried out using equation (3.1). The data interval is 1E-4, so that 20 data points with the distance between 0.1 to 2 mm can be obtained. The simulations are performed *via* the MATLAB 2019a script platform. The relevant results were described in **Figure 3.14**, shown a similar decrease trend with the experimental result in **Figure 3.13A**. It demonstrated that the analytical model fitted well with the experimental results.

For Non-Parallel Plate Capacitors, the capacitance is inversely proportional to the degree of rotation angle (**Figure 3.13B**). The method of bending angles measurement is displayed in **Figure 3.15**. The relevant theoretical analysis is based on a parallel connection of capacitors.

$$\Delta V = \int \vec{E} \cdot \overrightarrow{dk} = \int_0^{\theta} E(R) R d\varphi = E(r) R\theta \tag{3.5}$$

where V and E are the electric potential and electric field between two conductive fabrics; k specifies the electric field route between the two conductive fabrics; R and θ denote the relative rotating radius and angle of the integral element.

The surface charge density σ on the plates with radius of R is,

$$\sigma(R) = \varepsilon_1 \varepsilon_0 E(R) \tag{3.6}$$

where ε_1 is the relative permittivity of the media between the two conductive fabrics; ε_0 is the permittivity of the free space.

Combine equation (3.2) and (3.3),

$$\sigma(R) = \varepsilon_1 \varepsilon_0 \frac{\Delta V}{R\theta} \tag{3.7}$$

Therefore, the charge element is,

$$dq = \sigma(R) dS = \varepsilon_1 \varepsilon_0 \frac{\Delta V}{R\theta} a dR \tag{3.8}$$

where a is the length of the conductive fabrics.

Therefore, the integrated total charge on the capacitor is,

$$q = \frac{a\varepsilon_1\varepsilon_0\Delta V}{\theta}\int_r^{r+l}\frac{1}{R}dR = \frac{a\varepsilon_1\varepsilon_0\Delta V}{\theta}\ln\left(1+\frac{l}{r}\right) \tag{3.9}$$

where r represents the radius from electrodes to the rotation center and l represents the width of the conductive fabrics.

Thus, the overall capacitance of the capacitor is,

$$C = \frac{q}{\Delta V} = \frac{a\varepsilon_1\varepsilon_0}{\theta}\ln\left(1+\frac{l}{r}\right) \tag{3.10}$$

The relevant parameters are shown in the inset of **Figure 3.13B.**

By referring to the specifications of the Zurich impedance analyzer (https://www.zhinst.com/americas/products/mfia-impedance-analyzer), the minimum capacitance that the impedance analyzer can measure is 0.01 pF. By referring to capacitance signal as functions of distance and bending angle in **Figure 3.13**, the maximum change rate of the capacitance deviation is 50 pF/mm and 0.2 pF/degree. Consequently, the minimum distance and bending angle deviation that can be measured are 0.2 μm and 0.05 degrees, respectively. However, due to the limitation of the accuracy of the drive X-axis of the programmable C scan stage in the practical measurement, the minimum moving distance deviation is 0.019 mm. Compared with other textile-based sensor fabrication listed in **Table 3.1**, the conductive textile with very low resistance was fabricated *via* an easier and cheaper strategy. The as-prepared capacitive sensor shows outstanding sensitivity and a fast response rate.

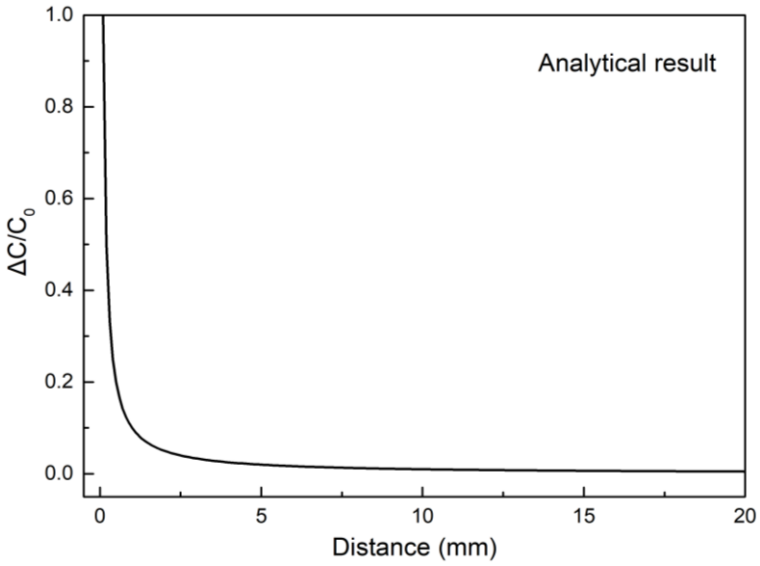

Figure 3.14 Analytical result for the capacitance changes of conductive sensor as functions of distance.

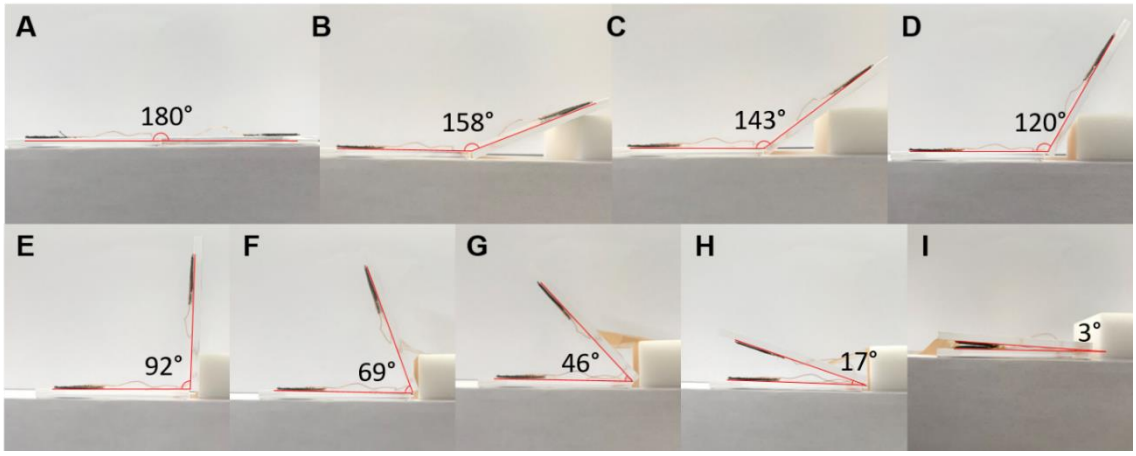

Figure 3.15 The photos of bending angles measurement.

Table 3.1 Properties of different flexible textile-based sensor reported in the literature.

Ref.	Conductive component	Fabrication strategy	Cost	Conductivity	Sensing Mechanism	Sensitivity	Response time
9	Graphene	Microfluidic spinning	Low	0.5 kΩ	Resistance	$\Delta R/R_0$=15 under 10% strain	
37	Silver nanowire (AgNW)	Screening printing	High		Capacitance	1.62 MPa^{-1} (~1.8 μm)	40 ms
38	Eutectic gallium−indium (eGaIn)	Injection	Low		Capacitance	Tunable	75 ms
39	Silica standard multimode fibres fibre	plane-polished with polymer buffer coating	Low		Light intensity	1.80°	
40	Carbon nanotubes (CNTs)	Spray coating	Low	30 -50 kΩ	Resistance	0.14 rad^{-1}	
41	Single-walled carbon nanotubes (SWCNTs)-filled binary polymer of poly vinylidene fluoride/poly	Applicator Coating on PET substrate	High	5.8 MΩ	Impedance	90 kΩ/°	~2 s

	(3,4-ethylenedioxythiophene)-poly(styrenesulfonate) (PVDF/PEDOT:PSS)						
42	Aluminum	Hot embossing technique	Low		Capacitance	1.15 mm	14 ms
43	Reduced graphene oxide (rGO)	Mixing, directional freezing, freeze-drying, and carbonization	Low	199 **Ω**	Resistance	0.052°	
44	Aluminum and silver	Sputtering technology	High		Resistance and capacitance		164 ms
This work	Nickel/Copper	Electroless deposition	Low	3-5 Ω cm^{-1}	Capacitance	0.2 µm and 0.05°	5 us

3.3.4 Diaphragmatic respiratory monitoring

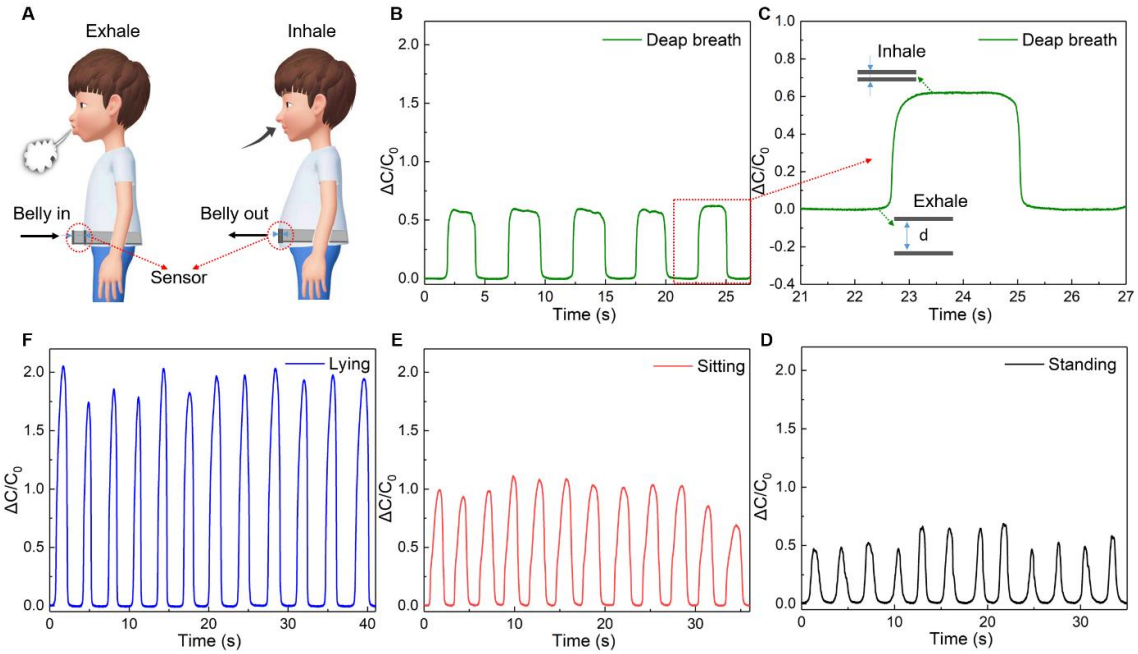

Figure 3.16 (A) General breathing mechanics during inhale and exhale process. Capacitance change as a function of time for distance change between two conductive fabrics affected by abdominal breathing exercise (B, C) deep breathing, and breathing activities during (D) standing, (E) sitting and (F) lying, respectively.

Lack of correct breathing mechanics can lead to chronic neck pain by placing abnormal loading on the front neck muscles, especially scalene, sternocleidomastoid and trapezius muscles.[45] When they become stiff and fatigued from overworking, the pain can radiate or travel into the shoulders, arms and hands. Hence, a proper breathing technique, called diaphragmatic breathing (also known as abdominal breathing), is of great significance.[46] When inhaling, the abdominal muscles relax, the diaphragm muscles contract, and the position moves down. When exhaling, the abdominal muscles contract, the diaphragm muscles relax and return to the original position. Diaphragmatic breathing brings air to the bottom portion of the chest to increase oxygenation, lowering blood pressure and relaxing muscles. In addition to reducing neck muscle strain, this breathing exercise can ensure effective ventilation of the lungs, and relieve symptoms of dyspnea. For those patients with chronic obstructive pulmonary disease (COPD) and pulmonary heart disease, the effect of

such rehabilitation training can be dramatic. According to the literature,[47] fast deep breathing possibly improved respiratory muscle strength and reduced inflammatory cytokines, which is better than slow deep breathing for patients with COPD. Based on the promising results of capacitance increase with the decrease of distance in **Figure 3.13A**, two as-prepared nickel-coated fabrics with 13 mm × 37 mm size served as a capacitive sensor was successfully applied to monitor fast and slow deep breathing during rehabilitation training. One fabric electrode was integrated into tights and another one was fixed on the inside of a belt. When an individual inhales, the abdominal muscles relax, causing belly out, and the distance between two conductive fabrics was reduced (**Figure 3.16A**), thereby generating an inhaled signal (**Figure 3.16B and 3.16C**). In reverse, when the individual exhales, the abdominal muscles contract and belly in, resulting in the distance to return to the original position to generate an exhaled signal. Here, each time interval represents a complete breathing cycle from exhalation to inspiration. **Figure 3.16B** shows that the person standing up slowly breathed 5 times in 27 seconds, and **Figure 3.16D** shows normal deep breathing of 12 times in 35 seconds. In this case, the individual standing up experiences a complete slow breathing cycle of 5.4 s, while a fast breathing cycle is 2.9 s. In the same way, the complete normal deep breathing cycle of sitting and lying is calculated as 3 s and 3.4 s, respectively (**Figure 3.16E and 3.16F**). In other words, the rate of normal diaphragmatic respiratory is the fastest when standing, the second when sitting, and the slowest when lying down. On the other hand, the capacitance sensor's sensitivity ($\Delta C/C_0$) of deep breathing is around 0.5 during standing, while the $\Delta C/C_0$ increase to around 1.0 and 2.0 for sitting and lying conditions respectively. Therefore, this sensor can monitor the breathing exercises in different states (standing, sitting and lying) and evaluate training intensity (slow or fast respiratory rate) to achieve different rehabilitation training effects in the same state (standing).

3.3.5 Speaking and other motions monitoring

Monitoring of voiceprint information is a powerful strategy to help assess the pronunciation of an individual to avoid speech delay and rehabilitation training for people with language

developmental delay or dysplasia. Based on the results, capacitance increase with the increase of bending angles in **Figure 3.13B**, the two conductive fabrics were set up on two sides of the middle throat to collect voice signal during language rehabilitation training. As shown in **Figure 3.17**, when a person spoke words ("Capacitance", "The University of Manchester" and "Freedom") or sentences ("Nice to meet you", "Research is my forever love" and "Thank you"), the sensor was allowed to capture the fine features of the speech by determining in real-time the change in capacitance with the movement of the vocal cords. Besides, a more significant change of capacitance was detected as the louder sound got, caused by the vibration of the vocal cords (**Figure 3.18**). The swallowing activity and head movement could also be monitored during rehabilitation exercise especially for head and neck cancer patients (**Figure 3.19 and 3.20**). Apart from that, another sensor (3×30 mm) was attached to the upper and lower eyelids to detect the blink speed (**Figure 3.21**). These results successfully imply the great performance of the textile sensor to real-time monitor fluctuation information for rehabilitation training.

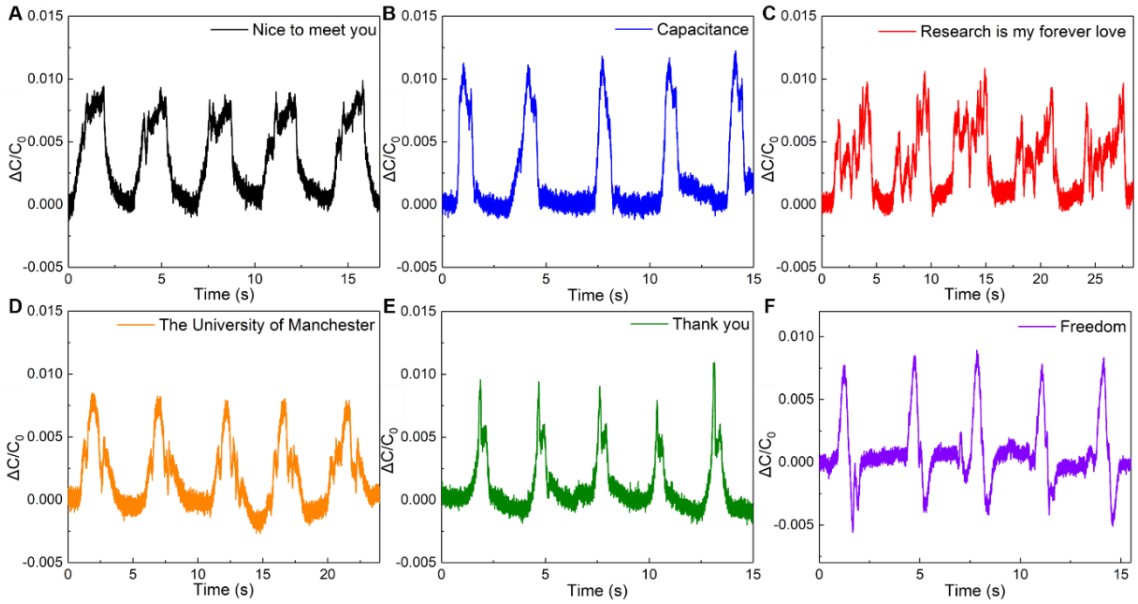

Figure 3.17 Capacitance fluctuation information for voiceprint recognition and correction. Repeated responses of a conductive fabric-based sensor to 6 different words (A) "Nice to meet you", (B) "Capacitance", (C) "Research is my forever love", (D) "The University of Manchester", (E) "Thank you" and (F) "Freedom".

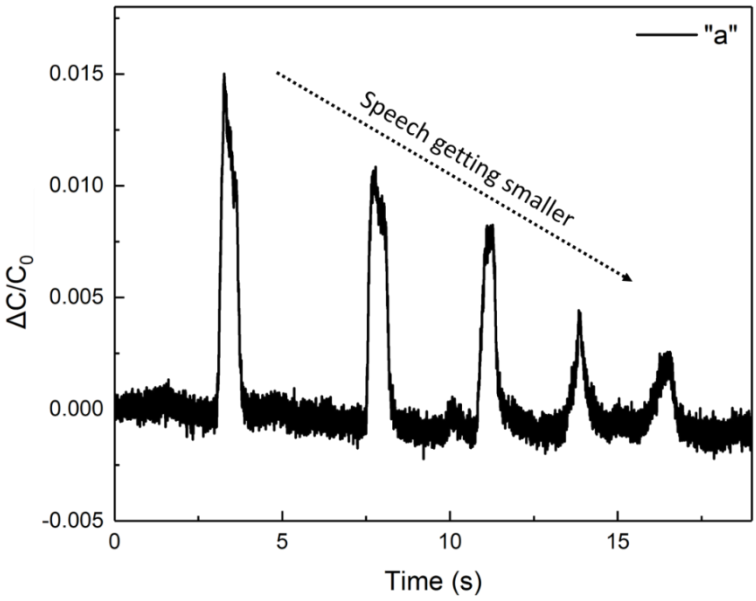

Figure 3.18 The changes of capacitance as the speech getting smaller.

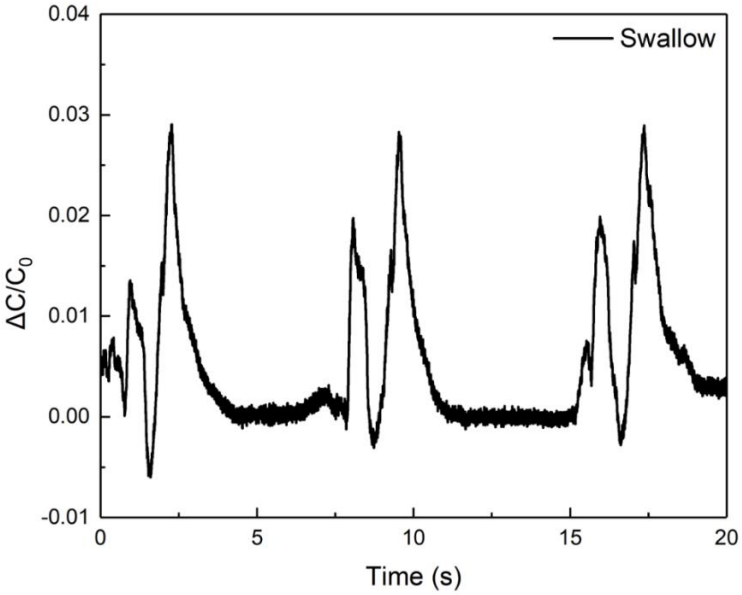

Figure 3.19 The changes of capacitance as swallowing.

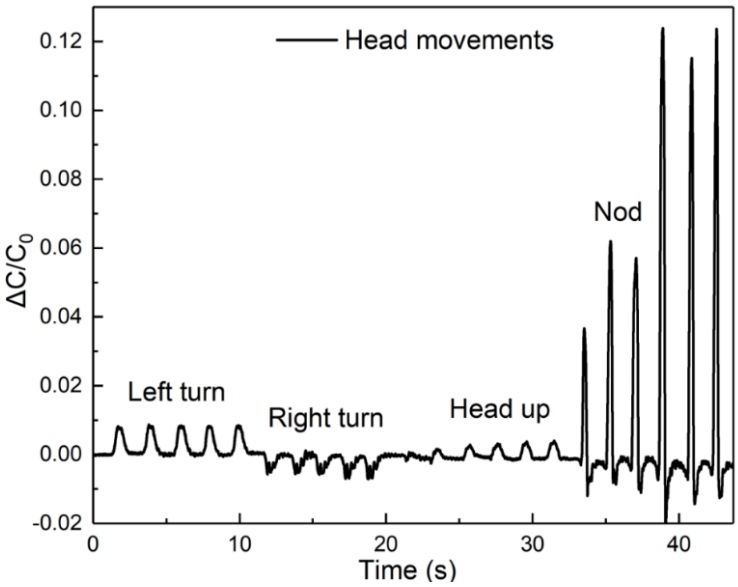

Figure 3.20 The changes of capacitance as the head movement.

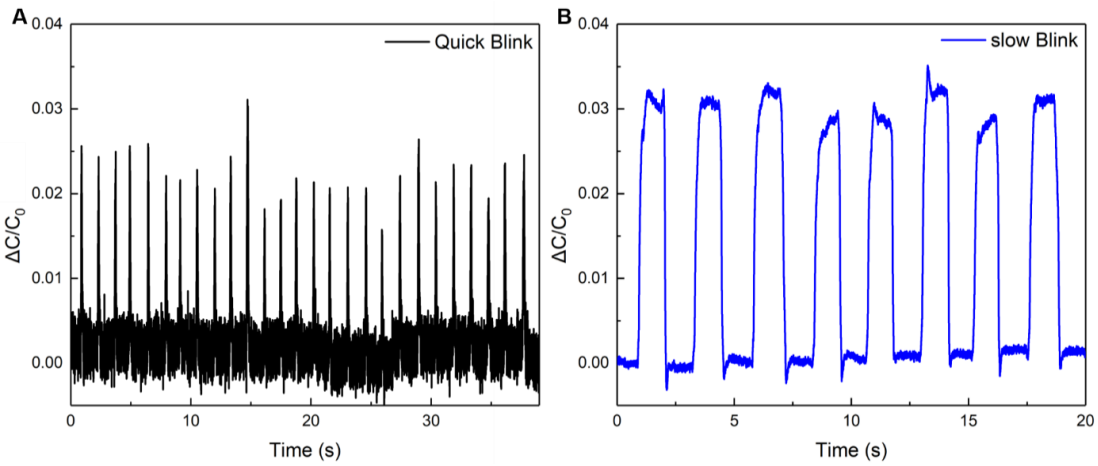

Figure 3.21 The changes of capacitance as fast and slow blink.

3.3.6 Stability property of capacitance sensor

Stability and durability are of great significance for practical applications of wearable sensors. An anthropomorphic robotic hand combining linkage-driven and tendon-driven systems was designed according to the size and geometry of a real hand, named MCR-Hand. This hand has 4 jointed fingers and 2-split palms. All joints of the MCR-Hand were driven by a built-in 18 servos to imitate all motions of a human hand (**Figure 3.22**). Two nickel-coated fabrics (7×16 mm) were attached to two sides of a second joint of the MCR-Hand middle finger (**Figure 3.22A**). The finger bending activities were repeated at a constant

speed driven by a built-in servomotor and a low-level control system. The repeated bending angle is about 90 degrees. Before I collected the data in **Figure 3.22B**, the MCR-Hand had carried out the bending activities for more than 1 h to observe the stable output. The bending speed was around 1 cycle/s. Some photos during the test process were taken and shown in **Figure 3.23**. **Figure 3.23** displayed the impedance-time (-300 to 0 s of the abscissa range) curve at different periods during the repeated finger bending activities monitoring. I selected the data with around the final 3 mins, containing 2,180,000 data points to show the stable output in **Figure 3.22B**. As shown in **Figure 3.22B**, a relative change in capacitance under repeated finger bending for hundreds of cycles exhibited high stability, durability and fast response during hundreds of cycles. The capacitance increases from around 24.3 to 26 pF during bending the middle finger joint of a human being (**Figure 3.24**). The capacitance changes (~0.023) of the MCR-Hand is a little lower than the monitoring of finger bending activity of the real human being (~0.07 in **Figure 3.24**), due to the smaller repeated bending angle. The selected zones are the enlarged regions of capacitance response as a function of time for anthropomorphic finger bending activities. Every measurement curve is reliably repeated well *via* the MCR-Hand built-in servo-motor control system. Besides, ordinary gloves could be worn by the robotic hand to make it match more closely to the human hand. By this way, the sensor for MCR-Hand joints motion monitoring could be assembled into normal gloves, which is user-friendly.

To further study the reliability of the sensor, I extracted three cycles of the curve from **Figure 3.22**, and analyzed them in detail the effect of the MCR-Hand finger bending process on the signal output (**Figure 3.25**). The signal output curve in every bending cycle is almost the same (very repeatable). The slight asymmetric nature, including 0.094 s, 0.13 s and 0.24 s of fluctuation, is due to the different velocity of joint motion during the MCR-Hand finger flexion/extension. The detailed explanation is as follows:

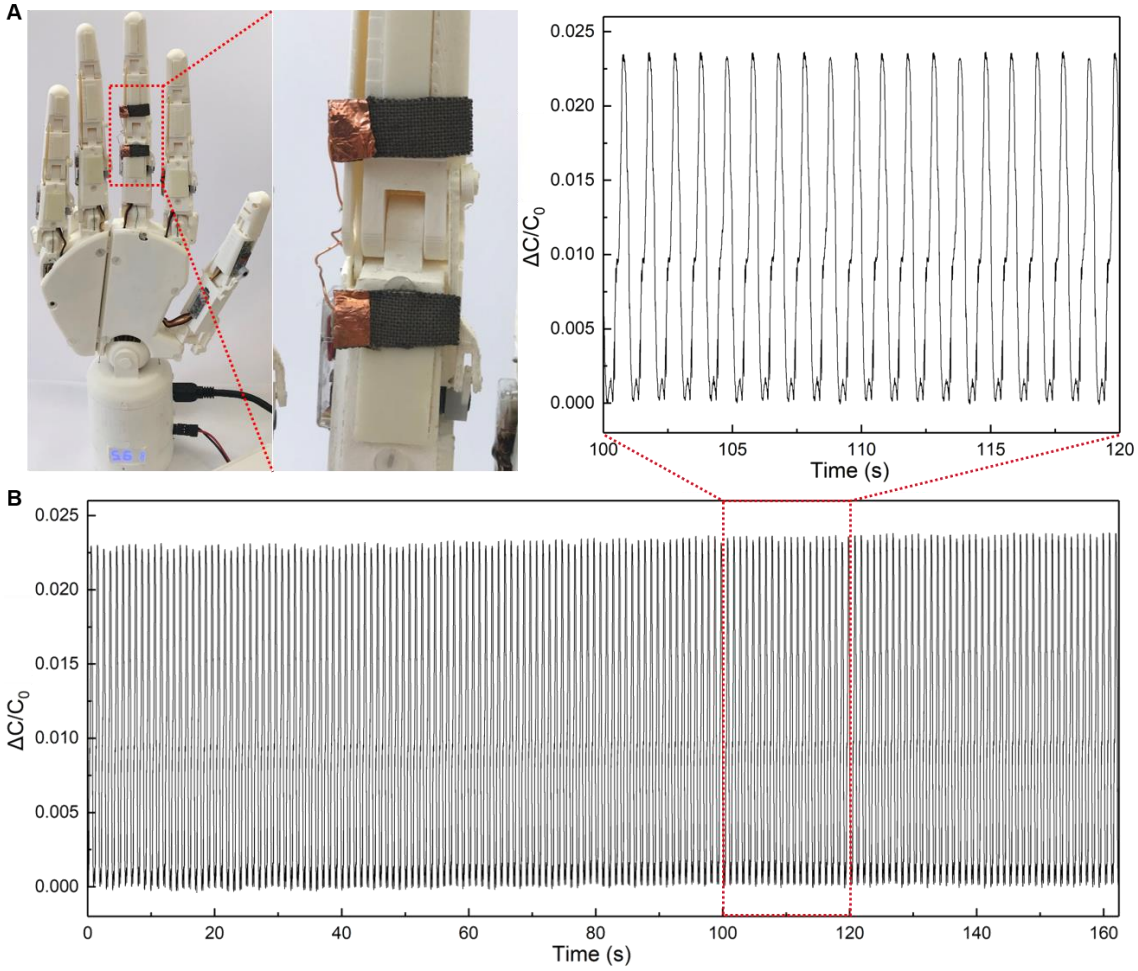

Figure 3.22 Relative change in capacitance under repeated finger bending of a MCR-Hand and imitating human finger bending about 90 degrees for hundreds of cycles, showing the stability and durability of the sensor.

Flexion/extension of the DIP joint in the robotic finger was involved in the MAR-Hand. The DIP joint is driven by a servo motor built in the proximal phalange through a four-bar mechanism (**Figure 3.26**). l_1 is the driving linkage (A refers to the motor output shaft), and l_3 is the driven linkage (D refers to the joint). During the flexion of the PIP joint, the motor accelerates to a constant speed w_1 with the set acceleration a_1. When l_1 perpendicular to l_0, l_3 will reach the maximum speed, and then the speed of $l_3$will decrease. At the moment when the acceleration changes to negative from positive, there may be a short signal fluctuation. Besides, it can be seen that the four-bar mechanism structure is located on the side of the finger. An problem with this arrangement is that when driving the DIP joint to flex, an

abduction torque is simultaneously produced on the joint. When l_1 perpendicular to l_0, the pressure angle is 90 °, and the maximum input torque will appear. At the same time, the maximum abduction torque will also appear. Due to the accuracy limitations of 3D printing and structural limitations, the friction will reach the maximum value, so movement stuck phenomenon occurs. As a result, after 0.117 s accelerated movement, there was a slight fluctuation of 0.094 s in **Figure S3**. When the finger is fully extended, the extension command is still running, and it will be a delay t before entering the flexion command. During the delay time t, the motor remains energized, the finger joints keep tighten. When the delay ends, before entering to the flexion command, the motor will momentarily power off and change the direction of rotation. During the power-off period, the finger joints will relax from the tight state. And the finger joints will naturally bounce and flex, so a small peak with a slight fluctuation of 0.24 s can be observed in **Figure S3**. Similarly, a fluctuation of 0.13 s can be seen when the finger is in the final bending state.

Figure 3.27 provides the excellent electrical stability and durability of the conductive fabric against repeated 1500 cycles of folding and 5 cycles of washing. For folding test, the conductive fabric was folded to near 180 degrees and then unfolded back to 0 degrees. The result implied that only a little increase of the resistance (around from 3.6 to 5 Ohms) was observed after 1500 folding cycles (**Figure 3.27A**). I further used commercial clothing cleanser to wash the as-prepared conductive fabric for 30 min, during which the fabric was also experienced to extensive rubbing. The resistance shows a little increased around from 3.6 to 4.9 Ohms, and maintained at around 4.9 Ohms after the fourth washing cycles (**Figure 3.27B**). Besides, no cracks occur during folding and washing tests. The stable resistance is mainly because of the topographical interactions between coatings and substrates, as well as the protection of PDMS.

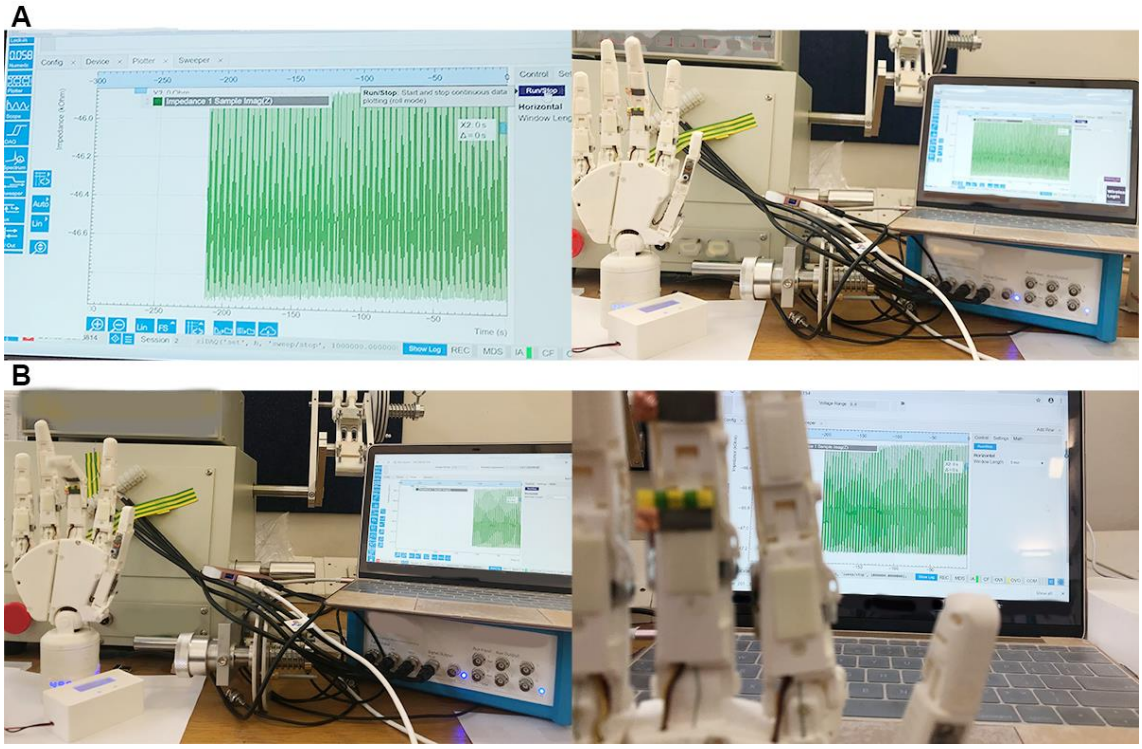

Figure 3.23 Experimental photos of the repeated finger bending of a MCR-Hand for the test of stability and durability of the sensor.

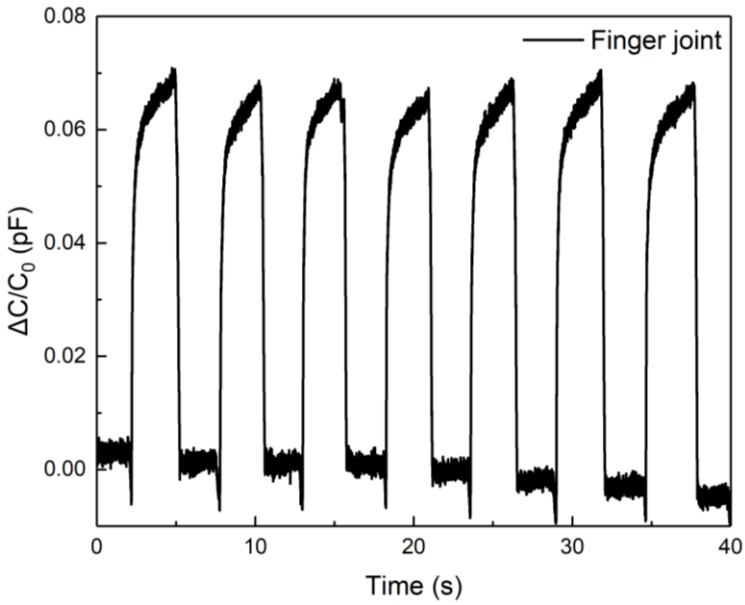

Figure 3.24 The changes of capacitance as finger joint bending activities.

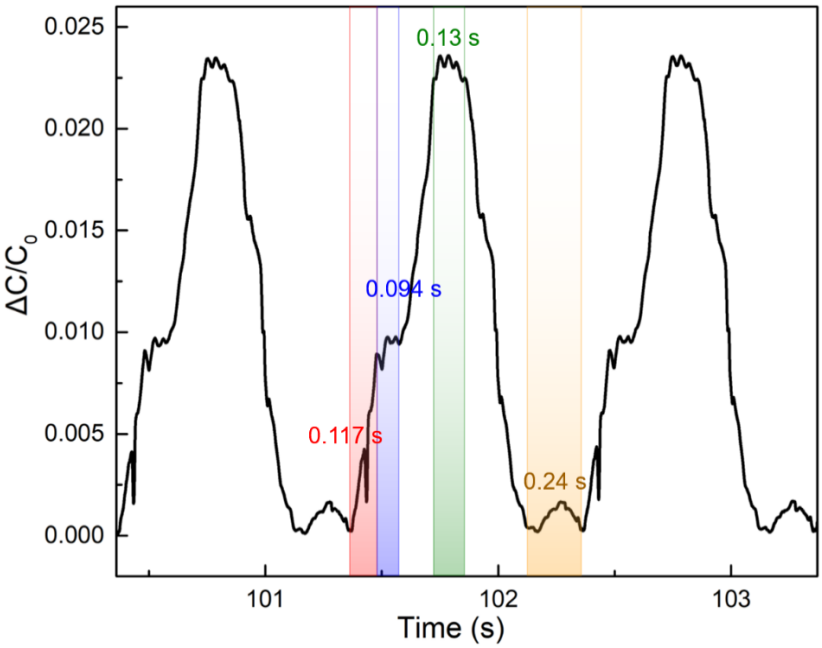

Figure 3.25 Three cycles of capacitance changes of MCR-Hand finger bending in **Figure 3.22**.

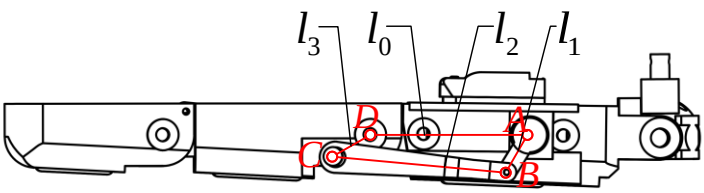

Figure 3.26 The four-bar mechanism of DIP joint.

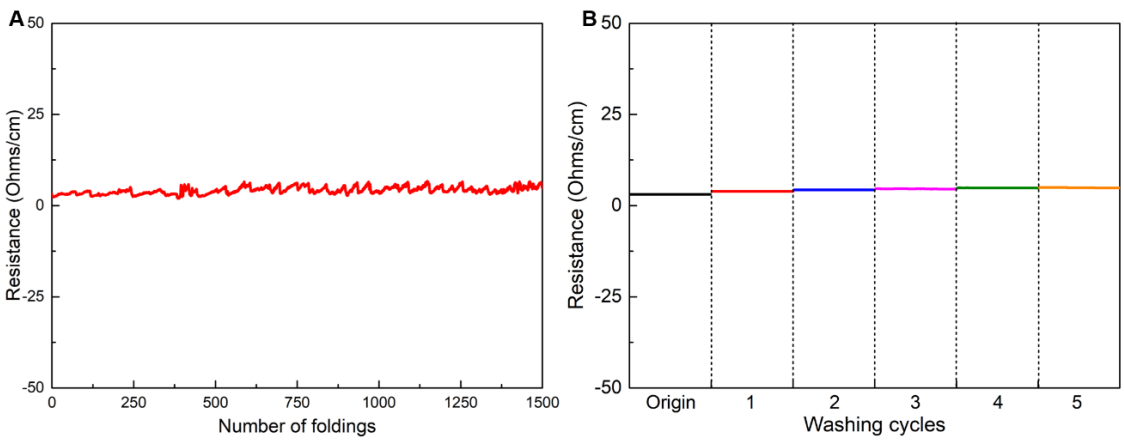

Figure 3.27 Electrical resistance changes of the prepared conductive nickel-coated fabric for (A) 1500 cycles of folding test, and (B) 5 cycles of washing ability test.

3.5 Summary

Topological genus-3 and genus-5 structures were introduced into fibre surface modification, to improve the adhesion and conductivity of metallic coating on the fibre surface. The ammonia-containing polymer was introduced into the soft cotton fabric to form a covalent and hydrogen-bonded entangled molecular topological cage to capture catalyst-based nickel seed crystal *via* a thermally induced radical polymerization technique. The modified ELD was used for the subsequent growth of nickel nanoparticles on the surface of the catalyst-based fabric. After 10 min ELD, the seed crystal began to break through the cage to form larger particles. The continual coating around 500 nm thickness nickel nano-films could realize excellent electrical properties of conductive fabric. The device was integrated into tights to simultaneously detect the capacitance level change with distance and angle changes between two electrodes. The monitoring results show that the sensor can be used to record dynamic information in real-time, such as breathing, speaking, blinking, head motions and joint motions in rehabilitation training. I believe this system can play a significant role in the development of high sensitivity, comfortable, durable and wearable sensors for a variety of human healthcare applications, *via* fibre surface topological modification.

References

[1] B. Wang, A. Facchetti, *Adv. Mater.* **2019**, 31, 1901408.

[2] S. Seyedin, P. Zhang, M. Naebe, S. Qin, J. Chen, X. Wang, J. M. Razal, *Mater. Horiz.* **2019**, 6, 219.

[3] M. Tessarolo, I. Gualandi, B. Fraboni, *Adv. Mater. Technol.* **2018**, 3, 1700310.

[4] J. S. Heo, J. Eom, Y. H. Kim, S. K. Park, *Small* **2018**, 141703034.

[5] S. Slatyer, S. M. Aoun, K. D. Hill, D. Walsh, D. Whitty, C. Toye, *BMC Health Serv. Res.* **2019**, 19, 220.

[6] C. O. Baker, X. Huang, W. Nelson, R. B. Kaner, *Chem. Soc. Rev.* **2017**, 46, 1510.

[7] T. R. Ray, J. Choi, A. J. Bandodkar, S. Krishnan, P. Gutruf, L. Tian, R. Ghaffari, J. A. Rogers, *Chem. Rev.* **2019**, 119, 5461.

[8] F. Sun, M. Tian, X. Sun, T. Xu, X. Liu, S. Zhu, X. Zhang, L. Qu, *Nano Lett.* **2019**, 19, 6592.

[9] X. Hu, M. Tian, T. Xu, X. Sun, B. Sun, C. Sun, X. Liu, X. Zhang, L. Qu, *ACS Nano* **2020**, 14, 559.

[10] M. Z. Seyedin, J. M. Razal, P. C. Innis, G. G. Wallace, *Adv. Funct. Mater.* **2014**, 24, 2957.

[11] Y. Guo, M. T. Otley, M. Li, X. Zhang, S. K. Sinha, G. M. Treich, G. A. Sotzing, *ACS Appl. Mater. Interfaces* **2016**, 8, 26998.

[12] H. M. Lee, S. Y. Choi, A. Jung, S. H. Ko, *Angew. Chem. Int. Ed. Engl.* **2013**, 52, 7718.

[13] J. Lee, H. Kwon, J. Seo, S. Shin, J. H. Koo, C. Pang, S. Son, J. H. Kim, Y. H. Jang, D. E. Kim, T. Lee, *Adv. Mater.* **2015**, 27, 2433.

[14] L. Chen, M. Lu, Y. Wang, Y. Huang, S. Zhu, J. Tang, C. Zhu, X. Liu, W. Yin, *Adv. Intell. Syst.* **2019**, 1, 1900037.

[15] J. S. Jur, W. J. Sweet, C. J. Oldham, G. N. Parsons, *Adv. Funct. Mater.* **2011**, 21, 1993.

[16] N. Selvakumar, H. C. Barshilia, *Sol. Energy Mater. Sol. Cells* **2012**, 98, 1.

[17] T. Loewenstein, A. Hastall, M. Mingebach, Y. Zimmermann, A. Neudeck, D. Schlettwein, *Phys. Chem. Chem. Phys.* **2008**, 10, 1844.

[18] H. Zhang, P. Zhang, H. Zhang, X. Li, L. Lei, L. Chen, Z. Zheng, Y. Yu, *ACS Appl. Mater. Interfaces* **2018**, 10, 28963.

[19] Y. Yu, X. Xiao, Y. Zhang, K. Li, C. Yan, X. Wei, L. Chen, H. Zhen, H. Zhou, S. Zhang, Z. Zheng, *Adv. Mater.* **2016**, 28, 4926.

[20] C. Zhu, X. Guan, X. Wang, Y. Li, E. Chalmers, X. Liu, *Adv. Mater. Interfaces* **2019**, 6, 1801547.

[21] L. Liu, Y. Yu, C. Yan, K. Li, Z. Zheng, *Nat. Commun.* **2015**, 6, 7260.

[22] P. Li, Y. Zhang, Z. Zheng, *Adv. Mater.* **2019**, 31, e1902987.

[23] X. Wang, C. Yan, H. Hu, X. Zhou, R. Guo, X. Liu, Z. Xie, Z. Huang, Z. Zheng, *Chem. Asian J.* **2014**, 9, 2170.

[24] X. Liu, H. Chang, Y. Li, W. T. Huck, Z. Zheng, *ACS Appl. Mater. Interfaces* **2010**, 2, 529.

[25]T. Du, B. Li, X. Wang, B. Yu, X. Pei, W. T. Huck, F. Zhou, *Angew. Chem. Int. Ed. Engl.* **2016**, 55, 4260.

[26]F. E. P. Hirzebruch, M. Kreck, *Notices Am. Math. Soc.* **2009**, 56, 713.

[27]M. Pandey, N. Mohamad, M. C. Amin, *Mol. Pharm.* **2014**, 11, 3596.

[28]J. Steck, J. Yang, Z. Suo, *ACS Macro Lett.* **2019**, 8, 754.

[29]J. Yang, R. Bai, J. Li, C. Yang, X. Yao, Q. Liu, J. J. Vlassak, D. J. Mooney, Z. Suo, *ACS Appl. Mater. Interfaces* **2019**, 11, 24802.

[30]M. Cintrón, D. Hinchliffe, *Fibers* **2015**, 3, 30.

[31]G. Bedek, F. Salaun, Z. Martinkovska, E. Devaux, D. Dupont, *Appl. Ergon.* **2011**, 42, 792.

[32]K. Kadapalayam Chinnasamy, P. Chidambaram, *Fibers Text. East. Eur.* **2017**, 25, 53.

[33]J. Polte, *CrystEngComm* **2015**, 17, 6809.

[34]J. Wang, C. F. Mbah, T. Przybilla, S. Englisch, E. Spiecker, M. Engel, N. Vogel, *ACS Nano* **2019**.

[35]J. Yang, R. Bai, B. Chen, Z. Suo, *Adv. Funct. Mater.* **2019**, 1901693.

[36]H. Xu, J. R. Salas Avila, F. Wu, M. J. Roy, Y. Xie, F. Zhou, A. Peyton, W. Yin, *NDT E Int.* **2018**, 98, 155.

[37]S. Yao, Y. Zhu, *Nanoscale* **2014**, 6, 2345.

[38]Q. Ye, Y. Wu, Y. Qi, L. Shi, S. Huang, L. Zhang, M. Li, W. Li, X. Zeng, H. Wo, X. Wang, S. Dong, S. Ramakrishna, J. Luo, *Nano Energy* **2019**, 61, 381.

[39]E. Fujiwara, M. Ferreira Marques Dos Santos, C. K. Suzuki, *IEEE Sens. J.* **2014**, 14, 3631.

[40]B. N. Sahoo, J. Woo, H. Algadi, J. Lee, T. Lee, *Adv. Mater. Technol.* **2019**, 4, 1900230.

[41]S. Aziz, S.-H. Chang, *Compos. Sci. Technol.* **2018**, 163, 1.

[42]A. Sadeghi, A. Mondini, M. Totaro, B. Mazzolai, L. Beccai, *Adv. Eng. Mater.* **2019**, 21, 1900886.

[43]H. Zhuo, Y. Hu, X. Tong, Z. Chen, L. Zhong, H. Lai, L. Liu, S. Jing, Q. Liu, C. Liu, X. Peng, R. Sun, *Adv. Mater.* **2018**, 30, 1706705.

[44]O. Atalay, A. Atalay, J. Gafford, H. Wang, R. Wood, C. Walsh, *Adv. Mater. Technol.* **2017**,

2, 1700081.

[45] I. Celhay, R. Cordova, R. Miralles, F. Meza, P. Erices, C. Barrientos, S. Valenzuela, *Cranio* **2015**, 33, 100.

[46] W. P. Yamaguti, R. C. Claudino, A. P. Neto, M. C. Chammas, A. C. Gomes, J. M. Salge, H. T. Moriya, A. Cukier, C. R. Carvalho, *Arch. Phys. Med. Rehabil.* **2012**, 93, 571.

[47] J. Leelarungrayub, R. Puntumetakul, T. Sriboonreung, Y. Pothasak, J. Klaphajone, *Int J. Chron. Obstruct. Pulmon. Dis.* **2018**, 13, 3909.

Chapter 4 Whole System Design of a Wearable Magnetic Induction Sensor for Physical Rehabilitation

Abstract

Wearable sensor technologies are attracting increasing attention for continuous monitoring of human health. Much effort has been devoted to exploiting well-designed materials to realize superior abilities, such as high sensitivity, stability and responsiveness. However, it hardly meets huge demands for practically wearable application simply focusing on the development of sensing materials in isolation. Comprehensive consideration should be given from upstream materials to enduse market, including materials design, sensor assembly, signal analysis, theoretical foundation and final system performance such as sensitivity, stability, responsiveness, cost, comfortability, and durability. Herein, I present a systematic design that combines conductive fibre fabrication based on surface nanotechnology, device assemble process optimization, signal acquisition and analysis and theoretical simulation, through a new multidisciplinary strategy integrating material science, textile technology, electromagnetics and electronic engineering. A relevant physical principle of how the inductance value changes with sensor's angle was analyzed and the result shows that the as-designed inductance changes are related to the functions of cos (θ/2). The as-constructed magnetic mutual-inductance sensing system shows approximate 6-times inductance change in regard to joint bending motions during rehabilitation exercises (*e.g.,* arm and belly), while near 2-time changes for the self-inductance sensing system setup. This integrated design strategy offers a new concept, namely whole sensing system design, for wearable technologies in real-time health monitoring applications.

4.1 Introduction

Electronics have been considered as the next generation wearable or portable devices because of their great potential in long-term and real-time human health monitoring,[1-2] implantable medical detection[3-4] and smart soft robots.[5-7] With the rapid demand of such devices, a great variety of sensing elements have been introduced by facilely contact with the human body, such as monitoring heart rate,[8] wrist pulse,[9] temperature,[10] motion,[11] blood pressure,[12] moisture (sweat, tear or respiratory), *etc.*.[13-15] One of the greatest challenges is to create electronic sensors with flexible, sensitive, quick-response, fast-recovery, stable, nontoxic and comfortable properties. Intensive research efforts have been devoted to exploit robust and effective sensing devices via exploiting advanced materials. For instance, Yan *et. al.* presented metal nanoparticles assemblies with charged organic ligands to realize different sensing functions.[16] Kim *et. al.* demonstrated a soft contact lens sensor to monitor glucose within tears.[17] Chen *et. al.* showed a dopamine-based composite film to record individual's dynamic moisture signals.[18] Most of the current sensing devices usually require a unique substrate to enhance output signal, such as interdigitated Ni/Au interdigital electrode. However, cracks or damages between the sensing materials and the substrate easily occur due to their mismatch in expansion coefficient and the lack of robust chemical bonding. Many recent works have oriented to deal with these issues via developing chemicals, self-assembly of advanced materials into 2D film and new copolymer ink printing.[19-20] Unfortunately, the long-term stability of those sensors are still insufficient, and many demands in practical wearable technologies are hardly satisfied only by improving the performance of the materials. A comprehensive system should be constructed combining materials design, assembly technology, properties characterization, signal analysis and theoretical foundation, to realize human health monitoring, in addition to study advanced materials in isolation.

On the other hand, the output of a magnetic induction sensor is stable as long as the sensor shape is maintained and the sensor requires no substrate. Especially, fibre-based magnetic induction sensing structure has received substantial interests due to its high comfort, lightweight, extreme flexibility and simple weaving process. Several works on textile-integrated

magnetic sensor in shirts as wearable devices have been reported. Wu *et. al.* fabricated an inhomogeneous fibres to construct wearable supercapacitors.[21] Dionisi *et. al.* designed an autonomous wearable device with energy-harvesting module for vital signs measurement.[22] Sardini *et. al.* reported a threadless wearable T-shirt for posture monitoring during rehabilitation exercises.[23] Teichmann *et. al.* suggested a textile-integrated magnetic induction sensor system for long-term monitoring of respiration and pulse.[24] However, the current wearable inductive sensing devices are mainly focused on the plain repetitive human activities using commercial silver conductive thread which is expensive with high resistance. A cheaper and more conductive thread is required. Besides, the variation tendency between the intensity of inductance and human motions has not been well studied. Particularly, the flexible conductive-textile-based thread in fabricating magnetic induction sensor for joints motion monitoring with precise angle measurement has also not been studied before. This is vital for monitoring rehabilitation exercises of ill-health people or maintaining standard movement during daily activities.

In this work, a systematic design of magnetic induction sensor was proposed, involving initial materials preparation via new surface nanotechnology, assemble process optimization to enhance fibres durability and stability by waxing, signal acquisition and analysis via novel equipment, and theoretical considerations in electromagnetics to support joint rehabilitation motion results. Firstly, the metal wires were synthesized by introducing chemical crosslinking reaction between catecholamines in PDA (from adhesive proteins, existed in mussels) and abundant amine groups in HPEI. According to the literature, catechols present the ability to adhere to almost any substrates, achieved a material independent surface functionalization.[25-27] The plentiful hydrogen bonds from hydroxyl and amine groups combining with chemical crosslinking network entangled the fibres, and then acted as roots to grow the conductive metal nanoparticles. This unique structure significantly enhanced the properties of flexibility and toughness. Then, a novel waxing approach was successfully introduced to improve the stability and durability of the conductive fibres during the processing. By directly sticking to the targeted position or weaving into a T-shirt, it allows

real-time recording signals of joint angle change during rehabilitation motions. Besides, the experimental results were in good agreement with the as-proposed theoretical model. The above comprehensive system was constructed, in addition to study advanced materials in isolation. The as-resulted nickel nanoparticles-coated cotton fibres thread (~ 48 Ohms/m) shows 2.6 times higher conductivity compared with commercial silver conductive fibres (~ 126 Ohms/m), since nickel shows 50-fold cheaper than silver according to the New York Commodity Exchange, (COMEX). Aluminum was also considered as one of the best metallic material for fibre conductor considering the price and biocompatibility. Recently, various aluminum based fibres on various fibrous materials were demonstrated.[28-30] However, the strategy to prepare nickel and copper-based conductive fibres is much easier, safer and greener. Apart from cotton thread, cotton fabric, woven/knitted polyester fabrics, polyester film (PET) and many other materials can be selected as the substrates to deposit nickel also copper, due to the robust adhesion of HPEI/PDA crosslinking network. During cooper deposition process, butyraldehyde was used as the reductant instead of toxic formaldehyde in conventional electroless deposition (ELD) approach in combination with sodium borohydride. Such system provides clinical data or long-term signals for daily psychological activities via a portable impedance analyzer in a convenient, comfortable, easy-to-use, money-saving, and noninvasive way. It opens a new door to constructing novel magnetic induction sensing device in a whole system design for realizing comfortable, reusable, long term and real-time rehabilitation motions monitoring and evaluation daily standard movement applications.

4.2 Experimental Section

Materials and Instrumentation

Silver conductive thread was obtained from Electro Fashion. All other chemicals were purchased from Sigma-Aldrich. All textile substrates were obtained from the Dye House at the University of Manchester. Scanning electron microscopy (SEM) was performed at a ZEISS

Ultra-55 instrument. X-ray diffraction (XRD) data were collected using a Bruker D8 Discover (A25) theta-theta diffractometer (660 mm diameter).

Polymer modification of cotton and polyester fibres

Firstly, 2 g/L dopamine and 1 g/L HPEI aqueous solution with 0.01 M Tris (hydroxymethyl) aminomethane (pH 8.5) buffer was used to dip textile substrates for 24 h stirring, or film formation for 5 min at 60 ℃. A 3×5 cm PET film was used to attach the HPEI/PDA film from top to bottom, and make the HPEI-rich side on the surface for the following ionic bonding with chloropalladium anions catalyst.

Palladium catalyst coated fibres

The HPEI/PDA modified substrates were washed with ultrapure water and hydrochloric acid (PH = 3~5) to protonate the amino groups, and immersed into a $(NH_4)_2PdCl_4$ aqueous solution (10×10^{-3} M) under dark condition for 2 h, followed by rinsing with water to remove the excess catalyst inks.

Nickel-coated fibres

Nickel-coated fibres synthesis is an improvement on our previous reports.[36] The nickel electroless plating was performed in an ELD bath containing 1:1 volumetric proportion of nickel-to-reductant stocks at room temperature. A nickel stock solution consisting of 20 g/L lactic acid, 40 g/L sodium citrate and 80 g/L nickel sulfate hexahydrate was prepared in advance. A fresh reductant solution containing 10 g/L dimethylamine borane in ultrapure water was prepared separately. After mixing, the solution was adjusted with sodium hydroxide to keep pH value as 8 to 10. The as-prepared nickel-coated fibres were washed with water and dried in the oven for future use.

Copper-coated fibres

The copper electroless plating was performed in an ELD bath containing 30:1 volumetric proportion of copper-to-reductant stocks at room temperature. A copper stock solution consisting of 13 g/L sodium hydroxide, 30 g/L potassium sodium tartrate and 15 g/L copper sulfate pentahydrate was prepared in advance. 1 mL butyraldehyde was added to 30 mL copper stock solution and the mixture is left to stand for the night. Then, 10 mL fresh sodium borohydride (2 mg/L) in ice water was prepared to accelerate the copper reduction process. The as-prepared copper-coated fibres were washed with water and dried at room temperature for future use. For conductive PET film preparation, copper was coated on one side first, and then a new HPEI/PDA film was transferred to the other side of PET substrate for nickel coating.

Conductive fibres waxing approach

An oven was set to keep high temperature to melt a white candle completely. The as-prepared conductive fibres were dipped into the melted wax, followed by using a smooth plastic wrap to remove the excess wax.

Sensor Description

The wearable self-inductance system was designed using the as-prepared nickel-based conductive fibre-thread. The exterior diameters and the distance between the turns of the sensor were about 40 and 0.4 mm respectively, while the number of turns was 8 (**Figure 4.8A**). The self-inductance varied according to the different test angles. Thus, the motion angle of the patient's arm joints and belly exercises were monitored via observing the changes of impedance value. A mutual inductance system was prepared by adhering another patterned fabric as receiving coil (**Figure 4.11B**). The planar receiving coil was woven into another fabric by another flexible fibre-thread of around 0.7-mm diameter. And the exterior diameters and the distance between the turns of the sensor were about 40 and 0.4 mm respectively, while the number of turns was 16 (**Figure 4.11A**).

Inductance Data Acquisition

The image scanning is operated using a Zurich Instruments MFIA Impedance Analyzer with for a frequency range of 5 MHz to 0.5 Hz with two input interfaces and two output interfaces. The sensor with 8 turns was placed on a table top connected with one input and one output interface of Impedance Analyzer system to observe the impedance changes effected by varying sensor's bending angles. Then, this sensor was connected with two input interfaces. The 16-turn sensor was superimposed on the top of the 8-turn sensor, and double-sided adhesive tape was used in the middle layer to avoid short circuit, which was connected to the two output interfaces of the impedance analyzer system. A frequency of 1000 Hz was used to measure the impedance as a function of sensor bending angles. The sensors were glued to arm and belly to record signals for different rehabilitation exercise of joints. All experiments were performed at room temperature (298 K).

The relationship between the sensor impedance and its inductance is described as

$$Z = R + j\omega L \tag{4.1}$$

where the real part of the impedance Z is probe resistance R, and imaginary part ωL represents reactance.

Generally, R is able to be neglected. After obtaining impedance results, real part L values controlled by bending angles are defined as

$$L = \frac{Z_{imag}}{\omega} \tag{4.2}$$

For a certain constant frequency (f), part ω is a fixed parameter

$$\omega = 2\pi f \tag{4.3}$$

where Z_{imag} is the impedance imaginary part of the sensor obtained from the Zurich Instruments MFIA Impedance Analyzer, and f was set as 1000 Hz during measurement. Therefore, different L values could be masured and calculated, which implied the inductance changes originated from magnetization when angle of inductive planar coil varied.

4.3 Results and Discussion

4.3.1 Preparation of conductive fibres

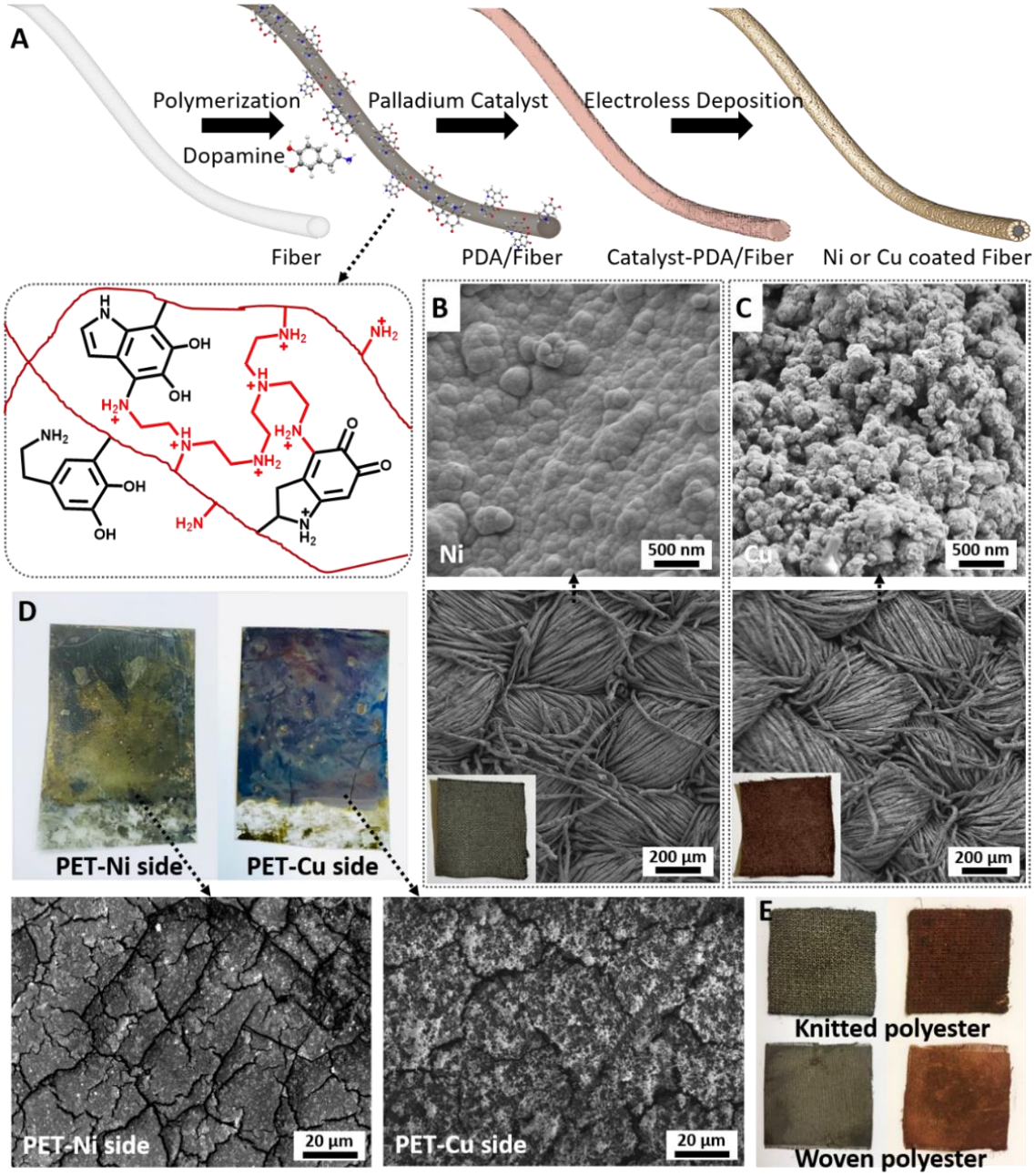

Figure 4.1 (A) The scheme illustration of nickel or copper-based conductive fibre fabrication via surface nanotechnology. Representative SEM images of the as-prepared (B) nickel, (C) copper-coated conductive cotton fibres as threads and fabrics. (D) Photo and SEM images of the polyester film (PET) coated with nickel on one side and copper on the other. (E) Photos of nickel/,-coated knitted and woven polyester fabrics. (Sizes of fabrics are around 2×2 cm; the PET film is around 3×5 cm).

A nickel-based conductive fibre thread was fabricated based on surface nanotechnology (**Figure 4.1A**). Firstly, a solution containing 2 g/L dopamine aqueous solution with 1g/L HPEI was prepared under alkaline condition to adhere textile substrates for 24 h stirring. Oxidative polymerization of dopamine took place within 3 hours, and the resulting PDA adhered to any substrate surface. The abundant amine groups from HPEI and catecholamine groups from PDA form robust chemical network via Michael addition reaction. Such various protonated amino groups under acidic condition provide effective ionic bond with chloro-palladium anions catalyst for subsequent ELD of nickel/copper nanoparticles to realize high conductivity of the fibres. The SEM images in **Figure 4.1B** displayed continuous compact nickel nanoparticles covered the entire surface of cotton fibres, led to excellent electrical conductivity of the fibres. Such surface nanotechnology can also be applied to the metal deposition on large areas fabrics (bottom of the **Figure 4.1B**). In **Figure 4.1C**, a friendly strategy was exploited to fabricate copper-coated fibres using butyraldehyde as the reducing agent assisted with sodium borohydride, instead of toxic formaldehyde in the traditional ELD process. Butyraldehyde was introduced to the copper solution to perform a preliminary copper nanoparticles reduction reaction. The addition of sodium borohydride greatly accelerates the reduction of copper nanoparticles, which can make up for the slow reduction reaction caused by the poor solubility of butyraldehyde in water. As sodium borohydride is highly reductive, many loose copper nanoparticles on the surface can be seen from SEM image, which can be used to fill the holes of butyraldehyde-reduced copper particles, thus greatly enhancing the conductivity of copper fibres.

In addition, under the acceleration of oxygen in air, dopamine molecules gradually self-polymerized into PDA and formed Janus-like HPEI/PDA thin films with two distinct domains at the air/water interface.[31-32] According to the literature,[32] the top layer on the surface of water is homogeneous and flat (catechol(amine)s-rich), while the bottom layer shows porous structures (HPEI-rich). Here, the adhesive film was attached to a PET from top to bottom, and adhered abundant amine groups on the surface of PET for bonding with chloropalladium anions catalyst and subsequent ELD reaction(**Figure 4.1D**). Because copper is more active

than nickel, copper nanoparticles can be reduced on one side of PET and then transfer another PDA film on the other side of PET to reduce nickel nanoparticles. Thus, PET film with one side of copper and the other side of nickel can be obtained. The SEM image of copper side of the PET film in **Figure 4.1D** shows many loose nanoparticles similar to those on the copper fibres in **Figure 4.1C**, while the nickel side is relatively compact and flat, confirming that the PET film reduced copper and nickel on both sides, respectively. Some cracks can be seen in SEM images in **Figure 4.1D**, originated from the porous structures of HPEI-rich side. The robust adhesion of PDA and sufficient amine groups in HPEI endow metal nanoparticles coating occurred on almost all types of substrates,[25-27] including cotton threads and fabrics, smooth PET film, polyester fabrics with woven and knitted fabrics (**Figure 4.1E**).

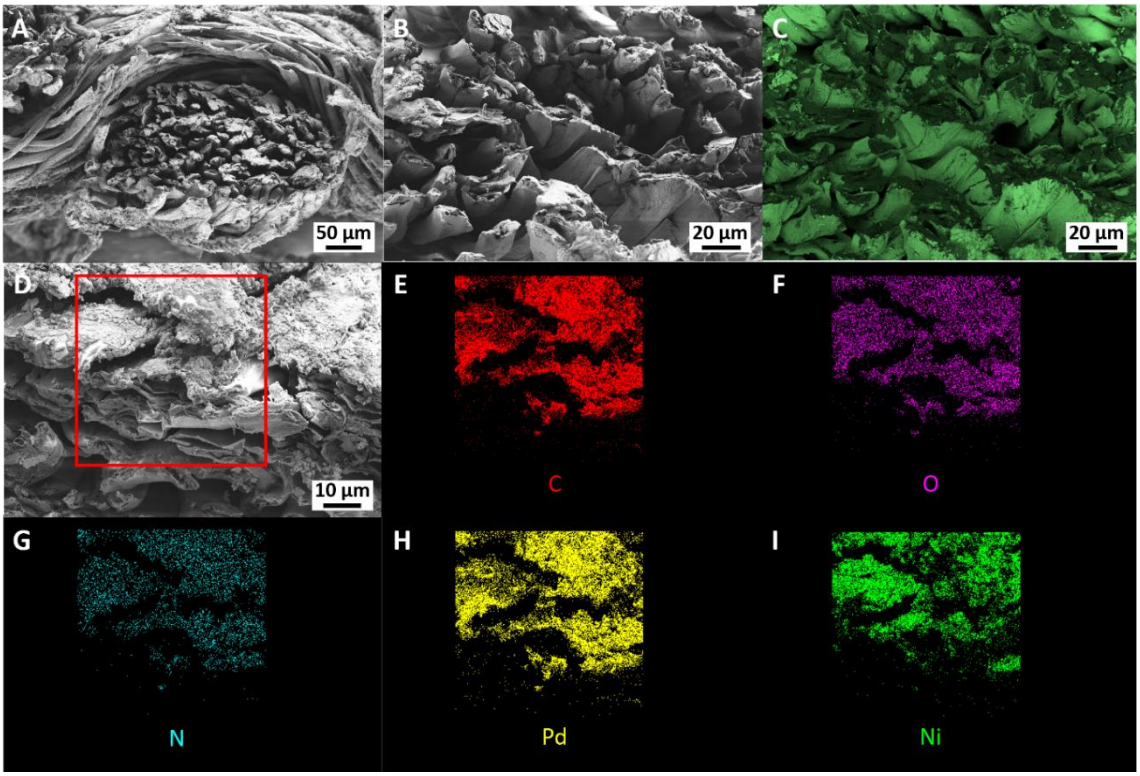

Figure 4.2 Cross-section microstructure of the as-prepared nickel-based conductive fibres (A, B), BSE image (C), magnified microstructure of image (D) and its mapping image for carbon (E), oxygen (F), nitrogen (G), palladium (H), nickel (I).

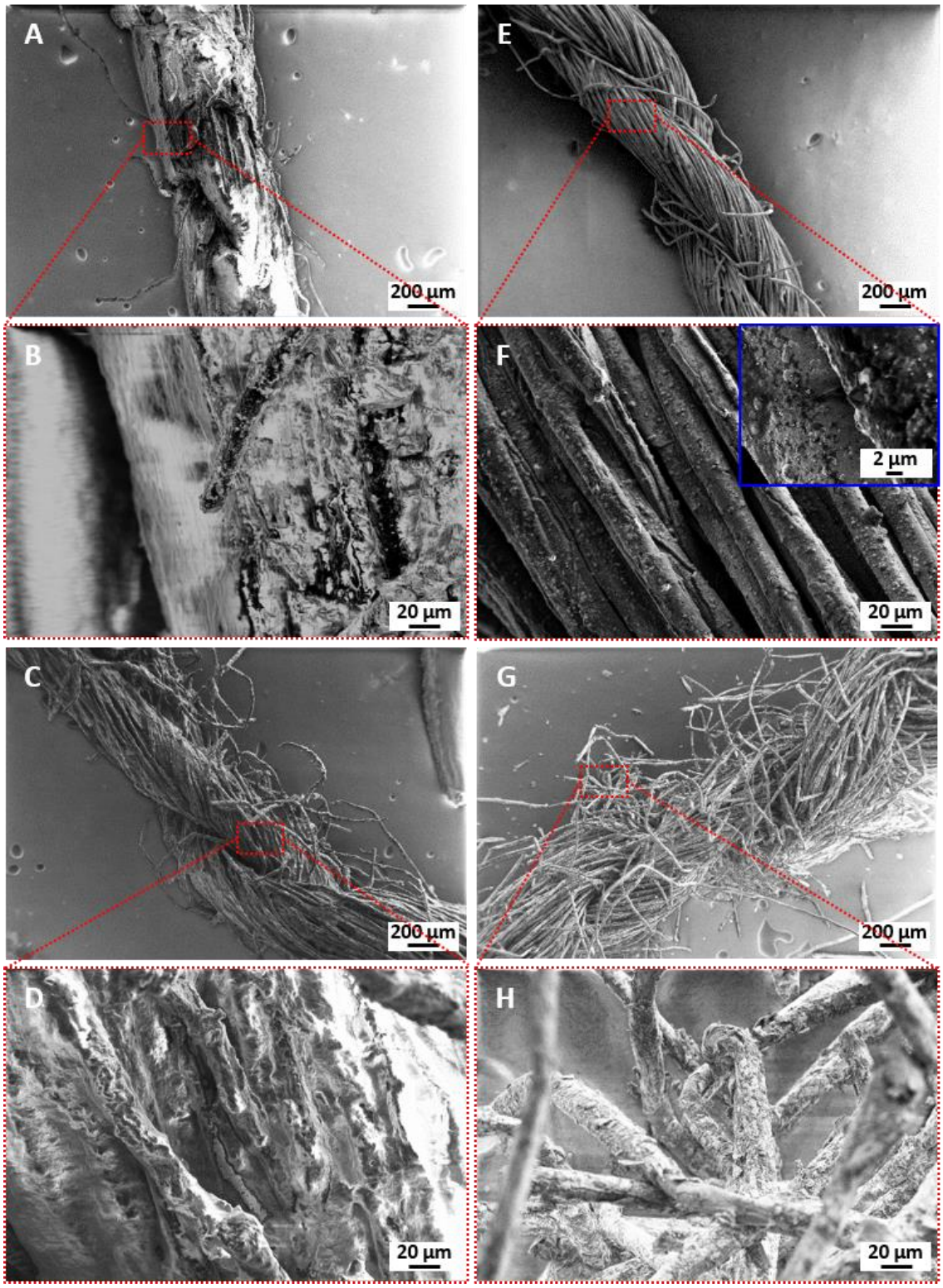

Figure 4.3 Representative SEM images of the as-prepared nickel-based conductive fibres before (A, B) and after (C, D) rubbing with wax infiltration, and before (E, F) and after (G, H) rubbing without wax infiltration.

As shown in **Figure 4.2A and S1B**, every cotton thread contains many fibres. The backscattered electron (BSE) image (**Figure 4.2C**, in the same area with the **Figure 4.2B**) displayed densely structured nickel nanoparticles films (well-lighted color) on the surface of all fibres of the thread, while in the cross-section the fibres were exposed, presented a darker color. The magnified images in **Figure 4.2D** confirmed the aggregation of very fine nickel nanoparticles on the surface of all fibres. The EDS mapping images (**Figure 4.2E, 4.2F, and 4.2G**) from the red frame in **Figure 4.2D** clearly shown that every fibre contains abundant carbon, oxygen and nitrogen elements, contributed from catechols and amines-rich polymer crosslinked with cellulose-based cotton thread. Palladium and nickel were well distributed throughout the cross-sections of fibrous fabric (**Figure 4.2H and 4.2I**), enhanced the electrical properties of the fibres.

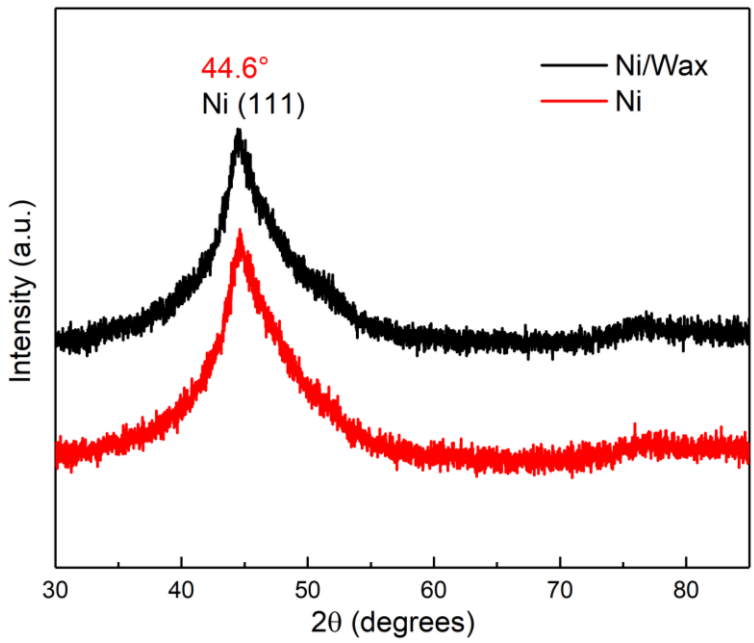

Figure 4.4 The XRD spectrum of the Nickel-coating conductive fibre before (Red) and after (Black) waxing.

Then, assembly technology with wax-dip processing was selected to enhance the stability and durability of as-formed fibres. In order to analyze the surface morphology and structures of the nickel conductive fibres which may cause significant impact on their electronic, mag-

netic properties and its stability, scanning electron microscopy (SEM) was employed to characterize the fibres with and without wax in **Figure 4.3**. **Figure 4.3A and 4.3B**) show that all fibres were glued together tightly by wax, while fibres without wax are much looser with many gaps (**Figure 4.3E and 4.3F**). While the distance between the conductive fibres is shortened, the process of wax infiltration may cause a small amount of conductive metal particles to fall off from the fibre surface. As consequence, the resistance of the 500 mm as-formed nickel-based fibre thread increases slightly from 23.8 to 25.5 Ohms, which has little impact on its application to the wearable device. To further investigate the impact of wax-dip on fibre conductivity, the resistance of a 500 mm commercial fibre was also measured and a similar trend was shown (resistance increases from 62.8 to 64.6 Ohms). On the other hand, after 60 repetitions of intense rubbing, the two fibres with and without wax-dip process perform differently. Slight breakage of the wax-impregnated fibres causes a little dislocation of the structure (**Figure 4.3C and 4.3D**). However, for the fibres without wax, there are many fractures and debris after rubbing under the same conditions (**Figure 4.3G and 4.3H**). These results suggest that fibres after wax-dip process exhibit more stable and durable as a wearable material. **Figure 4.4** shows the X-ray diffraction (XRD) patterns of the deposited nickel nanoparticles on the surface of cotton fibres before and after waxing. A main peak (red line) centered at around 44.6 ^{o}was observed from the pattern of nickel particles on cotton surface before wax-dip. According to the pure crystalline XRD spectra of the Joint Committee on Powder Diffraction Standards, the peak at 2θ value ascribed to 111 plane for nickel. Additionally, no noticeable changes were observed in the XRD peak (black line) after soaking wax into the fibres, suggesting that waxing has no impact on the structure of nickel particles.

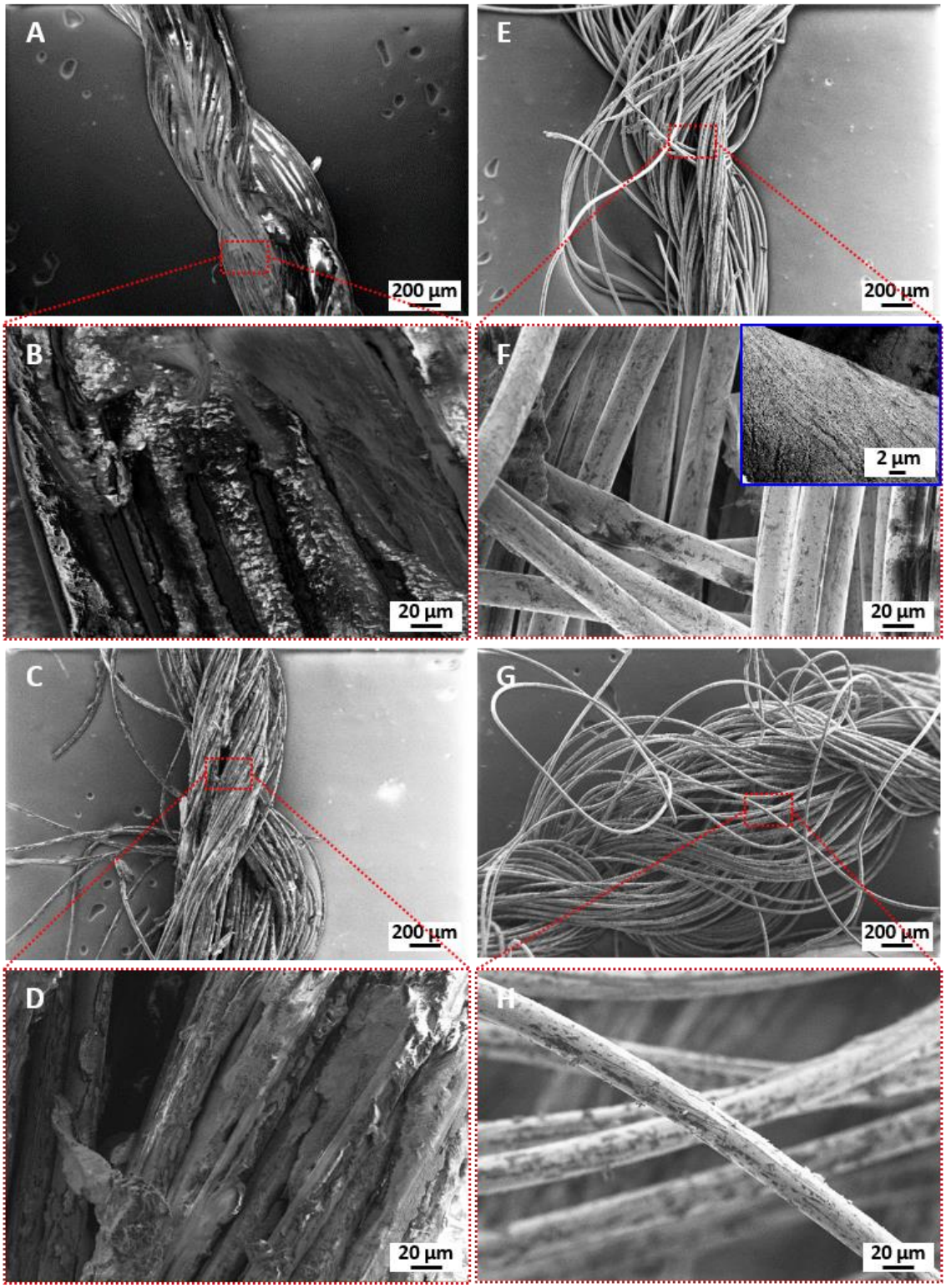

Figure 4.5 Representative SEM images of the commercial silver conductive fibres before (A, B) and after (C, D) rubbing with wax infiltration, and before (E, F) and after (G, H) rubbing without wax infiltration.

In order to confirm the universality of this soaking wax process, the commercial silver conductive fibres was studied via SEM and XRD spectroscopy, as shown in **Figure 4.5 and 4.6**. After soaking wax into fibres, the structures become denser (**Figure 4.5A and 4.5B**) than that of fibres without wax in **Figure 4.5E and 4.5F**, in parallel with the aforementioned nickel-coated cotton results. After 60 similar rubs, the chaotic structures of fibres without waxing could be observed in **Figure 4.5G and 4.5H**, while waxed fibres were generally ordered (**Figure 4.5C and 4.5D**). The relevant XRD patterns in **Figure 4.6**, compared with the Standard power diffraction card, demonstrated the silver species on the surface of commercial fibre, as evidenced by a set of 2θ values of 38.1º, 44.3 º, 64.5 ºand 77.4 º, assigned to 111, 200, 220 and 311 planes of silver, respectively. No changes were seen in the XRD peaks for two samples, which suggesting that waxing strategy did not alter the crystalline structure of the metal nanoparticles. These results implied that this waxing method is universal, not limited to the conductive fibres I prepared.

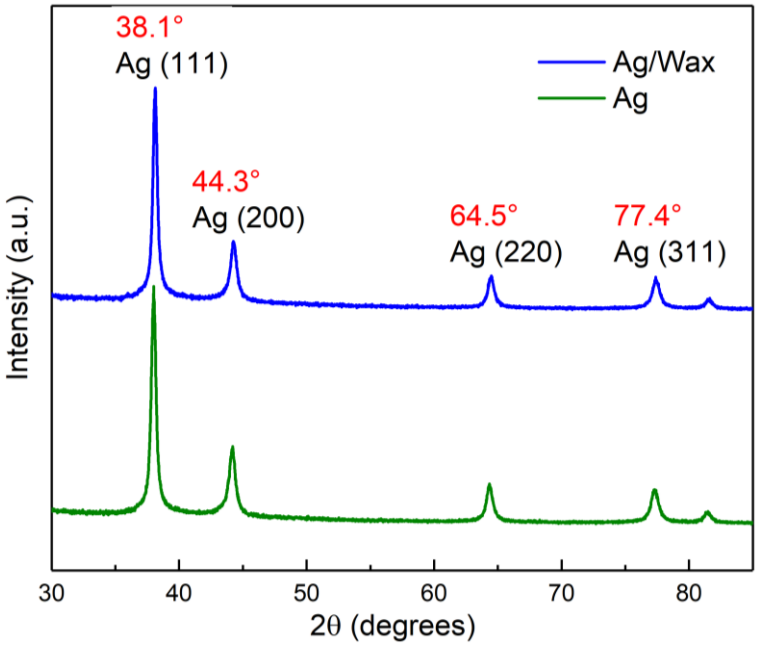

Figure 4.6 The XRD spectrum of the commercial silver conductive fibre before (Green) and after (Blue) waxing.

4.3.2 Self-inductance sensing system

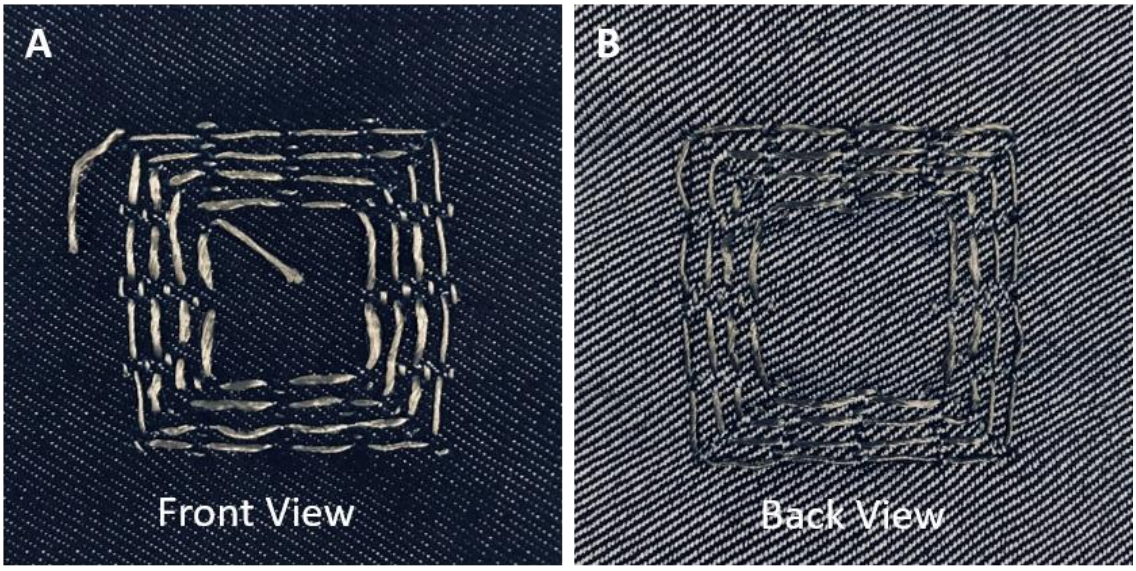

Figure 4.7 (A) The front view and (B) the back view of the as-formed fibre-based sensor used in experiments.

A wearable self-inductance system was assembled by the as-prepared nickel-based conductive fibre-thread, as shown in **Figure 4.7 and 4.8**. Inductance has multiple formats, as described in the literature.[33] Any flat format could be used in this project. For the convenience of modeling simulation, I chose a square format for this project. The exterior diameters and the distance between the turns of the sensor were about 40 and 0.4 mm respectively, while the number of turns was 8 (**Figure 4.8A**). As shown in **Figure 4.7A and B**, the fibre-thread was stitched with a square pattern on a fabric. It easily attaches onto any surface of human body or directly integrate into a T-shirt (**Figure 4.8B**). Measurements have been carried out to exploit the relationship between inductance changes and bending angles. In **Figure 4.8C**, inductance (L) gradually decreased from around 6 μH without any bending to approximately 3.7 μH when folding angle reaches 180°. A relevant physical principle of how the inductance value changes with sensor's angle was analyzed as described in the supporting information. The result shows that the as-designed inductance changes are related to the functions of cos (θ/2). The angle with different shape changes of the coil resulted in

the change of inductance of the sensor. The simulation result can be referred to theoretical considerations in the supporting information. Corresponding to the theoretical analysis parts, a variation trend of normalized inductance as the angle increases was simulated (**Figure 4.10**), suggested the same pattern with the experimental result. In addition, four kinds of folding ways were taken to achieve diagonal bending, vertical bending, front bending and back bending for comparing the effect of different folding orientation on self-inductance values under the same otherwise conditions. All of these folding ways displayed similar decreasing trend with slight difference under the same bending angle. This suggests that as long as the sensor is attached to human body tightly, the bending orientation of the sensor have little impact on the inductance values under the same joint activities. Here, the vertical bending method was introduced to evaluate joints motions (arm and belly) of individual, as shown in **Figure 4.8D**. The arm bending action produced around 2 μH inductance changes (from 5.8 to 3.8 μH), a little smaller than linear manual folding (2.3 μH). This is because that the wearable device angle changes in a non-planar surface of human body, instead of liner folding on a planar surface for the above four kinds of bending ways (**Figure 4.8E**). The inductance from the wearable device on the outside of the elbow changes around 0.13 μH with dozens of repetitive joint motions (**Figure 4.9**). From the magnification of green frame, 7 similar peaks can be observed. The blue line shows the inductance value at stretching states (~3.10 μH), while the red line demonstrates the inductance value at bending states (~2.97 μH).

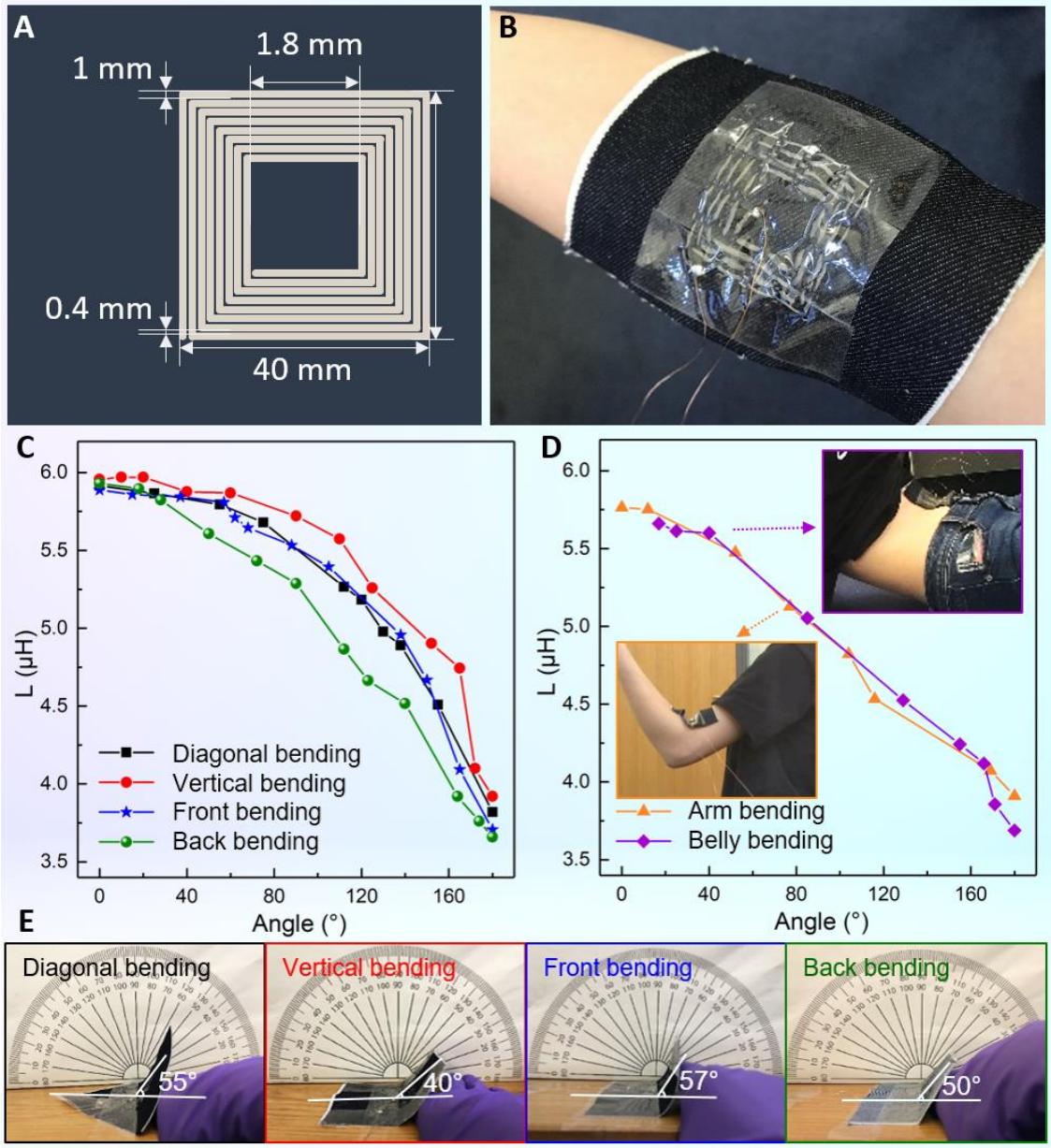

Figure 4.8 (A) Geometrical structure of the self-inductance planar coil, (B) the wearable self-inductance sensor used in experiments. Inductance changes at different angles processed by (C) central symmetry bending and (D) joints bending activities (arm and belly), (E) Photos for central symmetry bending of self-inductance sensor.

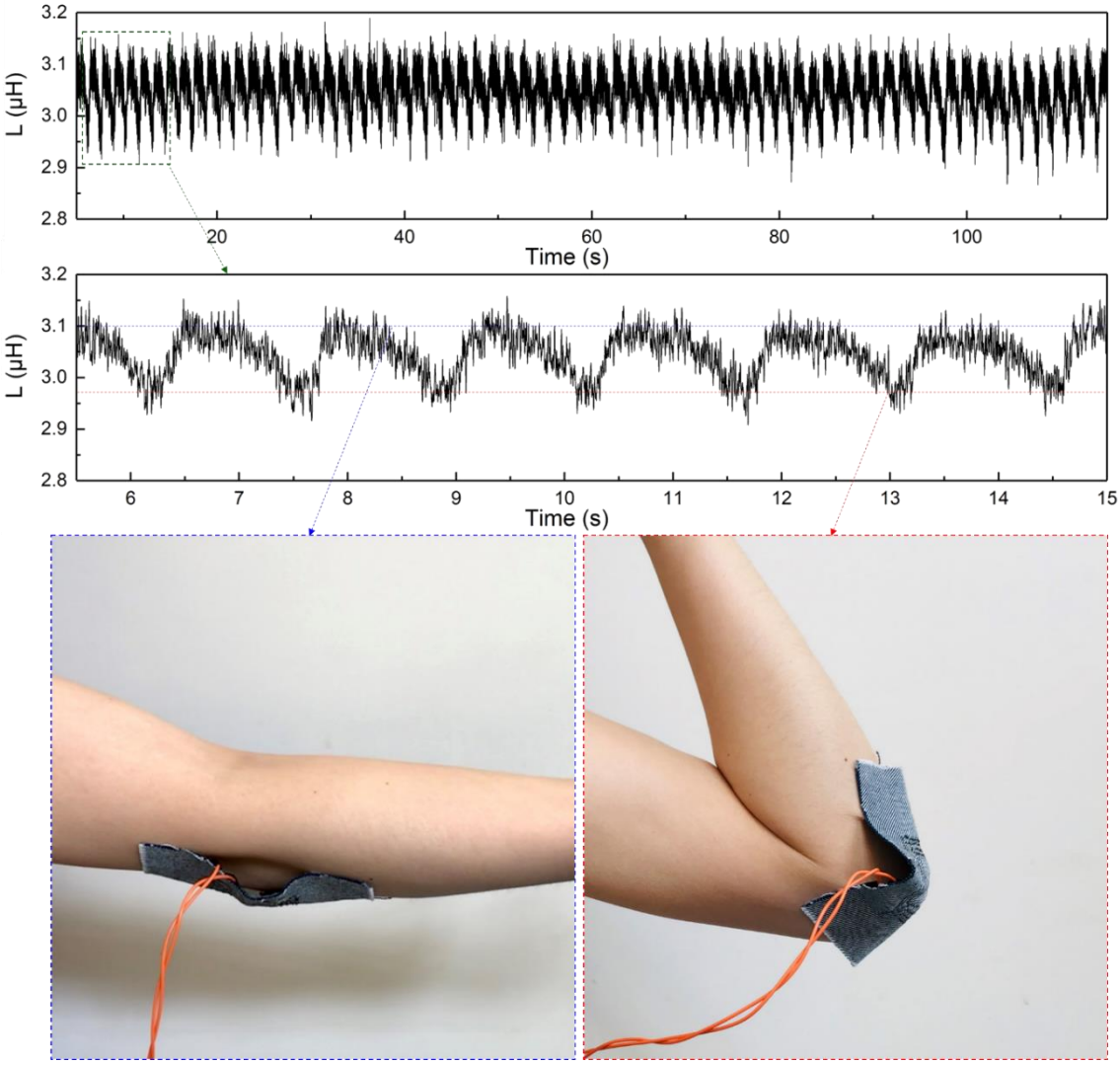

Figure 4.9 Time-dependent response self-inductance from the wearable device on the outside of the elbow switched by arm bending activities, and the relevant photos of the repeated joint motions under the same conditions.

4.3.3 Theoretical considerations

The relevant physical principle of how the inductance value changes with sensor's angle is described as follows.

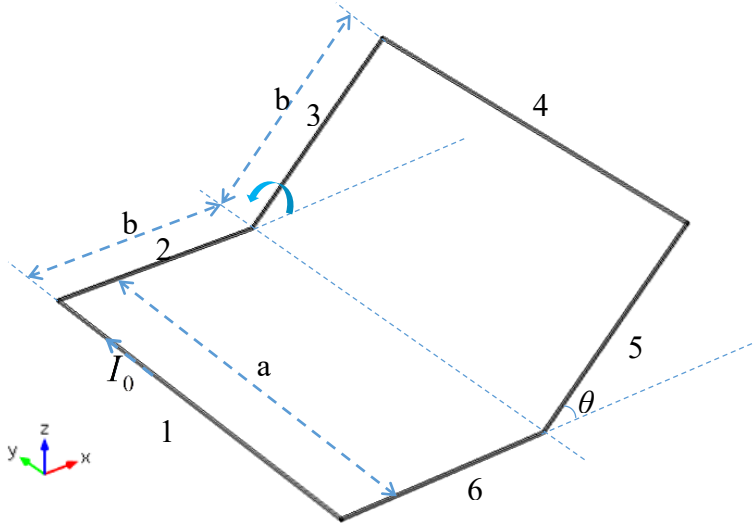

$$M_{12} = M_{13} = M_{15} = M_{16} = M_{24} = M_{34} = M_{45} = M_{46} = 0$$

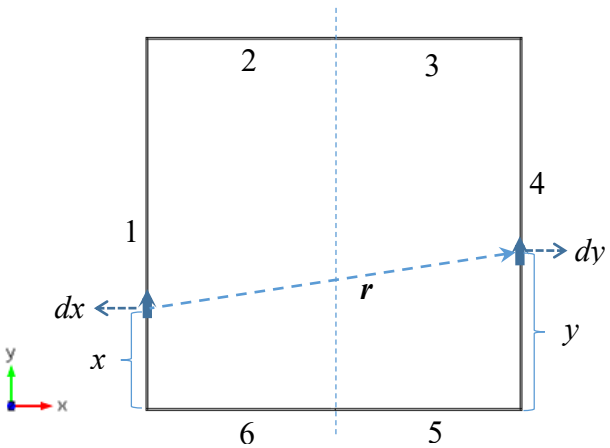

M_{14}:

The vector potential on dy in line 4 excited by current flows in line 1 is,

$$\boldsymbol{A} = \frac{\mu_0}{4\pi}\int_c \frac{d\boldsymbol{I}}{|\boldsymbol{r}|} = \frac{\mu_0 I_0}{4\pi}\int_0^a \frac{dx}{|\boldsymbol{r}|} \text{ where, } |\boldsymbol{r}| = \sqrt{(x-y)^2 + (b\cos(\theta/2))^2} \tag{4.4}$$

Further, the induced voltage between line 1 and line 4 of single loop is,

$$V = j\omega\int_c \boldsymbol{A}ds = j\omega\int_0^a \boldsymbol{A}dy \tag{4.5}$$

Therefore, the mutual inductance between line 1 and line 4 is,

$$M_{14} = \int_0^a \boldsymbol{A}dy / I_0 = \frac{\mu_0}{4\pi}\int_0^a\int_0^a \frac{dxdy}{\sqrt{(x-y)^2 + (b\cos(\theta/2))^2}} \tag{4.6}$$

Similarly, the mutual inductance M_{26} and M_{35} are,

$$M_{35} = M_{26} = \frac{\mu_0}{4\pi}\int_0^b\int_0^b \frac{dxdy}{\sqrt{(x-y)^2 + a^2}} \tag{4.7}$$

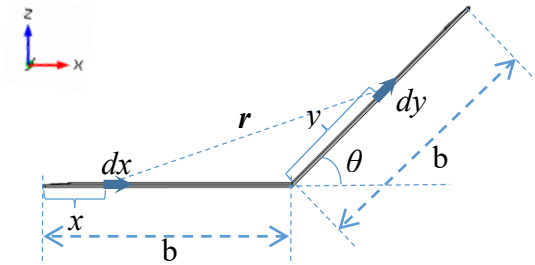

For the mutual inductance M_{23} and M_{56},

$$|\boldsymbol{r}| = \sqrt{(b - x + y\cos\theta)^2 + (y\sin\theta)^2} \tag{4.8}$$

The induced voltage is,

$$V = j\omega\int_c \boldsymbol{A}ds = j\omega\int_0^a \cos\theta \boldsymbol{A}dy \tag{4.9}$$

Therefore,

$$M_{23} = M_{56} = \frac{\mu_0}{4\pi}\int_0^b\int_0^b \frac{\cos\theta dxdy}{\sqrt{(b - x + y\cos\theta)^2 + (y\sin\theta)^2}} \tag{4.10}$$

Similarly, the mutual inductance M_{25} and M_{36} are,

$$M_{25} = M_{36} = \frac{\mu_0}{4\pi}\int_0^b\int_0^b \frac{\cos\theta dxdy}{\sqrt{(b - x + y\cos\theta)^2 + (y\sin\theta)^2 + a^2}} \tag{4.11}$$

Combining equations (4.3), (4.4), (4.7), and (4.8), the mutual inductance of the whole folding coil is,

$$\begin{aligned} M_C = \frac{\mu_0}{2\pi}\Big(&\int_0^a\int_0^a \frac{dxdy}{\sqrt{(x-y)^2 + (b\cos(\theta/2))^2}} + \int_0^b\int_0^b \frac{dxdy}{\sqrt{(x-y)^2 + a^2}} \\ &+ \int_0^b\int_0^b \frac{\cos\theta dxdy}{\sqrt{(b - x + y\cos\theta)^2 + (y\sin\theta)^2}} + \int_0^b\int_0^b \frac{\cos\theta dxdy}{\sqrt{(b - x + y\cos\theta)^2 + (y\sin\theta)^2 + a^2}}\Big) \end{aligned} \tag{4.12}$$

Considering the condition $a >> b$,

$$M_{23} = M_{56} = \frac{\mu_0}{4\pi}\int_0^b\int_0^b \frac{\cos\theta dxdy}{\sqrt{(b - x + y\cos\theta)^2 + (y\sin\theta)^2}} \approx 0 \tag{4.13}$$

$$M_{35} = M_{26} = \frac{\mu_0}{4\pi}\int_0^b\int_0^b \frac{dxdy}{\sqrt{(x-y)^2 + a^2}} \approx 0 \tag{4.14}$$

$$M_{25} = M_{36} = \frac{\mu_0}{4\pi}\int_0^b\int_0^b \frac{\cos\theta dxdy}{\sqrt{(b-x+y\cos\theta)^2 + (y\sin\theta)^2 + a^2}} \approx 0 \tag{4.15}$$

$$\begin{aligned} M_{14} &= \frac{\mu_0}{4\pi}\int_0^a\int_0^a \frac{dxdy}{\sqrt{(x-y)^2 + (b\cos(\theta/2))^2}} \\ &= \frac{\mu_0}{2\pi}\left(\sqrt{b^2\cos(\theta/2)^2 + a^2} - b\cos(\theta/2) + a\ln\left(\frac{-a+\sqrt{b^2\cos(\theta/2)^2 + a^2}}{b\cos(\theta/2)}\right)\right) \end{aligned} \tag{4.16}$$

Therefore,

$$M_C = \frac{\mu_0}{2\pi}\left(\sqrt{b^2\cos(\theta/2)^2 + a^2} - b\cos(\theta/2) + a\ln\left(\frac{-a+\sqrt{b^2\cos(\theta/2)^2 + a^2}}{b\cos(\theta/2)}\right)\right) \tag{4.17}$$

Example: a=0.02m

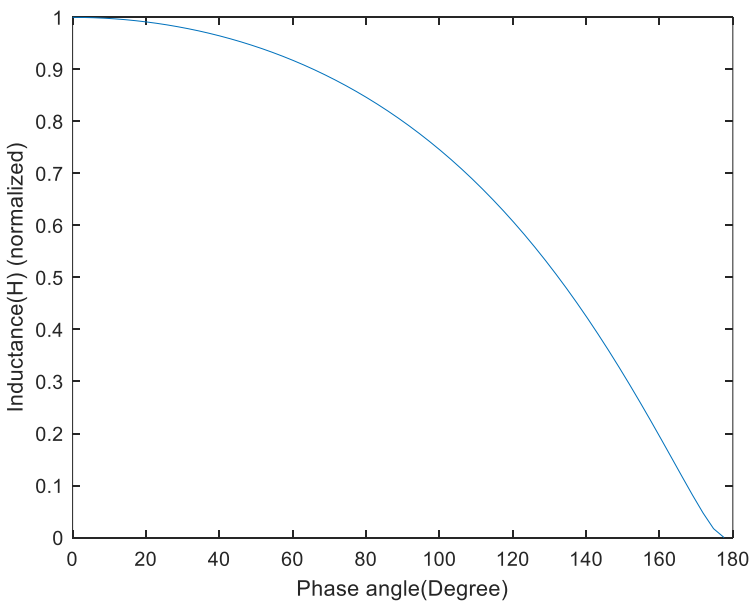

Figure 4.10 The simulated inductance changes at different angles as described in above.

4.3.4 Mutual-inductance sensing system

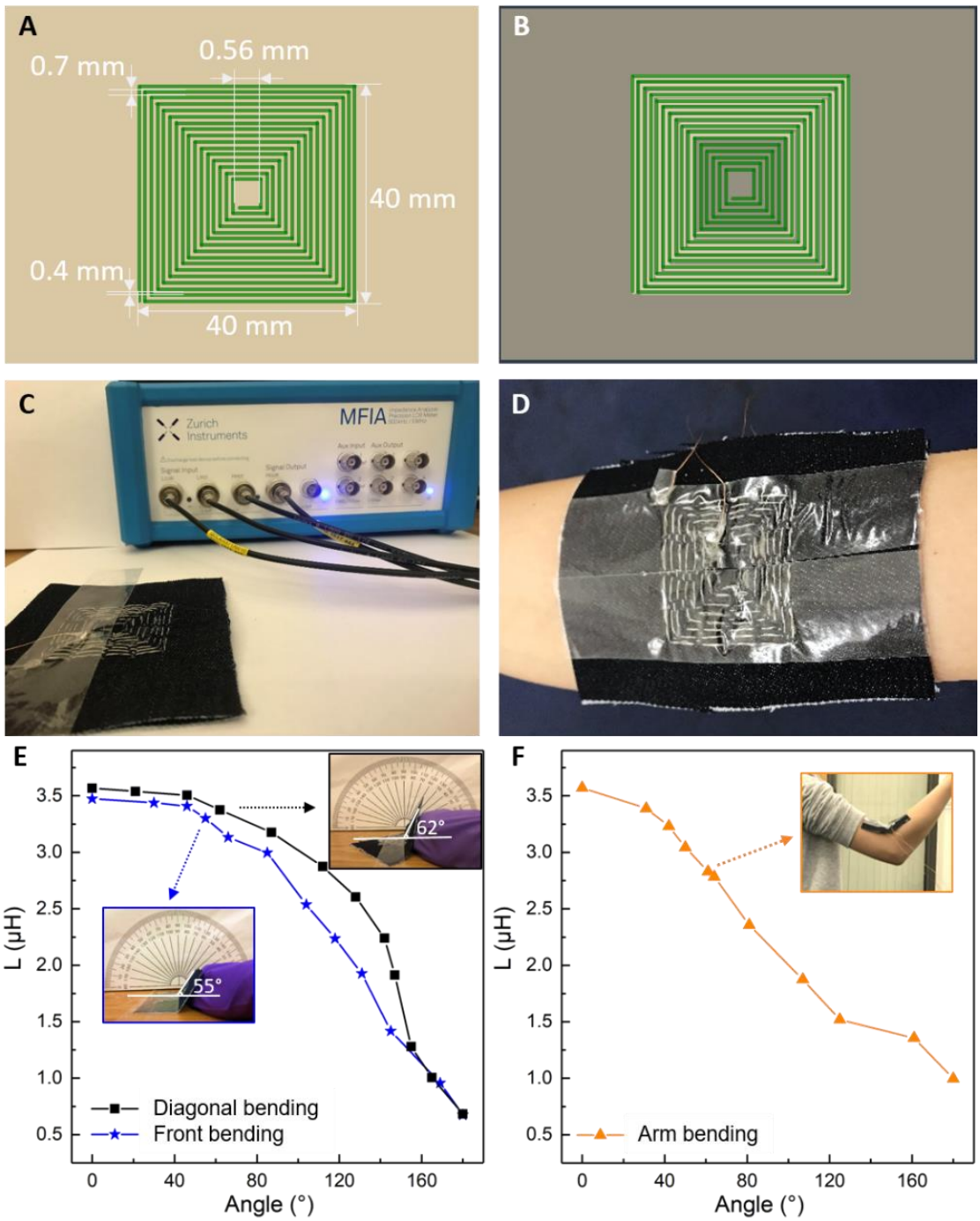

Figure 4.11 (A) Geometrical structure of the other planar coil, (B) the assembly of mutual inductance system, (C) photos of the Impedance Analyzer system, (D) the wearable mutual inductance sensor used in experiments, (E) such sensor's inductance changes at different angles processed by central symmetry bending and (F) arm bending activities.

Another conductive thread with 16 turns was used to get further information on the mutual inductance combining with the above planar coil. **Figure 4.11A** shows the geometrical structure of hand-sewn thread which was described in the experiment part in detail. Then, the mutual-inductive system was designed by just gluing these two planar coils together, and in the interlayer, a thin flexible tape was used to avoid direct electrical contact of two coils during experiments (**Figure 4.11B**). The Zurich Instruments MFIA Impedance Analyzer connecting with the mutual-inductive system was operated to gain sensing signal during rehabilitation exercise of volunteer 1, as described in **Figure 4.11C**. The wearable mutual inductance sensor was attached to arm joints firmly, similar as the single coil (**Figure 4.11D**). Before testing wearable device, two basic research about diagonal folding and front folding was processed via different liner folding way, and the photos were demonstrated in black and blue frames in the insets of **Figure 4.11E**, respectively. As shown in **Figure 4.11E**, the mutual inductance decreased from 3.5 to 0.6 μH approximately, which was around 6 times variation (~ 3 μH). When the wearable sensor was put on the arm of volunteer 1, the inductance values declined around from 3.5 to 1.0 μH. Since it does not reach 180°during arm bending activities, the inductance drops to 1.0 instead of 0.6 μH (**Figure 4.11F**). Compared with self-inductance sensing system (near 2-time changes, from 6.0 to 3.7 μH), the inductance value with the superposition of two coils (6 times changes) is more sensitive.

4.3.5 Real-time monitoring

Based on the promising results of the magnetic mutual-inductive sensor, the ability to develop a wearable device to real-time monitor arm bending activities was further studied during rehabilitation exercise of volunteer 2. As shown in **Figure 4.12A**, the inductance change (ΔL) shows around 2.2 μH with 6 arm bends with the same angle (**Figure 4.12A** a-f curves). Each peak is related to the photo of bending state in the **Figure 4.12B**. From six repeated similar bending actions, no obvious fluctuations of peak values were observed, implying excellent stability and good reproducibility of such wearable sensor. To study the excellent stability of the magnetic induction sensor, after thousands of repetitive bending experiments and six months of placement, the sensor was again used to monitor joint bending activity.

As shown in **Figure 4.13**, the results make clear that every repetitive joint bend leads to a stable change of inductance. **Figure 4.12C** depicts the real-time monitoring of inductance related to the increased bending angles. When the angle was as "a" position (~53°) in **Figure 4.12D**, the ΔL displayed around 0.35 μH. The angle was turned to zero and then increased to "b" position (~62°), the ΔL achieved about 0.64 μH. After that, the angle changed "c" position (~76°), resulted around 1.33 μH changes of inductance value. Then the angle changes was increased "d" (~120°), "e" (~140°), and "f" position (~180°), led to 1.92, 2.04, 2.28 μH changes of inductance, respectively. These results implied that the sensor enabled real-time monitoring of rehabilitation activities, as well as recording of every action's bending angle during daily training. To further study the reproducibility of the sensor under different bending angles conditions, the inductance variation of the device was performed under different angle positions from 0 °to the arm bending limit (near 180°) (**Figure 4.14**). Besides, the sensor is quite stable during bending actions, since the curve for real-time monitoring shows no obvious signal fluctuation under the same bending angles.

During inductance measurement as the angle increases, hundreds of inductance test data were obtained for every angle changes, and the average value was taken. The standard deviation of all tests is less than 0.3%, implied high measurement accuracy. Besides, the magnetic induction sensor changes according to the magnetic field, offered nanosecond response time.[34-35] As soon as the magnetic field changes, the inductive sensor responds immediately, much more responsive than temperature/humidity/pressure based resistance sensor. In other word, no delay time is observed for the as-fabricated magnetic induction sensor, in contrast to the resistance sensing system where specific response and recovery time normally occur. The chemical interaction between nickel nanoparticles and cotton fibres endows nickel robust interaction with the surface of fibres like tree roots, resulting in the particles not easily to fall off or peel off. Besides, this sensor is a non-contact sensor, avoided direct contact with human skin. In this way, nickel is not inhaled or cause any skin problem. Note that the volunteers in the process of joint motions monitoring did not suffer from any allergic reaction, which supported the sensing material of proper safety from

another aspect.

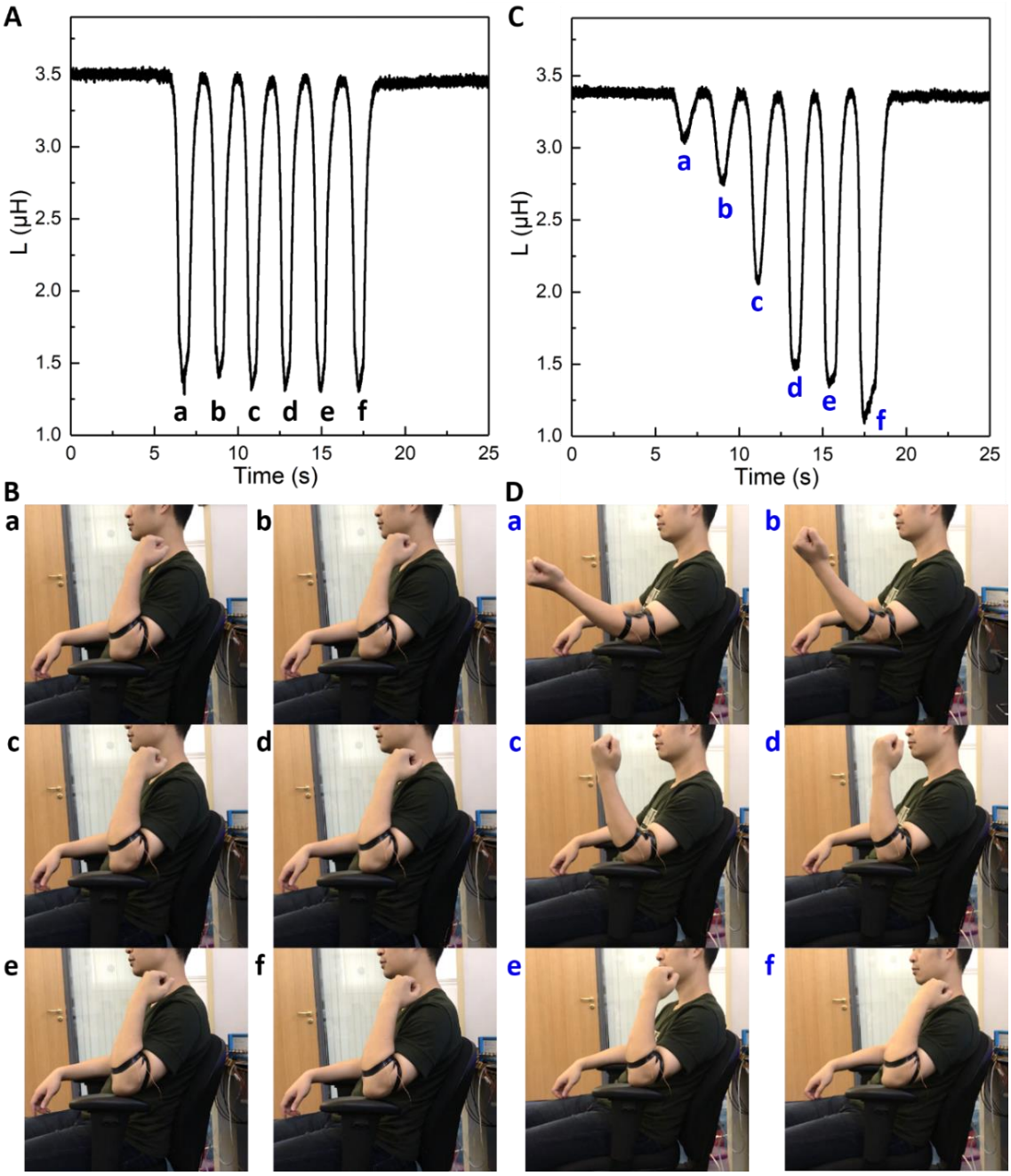

Figure 4.12 Time-dependent response mutual-inductance from the wearable device switched by arm bending activities. (A) The changes monitoring curve and (B) relevant photos of six repeated bends, (C) The changes monitoring curve and (D) the photos of the sensor increases with the rise of bending angles under the same conditions.

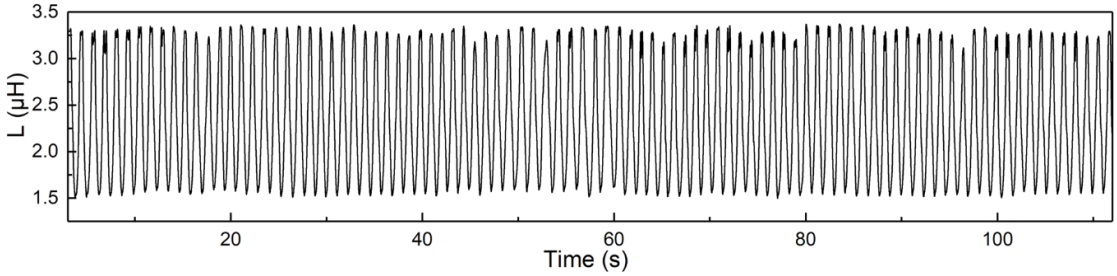

Figure 4.13 Time-dependent response self-inductance from the wearable device switched by arm bending activities and the photos of the repeated joint motions under the same conditions.

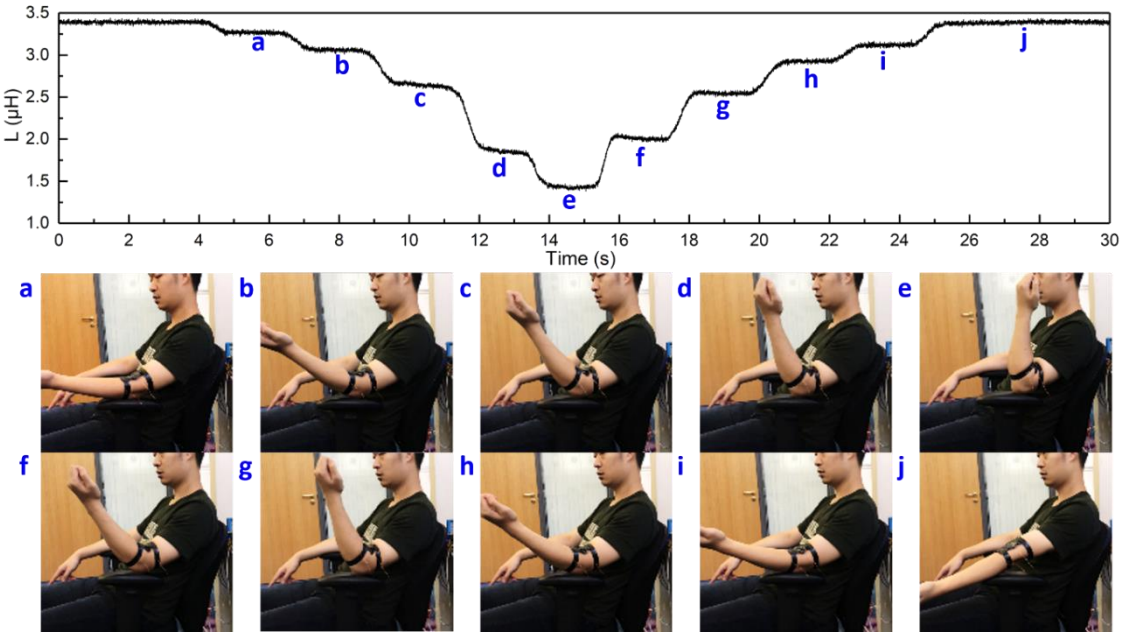

Figure 4.14 The changes in the measured mutual inductance and the relevant photos from the device at five times increase and then five times decrease of arm bending angles.

4.4 Summary

A flexible magnetic induction sensing device was systematically designed for recording different inductance signals induced by changing bending angles during rehabilitation exercise of joints (*e.g.,* arm and belly). Whole system design of the magnetic induction sensor is a multiple and integrated process from conductive fibre preparation, thread surface lubrication by wax-dip, signal analysis and simulation study. Strong adhesive PDA and

amine-rich HPEI were designed to stick firmly to the surface of the fibres via chemical crosslinking reaction for ionic bonding with chloropalladium anions catalyst and subsequent nickel or copper ELD reaction. Such sensor can not only be integrated into a T-shirt textile, but also woven into an independent fabric to adhere to different positions of the human body to form as-designed inductance patterns for different human joints training monitoring. The results show 6 times changes of the inductance value with the superposition of two coils, while near 2-time changes for the single coil setup. Measurements with two volunteers have revealed the high sensitivity, reliability and repeatability to monitor patient's rehabilitation and individual's daily joints activities. The flexible, facilely attachable, noninvasive, lightweight and comfortable characteristics of the wearable magnetic induction sensor provide novel insights into the whole system development of wearable electronics for real-time and long-term monitoring applications.

References

[1] T. P. Huynh, H. Haick, *Adv. Mater.* **2018**, 30, 1802337.

[2] T. Wang, H. Yang, D. Qi, Z. Liu, P. Cai, H. Zhang, X. Chen, *Small* **2018**, 14, 1702933.

[3] Y. Khan, A. E. Ostfeld, C. M. Lochner, A. Pierre, A. C. Arias, *Adv. Mater.* **2016**, 28, 4373.

[4] E. K. Sackmann, A. L. Fulton, D. J. Beebe, *Nature* **2014**, 507, 181.

[5] L. Y. Zhou, Q. Gao, J. F. Zhan, C. Q. Xie, J. Z. Fu, Y. He, *ACS Appl. Mater. Interfaces* **2018**, 10, 23208.

[6] S. Liu, M. C. Yuen, E. L. White, J. W. Boley, B. Deng, G. J. Cheng, R. Kramer-Bottiglio, *ACS Appl. Mater. Interfaces* **2018**, 10, 28232.

[7] D. Rus, M. T. Tolley, *Nature* **2015**, 521, 467.

[8] G. Kiruthiga, A. Sharmila, P. Mahalakshmi, M. Muruganandam, *J. Med. Eng. Technol.* **2017**, 41, 288.

[9] Z. Lou, Li, L. Wang, G. Shen, *Small* **2017**, 13.

[10] H. Joh, S. W. Lee, M. Seong, W. S. Lee, S. J. Oh, *Small* **2017**, 13.

[11] C. L. Shen, T. H. Huang, P. C. Hsu, Y. C. Ko, F. L. Chen, W. C. Wang, T. Kao, C. T.

Chan, *J. Med. Biol. Eng.* **2017**, 37, 826.

[12] K. Meng, J. Chen, X. Li, Y. Wu, W. Fan, Z. Zhou, Q. He, X. Wang, X. Fan, Y. Zhang, J. Yang, Z. L. Wang, *Adv. Funct. Mater.* **2019**, 29, 1806388.

[13] H. Guo, C. Lan, Z. Zhou, P. Sun, D. Wei, C. Li, *Nanoscale* **2017**, 9, 6246.

[14] Q. Hua, J. Sun, H. Liu, R. Bao, R. Yu, J. Zhai, C. Pan, Z. L. Wang, *Nat. Commun.* **2018**, 9, 244.

[15] H. Yan, S. Guo, F. Wu, P. Yu, H. Liu, Y. Li, L. Mao, *Angew. Chem. Int. Ed. Engl.* **2018**, 57, 3922.

[16] Y. Yan, S. C. Warren, P. Fuller, B. A. Grzybowski, *Nat. Nanotechnol.* **2016**, 11, 603.

[17] J. Kim, M. Kim, M. S. Lee, K. Kim, S. Ji, Y. T. Kim, J. Park, K. Na, K. H. Bae, H. Kyun Kim, F. Bien, C. Young Lee, J. U. Park, *Nat. Commun.* **2017**, 8, 14997.

[18] J. He, Peng Xiao, Jiangwei Shi, Yun Liang, Wei Lu, Yousi Chen, Wenqin Wang, Patrick Théato, Shiao-Wei Kuo, T. Chen., *Chem. Mater.* **2018**, 30, 4343.

[19] W. Zhao, W. Jia, M. Sun, X. Liu, Q. Zhang, C. Zong, J. Qu, H. Gai, *Sens. Actuators, B* **2016**, 223, 411.

[20] Y. Yu, X. Xiao, Y. Zhang, K. Li, C. Yan, X. Wei, L. Chen, H. Zhen, H. Zhou, S. Zhang, Z. Zheng, *Adv. Mater.* **2016**, 28, 4926.

[21] G. Wu, P. Tan, X. Wu, L. Peng, H. Cheng, C. F. Wang, W. Chen, Z. Yu, S. Chen, *Adv. Funct. Mater.* **2017**, 27, 1702493.

[22] A. Dionisi, D. Marioli, E. Sardini, M. Serpelloni, *IEEE Trans. Instrum. Meas.* **2016**, 65, 1423.

[23] E. Sardini, Mauro Serpelloni, V. Pasqui, *IEEE Trans. Instrum. Meas.* **2015**, 64, 439.

[24] D. Teichmann, A. Kuhn, S. Leonhardt, M. Walter, *Sensors (Basel)* **2014**, 14, 1039.

[25] H. Lee, S. M. Dellatore, W. M. Miller, P. B. Messersmith, *Science* **2007**, 318, 426.

[26] H. Lee, B. P. Lee, P. B. Messersmith, *Nature* **2007**, 448, 338.

[27] G. Marcelo, A. Muñoz-Bonilla, J. Rodríguez-Hernández, M. Fernández-García, *Polym. Chem.* **2013**, 4, 558.

[28] H. M. Lee, S. Y. Choi, A. Jung, S. H. Ko, *Angew. Chem. Int. Ed. Engl.* **2013**, 52, 7718.

[29] H. M. Lee, J. Y. Seo, A. Jung, S. Y. Choi, S. H. Ko, J. Jo, S. B. Park, D. Park, *ACS*

Appl. Mater. Interfaces **2014**, 6, 15480.

[30] H. M. Lee, H. B. Lee, D. S. Jung, J. Y. Yun, S. H. Ko, S. B. Park, *Langmuir* **2012**, 28, 13127.

[31] L. Zhang, P. Xiao, W. Lu, J. Zhang, J. Gu, Y. Huang, T. Chen, *Adv. Mater. Interfaces* **2016**, 3, 1600170.

[32] S. Hong, C. F. Schaber, K. Dening, E. Appel, S. N. Gorb, H. Lee, *Adv. Mater.* **2014**, 26, 7581.

[33] C. Pacurar, Vasile Topa, Adina Racasan, C. Munteanu, in *2012 13th International Conference on Optimization of Electrical and Electronic Equipment (OPTIM)*, 2012, 225.

[34] M. Liu, Bin Lang, T. Huang, in *2019 3rd International Forum on Environment, Materials and Energy (IFEME 2019)*, 2019, 507.

[35] J. Lenz, S. Edelstein, *IEEE Sens. J.* **2006**, 6, 631.

[36] C. Zhu, X. Guan, X. Wang, Y. Li, E. Chalmers, X. Liu, *Adv. Mater. Interfaces* **2019**, 6, 1801547.

Chapter 5 Wireless Humidity Sensors with Enhanched Stability and sensitivity made with Water-based Hexagonal Boron Nitride Inks

Abstract

Hexagonal boron nitride (h-BN), a new generation of two-dimensional (2D) material has been recognized by its excellent stability under high temperature, high pressure and corrosive environment. However, the application of h-BN is still very limited. Here, I prepared hydrophilic h-BN via ultrasonic exfoliation technology and opened a new door to the application of h-BN in humidity sensing. Reversible dynamic process of hydrogen bond (H-O-S) formation and cleavage endows a decrease of resistance over six orders of magnitude and an increase of capacitance from 5% to 100% in the relative humidity (RH) range. Based on the effective sensor, a wearable respiration monitoring system with a user-friendly and portable wireless transmission module were constructed to record signals of different individuals and daily activities (*e.g.*, watching video, reading, running, deep breathing and swallowing) in real time. More importantly, the breathing sensor is successfully used to monitor several common symptoms of COVID-19 and flu, including cough, fever, runny and stuffy nose caused shortness of breath or difficulty breathing. The successful sensing system will accelerate the development of the next generation 2D material like h-BN in the field of long-term, real-time and non-contact wireless human health monitoring.

5.1 Introduction

Wearable electronics have emerged as powerful platform for the treatment of many medical conditions since they can continuously and intimately monitor human health status, therefore providing personalized diagnostic and treatments.[1-5] In particular, humidity sensors are strongly needed for breath rate monitoring, touch-free skin examination, non-contact switch, and spatial localization monitoring.[6]

Advanced materials have been widely exploited as sensing elements in humidity sensors.[7-10] In particular, two-dimensional (2D) crystals show great potential in sensing mostly due to their dimensionality: the high surface area to volume ratio make them very sensitive to changes in the environment. In addition, many 2D crystals can be made by solution processing,[11-14] allowing low cost and mass scalable methods to be used for fabrication of the sensor. In particular, graphene oxide (GO) and reduced GO (rGO) have been widely exploited for humidity sensing because their abundant oxygen bearing functional groups, provide a highly hydrophilic surface, thus improving the humidity sensitivity by monitoring a simple change in resistance.[15-17] However, sensitivity is not the only parameter to take into account when developing a humidity sensor: stability and reproducibility as well as fabrication costs are also of fundamental importance. For example, it is well known that resistive-based GO and rGO based humidity sensors suffers from large hysteresis[18] and they can operate only in a small range of temperature, as the material has limited thermal stability.[15] Hence, those sensors can be used only for single sensing, but not for multiple sensing under different environmental conditions. In addition, the resistive readout is also subjected to strong cross-sensitivity issues, as any multiple change in humidity, strain, temperature, *etc.* will also all contribute to a change in resistance.

In this work I propose another approach towards the development of 2D materials-based humidity sensors with enhanced stability and reliability, based on an impedance readout and non-covalent functionalization of hexagonal boron nitride (h-BN) nanoflakes. The capacitive readout allows for simple and cheap device fabrication, easy user interface, and good

performance, while h-BN is well known for its dielectric properties as well as its excellent thermal and chemical stabilities.[19, 20] Solution-processed h-BN has been successfully used as dielectric film in capacitors[21-25] and in printed transistors.[26-28] However, the use of solution processed h-BN in sensing applications has been very limited. Only two studies, to our knowledge, have mentioned the usage of an h-BN for humidity sensing. Gautam et al. synthesized a 3D porous h-BN based material using a solid-state approach with the assistance of boron trioxide and sintering at the temperature of 1000 °C.[29] Sajid et al. reported the use of an h-BN/polyethylene oxide (PEO) composite ink, as sensing element on a piezoelectric substrate, served as the sensor's transducing portion. They obtained a near liner sensitivity of ~24 kΩ/%RH.[30] However, PEO had to be used to enhance the affinity of the sensing element to water, being h-BN hydrophobic. Herein, I show that a one-pot supramolecular approach based on the use of pyrene derivatives-assisted liquid exfoliation method (LPE)[31] allows to make hydrophilic h-BN nanoflakes, which show an enhanced sensitivity to humidity, without use of any polymeric additive. The h-BN based humidity sensor results in the high resistance sensitivity $(R-R_{RH5})/(RH-RH_5)\%$[32] is 1.8×10^{10} Ohms/%RH in 5% (RH_5) - 100%RH at 20 ℃. The maximum capacitance sensitivity $(C-C_{RH50})/(RH-RH_{50})\%$ is 0.75 pf/%RH in 50% (RH_{50}) - 100%RH. I finally constructed a breathing sensing device by making wireless and portable h-BN based humidity sensors able to record in real-time signals from different individuals in daily activities (*e.g.*, watching TV, reading, running, deep breathing and swallowing). More importantly, the breathing sensor is successfully used to real-time monitor several common symptoms of COVID-19 and flu, including cough, fever, runny and stuffy nose, shortness of breath or difficulty breathing.

5.2 Experimental Section

Materials

General chemicals of chemical reagents were analytical reagent grade and were received from were purchased from Sigma-Aldrich. Ethanol and deionized water were used as rinsing solvents.

Preparation of 2D material dispersions

The dispersions of h-BN, graphene, MoS_2, and WS_2 were prepared via pyrene-assisted liquid-phase exfoliation (LPE) method by using the h-BN powder (Sigma-Aldrich, >1 μm, 98%), graphene (Sigma Aldrich, 100+mesh) powder, MoS_2 (Sigma Aldrich, < 2 μm, 98%) and WS_2 (Sigma Aldrich, < 2 μm, 98%) as the bulk materials, respectively. 2D materials bulk powders were added to de-ionized (DI) water at a concentration of 3 mg/ml, mixed with 1mg/ml 1-pyrenesulfonic acid sodium salt (PS1) (Sigma-Aldrich, >97%). The mixture was sonicated using a 600W Hilsonic HS1900/HIlsonic FMG 600 bath sonicator at room temperature for 5 days, followed by the centrifugation at 3500 rpm (g factor=903) for 20 min using a Sigma 1-14K refrigerrated centrifuge to remove the unexfoliated bulk materials. Afterwards, the collected the upper 2/3 supernatant was further centrifuged at 13800 rpm for 2h to wash away the excess PS1. UV-vis spectroscopy was performed to determine the concentration of the exfoliated dispersions using the absorption coefficient of 2460 L g^{-1} m^{-1} for graphene, 1000 L g^{-1} m^{-1} for h-BN, 3400 L g^{-1} m^{-1} for MoS_2, and 2756 L g^{-1} m^{-1} for WS_2, respectively. The concentration of h-BN, MoS_2, graphene and WS_2 was extracted to be ~2 mg/ml for the comparison of the humidity sensing performance.

Sensor fabrication

0.05 ml prepared h-BN aqueous solution was directly drop casted onto the surface of the IDE which was sputter-deposited on the polyimide (PI) substrate (Ni: 3 μm thick; Au: 0.07 μm thick). The IDE pattern on the PI substrate provided an outline dimension of 10 mm × 10 mm. Typical dimensions of the interdigitated electrodes were 100 μm electrode width, 100 μm electrode separation, 0.75 mm electrode length, and number of electrodes was 10. The as-prepared sensor based on h-BN was connected to an Impedance Analyzer for further humidity sensing and respiratory monitoring applications.

Signal acquisition

The electrical impendence measurements were carried out using a Zurich Instruments MFIA

Impedance Analyzer with a frequency range of 5 MHz to 0.5 Hz with two input interfaces and two output interfaces. The voltage is fixed at 1 V and the frequency is fixed at 10 KHz. The controlled humidity environments were achieved at a constant temperature (~20 ºC) and humidity room (~20%). The environment temperature and humidity were monitored by using a hygrometer (TESTO 608-H2). The normalised response and sensitivity, which are defined by Re = Z0/Zx and S = ΔZ/ΔRH, respectively, are used as figures of merit to evaluate the performance of the humidity sensor, where Z0 and Zx are the impedance of the sensor at 0%RH and x%RH, respectively, ΔZ is the change in impedance, and ΔRH is the RH change.

Characterization

Scanning electron microscopy (SEM) was performed at a ZEISS Ultra-55 instrument. X-ray diffraction (XRD) data were collected using a Bruker D8 Discover (A25) theta-theta diffractometer (660 mm diameter) with a LynxEye 1D Strip detector in Bragg-Brentano geometry employing Cobalt Point/Line Focus X-ray tube with Iron kβ absorber (0.02 mm; Kβ = 1.62079 Angstrom) producing Kα radiation (Kα1 = 1.78897 Angstrom, Kα2 = 1.79285 Angstrom, Kα ratio 0.5, Kαav = 1.79026 Angstrom). The surface composition of the sample was analyzed by Near Ambient Pressure X-ray Photoelectron Spectroscopy (NAP-XPS). Fourier transform infrared (FTIR) spectra were recorded with a Nicolet NEXUS 670 FTIR spectrometer with a liquid nitrogen cooled high-sensitivity mercury cadmium telluride (MCT) detector.

According to the results of X-ray photoelectron spectroscopy (XPS), X-ray diffraction (XRD) and Fourier-transform infrared spectroscopy (FTIR) (**Figure S1 and S2**), the exfoliated h-BN nanoflakes manifest high quality and were absorbed by the PS1 molecules. Therefore, the utilization of amphoteric pyrene molecules plays the following important roles: (i) assisting the exfoliation of h-BN; (ii) stabilizing the exfoliated suspension; (iii) promoting the water absorption of h-BN; and (iv) bridging the channel of H_3O^+ proton conduction via hydrogen bond between h-BN layers. The Energy-dispersive X-ray spectroscopy (EDS) shown in **Figure S3** confirms the existence of B, N and O elements, and clearly demonstrates

that the O element of the prepared material increases from 2.34% to 12.19% as RH increases to 90%, suggesting the formation of hydrogen bond between the h-BN and water molecules.

5.3 Results and Discussion

The h-BN nanosheets were prepared via LPE in water by using an amphiphilic molecule, which allows stabilization in water as well as non-covalent functionalization of the nanosheets.[31] In particular, 1-Pyrenesulfonic acid sodium salt (PS1) is used as stabilizer as this molecule allows the preparation of highly concentrated and stable (for several months) h-BN dispersions in water.[22, 33, 34] The schematic of the exfoliation process is shown in **Figure 5.1A**. Details of the LPE are reported in Methods. Note that in contrast to graphite, h-BN can be exfoliated in water without any stabilizer,[35] but the concentration is lower than the one obtained by using PS1. The average lateral size of the exfoliated h-BN nanosheet is ~160 nm, while the average thickness is ~2.4 nm.[22] Note that the thickness cannot be directly converted into number of layers because of the adsorbed PS1 molecules. Additional characterization is provided in the Supporting Information.

The sensor was fabricated by drop casting ~50 µL of the obtained h-BN dispersion onto Ni/Au interdigitated electrodes (IDE), **Figure 5.1B**. The material was left to dry in the air and then the humidity response was collected by an impedance analyzer (**Figure 5.1B**). All measurements were performed at 10 kHz. For comparison, I also prepared and tested under the same conditions h-BN nanosheets produced by LPE in water without using any stabilizer and MoS_2 dispersions produced by PS1-assisted LPE in water. Additionally, commercially available GO was also tested.

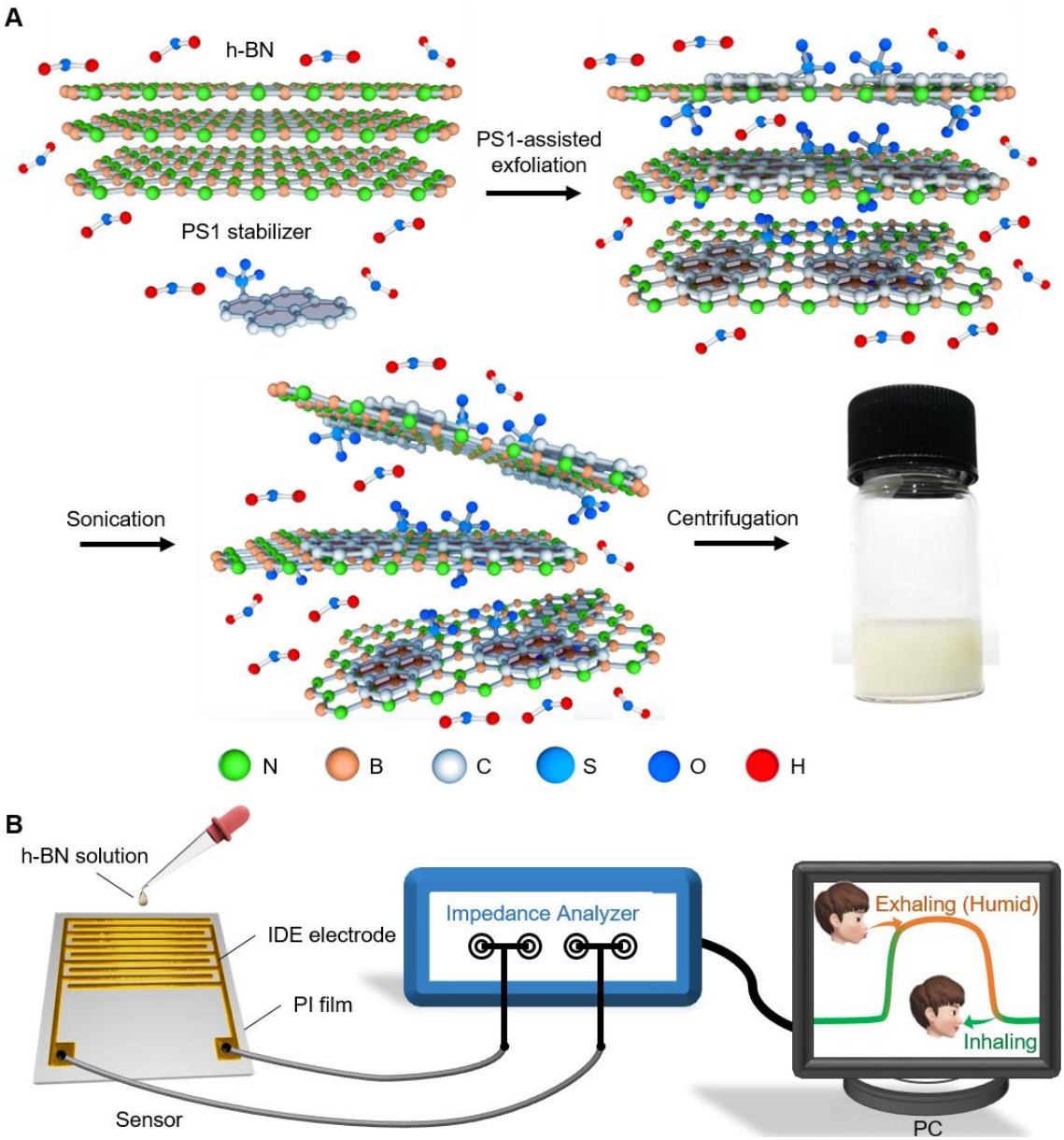

Figure 5.1 (A) Pyrene-assisted exfoliation of h-BN, (B) Schematic image of h-BN-based humidity sensor fabrication and testing by impedance analyzer.

Figure 5.2A and 2B show that both the imaginary (Z_{imag}) and real parts (Z_{real}) of the impedance are sensitive to changes in humidity produced by adding humid air on the device made with the functionalized h-BN nanosheets. In contrast, no changes in both parameters are observed in the case of pristine h-BN. This observation shows that the non-covalent functionalization with PS1 enables enhancement of the h-BN sensitivity to water: the sulfonic group allows the material to interact with the water molecules via hydrogen bonding, **Figure**

2C. The time interval for response/recovery duration was 1/(10k Hz) as 0.1 ms. The observed response and recovery time during breathing is 0.15 s and 0.09 s, respectively.

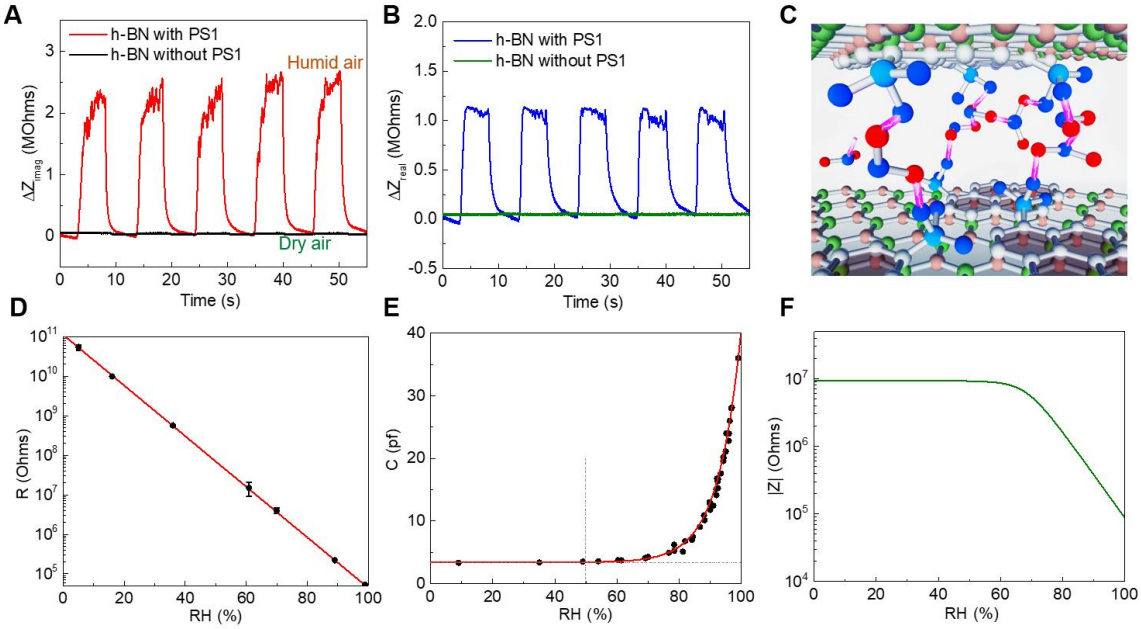

Figure 5.2 (A) ΔZ_{imag} and (B) ΔZ_{real} vs. time for exfoliated BN without PS1 (black and green line) and BN with PS1 (red and blue line) when RH was switched between the low level and high level for three cycles. (C) Sensing mechanism of the h-BN humidity sensor. (D) Linear dependence of lgR (Ohms) on %RH at 20°C. (E) Exponential dependence of C (pf) on %RH. (F) |Z| as a function of the %RH.

In order to elucidate the sensing mechanism, the changes in resistance were directly measured by using a multi-meter, while the capacitance was measured by using the impedance analyzer. **Figure 5.2D** shows an approximately linear correlation between the logarithm of resistance and the RH: the resistance decreases of more than 6 orders of magnitude for increasing RH from 5% to 100% at 20 ℃, giving rise to a sensitivity of 1.8×10^{10} Ohms/%RH (**Figure S4A**). **Figure 5.2E** displayed that the capacitance increases exponentially starting from RH > 50%, possibly because only above this humidity level there is enough water interacting with the h-BN to cause an appreciable change in the dielectric constant: the dielectric constant of water (78.5) is much higher than that of h-BN (~4).[22] This results in a

sensitivity of 0.75 pf/%RH in range of 50%-100%RH at 10k Hz (**Figure S4B**). The corresponding empirical equations are shown in equations (5.1) and (5.2), respectively.

$$lgR(RH) = 11.041 - 0.063RH \tag{5.1}$$

$$C(RH) = 3.400 + 5.132 \times 10^{-6} e^{(0.135RH)} \tag{5.2}$$

Using the equivalent RC parallel circuit (**Figure S7**), a decrease in |Z| is ascribed to a decrease in resistance and/or an increase in capacitance (equations 5.3 – 5.5). The measurements show that the resistance decreases, while the capacitance increase for increasing RH above 50%, hence causing the observed decrease in |Z|. **Figure 5.2F** indicates a strong linear decrease in |Z| for RH > 50%, from which a |Z| sensitivity of 3.1×10^5 Ohms/% RH can be extracted in the same RH range (**Figure S5**). The decrease of |Z| with increasing RH is in agreement with results obtained with other hydrophilic materials, such as polyethylene oxide-based thin films[30, 36] Exhaling on the device increase the RH leading to a decrease in the value of |Z|, suggesting the RH level during exhaling is near 100% (much higher than 50%), in agreement with previous works.[37]

$$Z_{real} = \frac{1}{1/_{R} + R(2\pi fC)^2} \tag{5.3}$$

$$Z_{imag} = -\frac{1}{1/_{(2\pi fCR^2)} + 2\pi fC} \tag{5.4}$$

$$|Z| = \sqrt{{Z_{real}}^2 + {Z_{imag}}^2} \tag{5.5}$$

In order to get further insights on the electrical readout, the equivalent RC parallel circuit was simulated by using the COMSOL software package (Supporting Information). **Figure 5.3A** shows the electric potential distribution on the surface of the IDE structure, suggesting the large effect of the electric field on sensing electrical signal output via capacitance. The calculated capacitance variation range (3.2 - 52 pf) from the COMSOL simulation is consistent with the experimental results (**Figure S9**). The calculated Z_{real} (equation 5.3) increases by 4 orders of magnitude in range of 0 to 68%RH, and reach the maximum value at ~68%RH, and then decreases by 2 orders of magnitude in range of 68 to 100%RH, **Figure 5.3B** (blue line). The maximum sensitivity of Z_{real} is obtained at ~68% RH (blue line, **Figure**

5.3C). The calculated Z_{imag} (equation 5.4) decreases by 3 orders of magnitude between 50 to 100% RH, giving rise to a sensitivity of 3.1×10^5 Ohms/%RH in this range (red line, **Figure 5.3B and 5.3C**). These results indicate that changes in Z_{real} are dominated by the changes in resistance for RH < 50%, while changes in both resistance and capacitance affect Z_{real} for RH > 50%. On the other hand, Z_{imag} is dominated by the changes in capacitance, and shows higher sensitivity compared to Z_{real} when RH > 70%. By recording (line) and calculating (black scatter points) the |Z|, Z_{real} and Z_{imag} for 11 cycles of repeated breathing in **Figure 5.3D and Figure S10**, all calculated data are entirely consistent with the experimental results, which confirms that the impedance is a bivariate function of resistance and capacitance.

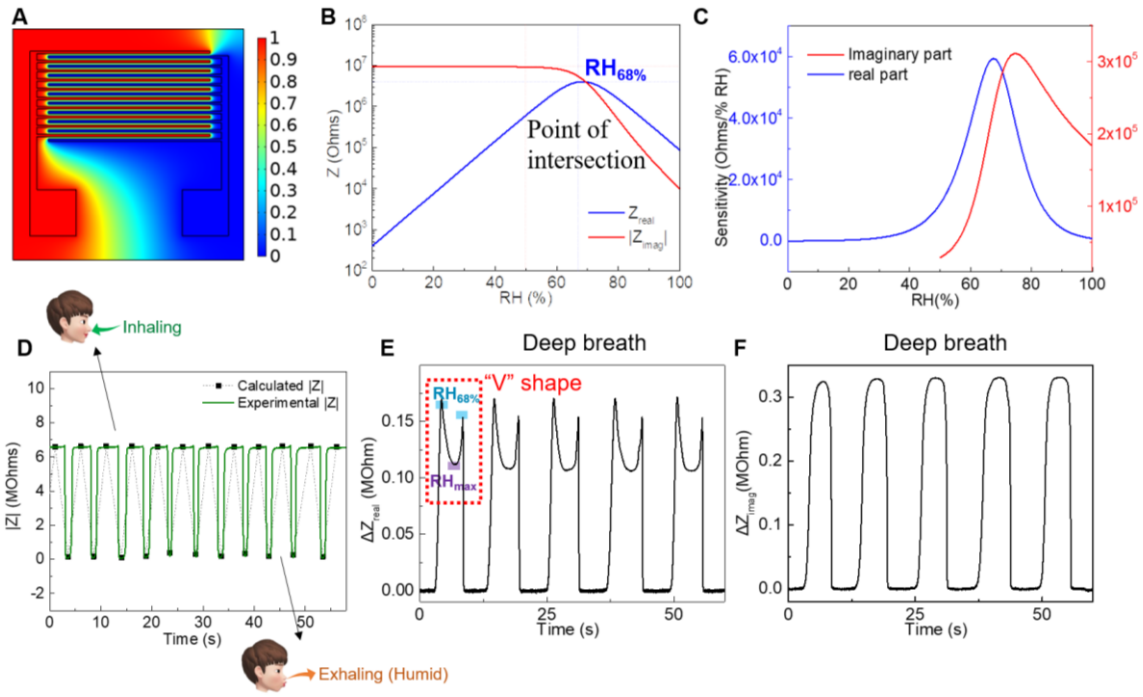

Figure 5.3 (A) Simulations of designed capacitive interdigital sensor. (B) Real (blue line) and imaginary parts (red line) of impedance change as a function of RH at 10k Hz. (C) Humidity sensor's sensitivity *vs*. RH at 10k Hz. (D) Change of |Z| variation with time for 11 cycles of repeated breath and compared with the relative theoretical impedance calculated by equations (5.3) and (5.4). (E) and (F) Deep breath monitoring.

During applying the humidity sensor for monitoring of deep breathing, a very interesting "V" shape occurred (**Figure 5.3E**) in every breathing cycles. The "V" shape is due to the Z_{real}

changing trend (increasing – decreasing - increasing – decreasing) of a breathing cycle (exhaling - inhaling process), assisted by using the signal analysis result in **Figure 5.3B**. In particular, exhaling (RH > 68%) allows Z_{real} to enhance initially when RH increases from surrounding RH (~20%) to 68%, and then decrease after turning point of 68%RH to the maximum RH. In contrast, inhaling (RH < 68%) enables Z_{real} to increase when RH decreases from maximum RH to 68%, and then decrease after RH below 68%. These results indicate that signal analysis can help understand the meaning of breathing curve and expand Z_{real} working range to 0-100%RH. The 5 well-repeated breathing cycles in **Figure 5.3E and Figure 5.3F** show that the humidity sensor can be used as a reliable breathing sensor.

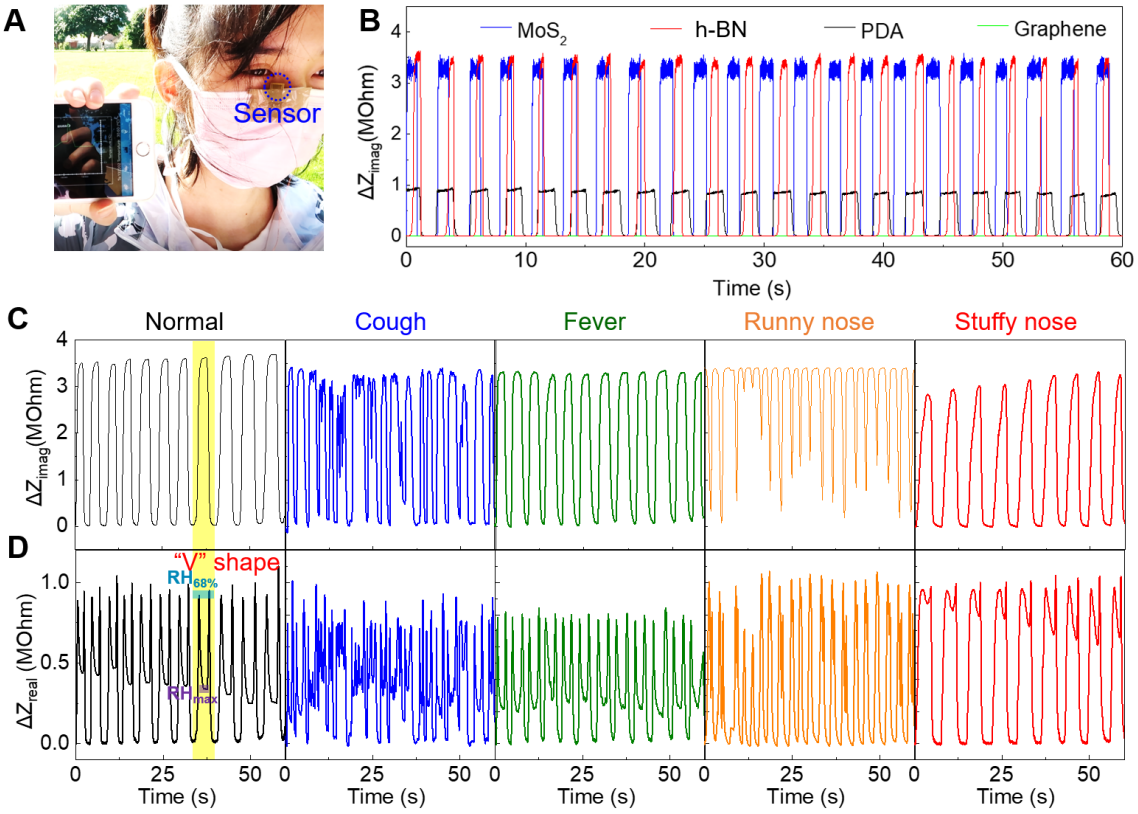

Figure 5.4 Wearable masks for human breathing real-time monitoring. (a) Breath test of sensor made by MoS_2 (blue), h-BN (red), PDA (black) and graphene (green). (b) Photo of breath test of humidity sensor based on h-BN. (c) Breathing sensor for monitoring different common symptoms of COVID-19 and flu, including Cough, Fever, Runny and stuffy nose.

In order to test for any cross-sensitivity with the temperature, I conducted experiments at fixed RH while changing the temperature. **Figure S11** demonstrates when the temperature changes (25.60 ℃), the sensor still works well. **Figure S12** indicates that the humidity sensor can detect the moisture during breathing with great cross-sensitivity (insensitive response to motions, airflow and temperature). These results suggest that the effect of temperature can be ignored and PS1/h-BN is a promising humidity sensor. These results are then compared with solution-processed graphene, MoS_2 and WS_2 produced by pyrene-assisted LPE[33], as well as GO. The humidity sensors based on MoS_2, WS_2 and GO were fabricated by drop-casting the solutions on the IDE. As expected, RH-dependent resistance plot (**Figure S13A**) illustrates the similar decreasing trend with the increase of RH. The sensitivities of these materials-based humidity sensors exhibit certain distinction possibly due to the difference of electronic structure and binding energy between PS1, 2D materials and water molecules. **Figure S13B** and **S13C** further reveal that the sensitivity and response speed of PS1-assisted MoS_2 are almost similar as h-BN, while that of WS_2 and GO are smaller at a certain RH change range, but all of them are all qualified candidates for humidity sensors.

Table 5.1 shows the key performance parameters of the RH sensors against the state of art. One can see that a simple one-pot approach based on supramolecular chemistry enables fabrication of RH sensors with 3.1×10^5 Ohms/%RH sensitivity, comparable with those sensors by chemical vapor deposition (CVD) process[37-39], which are more time consuming/expensive etc. to fabricate/produce.

Table 5.1 Comparison of humidity sensors performances with other solution processed 2D materials that are described in the literature.

Sensor type	Sensing material	Measurement range	Sensitivity	Response time	Recovery time	Ref.
Impedance	GO	40-80%	25	20 ms	30 ms	[15]
Capacitance	GO	11-97%	4.45×10^4	2.7 s	4.6 s	[16]
Resistance	rGO	0-100%	0.33	25 ms	127 ms	[18]
Resistance	MoS_2	0-60%	3.0	9 s	17 s	[40]
Impedance	1T-WS_2					[41]
Resistance	VS_2	0-100%	30	30-40 s	12-50 s	[42]
Capacitance	BP	11-97%	5.08×10^3	4.7 s	3.0 s	[16]
Resistance	BP	10-85%	$\sim10^3$		1-5 s	[43]
Resistance	rGO/PDA	0-97%	10^4	20 ms	17ms	[44]
Resistance	PDA/HPEI/AuNPs	29-97%	10^3	0.15 s	0.2 s	[45]
Impedance Resistance Capacitance	h-BN	5-100% 50-100%	3.1×10^5 Ohms/%RH 1.8×10^{10} Ohms/%RH 0.75 pf/%RH	0.1 - 150 ms	0.1 - 90 ms	This work

We finally demonstrate practical use of the sensors for respiration monitoring. The humidity sensors were attached to a mask closely to the nose to monitor a person's health status in real time by recording breathing signals. The result shows that the PS1-assisted h-BN and MoS_2 were much more sensitive than the humidity sensing materials, PDA and graphene, that we previously studied (**Figure 5.4A**).[44, 45] For daily safe use, I made wearable devices by sticking the sensor on the outside of masks, and found that the sensor can still be used to monitor human breathing in real time with high sensitivity (**Figure 5.4B**). I show that the humidity sensor can record in real-time the respiration signals of different individuals and different daily activities (*e.g.*, deep breathing, reading, watching video, running, and swallowing),

Figure S14. The real-time breathing response curves of the five volunteers shows that different individuals differed in the inhale/exhale of the moisture and the duration of one breath cycle (**Figure S14**). Different human activities, including deep breathing, reading, watching video, swallowing and running also exhibit different breath curves (**Figure S15**).

Figure 5.4C and 5.4D demonstrated the breathing sensor as an effective device to monitor several common symptoms that COVID-19 and flu share include: cough, fever, runny and stuffy nose. During coughing, breath is short and discontinuous. During fever, the breath is slightly fast than that of normal state. Runny nose induces high moisture concentration in the nose (High RH) and enhanced inhaling to avoid the mucus come out of the nostrils, and thus the imaginary part of impedance hardly back to the base line (low RH) for every breathing cycle. Stuffy nose leads to difficulty breathing, thus the breath is slow and the imaginary part of impedance is smaller than that of normal state. The smaller "V" shape in real part of impedance monitoring curve also indicates that the maximum RH value is lower than in the normal state.

The device can also be easily coupled to a wireless transmission module to make the wearable sensor more practical (**Figure 5.5**). An app, named ST BLE Sensor, was used to receive and demonstrate the data in a graphical way for users in the mobile phone (phone image in the right of **Figure 5.5)**. The wearable humidity sensor contains h-BN-coated IDE and a fixed value resistor which are connected together in series. As shown in **Figure 5.5**, the SensiEDGE SensiBLE MCU Development Kit applied a 5 V DC voltage on the humidity sensor and received the sensed voltage from an input pin of the microcontroller (**Figure S16**). The hydrophilic h-BN nanomaterial is sensitive to moisture, and thus the sensed voltage varies with RH level. The sensed voltage value is then converted from analogue signal to digital signal by an on-board analogue-to-digital converter (ADC). It is worth noting that new code has been developed for the system in order to receive the signal from the external wearable humidity sensor.

The working principle of the humidity sensor can be explained as shown in **Figure S16**. As aforementioned, the sensor made of h-BN-coated IDE was connected with a fixed value resistor in series. During the experiments, the user put the wearable humidity sensor on a facial mask and the RH level can be reflected by the resistance of the h-BN-coated IDE electrode due to the absorption of moisture on h-BN surface. If the RH level decreases (inhaling) in the sensor, the resistance of the material increases and hence the sensed voltage on the material rises, which can be demonstrated visually in the app on the mobile phone. On the contrary, if the humidity level increases in the sensor, the sensed voltage will decrease which indicate an exhaling behaviour of the user. Fundamentally, the humidity sensing system is capable of obtaining the RH level with a portable voltage source by measuring the sensed voltage on the humidity sensor.

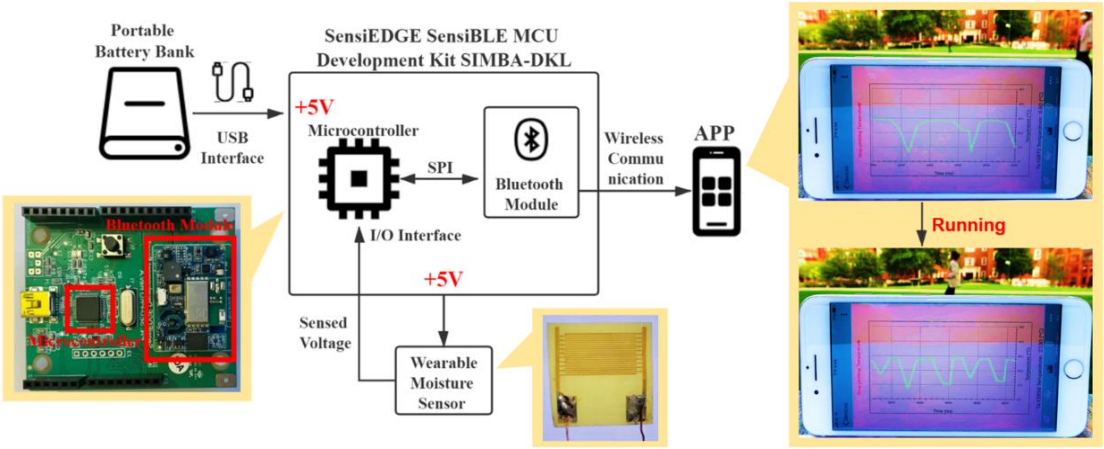

Figure 5.5 Block diagram of the wireless humidity sensing system.

5.4 Summary

A uniform h-BN nanoflake water solution was prepared via pyrene derivatives-assisted ultrasonic exfoliation technology. The pyrene molecules endow h-BN excellent hydrophilic performance with abundant hydrogen bond. The formation and breaking of hydrogen bond between PS1-assisted h-BN and water molecules endows the h-BN sensitive humidity sensing ability. This technology is universal, suitable for preparing different hydrophilic 2D

material, including h-BN, MoS_2, and WS_2, and their application is expanded to the field of humidity sensing. The results demonstrate that the maximum resistance sensitivity of h-BN is more than six orders of magnitude in the RH range of 5 ~ 100%. The signal analysis based on experiment and theoretical (combining formula derivation and COMSOL simulation) results indicated clearly the increase of real part of impedance and the decrease of imaginary part of impedance with the increase of RH. Moreover, the effective humidity sensor was developed to monitor wearable human health status, which could real-time record the subtlest changes of respiratory signals in different daily physiological activities and various symptoms of COVID-19 and flu in a noncontact way. The wireless module was introduced to realize user-friendly and portability of the sensing system. This sensing system has a promising prospect in wearable health sensing application and other hydrogen bond molecular detection occasions.

References

[1] I. You, D. G. Mackanic, N. Matsuhisa, J. Kang, J. Kwon, L. Beker, J. Mun, W. Suh, T. Y. Kim, J. B.-H. Tok, *Science* **2020**, 370, 961.

[2] Z. Ma, Q. Huang, Q. Xu, Q. Zhuang, X. Zhao, Y. Yang, H. Qiu, Z. Yang, C. Wang, Y. Chai, Z. Zheng, *Nat. Mater.* **2021**.

[3] G. Quer, J. M. Radin, M. Gadaleta, K. Baca-Motes, L. Ariniello, E. Ramos, V. Kheterpal, E. J. Topol, S. R. Steinhubl, *Nat. Med.* **2021**, 27, 73.

[4] L. Chen, M. Lu, H. Yang, J. R. Salas Avila, B. Shi, L. Ren, G. Wei, X. Liu, W. Yin, *ACS Nano* **2020**, 14, 8191.

[5] L. Chen, M. Lu, Y. Wang, Y. Huang, S. Zhu, J. Tang, C. Zhu, X. Liu, W. Yin, *Adv. Intell. Syst.* **2019**, 1.

[6] Z. Duan, Y. Jiang, M. Yan, S. Wang, Z. Yuan, Q. Zhao, P. Sun, G. Xie, X. Du, H. Tai, *ACS Appl. Mater. Interfaces* **2019**, 11, 21840.

[7] Y. Yang, Y. Song, X. Bo, J. Min, O. S. Pak, L. Zhu, M. Wang, J. Tu, A. Kogan, H. Zhang, T. K. Hsiai, Z. Li, W. Gao, *Nat. Biotechnol.* **2020**, 38, 217.

[8] D. Akinwande, D. Kireev, Nature Publishing Group, 2019.

[9] J. A. Rogers, *Nat. Nanotechnol.* **2017**, 12, 839.

[10] M. Bariya, H. Y. Y. Nyein, A. Javey, *Nat. Electron.* **2018**, 1, 160.

[11] J. N. Coleman, M. Lotya, A. O'Neill, S. D. Bergin, P. J. King, U. Khan, K. Young, A. Gaucher, S. De, R. J. Smith, *Science* **2011**, 331, 568.

[12] Y. Hernandez, V. Nicolosi, M. Lotya, F. M. Blighe, Z. Sun, S. De, I. T. McGovern, B. Holland, M. Byrne, Y. K. Gun'Ko, J. J. Boland, P. Niraj, G. Duesberg, S. Krishnamurthy, R. Goodhue, J. Hutchison, V. Scardaci, A. C. Ferrari, J. N. Coleman, *Nat. Nanotechnol.* **2008**, 3, 563.

[13] C. Backes, T. M. Higgins, A. Kelly, C. Boland, A. Harvey, D. Hanlon, J. N. Coleman, *Chem. Mater.* **2016**, 29, 243.

[14] A. Ciesielski, P. Samori, *Chem. Soc. Rev.* **2014**, 43, 381.

[15] S. Borini, R. White, D. Wei, M. Astley, S. Haque, E. Spigone, N. Harris, J. Kivioja, T. Ryhanen, *ACS Nano* **2013**, 7, 11166.

[16] P. He, J. R. Brent, H. Ding, J. Yang, D. J. Lewis, P. O'Brien, B. Derby, *Nanoscale* **2018**, 10, 5599.

[17] H. Bi, K. Yin, X. Xie, J. Ji, S. Wan, L. Sun, M. Terrones, M. S. Dresselhaus, *Sci. Rep.* **2013**, 3, 2714.

[18] C. Anichini, A. Aliprandi, S. M. Gali, F. Liscio, V. Morandi, A. Minoia, D. Beljonne, A. Ciesielski, P. Samori, *ACS Appl. Mater. Interfaces* **2020**, 12, 44017.

[19] Z. Liu, Y. Gong, W. Zhou, L. Ma, J. Yu, J. C. Idrobo, J. Jung, A. H. MacDonald, R. Vajtai, J. Lou, P. M. Ajayan, *Nat. Commun.* **2013**, 4, 2541.

[20] L. H. Li, J. Cervenka, K. Watanabe, T. Taniguchi, Y. Chen, *ACS Nano* **2014**, 8, 1457.

[21] J. Zhu, J. Kang, J. Kang, D. Jariwala, J. D. Wood, J. W. Seo, K. S. Chen, T. J. Marks, M. C. Hersam, *Nano Lett.* **2015**, 15, 7029.

[22] R. Worsley, L. Pimpolari, D. McManus, N. Ge, R. Ionescu, J. A. Wittkopf, A. Alieva, G. Basso, M. Macucci, G. Iannaccone, K. S. Novoselov, H. Holder, G. Fiori, C. Casiraghi, *ACS Nano* **2019**, 13, 54.

[23] A. M. Joseph, B. Nagendra, E. Bhoje Gowd, K. P. Surendran, *ACS Omega* **2016**, 1, 1220.

[24] A. G. Kelly, D. Finn, A. Harvey, T. Hallam, J. N. Coleman, *Appl. Phys. Lett.* **2016**, 109,

023107.

[25]B. Gupta, H. S. S. R. Matte, *ACS Applied Electronic Materials* **2019**, 1, 2130.

[26]S. Lu, J. A. Cardenas, R. Worsley, N. X. Williams, J. B. Andrews, C. Casiraghi, A. D. Franklin, *ACS Nano* **2019**, 13, 11263.

[27]T. Carey, S. Cacovich, G. Divitini, J. Ren, A. Mansouri, J. M. Kim, C. Wang, C. Ducati, R. Sordan, F. Torrisi, *Nat. Commun.* **2017**, 8, 1202.

[28]S. Conti, L. Pimpolari, G. Calabrese, R. Worsley, S. Majee, D. K. Polyushkin, M. Paur, S. Pace, D. H. Keum, F. Fabbri, G. Iannaccone, M. Macucci, C. Coletti, T. Mueller, C. Casiraghi, G. Fiori, *Nat. Commun.* **2020**, 11, 3566.

[29]C. Gautam, C. S. Tiwary, L. D. Machado, S. Jose, S. Ozden, S. Biradar, D. S. Galvao, R. K. Sonker, B. C. Yadav, R. Vajtai, P. M. Ajayan, *RSC Advances* **2016**, 6, 87888.

[30]M. Sajid, H. B. Kim, J. H. Lim, K. H. Choi, *Journal of Materials Chemistry C* **2018**, 6, 1421.

[31]C. X. Hu, Y. Shin, O. Read, C. Casiraghi, *Nanoscale* **2021**, 13, 460.

[32]D. Zhang, X. Zong, Z. Wu, Y. Zhang, *Sensors and Actuators B: Chemical* **2018**, 266, 52.

[33]D. McManus, S. Vranic, F. Withers, V. Sanchez-Romaguera, M. Macucci, H. Yang, R. Sorrentino, K. Parvez, S. K. Son, G. Iannaccone, K. Kostarelos, G. Fiori, C. Casiraghi, *Nat. Nanotechnol.* **2017**, 12, 343.

[34]H. Yang, F. Withers, E. Gebremedhn, E. Lewis, L. Britnell, A. Felten, V. Palermo, S. Haigh, D. Beljonne, C. Casiraghi, *2D Materials* **2014**, 1, 011012.

[35]Y. Lin, T. V. Williams, T.-B. Xu, W. Cao, H. E. Elsayed-Ali, J. W. Connell, *The Journal of Physical Chemistry C* **2011**, 115, 2679.

[36]Y. Wang, Y. Zhou, G. Xie, J. Li, Y. Wang, X. Liu, Z. Zang, *ACS Appl. Mater. Interfaces* **2021**.

[37]A. S. Pawbake, R. G. Waykar, D. J. Late, S. R. Jadkar, *ACS Appl. Mater. Interfaces* **2016**, 8, 3359.

[38]Z. Zhen, Z. Li, X. Zhao, Y. Zhong, L. Zhang, Q. Chen, T. Yang, H. Zhu, *Small* **2018**, 14, 1703848.

[39] J. Zhao, N. Li, H. Yu, Z. Wei, M. Liao, P. Chen, S. Wang, D. Shi, Q. Sun, G. Zhang, *Adv. Mater.* **2017**, 29.

[40] S.-L. Zhang, H.-H. Choi, H.-Y. Yue, W.-C. Yang, *Current Applied Physics* **2014**, 14, 264.

[41] C. C. Mayorga-Martinez, A. Ambrosi, A. Y. S. Eng, Z. Sofer, M. Pumera, *Adv. Funct. Mater.* **2015**, 25, 5611.

[42] J. Feng, L. Peng, C. Wu, X. Sun, S. Hu, C. Lin, J. Dai, J. Yang, Y. Xie, *Adv. Mater.* **2012**, 24, 1969.

[43] P. Yasaei, A. Behranginia, T. Foroozan, M. Asadi, K. Kim, F. Khalili-Araghi, A. Salehi-Khojin, *ACS Nano* **2015**, 9, 9898.

[44] J. He, P. Xiao, J. Shi, Y. Liang, W. Lu, Y. Chen, W. Wang, P. Théato, S.-W. Kuo, T. Chen, *Chem. Mater.* **2018**, 30, 4343.

[45] L. Chen, Y. Huang, L. Song, W. Yin, L. Hou, X. Liu, T. Chen, *ACS Appl. Mater. Interfaces* **2019**, 11, 36259.

Supplementary Information

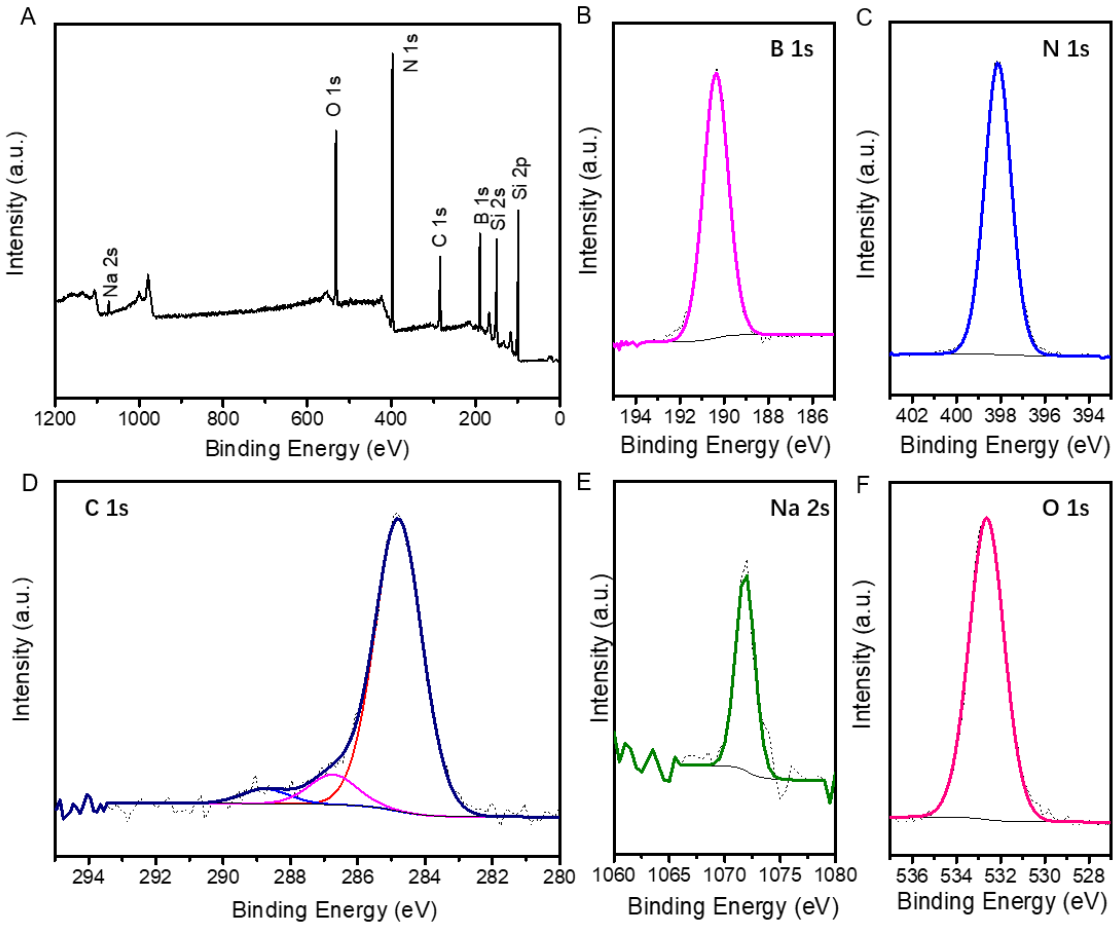

Figure S1 (A) XPS survey spectrum of h-BN. XPS spectrum of B 1s (B), N 1s (C), C 1s (D), Na 2s (E) and O 1s (F). XPS was employed to characterize the chemical composition of the exfoliated h-BN. All the XPS spectra were calibrated with the reference of C 1s peak located at 284.8 eV. The binding energies of B1s and N 1s were located at 190.4 and 398.1 eV, consistent with the reported value. The B/N ratio is calculated to be 1.01, indicating the nearly stoichiometric composition of the exfoliated h-BN. The XPS spectra of Na 1s located 1071.8 eV and O 1s at 532.6 eV demonstrated the existence of PS1 absorbed on h-BN. The XPS spectrum of C 1s were fitted with three peaks, which were located at 284.8 eV, 288.8 eV and 286.7 eV, respectively.

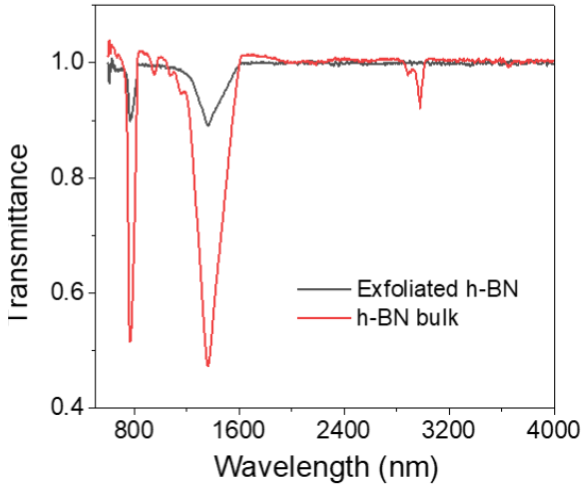

Figure S2 (a) FTIR spectra of exfoliated h-BN and h-BN bulk. Two strong characteristic bands of bulk h-BN powder were located at 1361 and 767 cm^{-1}, which can be assigned to in-plane ring B-N stretching vibration (E_u mode) and out of plane B-N-B bending vibration (A_{2u} mode). The FTIR spectrum performed on the exfoliated h-BN displays two broad peaks shift to 1365 and 769 cm^{-1} respectively, demonstrating the main structure of h-BN after exfoliation. The shifting and broadening of the peak are attribute to the change of domain size and thickness of exfoliated h-BN flakes.

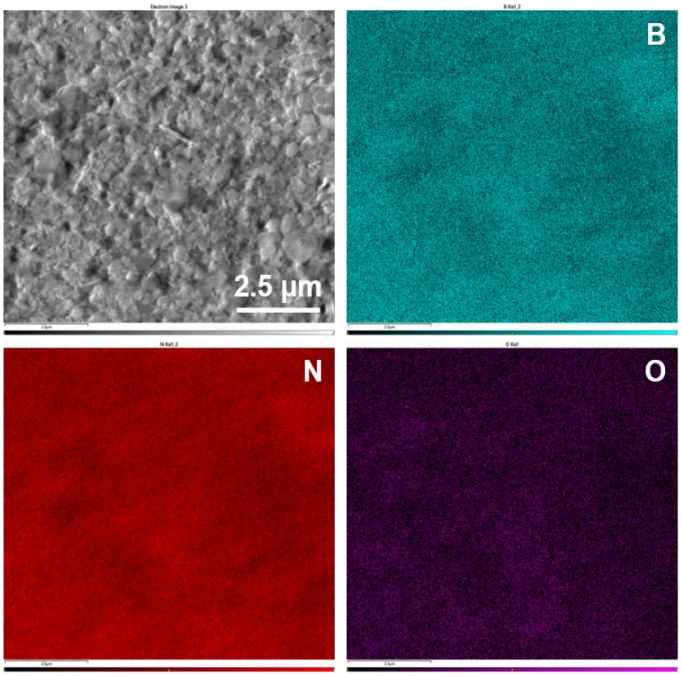

RH % \ Element %	B	N	O
Low Vacuum	49.53	48.13	2.34
20%	48.04	46.12	5.84
90%	42.32	45.49	12.19

Figure S3 SEM and mapping images of h-BN, and the atomic percentage at low vac EDX, 20%RH and 90%RH ESEM.

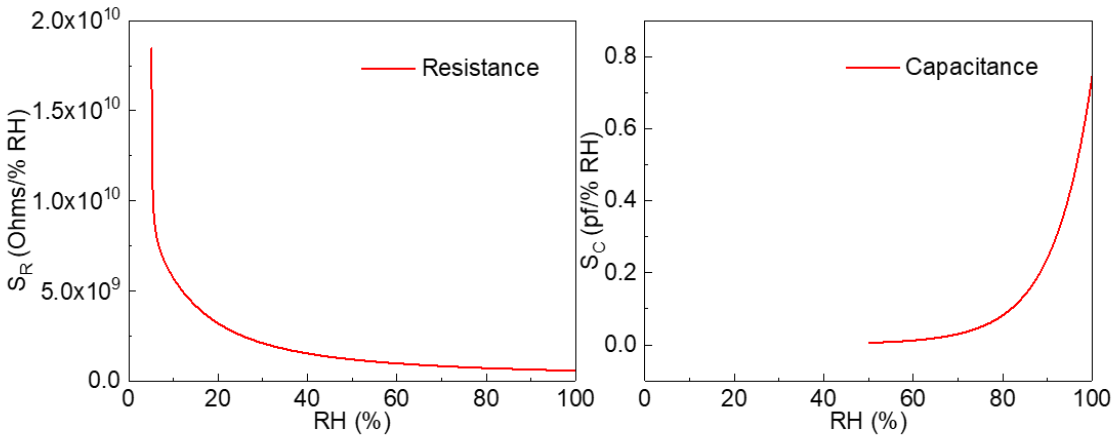

Figure S4 Sensitivity of resistance and capacitance of the humidity sensor as a function of RH.

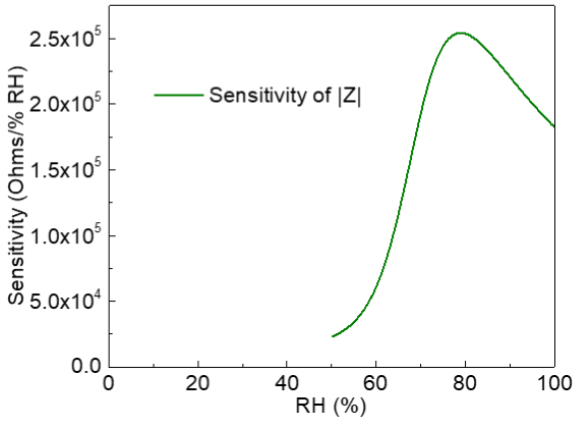

Figure S5 Sensitivity of (a) resistance and (b) capacitance of the humidity sensor as a function of RH.

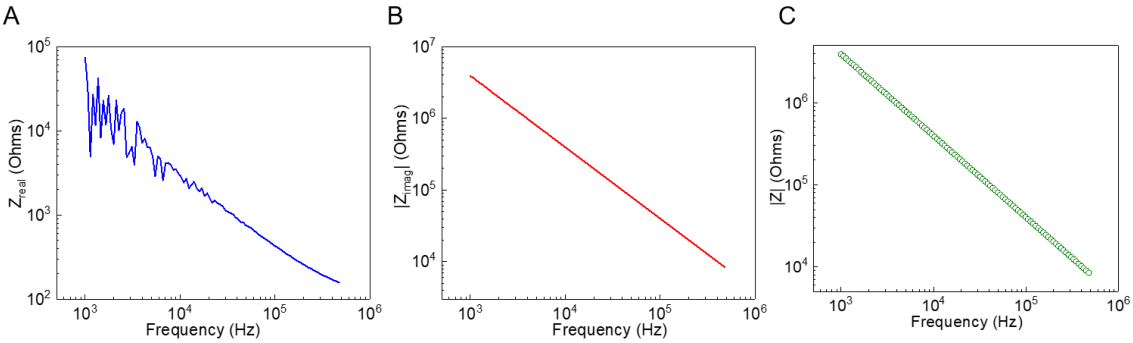

Figure S6 (A) Z_{real} and (B) Z_{imag} (C) vs. frequency changes from 1k to 550k Hz.

RC Parallel sensor theoretical analysis

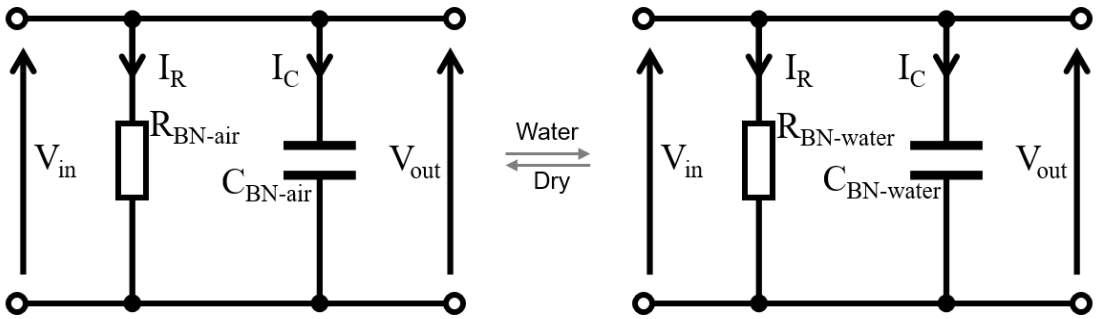

Figure S7 RC parallel circuit under water and dry conditions.

For two parallel coplanar strips, the capacitance per length is

$$C_g = \varepsilon \frac{K\sqrt{1-k^2}}{K(k)} \tag{S1}$$

For the capacitive interdigital structure, the unit cell capacitance per length is

$$C_{uc} = \varepsilon_0(\varepsilon_r + \varepsilon_k)\frac{K\sqrt{1-k^2}}{K(k)} + 2\varepsilon_0\varepsilon_k\frac{t}{w} \quad \text{(S2)}$$

$$\mathrm{k = w/z} \quad \text{(S3)}$$

$$\mathrm{z = 2(w + s)} \quad \text{(S4)}$$

where ε_0 is the dielectric constant in the free space, $\varepsilon_0 = 8.8542 \times 10^{-12} F/m$.

$\varepsilon_{r,}\varepsilon_k$ are the dielectric constants of the PI substrate and the dielectric film, respectively.

N is the number of unit cells in the capacitor, 10.

L is the length of the electrode fingers, 0.7 mm.

w is electrode's width, 100 μm.

t is electrode's thickness, Ni: 3 μm thick; Au: 0.07 μm thick.

s is distance between the adjacent electrodes, 100 μm.

K: Complete elliptic integral of the first kind.

The total capacitance of the capacitive interdigital structure is

$$\mathrm{C} = C_{uc}(N-1)L \quad \text{(S5)}$$

The current flowing in the capacitor current and resistor are described as

$$I_R = \frac{V_{in}}{R} \quad \text{(S6)}$$

$$I_C = j\omega C V_{in} \quad \text{(S7)}$$

The equivalent impedance measured from the output is

$$\mathrm{Z} = \frac{V_{out}}{V_{in}} = \frac{R}{1+j\omega CR} \quad \text{(S8)}$$

By splitting the real part and imaginary part, equation (S8) becomes

$$\mathrm{Z} = \frac{R}{1+j\omega CR} \times \frac{1-j\omega CR}{1-j\omega CR} = \frac{R}{1+(\omega CR)^2} - \frac{j\omega CR^2}{1+(\omega CR)^2} \quad \text{(S9)}$$

The real part of impedance is

$$Z_{real} = \frac{R}{1+(\omega CR)^2} \quad \text{(S10)}$$

$$Z_{real} = \frac{1}{1/_R + R(\omega C)^2} \quad \text{(S11)}$$

The imaginary part of impedance is

$$Z_{imag} = -\frac{\omega CR^2}{1+(\omega CR)^2} \quad \text{(S12)}$$

$$Z_{imag} = -\frac{1}{1/_{(\omega CR^2)} + \omega C} \quad \text{(S13)}$$

The Z_{real} and Z_{imag} were measured by the sensor connected with the Zurich Instruments MFIA Impedance Analyzer.

For a certain constant frequency (f),ω is the angular frequency and equals

$$\omega = 2\pi f \tag{S14}$$

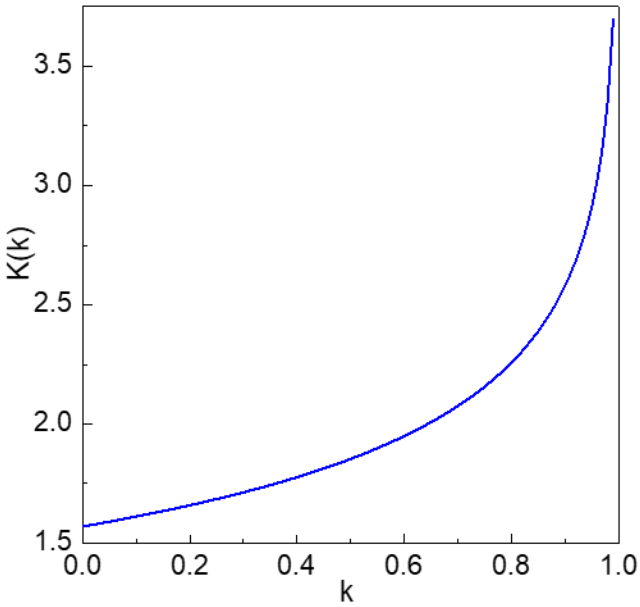

Figure S8 Complete elliptic integral of the first kind K(k) when variable k changes from 0 to 1.

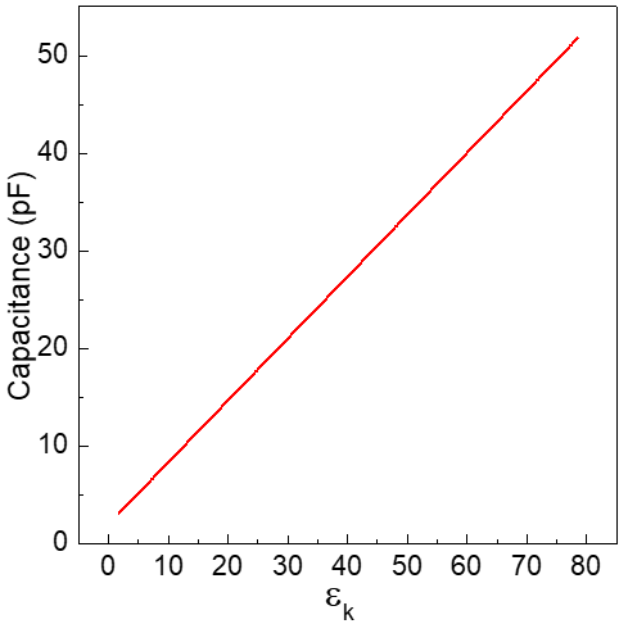

Figure S9 The total capacitance changes with the dielectric constant of sensing layer, ε_k, when $\varepsilon_k(BN) = 1.78$, the minimum C is 3.2 pf; when $\varepsilon_k(Water) = 78.5$, the maximum C is 52 pf. The capacitance changes within the range of 3.2 to 52 pf when the RH changes.

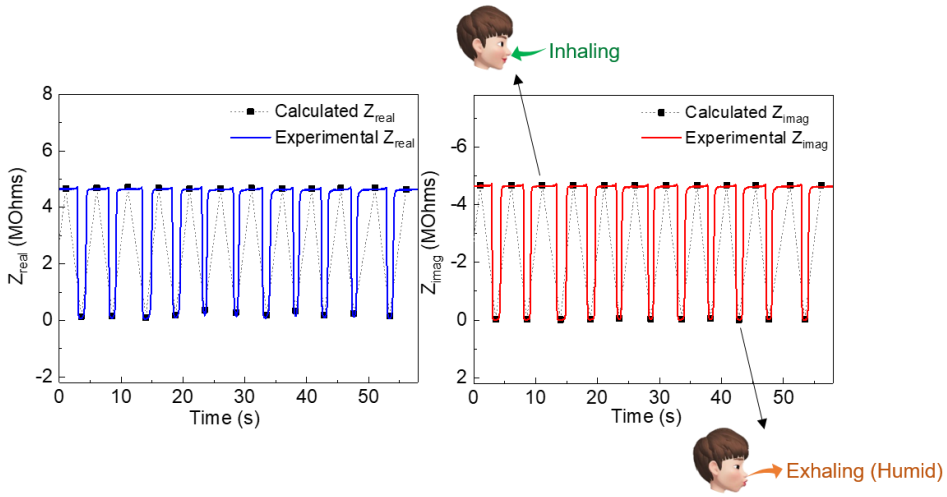

Figure S10 Change of real and imaginary parts of impedance variation with time for 11 cycles of repeated breath and compared with the relative theoretical impedance calculated by equations (S3) and (S4).

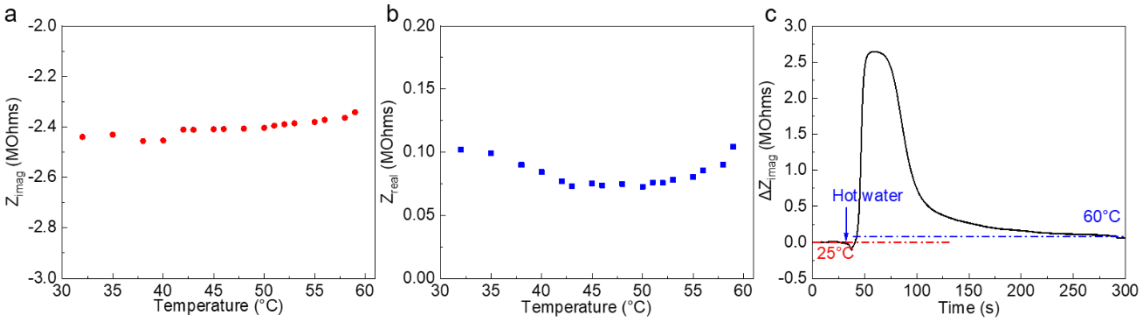

Figure S11 The imaginary (a) and real parts (b) of impedance of the humidity sensor as a function of Temperature at a fixed RH. (c) When the sensor was attached onto the exteral surface of a bottle and boiling water ia added into the bottle, the imaginary part of impedance of the humidity sensor changes with the RH changes. It returns to close to the baseline level, although the temperature enhanced from 25 to 60°C.

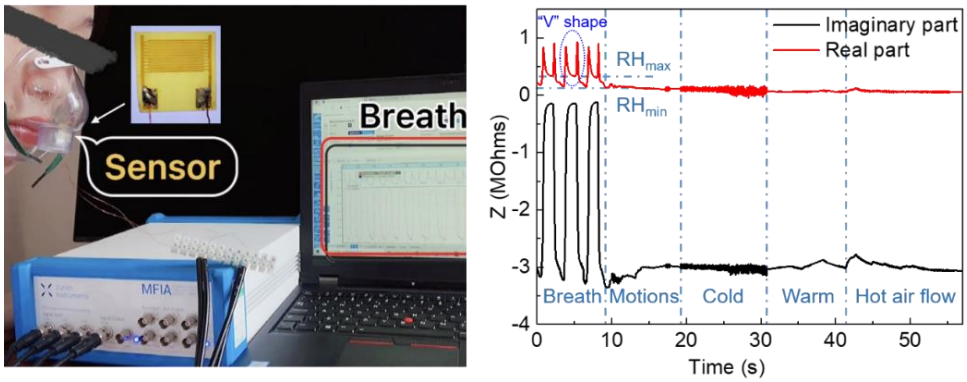

Figure S12 Breathing monitoring using the humidity sensor, and cross-sensitivity test with changes in breathing, motions, airflow and temperature (cold ~20 ºC, warm ~40 ºC and hot ~60 ºC).

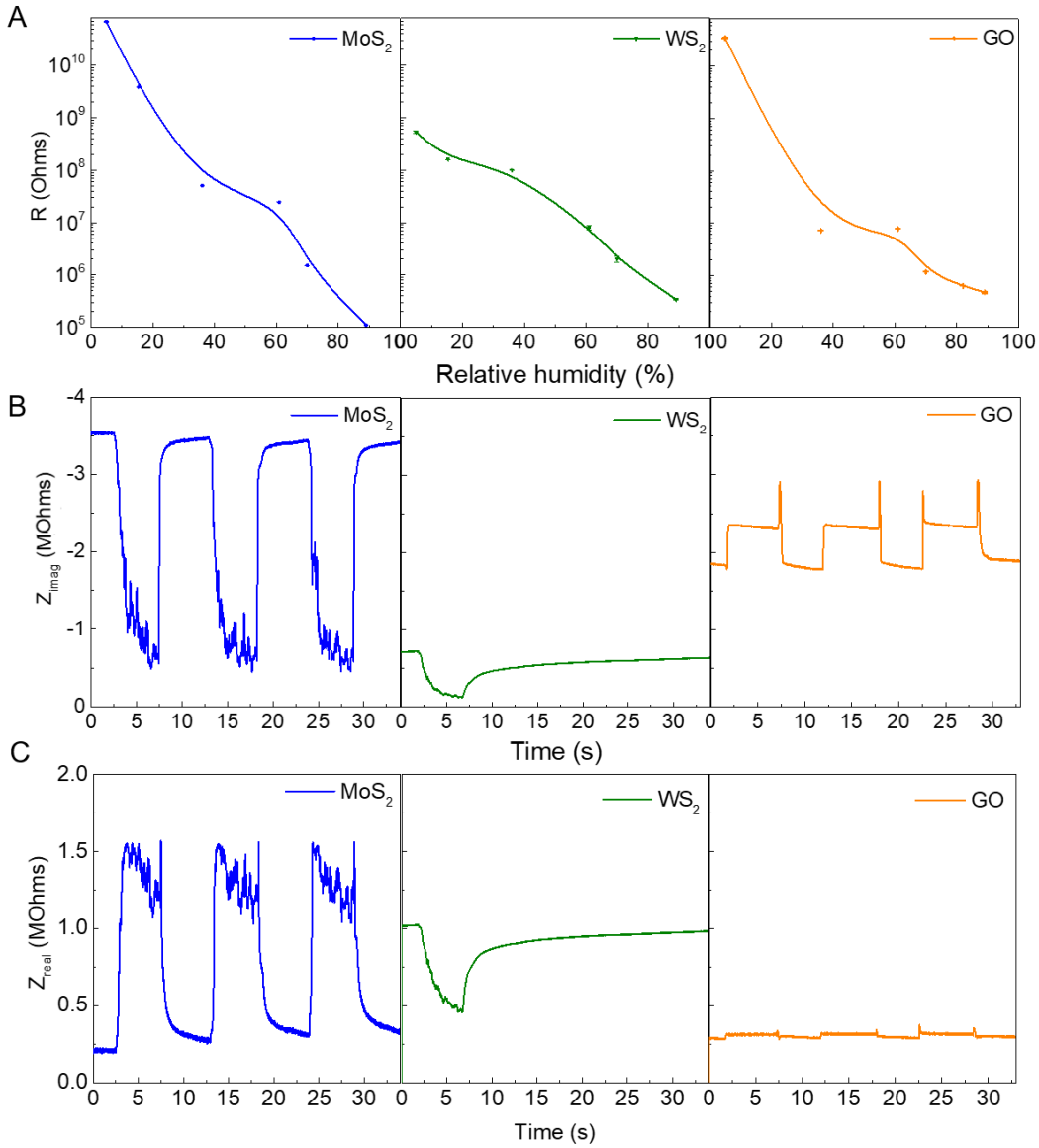

Figure S13 (A) Linear dependence of lgR (Ohms) on %RH at 20°C. Time-dependent response (B) Z_{imag} and (C) Z_{real} of different material: MoS_2, WS_2 and GO as RH was switched between the low level and high level.

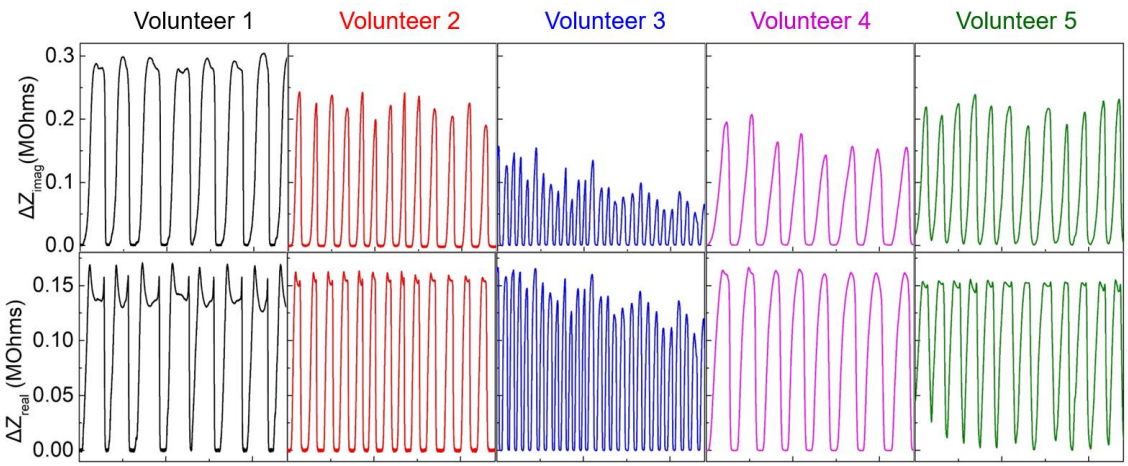

Figure S14 Wearable masks for real-time monitoring human activities. Response curve of breath testing by different volunteers.

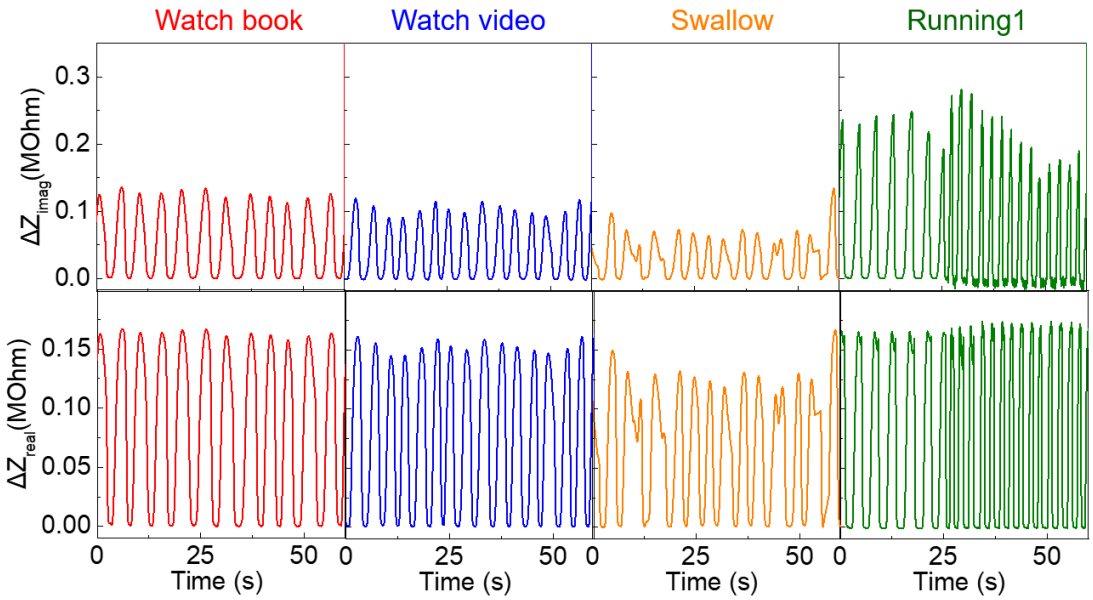

Figure S15 Breathing sensor for monitoring different physical activities, including deep breathing, reading, watching video, swallowing and running.

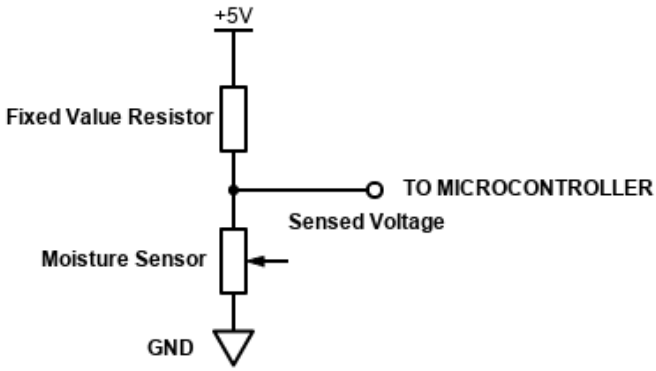

Figure S16 Schematic of the humidity sensor wireless system.

Chapter 6 Construction of Self-powered Wearable Sensor by Introducing a High Performance Nanogenerator

6.1 High Charge Density Triboelectric Nanogenerators based on Liquid Metal Nanoparticles Assembled Films

Abstract

Coupled with contact electrification (CE) and electrostatic induction, triboelectric nanogenerators (TENGs) can harvest mechanical energy from the surrounding environment and convert it into electricity, hence are excellent candidates as a sustainable and mobile power source. CE occurs when the interatomic distance is shorter than the bonding length, however, only a small fraction of atoms from two solid surfaces can occur CE due to the roughness and mismatch natures of solid surfaces, which greatly limits the TENG performance. Here, liquid metal nanoparticles (LMNPs) film is assembled at the water-air interface via Marangoni effect and Capillary force. It can be transferred to a solid surface to realize full contact between the two different solid surfaces, attributed by liquid-like extrusion deformation behaviour of LMNPs. The full contact allows the great enhancement of contact surface, and thus increases the charge density by more than three times (from ~100 to 311 μC m^{-2}). This work shows a universal strategy to improve the performance of different TENGs through full contact between the two solid surfaces, with great prospects.

6.1.1 Introduction

The rapid growth of autonomous Internet-of-Things systems and portable/wearable electronics has propelled the emergent requirement for power sources that are flexible and sustainable during practical utilization.[1-5] Triboelectric nanogenerators (TENGs) have shown great potential for powering these electronics by harvesting various mechanical energies, even the slow motions and oscillations in random directions such as wind, water wave, vibration and human motion.[6-12] TENG that is mainly made of polymers such as polyamide (PA6), polyethylene oxide (PEO) and polytetrafluoroethylene (PTFE), offers unique advantages such as lightweight, flexibility, and scalability as it can be made by low-cost manufacturing techniques.[13-17] This shows great advantages in contrast with the conventional big, heavy, electromagnetic noise and no-load power loss transformers that are made up of propellers, magnets and metal coils.

Combining tribo-electrification and electrostatic induction effects, TENG can generate high voltage, while the low charge density (~100 μC m^{-2}) leads to low power output.[18, 19] To improve the charge density, the process of tribo-electrification should be well understood. Contact-electrification (CE) is a well-known physical phenomenon about charge transfer when two surfaces are brought into contact and then separated, since the ancient Greek era of 2600 years ago.[20] Wang et al. demonstrated the CE mechanism in TENG and proposed an electron cloud-potential well model (**Figure 6.1.1A**).[21-24] The charge transfers when the distance between two atoms from different dielectric materials is shorter than the bonding length (D_2). However, only parts of atoms from two surfaces, called active area, are close to D_2 due to the roughness of solid materials and mismatch between the two surfaces, especially to the microscopic level (**Figure 6.1.1B**).

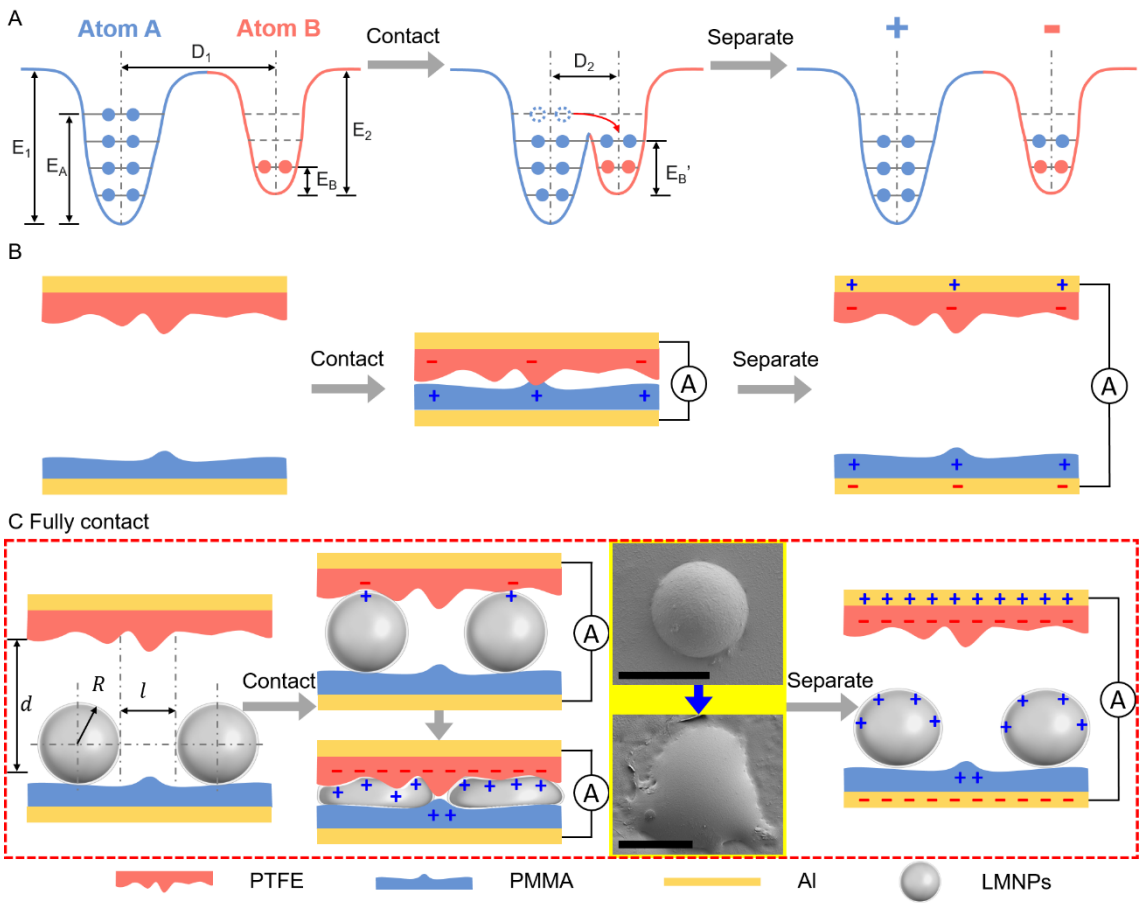

Figure 6.1.1 (A) The electron cloud-potential well model to explain the two atoms from two surfaces that are brought into contact and then separated. D1 and D2 are the distances between two atom centers. E1 and E2 are the required potential energies for electrons to escape from the atom surfaces. EA and EB (or EB') are the occupied energy levels of electrons in the atoms of two dielectrics. (B) The two solid surfaces with certain roughness are brought into contact and then separated. (C) The surface with soft LMNPs film is in contact with another surface and then separate to realize fully contact, thus inducing more transfer of charges.

Here, a LMNPs film with a liquid-like extrusion deformation behaviour was introduced between two solid surfaces to greatly enhance the contact surface when the two solid surfaces came into contact with each other. The LMNPs film, with its large-scale, uniform and condensed properties, is assembled on the surface of the water in a facile and low-cost way via Marangoni effect and Capillary force, inspired by “tears of wine”. The film was universally

transferred onto different surfaces of TENGs, such as poly(methyl methacrylate) (PMMA), Paper, Al and PA6. The TENGs maintain both of mechanical strength and liquid-like behaviour to realize fully contact due to deformability and conformability of LMNPs, and thus enhance the contact surface (**Figure 6.1.1C**). The SEM images (in green color) before and after contact demonstrate the slight micro-deformation from spheres to ellipsoids. The result shows that the prepared TENG, made of LM-PMMA and PTFE, realized the maximum voltage ~1000 V and charge density ~311 μC m^{-2}. While for ordinary liquid metal surfaces, low friction, weak mechanical strength caused by the liquid phase state and liquid residue on solid surfaces seriously impede their electrical output (charge density ≤ 100 μC m^{-2} and voltage ≤ 355 V).[25-27] This finding enables the LMNPs to open promising prospects for the TENG application, which is vital in the development of flexible energy harvesting devices and self-powered wearable electronics.

6.1.2 Experimental Section

Materials and instrument

General chemicals of chemical reagents were analytical reagent grade and were received from Sinopharm Chemical Reagent. Ethanol and deionized water were used as rinsing solvents. SEM and EDX were carried out by a JSM-IT500A scanning microscope. AFM images were taken by a Veeco-Multimode-V AFM. TENG performance was evaluated by a dynamic fatigue tester system (Popwil Model YPS-1) with controllable working parameters including contact force, frequency and separation distance. An oscilloscope (Tektronix MDO3022) with an internal load resistance of 100 MΩ and a picoammeter (Keysight B2981A) were connected in parallel or serial, respectively, to test the voltage output and the short-circuit current, respectively. Output charge density was derived from the effective contact area under the current density curves for one contact/separation cycle.

Synthesis of LM solution

A 0.5 mL of liquid metal was added to a vial (5 mL), which was then filled with ethanol to

a total volume of 5 mL without the addition of any surfactants (solution A). Solution B also contains 0.5 mL of liquid metal, only changing the amount of ethanol solution to 10 mL. Solution A and B were sonicated with an ultrasonic power of 80 W and an ultrasonic frequency of 53 kHz (Kudos, SK3310HP, Shanghai, China) for 3 days.

Formation of 2D LM particles film

The ethanol-assisted LM dispersion was sprayed onto the water surface for appropriate volume (about 10 presses) using a 40 mL hand-held plastic sprayer. Then, a uniform film was finally formed at the liquid/air interface. Importantly, a large number of macroscopic holes may occur when there are not enough jets (about 8 presses).

Compression of 2D LM particles film

After appropriate spray and film formation, capillary substances like tissue or microporous sponges were selected to put on one side of the surface of the water to quickly siphon water from the system, followed by a prominent compression of the film area. Notably, the homogeneous oxides film was closely packed toward the opposite direction of the siphoned direction. When the movement of the film stopped and further siphoning could not drive the film, the resulting film was ultimately formed, indicating a closely packed structure.

Transference of the As-prepared Film

In the system, the resulting film was transferred to different target substrates including silicon wafers, glass wafer, flexible polydimethylsiloxane (PDMS), polyimide (PI) tape and paper, using the horizontal transfer method, followed by an air-drying procedure.

Preparation of solid electrolyte polymer films

The PMMA solution was spin-coated on conductive aluminum (Al) attached acrylic substrates (20×20×1 mm) at a rotation speed of 500 rpm for 5 s, followed by 2000 rpm for 15 s.

Then the PMMA/Al electrode was used as a substrate to transfer LM particles film. The prepared LM-PMMA film was acted as the tribo-positive layers. The tribo-negative layer was produced by attaching a PTFE thin film.

6.1.3 Results and Discussion

To obtain transferrable, dense and porous LMNPs film in a controllable way, inspired by "Tears of wine" a facile, low-cost, reliable and efficient LB method via Marangoni effect is firstly introduced to assemble LMNPs into a thin film at the air/water interface (**Figure 6.1.2**). The ethanol solution with LMNPs shows much lower surface tension (γ) than water, induced Marangoni flow from low γ to high γ direction (**Figure 6.1.2A**). In this case, a film is assembled rapidly at the air/water interface under the Marangoni stress, and the area could be scaled up by simply adjusting the size of vessels (**Figure 6.1.2B**). By using excellent absorbent materials like tissues or other porous structures, a strong capillary force was induced to drive the sharp compression of LMNPs film on the surface of the water (**Figure 6.1.2C**). The novel strategy allows us to achieve scalable and low-cost fabrication of LMNPs with low dimensionality. Subsequently, different from the conventional LB strategy for achieving a closely packed structure via movable barriers,[28, 29] a capillary substance like tissue was placed on one side of the interface to swiftly siphon water from the system. In this case, the floating LMNPs immediately and spontaneously moved to the opposite side of the absorption orientation, followed by an approximately 4-fold decrease of the film area (left of **Figure 6.1.2E** and **S3B**). This process was completed within several seconds. This tissue introduced capillary force indeed led to the compression of LMNPs film. **Figure 6.1.2D and 6.1.2E** show the SEM images and photos before and after compression, confirmed the greatly tight-packed microscopic structures after compression. The diameter of the particles is ~ 1 μm.

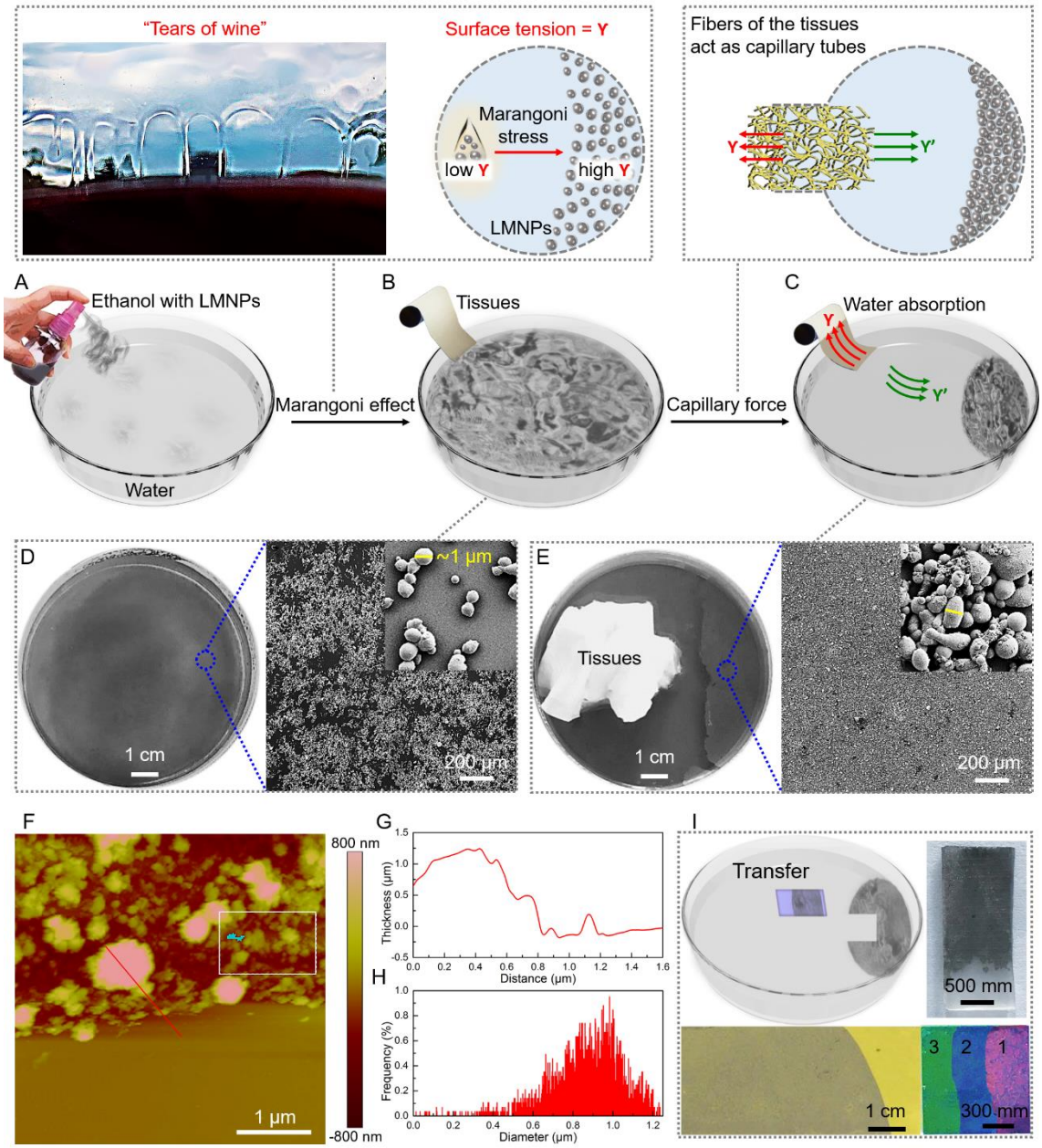

Figure 6.1.2 Schematic illustration of the preparation of macroscopic 2D LMNPs film driven by Marangoni effect in combination with capillary force induced compression at the air-water interface, inspired by "Tears of wine" phenomenon. (A) Spraying LM ethanol dispersions onto the surface of the water. (B) The formative stage of the LMNPs film (C) Tissues assisted capillary force driven compression process for a closely packed oxides film. The corresponding photographs of as-formed LMNPs films on the surface of water via spraying (about 10 presses) using solution B and the corresponding SEM images (D) before and (E) after the capillary force driven compression process. (F) AFM images, (G) thickness profile determined at the red line and (H) size distribution counted in the white frame the

LMNPs film. (I) The method of the transference of as-formed film and photos of the LMNPs film on different solid substrates, PI tape, vertical striped patterned PDMS substrate, and silicon wafers with multiple layers.

To further characterize the as-prepared thin film, atomic force microscopy (AFM) was conducted. The prepared film featured a porous and uniformly distributed appearance under AFM imaging (**Figure 6.1.2F**). It shows approximately 1 μm both of thickness (**Figure 6.1.2G**) and diameter (**Figure 6.1.2H**). Owing to the stabilization of LMNPs, the film can be transferred facially and integrally to various target substrates (*e.g.*, silicon wafers, polyimide (PI) tape and patterned polydimethylsiloxane (PDMS)) without any damage (**Figure 6.1.2I**), displaying perfect transferrable properties. Note that the transferred LMNPs film also enabled be used as the supporting substrate again for a subsequent multiple-transfer to gain multilayer thin film with the desired thickness (**Bottom right of Figure 6.1.2I**). The advantage of transferable LMNPs film provides a compatible and convenient way to fabricate intelligent and flexible electronic devices in practical applications.

As an example of promising potential in electronic application, the LMNPs film (abbreviated to LM below) was transferred onto the PMMA/Al substrates and used as a TENG. As shown in **Figure 6.1.3A**, the working principle of LM-TENG was performed step by step. A dielectric-dielectric TENG under vertical contact-separation mode was operated, consisting of a top PTFE and a bottom PMMA with back Al electrodes attached to them. When the two slices are in contact, due to the different electron-attractive ability, the electrons will be induced and transferred from PMMA to PTFE side, which will result in net negative charges on the PTFE surface and net positive charges on the PMMA surface. According to the literature, [30] the liquid metal tends to attract positive charges during contact with the PTFE layer. Thus, the LM was transferred onto the PMMA surface. After contact-separation, the LM-PMMA surface was characterized by SEM (**Figure S5**). The SEM image, EDS and mapping images show a self-limiting dense and thin oxide layer on the LMNPs surface. The LMNPs core can significantly improve the electron transfer rate of the internal LMNPs. At the same

time, the dense oxide shell layer allows preventing neighbouring LMNPs from contacting to form a continuous conductor and to help store charges on the surface. Compared with the parent flat PMMA film and even the film modified with rigid solid nanoparticles, the LMNPs tend to increase the contact area and contact time through the liquid-like extrusion deformation from sphere to ellipsoid under contact-separation mode, inducing capacitance enhancement (**Figure 6.1.1C**). The maximum energy storage and electrical output can be achieved due to the increased capacitance of the device. I considered PMMA film on Al electrodes as a flat surface and LMNPs as hemispheres (**Figure S6**) and calculated the relevant capacitance.

The capacitance between a hemisphere and a flat surface is given by, [30]

$$C_s = 2\pi\varepsilon_r\varepsilon_0 R\ln\left(1+\frac{R}{d-R}\right) \tag{6.1.1}$$

Assume the number of hemispheres and flat segments along one side are N and $N-1$

$$2RN + l(N-1) = \sqrt{A} \tag{6.1.2}$$

where A is the area of the square electrode. l denotes the length of the square flat segments.

Then,

$$N = \frac{\sqrt{A}+l}{2R+l} \tag{6.1.3}$$

The capacitance between two separated parallel flat segments is,

$$C_f = \frac{\varepsilon_r\varepsilon_0 A_f}{d} \tag{6.1.4}$$

where A_f specifies the area of two separated parallel flats.

$$A_f = \frac{A-\pi N^2R^2}{(N-1)^2} \tag{6.1.5}$$

Therefore, the overall capacitance between PMMA/Al electrode surfaces of hemispheres and flats is,

$$C = N^2C_s + (N-1)^2C_f = \varepsilon_r\varepsilon_0\left(2N^2\pi R\ln\left(1+\frac{R}{d-R}\right)+\frac{A-\pi N^2R^2}{d}\right), \text{ with } N = \frac{\sqrt{A}+l}{2R+l} \tag{6.1.6}$$

The charge density can be calculated as,

$$Q = \frac{CU}{A} \tag{6.1.7}$$

where U is the tested voltage.

At pressed state, the increased contact area enables more positive charges to generate on the surface, and the metal core will accelerate electrons transfer due to the excellent conductivity inside. As the PTFE slice released from the LM-PMMA surface, the resulting charges in the contact interface will be separated, induced a potential difference in the dielectric films. Therefore, the electrons will be transferred from PTFE inducted electrode to LM-PMMA inducted electrode via an external load, and the current flow will be formed in the reverse direction. When the two slices are in contact again, the potential difference will reduce, causing electrons flow in the opposite direction from LM-PMMA inducted electrode to PTFE inducted electrode (**Figure 6.1.3A**).

The electrical outputs of the LM-TENG are measured using a programmable linear motor with an impact force of 50 N, a working frequency of 5 Hz and a spacer distance of 5 mm. All prepared devices have an active area of 20 × 20 mm^2, and external resistance is 100 MΩ. **Figure 6.1.3B** shows the short-circuit current density and charge density with different content of LM on the surface of PMMA by controlling the spraying times (0, 4, 8 10, 30 and 60 times; named as 0, LM4, LM8, LM10, LM30 and LM60) and compression of LM30 and LM60 films (named as LM30C and LM60C). Both the peak-to-peak short-circuit current (J_{P-P}) and output charge density increase with the increase of spraying times and reach the maximum values of 78 mA m^{-2} and 311 μC m^{-2}. The J_{P-P} and charge density of LM60C sample slightly decreased to 63 mA m^{-2} and 239 μC m^{-2}, respectively. To study the reason for output change trend, microscopic structures of the relevant samples were characterized via SEM (**Figure 6.1.3D, 3E and S7**). When increasing the spraying time or compression, more LMNPs modifies the surface of PMMA films and become denser, so that the effective contact area is enhanced and more tribocharges are able to be generated. When LMNPs are over close to each other (LM60 and LM60C), the metal core starts to break the oxide layer

shell and lose the nanostructure, as shown in **Figure S8**, and thus lose the ability to induce and store charges. On the other hand, the peak-to-peak open-circuit voltage (V_{P-P}) displayed an increasing trend with the spraying times and compression process and reached a maximum of 1394 V (**Figure 6.1.3C**).

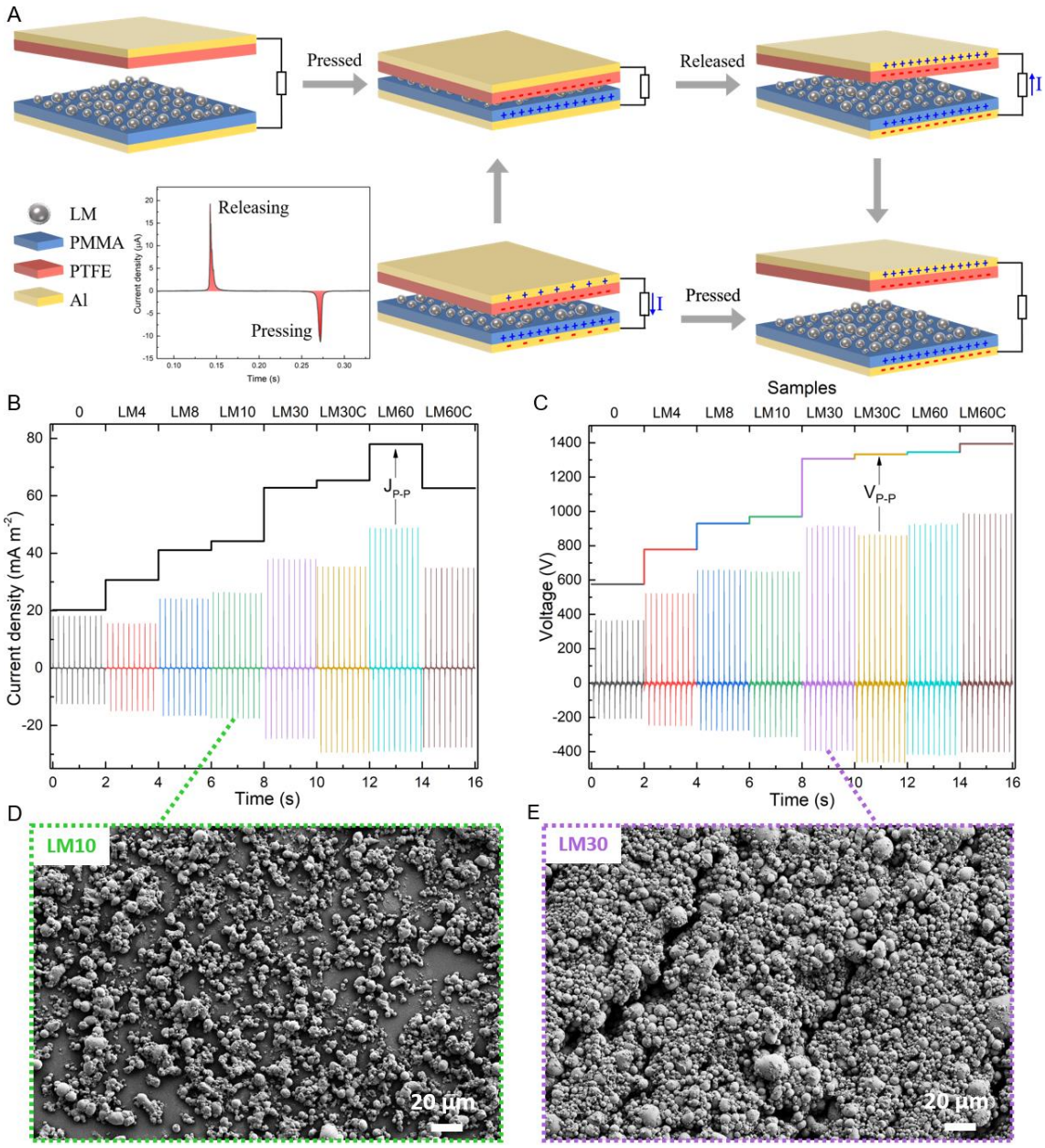

Figure 6.1.3 Working principle and output performance of the LM-TENG. (A) Working principle, (B) current density and (C) voltage of the TENG. SEM images of (D) LM10 and (E) LM30.

Figure 6.1.4A illustrates the charge density obtained from experiment and theoretical analysis (equation S7). For samples 0, LM4, LM8, LM10, LM30, LM30C and LM60, it demonstrated the almost the same charge density values and the enhancement trend with the increase of LM content, verified surface modification of the as-prepared LMNPs film offers a reliable and effective strategy to improve the output performance of TENG. On the other hand, for LM60C sample, the experimental charge density is much smaller than that of theoretical analysis, which is mainly because of the destruction of the nanostructures during the practical operation (consistent with the results in **Figure S8**). Compared with other formation of LM-TENG from the literature,[19, 25, 26, 31-36] the electrical output, including voltage and charge density, in this work are quite higher, which is mainly due to combining the advantage of CE of the solid and liquid surface (**Figure 6.1.4B**). COMSOL was used to simulate the charge density and potential distribution between positive tribo-layer (0, LM10 and LM30) and negative tribo-layer (PTFE) during incresing separate distances, as shown in **Figure 6.1.4C**.[35, 37] The increased rate of charge density is sorted as: LM30 > LM10 > 0 sample, confirmed that more LMNPs provide a larger contact area and change in contact area upon contact and separation, thereby increasing the charge density more effectively. The potential contour clearly demonstrates the potential difference has been increased slightly during the seperate process. It confirms the working principle in **Figure 6.1.3A**; the current flow of induced electrons is established via the external load from the electrode in LM-PMMA side to the electrode in PTFE side. The potential contour also displayed the order of potential difference is LM30 > LM10 > 0 sample, suggest the same consequence with the increased rate of charge density.

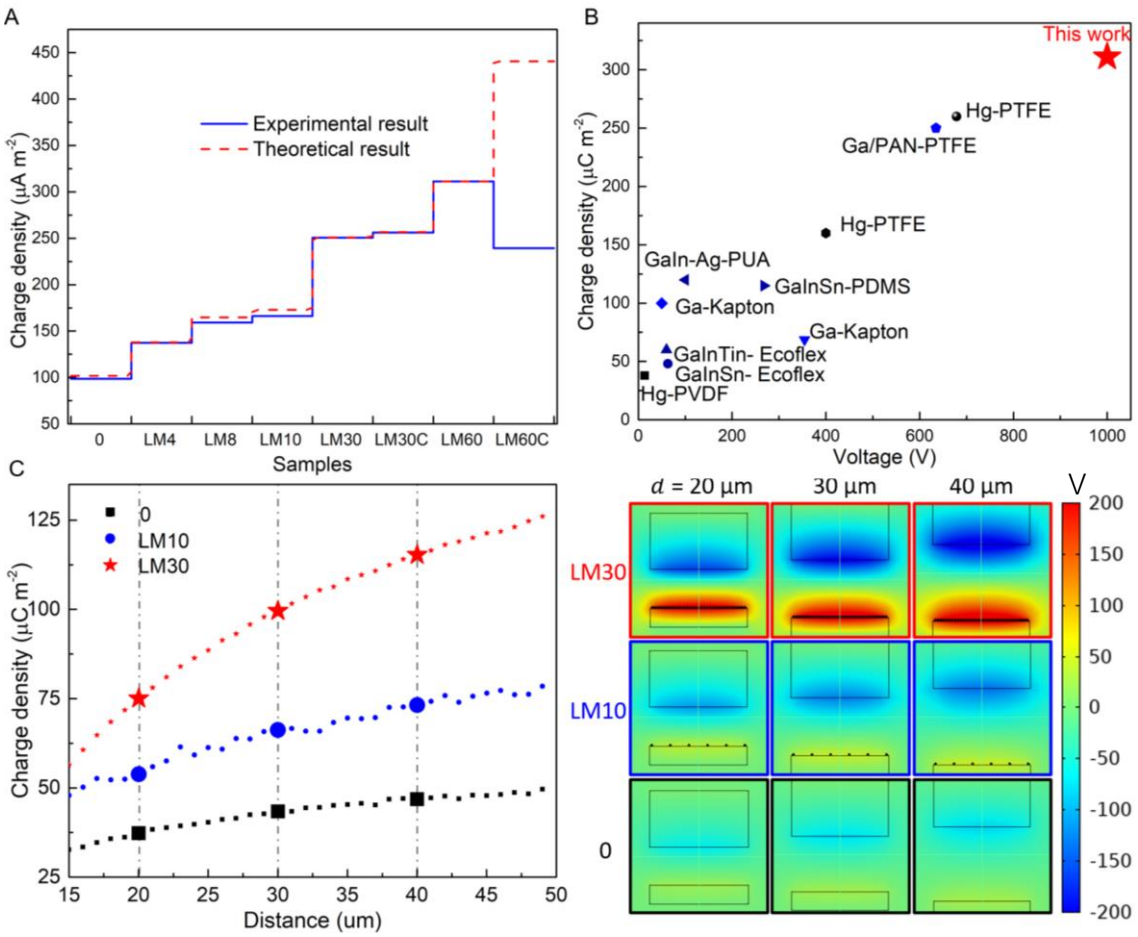

Figure 6.1.4 (A) Experimental and theoretical charge density of the LM-TENG, (B) The electrical output of TENG in this work compared with literature.[8, 18, 24, 25, 29-33] (C) Numerical calculations on charge density and potential differences at electrostatic induction by COMSOL.

As for long-term practical use, it is essential to study the stability and reliability of TENG. **Figure 6.1.5A and 6.1.5B** described the output current density and voltage of the LM30C-PMMA/PTFE TENG for 18000 cycles at a contact frequency of 5 Hz, an impact force of 50 N and a spacer distance of 5 mm. No any attenuation of the current density and voltage was observed. Besides, the PTFE films after contact-separation test with PMMA, LM4, LM10, LM30 and LM60 samples were characterized by SEM, shown no noticeable microscopic changes on the surface (**Figure S9**). These results implied that the LM surface modification is a powerful practical strategy to enhance the electrical output of TENGs. External contact force and working frequencies will change a lot at different application occasions, so they

are important parameters to be researched. **Figure 6.1.5C and 6.1.5D** show both current density and voltage of the LM30C-PMMA/PTFE TENG increase gradually with the enhancement of external contact force from 10 to 50 N, under conditions of 5 Hz contact frequency and 5 mm spacer distance. Similarly, increasing the working frequency will carry out better performance of electrical output (current density and voltage, **Figure 6.1.5E and 6.1.5F**). To verify the universal ability of the LM surface modification for different triboelectric materials, Al (**Figure 6.1.6A and 6.1.6B**), PA6 (**Figure 6.1.6C and 6.1.6D**) and Paper (**Figure 6.1.6E and 6.1.6F**) were modified with LM10 and LM30C, and served as TENG devices. The current density and voltage of all TENGs largely increase and present the same uptrend with the result of PMMA-based TENG while increasing the content of LMNPs. Therefore, this surface modification strategy is universal for different triboelectric materials.

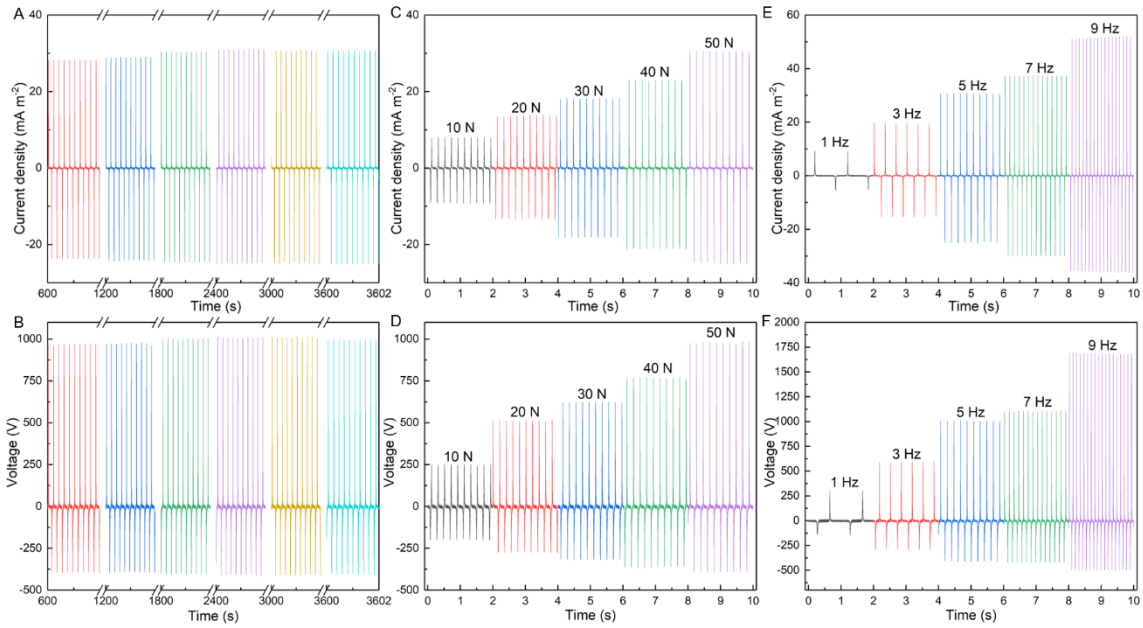

Figure 6.1.5 Short-circuit current density and output voltage of the LM30C/PTFE TENG (A, B) for 18000 cycles at a contact frequency of 5 Hz and forces of 50 N, (C, D) under different contact frequencies from 1 to 9 Hz, and (E, F) under different contact forces from 10 to 50 N.

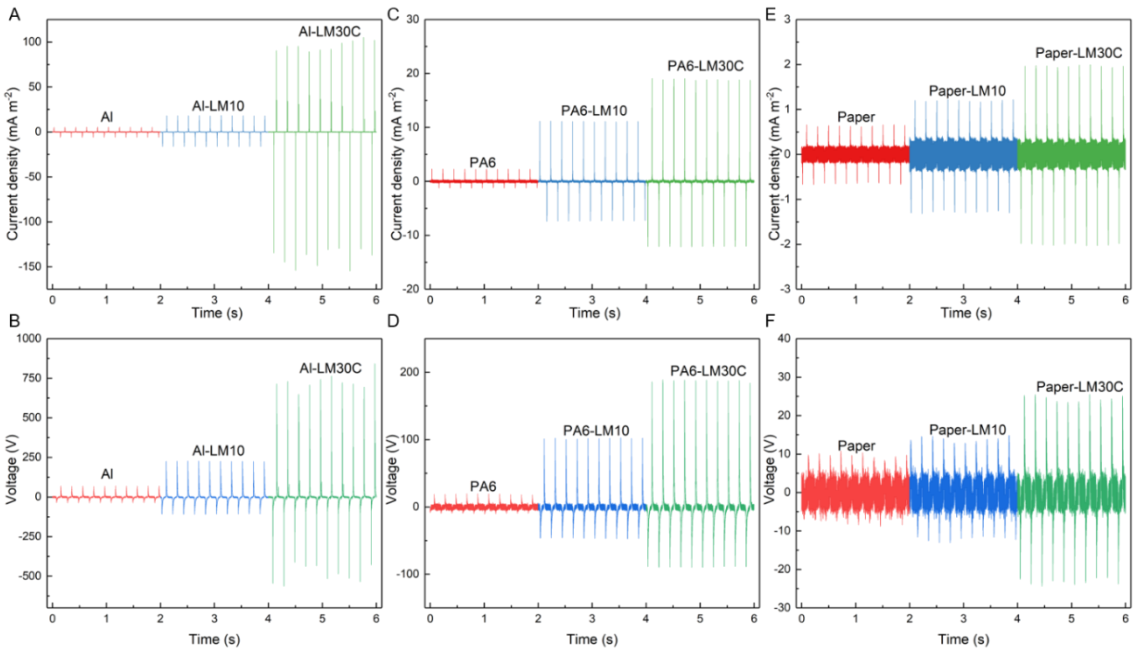

Figure 6.1.6 Short-circuit current density and output voltage of the LM on the (A, B) Al, (C, D) PA6 and (E, F) Paper surface as positive sides of TENGs at contact frequency of 5 Hz and forces of 50 N.

6.1.4 Summary

A facile and cost-efficient LB approach is firstly proposed to fabricate LMNPs film, with liquid-like behaviour, contributed by the cooperation between Marangoni effect and capillary force. The thin film allows the perfectly transfer to other substrates to realize various electronic, magnetic, optical, and catalytic applications. As a concept, a high-performance LM-TENG was successfully fabricated. The result shows that the prepared LM-PMMA/PTFE TENG achieved the maximum $V_{P\text{-}P}$ ~1394 V and an output charge density ~311 μC m^{-2}. It shows more than three times enhancement of charge density than the parent PMMA/PTFE TENG due to the increase of contact surface and time through liquid-like extrusion deformation from sphere to ellipsoid under contact-separation mode. This implies promising prospects for the development of energy harvesting devices and electronics sustainable power sources. The calculated charge density via theoretical analysis method shows the same reliable charge density outputs with the experimental result. The contact-separate work principle is proposed, verified by COMSOL simulation result. The LM film surface

modification strategy is universal for different triboelectric materials, like PMMA, Al, PA6 and Paper. This work not only opens a new door to assemble soft particles into a freestanding film on the surface of the water, but also provides a reliable and stable approach to improve different TENGs output performance combining the advantages of liquid surface contact and solid surface contact.

References

[1] J. A. Rogers, *Nat. Nanotechnol.* **2017**, 12, 839.

[2] M. Bariya, H. Y. Y. Nyein, A. Javey, *Nat. Electron.* **2018**, 1, 160.

[3] L. Chen, M. Lu, H. Yang, J. R. Salas Avila, B. Shi, L. Ren, G. Wei, X. Liu, W. Yin, *ACS Nano* **2020**, 14, 8191.

[4] Y. Lee, S. H. Cha, Y. W. Kim, D. Choi, J. Y. Sun, *Nat. Commun.* **2018**, 9, 1804.

[5] K. Dong, Z. Wu, J. Deng, A. C. Wang, H. Zou, C. Chen, D. Hu, B. Gu, B. Sun, Z. L. Wang, *Adv. Mater.* **2018**, 30, e1804944.

[6] W. Xu, H. Zheng, Y. Liu, X. Zhou, C. Zhang, Y. Song, X. Deng, M. Leung, Z. Yang, R. X. Xu, Z. L. Wang, X. C. Zeng, Z. Wang, *Nature* **2020**, 578, 392.

[7] Z. L. Wang, *Nature* **2017**, 542, 159.

[8] Y. Yang, N. Sun, Z. Wen, P. Cheng, H. Zheng, H. Shao, Y. Xia, C. Chen, H. Lan, X. Xie, C. Zhou, J. Zhong, X. Sun, S. T. Lee, *ACS Nano* **2018**, 12, 2027.

[9] W. Wang, A. Yu, X. Liu, Y. Liu, Y. Zhang, Y. Zhu, Y. Lei, M. Jia, J. Zhai, Z. L. Wang, *Nano Energy* **2020**, 71, 104605.

[10] Z. L. Wang, *Mater. Today* **2017**, 20, 74.

[11] W. Yin, Y. Xie, J. Long, P. Zhao, J. Chen, J. Luo, X. Wang, S. Dong, *Nano Energy* **2018**, 50, 16.

[12] P. Zhao, N. Soin, K. Prashanthi, J. Chen, S. Dong, E. Zhou, Z. Zhu, A. A. Narasimulu, C. D. Montemagno, L. Yu, J. Luo, *ACS Appl. Mater. Interfaces* **2018**, 10, 5880.

[13] L. Shi, S. Dong, P. Ding, J. Chen, S. Liu, S. Huang, H. Xu, U. Farooq, S. Zhang, S. Li, J. Luo, *Nano Energy* **2019**, 55, 548.

[14] W. Gong, C. Hou, J. Zhou, Y. Guo, W. Zhang, Y. Li, Q. Zhang, H. Wang, *Nat. Commun.*

2019, 10, 868.

[15]P. Ding, J. Chen, U. Farooq, P. Zhao, N. Soin, L. Yu, H. Jin, X. Wang, S. Dong, J. Luo, *Nano Energy* **2018**, 46, 63.

[16]H. Zou, L. Guo, H. Xue, Y. Zhang, X. Shen, X. Liu, P. Wang, X. He, G. Dai, P. Jiang, H. Zheng, B. Zhang, C. Xu, Z. L. Wang, *Nat. Commun.* **2020**, 11, 2093.

[17]W. Liu, Z. Wang, G. Wang, Q. Zeng, W. He, L. Liu, X. Wang, Y. Xi, H. Guo, C. Hu, Z. L. Wang, *Nat. Commun.* **2020**, 11, 1883.

[18]W. Tang, T. Jiang, F. R. Fan, A. F. Yu, C. Zhang, X. Cao, Z. L. Wang, *Adv. Funct. Mater.* **2015**, 25, 3718.

[19]H. Baytekin, A. Patashinski, M. Branicki, B. Baytekin, S. Soh, B. A. Grzybowski, *Science* **2011**, 333, 308.

[20]A. C. Wang, B. Zhang, C. Xu, H. Zou, Z. Lin, Z. L. Wang, *Adv. Funct. Mater.* **2020**, 30.

[21]S. Lin, L. Xu, L. Zhu, X. Chen, Z. L. Wang, *Adv. Mater.* **2019**, 31, e1901418.

[22]C. Xu, Y. Zi, A. C. Wang, H. Zou, Y. Dai, X. He, P. Wang, Y. C. Wang, P. Feng, D. Li, Z. L. Wang, *Adv. Mater.* **2018**, 30, e1706790.

[23]X. Li, J. Tao, X. Wang, J. Zhu, C. Pan, Z. L. Wang, *Adv. Energy Mater.* **2018**, 8, 1800705.

[24]K. Parida, G. Thangavel, G. Cai, X. Zhou, S. Park, J. Xiong, P. S. Lee, *Nat. Commun.* **2019**, 10, 2158.

[25]J. Chen, W. Tang, C. Lu, L. Xu, Z. Yang, B. Chen, T. Jiang, Z. Lin Wang, *Appl. Phys. Lett.* **2017**, 110, 201603.

[26]S. Acharya, J. P. Hill, K. Ariga, *Adv. Mater.* **2009**, 21, 2959.

[27]T. Andryszewski, M. Iwan, M. Hołdyński, M. Fiałkowski, *Chem. Mater.* **2016**, 28, 5304.

[28]N. A. Clark, A. Eremin, M. A. Glaser, N. Hall, K. Harth, C. Klopp, J. E. Maclennan, C. S. Park, R. Stannarius, P. Tin, W. N. Thurmes, T. Trittel, *Adv. Space Res.* **2017**, 60, 737.

[29]Q. Ye, Y. Wu, Y. Qi, L. Shi, S. Huang, L. Zhang, M. Li, W. Li, X. Zeng, H. Wo, X. Wang, S. Dong, S. Ramakrishna, J. Luo, *Nano Energy* **2019**, 61, 381.

[30]S. Nayak, Y. Li, W. Tay, E. Zamburg, D. Singh, C. Lee, S. J. A. Koh, P. Chia, A. V.-Y. Thean, *Nano Energy* **2019**, 64, 103912.

[31]Y. Yang, J. Han, J. Huang, J. Sun, Z. L. Wang, S. Seo, Q. Sun, *Adv. Funct. Mater.* **2020**,

30, 1909652.

[32] S. Gao, R. Wang, C. Ma, Z. Chen, Y. Wang, M. Wu, Z. Tang, N. Bao, D. Ding, W. Wu, F. Fan, W. Wu, *J. Mater. Chem. A* **2019**, 7, 7109.

[33] B. Zhang, L. Zhang, W. Deng, L. Jin, F. Chun, H. Pan, B. Gu, H. Zhang, Z. Lv, W. Yang, Z. L. Wang, *ACS Nano* **2017**, 11, 7440.

[34] P. Cui, J. Wang, J. Xiong, S. Li, W. Zhang, X. Liu, G. Gu, J. Guo, B. Zhang, G. Cheng, Z. Du, *Nano Energy* **2020**, 71, 104646.

Supplementary Information

The LM is easily oxidized in air, and hardly dissolved in normal solvents, so the ultrasonication technology is adopted to dissolve LM droplets in an ethanol solution (the volume ratio of LM to ethanol (LM/EtOH) was set as 1:10, denoted as "solution A"; 1:20, denoted as "solution B",) and the as-prepared solution was displayed in **Figure S1**. Higher LM/EtOH volume ratio shows a darker colour solution. **Figure S2** illustrate the scanning electron microscopy (SEM) images and photos of the formation of freestanding and large-scale LM particles film using solution B before and after introducing capillary force. As expected, when the LM dispersion in ethanol was sprayed onto the air-water interface (about 10 presses), they were rapidly pushed outward from ethanol-rich regions with low γ to water-rich regions with high γ attributed to the Marangoni effect. When the amount of spray is insufficient (about 8 presses), more macroscopic holes and cracks could be observed (**Figure S2A**). And when the concentration is higher (solution A), a much darker film was obtained after spraying 10 times (**Figure S3A**).

On the other hand, for the film prepared via insufficient spray volume (about 8 presses), some big holes still existed after compression (bottom inset of **Figure S2B**). Correspondingly, SEM image in **Figure S2B** shows more macroscopic holes and cracks in the compressed structures compared with microscopic structures in **Figure 2E**. The much larger particles are likely to sink in to the bottom of water under the influence of gravitational force according to the literature.[28] As shown in the red frame of the bottom inset of **Figure S2B**, the vessel is colourless, and after forming an LM particles film on the surface of the water, there is thick oxides film at the bottom. This result illustrated that the high-simplified LB strategy allows us to obtain a more uniform oxides film by separating the small LM particles from the much larger ones. The SEM images in **Figure S3C** exhibits a much larger size of LM particles in the freestanding film using solution A than the film prepared by solution B in **Figure 6.1.2E**. These above results suggest that a higher volume of LM in the ethanol solvent enhance the size of particles of the film on the water surface, while fewer spray times

will cause many holes of the film. Compared with direct dropping, the prepared film surface indicated greater hydrophobicity, suggesting that the film is denser and uniform (**Figure S4**).

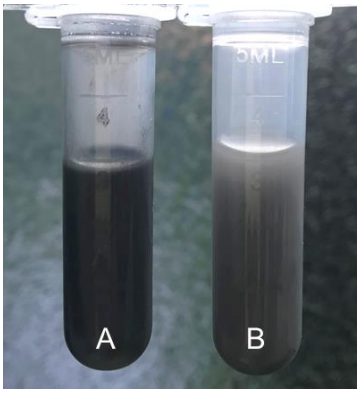

Figure S1. A Photo of LM solutions.

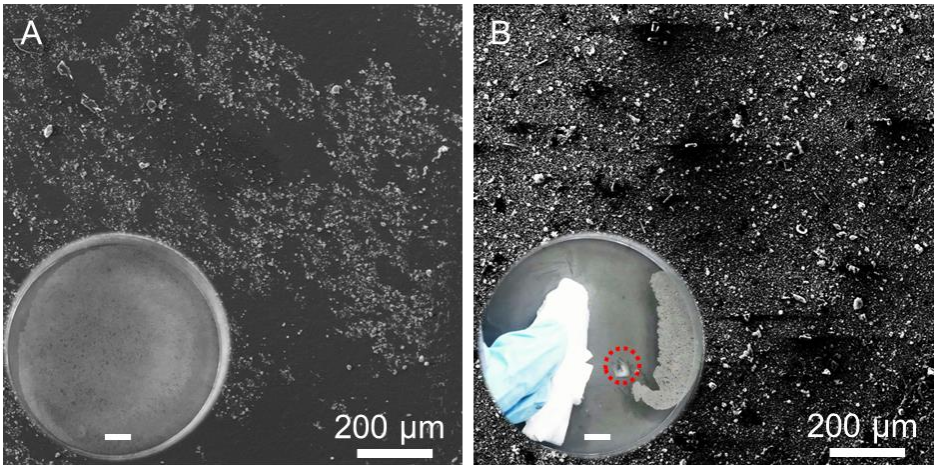

Figure S2. SEM images of the LM film prepared via spraying (about 8 presses) (A) before and (B) after the capillary force driven compression process Bottom inset: the corresponding photographs of as-formed films on the surface of water using solution B; scale bar, 1 cm.

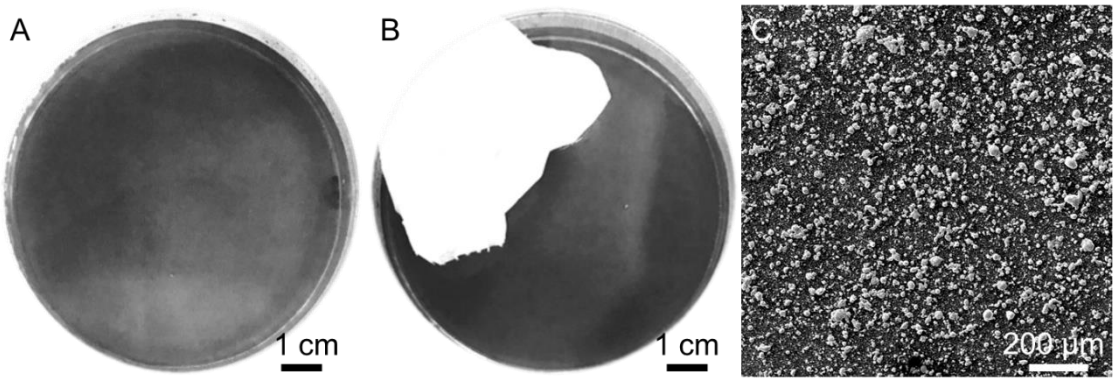

Figure S3. Photos of the LM film formed via spraying (about 10 presses) on the surface of water using solution A (A) before, (B) after the capillary force driven compression process and (C) the SEM images of the closely packed film.

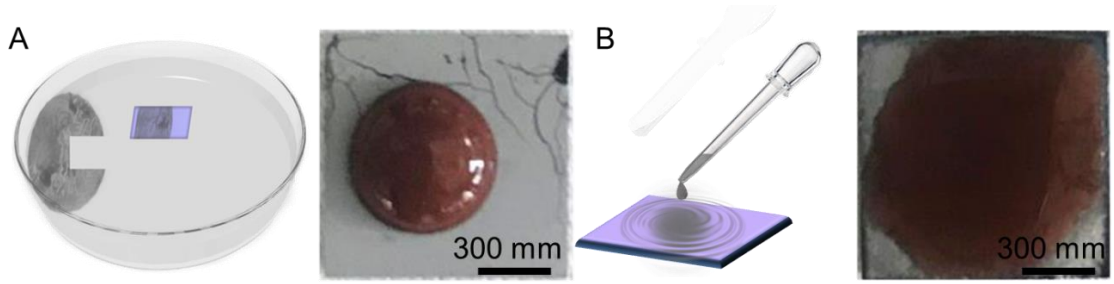

Figure S4. Photos of the LM film prepared by (A) facile LB approach, (B) dropping method and their red-water contact angles after drying in air.

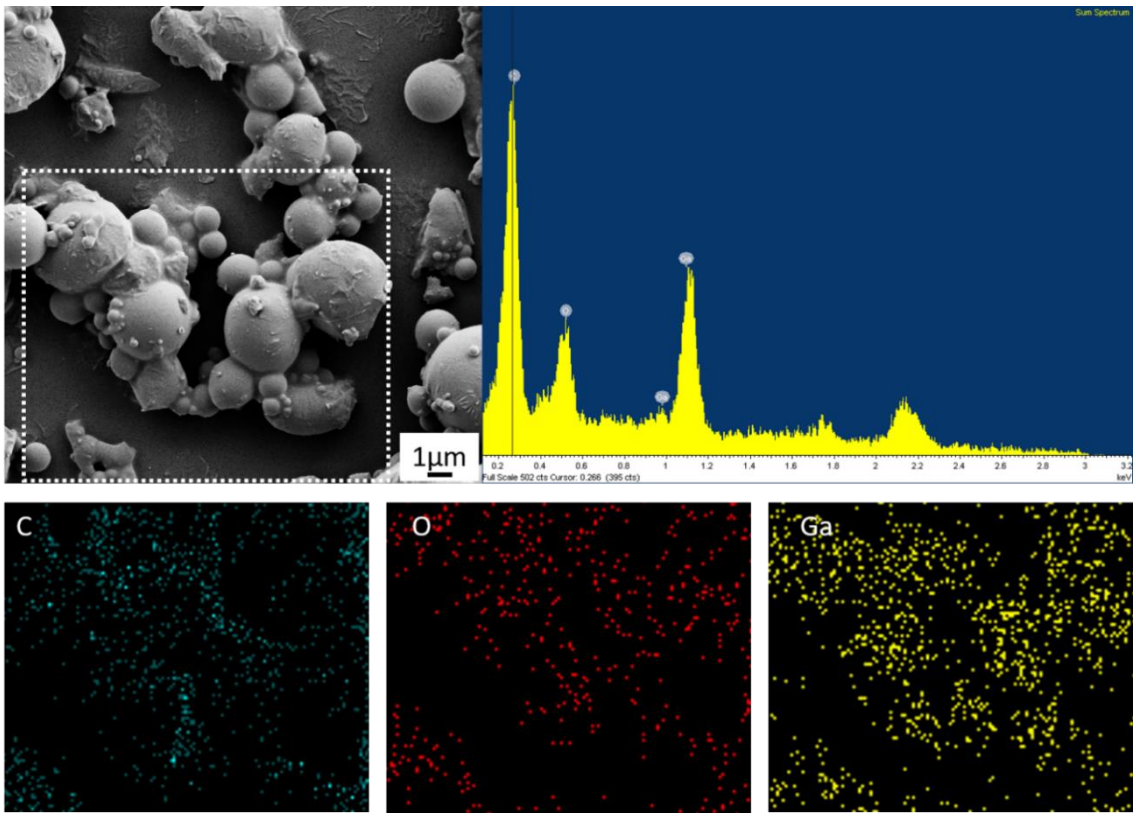

Figure S5. SEM images, EDS and mapping images (C, O and Ga) of the LM10 sample.

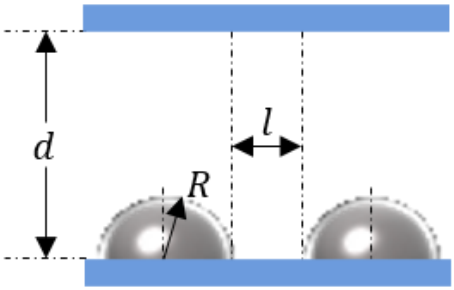

Figure S6. The LM-TENG mode for capacitance calculation, regarding PMMA film on Al electrode as a flat and LM as hemispheres on the surface of the PMMA plat.

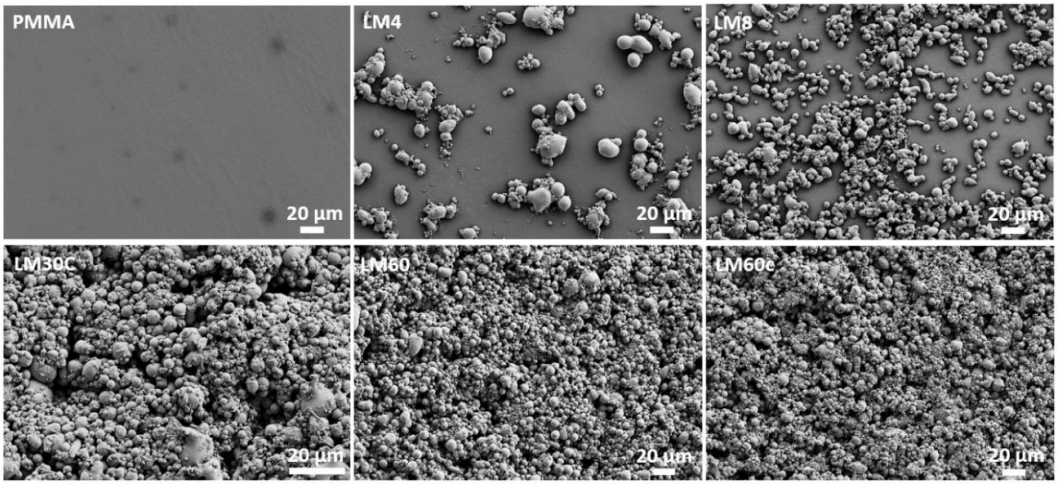

Figure S7. SEM images of the pure PMMA, LM4, LM8, LM30C, LM60 and LM60C.

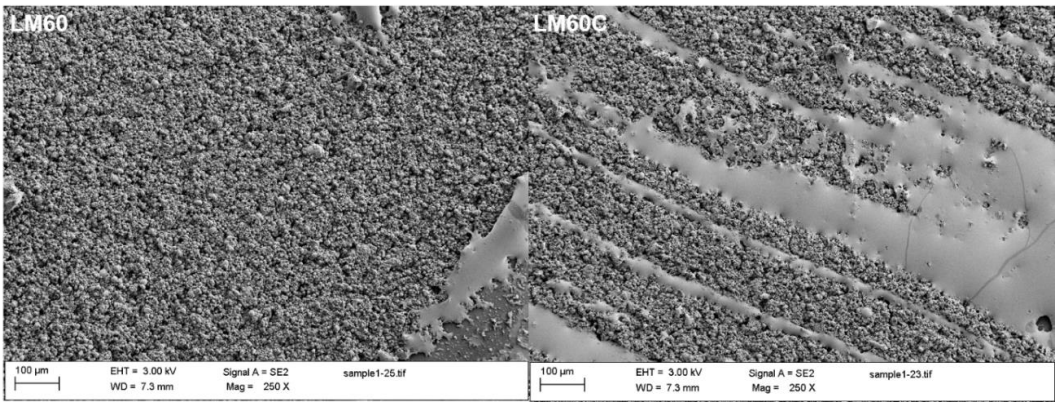

Figure S8. SEM images of LM60 and LM60C samples after contact-separation process.

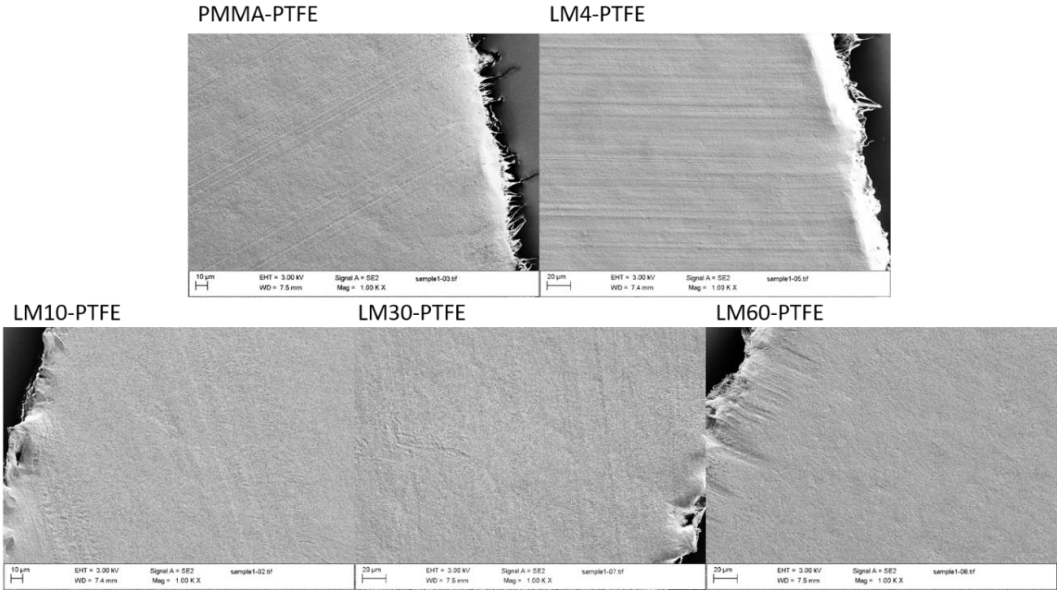

Figure S9. SEM images of PTFE films after contact-separation test with PMMA, LM4, LM10, LM30 and LM60 samples.

6.2 A Novel High Performance Nanogenerator - Field Electrification Nanogenerator

Abstract

TENGs can convert mechanical energy into electricity to serve as a sustainable and mobile power source for smart electronics. However, the output performance of conventional TENG is limited by low charge density, since only a small portion of atoms from two solid tribo-layers can be brought into contact electrification. Here, a self-powered Field Electrification Nanogenerator (FENG) is proposed, consisting of a charge excitation system, an energy management module and a typical dielectric-dielectric nanogenerator, to realize the maximum electrification between two tribo-layers. The proposed charge excitation system can supply a strong electric field, which causes the extra abundant positive/negative charge on tribo-surfaces due to quantum tunnelling effect, led to the maximum ~134-fold enhancement of output power density. Correspondingly, electrostatic potential (ESP) theoretical analysis and Kelvin Probe Force Microscopy (KPFM) measurement were carried out to illuminate the proposed FENG's enhanced electron transferring and potential distributions, respectively, which agree with the electrical output results. Using the FENG as a sustainable power unit, a self-powered humidity sensor was designed as a novel design concept to passively monitor human health in real-time.

6.2.1 Introduction

With rapid development of the Internet-of-Things and smart electronics such as portable, wearable and implantable electronics, power consumption will reach an incredible level in near future (*1-5*). To address the energy crisis, significant efforts have been devoted to providing lifelong power sources by harvesting energy from surrounding environment, and to exploiting sustainable self-powered systems (*6-11*). TENG, based on conjugation of triboelectrification and electrostatic induction, is attracting increasing attention for harvesting almost all forms of mechanical energies, such as wind, water wave, vibration and human motion (*12-17*). However, a challenging problem of a typical TENG is low triboelectric charge density on the surface, which results in a low output power.

Various strategies have been developed to enhance surface charge density, such as triboelectric materials selection (*18-20*), surface modification of materials (*21, 22*), contact optimization (*23-25*), and environment control (*26*), etc. Charge injection method has been regarded as a useful means to increase charge density due to easy operation in ambient environment (*23, 24*). The charge density of tribo-layers PTFE/polyamide 6 (PA6) TENG after ion injection 149 μC m^{-2} has been realized (*23*). The ionized-air injection method allows the fluorinated ethylene propylene (FEP) TENG to achieve maximum ~ 240 μC m^{-2} (*24*). Unfortunately, the charges acquired vary with each operation and the process cannot be well adjusted and stabilized. The surface charge density was improved to 283 μC m^{-2} by using high voltage corona discharge, while complex and bulky equipment is required to provide high voltage (*27, 28*). High vacuum protection is an effective approach to realize high output charge density. Wang *et. al.* reported that surface and dielectric polarization from a ferroelectric material can enhance the output charge density to 1003 μC m^{-2}, which improves the maximum output power density from 0.75 to 50 W m^{-2} in high vacuum (*26*). Still, the required vacuum condition and the bulky equipment makes the process less attractive. Very recently, a supplementary charge pump has been proposed to realize the maximum 1250 μC m^{-2} of the charge density and 38.2 W m^{-2} of the power density in ambient conditions, but a continuously supplementary excitation device is introduced (*25, 29*). Until now, a safe, facile,

universal and efficient strategy is still highly desired to enhance the output power density of the device to satisfy larger power consumption in practical applications.

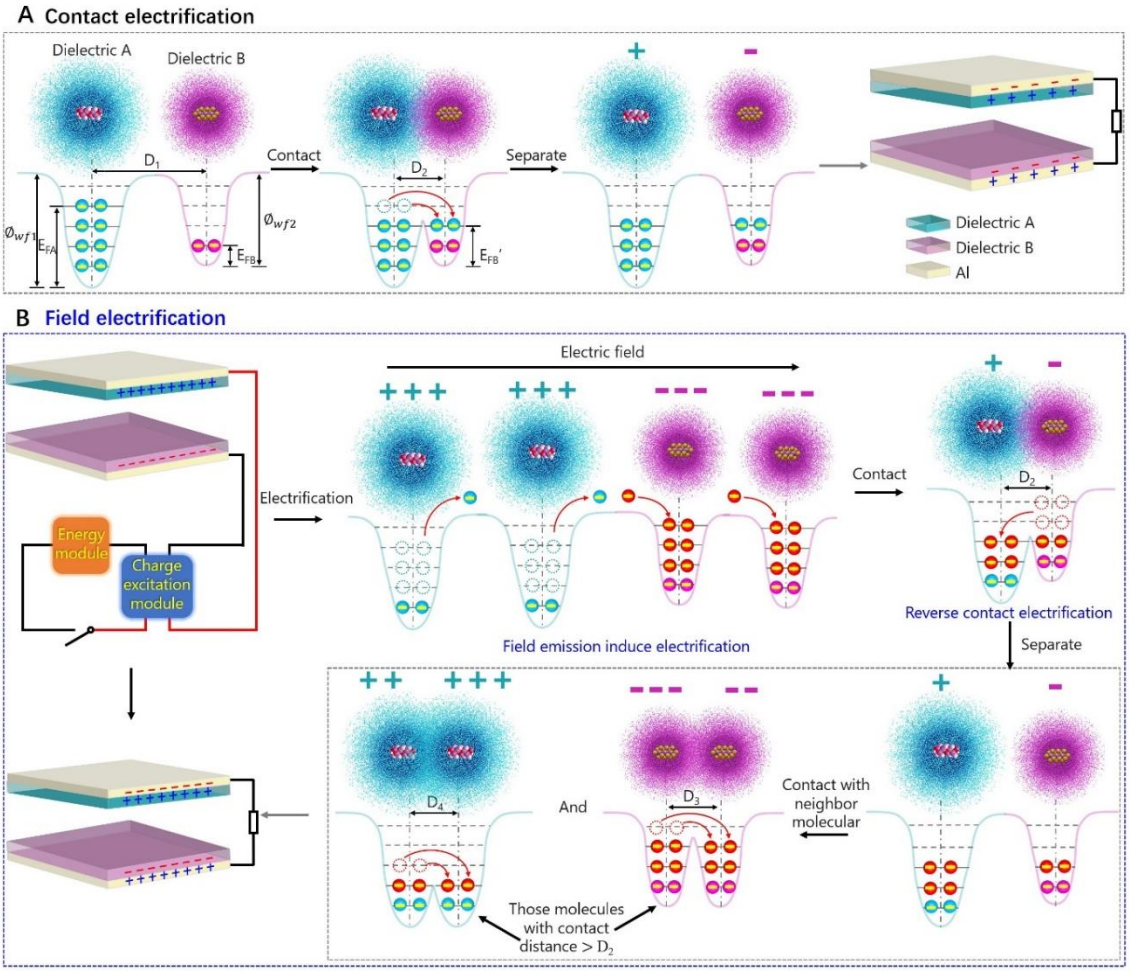

Figure 6.2.1 (A) The coupling effect of contact electrification (CE) and electrostatic induction (EI) explained by electron-cloud-potential-well model. The D is the distance between two atom centers. (B) The field emission induce electrification under a strong electric field to realize the maximum surface charging under the negative influence of contact electrification.

To truly and effectively enhance the output performance of TENG, clear understanding of the working principle of TENG is required. Wang *et. al.* has in-depth studied the electron transfer as the contact electrification (CE) mechanism by thermionic emission theory (high temperatures) and photoelectron emission (UV light irradiation) (*30-33*). **Figure 6.2.1A** demonstrates the electron-cloud-potential well model proposed to explain charge transfer

mechanism during contact and separation of two different dielectrics. When two atoms (from dielectric A and B, respectively) come into close with distance between two atom centers (D) ≤ D_2, the electron clouds overlap and the two potential wells merge into one. The electron could hop from high energy orbitals (dielectric A) to low energy orbitals (dielectric B). The obtained electrons in dielectric B could be kept since the E_B' is still smaller than E_2 after separation. **Figure S1** shows that the resulting charge separation will cause a potential difference between two Al electrodes, and generate a current flow if the device is connected to an external circuit. When the two films are in contact again, the current flow is reversed. However, an important corollary is that not all of surface groups on the material's surface affected by CE, due to the inherent limitation (*e.g.,* roughness and holes) of solid surface.

Field electrification (FE) is proposed to realize the maximum surface charge of almost every atom on the surface of a typical dielectric-dielectric TENG (**Figure 6.2.1B**). Field emission is the process of field-induced electrons emission impacted by an external strong electrostatic field, in terms of quantum physics, the electrons tunnel through the barrier under a strong electric field. The relationship between the external electric field and the electric potential energy along the distance from the material can be presented, as shown in Equation (6.2.1), which describes how the electrostatic fields affect the electron states.

$$e_{ep} = e \cdot \emptyset_{wf} - \frac{e^2}{16x \cdot \pi\varepsilon_0} - x \cdot eE_{out} \tag{6.2.1}$$

where e_{ep} is the electric potential energy, $\emptyset_{wf}$ is the sum of the work function, ε_0 is the permittivity of vacuum, E_{out} is the external electric field generated from the designed charge excitation system, and x is the distance from the substance, which is the tribo-layer in this work. Work function means the minimum energy required to extract / withdraw an electron from the tribo-layers to the region beyond the surface of the tribo-layer (*34, 35*). Typically, the applied electric field required is with a gradient of 10^9 V/m or larger.

The current density of field emission in terms of Fermi-Dirac statistics is shown in Equation (6.2.2 – 6.2.4),

$$j = \int n(E_x, T) \cdot D(E_x, E_{out}) dE_x \tag{6.2.2}$$

$$D(E_x, E_{out}) = \exp[\frac{-8\pi\sqrt{2m}}{3he} \cdot \frac{E_x^{\frac{3}{2}}}{E_0} \cdot (1 - 0.142 \cdot \frac{\sqrt{e^3 \cdot E_{out}}}{\emptyset_{wf}} - 0.855 \cdot (\frac{\sqrt{e^3 \cdot E_{out}}}{\emptyset_{wf}})^2)] \quad (6.2.3)$$

$$n(E_x, T) = \frac{4\pi m k_B T}{h^3} \cdot \ln(1 + \exp(\frac{E_x - E_F}{\emptyset_{wf}})) \quad (6.2.4)$$

where j is the field emission current density, E_x is the energy of single-particle state, E_F is the total potential, h is Planck constant, m is the electron mass, k_B is Boltzmann's constant; T is the absolute temperature. Hence, the field emission current density is significantly dependent on the external applied electric field. The FENG consists of a charge excitation system, an energy management module and a mechanical switch, directly connected to the two electrodes of the nanogenerator (**Figure 6.2.1B and Figure S2**, detailed introduction is shown in the supporting information). After switching on the electric field, all energy orbitals of the atoms on the surface of dielectric B were filled with electrons and negatively charged (red "---"), while the orbitals of the atoms on the surface dielectric A were empty and positive charged (blue "+++").

Driven by field emission with the direction from B to A, the electrons in the B potential well can obtain an energy ΔE. When the B original occupied energy $E_{FB} + \Delta E > \emptyset_{wf}$, the electrons are no longer bound to the potential well due to quantum tunnelling effect (*36*). On the contrary, the electrons in the A potential well will lose an energy ΔE, and the electrons with A original occupied energy $E_{FA} + \Delta E < \emptyset_{wf}$ will be bound to the potential well. These phenomena are related to field emission induce electrification. After separation, the electron states (potential) of the contact-electrified atoms and noncontact atoms on the surface of dielectric A and B are in reality random "mosaics" (**Figure S3**). According to the literature (*37*), the random "mosaics" can realize uniform charging eventually due to the electrons transfer between neighbour atoms ($D \leq D_3$ in dielectric B and $D \leq D_4$ in dielectric A) in the same dielectric (**Figure 6.2.1B bottom**). The total potential difference between two Al electrodes will be improved greatly (**Figure 6.2.2A and 6.2.2B**), thereby realising a higher output performance. Conversely, when an opposite electric field is applied, fewer charges separation in contact state and adverse to the electrical output (**Figure S4A**).

6.2.2 Experimental Section

Materials

Ammonium PTFE films (~0.03 mm thickness) for fabricating tribo-negative layers were obtained from the College Hardware, China. Poly(ethylene oxide) (PEO, average M_w ~600000 g mol^{-1}) was purchased from BDH Chemicals. Polyamide 6 (PA6) was purchased from Rhodia Ltd. The charge injection on PTFE films was carried out using a commercial antistatic gun (Zerostat 3, Milty). Polyvinyl alcohol (PVA, average M_w 120000-160000 g mol^{-1}), dopamine hydrochloride and other reagents were analytical reagent grade and were used as received from Sigma Aldrich (United Kingdom).

Preparation of solid electrolyte polymer films

20 wt% PA6 solution was prepared in formic acid by gently stirring at 70 ℃ for 3 h. 10 wt% PEO aqueous solution was continuously stirred at 60 ℃ for 6 h. 5 wt% PVA aqueous solution was stirred at 90 ℃ for 6 h. To prepare PA6, PEO and PVA films, respectively, the above solution was spin-coated on a conductive aluminum (Al) attached acrylic substrates (20×20×1 mm) at a rotation speed of 500 rpm for 5 s, followed by 1000 rpm for 15 s. The synthesized solid electrolyte polymer films were acted as the tribo-positive layers. The tribo-negative layer was produced by attaching a PTFE thin film.

Fabrication of PDA-based humidity sensor

First, 40 mg of dopamine hydrochloride dissolved in deionized water (18 mL) and 2 mL of tris-buffer solution (100 mM, pH = 8.5) was added. The solution was kept stable in an opened Petri-dish (diameter as 75 mm) and incubated in air for 12 h. Dopamine can self-polymerized and form PDA film at air/water interface. The film was subsequently transferred from the solution and washed with distilled. Then the as-prepared PDA film was transferred onto the surface of the interdigitated Ni/Au interdigital electrode (IDE, Ni: 3 μm thick; Au: 0.07 μm thick, sputter-deposited on a polyimide substrate) for further humidity testing experiments.

Measurement

The two layers were assembled into vertical contact-separate mode dielectric-dielectric nanogenerators. Conductive Al tapes were adhered to the acrylic substrates before the polymer coating process, with a 10 mm extension from the active area of 20×20 mm for electrical connection for measurements. Electrical output performance of FENG was evaluated by a dynamic fatigue tester system (Popwil Model YPS-1) with controllable working parameters including contact force, frequency and separation distance. An oscilloscope (Tektronix MDO3022) with an internal load resistance of 100 MΩ and a picoammeter (Keysight B2981A) were connected in parallel or serial, respectively, to test the voltage output and the short-circuit current, respectively. Output charge density was derived from the area under the current density curves for one contact/separation cycle. In a typical test, the Al electrode of the polymer-coated side was connected to the positive lead of the oscilloscope and picoammeter, while the PTFE side Al was grounded. KPFM was performed using an Atomic Force Microscopy (AFM) Oxford Instruments (Asylum Research) Cypher. The PEO and PTFE samples were placed face to face with a gap of 200μm. The positive and negative electric field were created by connecting to the two electrodes of the high voltage source with 2 kV processing for 10 min, respectively.

6.2.3 Results and Discussion

The contact-separation movement was carried out to study the electrical output of the FENG, using a programmable linear motor with an impact force of 50 N, a working frequency of 5 Hz and a spacer distance of 5 mm. All prepared devices have an active area of 20 × 20 mm^2. The charge excitation system was switched on for different number of cycles (1, 2, 5, 10 and 20 cycles). Each cycle duration of charge excitation was around 0.5 s. **Figure 6.2.2C** displayed the current density, voltage and power density with 1 cycle excitation with various resistance load from 500 KΩ to 1000 MΩ. The power density reached the maximum value with load of 100 MΩ. The output of FENG rapidly increases with the increasing of charge excitation cycles initially and reaches maximum at around 10 cycles, following by a slight decrease thereafter. The maximum output power density ~63 W m^{-2} (134-fold, in **Figure 6.2.2D**), voltage ~1580 V (11.5-fold, in **Figure 6.2.2E**), current density ~86.0 mA m^{-2} (16.9-

fold, in **Figure 6.2.2F**) are obtained after 10 cycles charge excitation. The output charge density reaches the highest level around ~269 μC m^{-2} after 5 cycles charge excitation (2.4-fold, in **Figure 6.2.2F** top). The charge excitation system can also create an electric field in the opposite direction to transfer charges from the PTFE side to the PEO side, create the reverse effect on the nanogenerator output, as shown in **Figure S4B and S4C**. The current density and voltage decrease from ~5.1 mA m^{-2} and ~138 V to ~3.2 mA m^{-2} and ~56 V, respectively. The corresponding charge density decrease from ~111 to ~67 μC m^{-2}. Therefore, this charge excitation system is an effective way to tune the electrical output of nanogenerators.

The voltage and current density controlled by different external impact forces of 10 to 50 N, with the 5 Hz contact frequency and 5 mm spacer distance, are shown in **Figure S5A and S5B**. The current density shows no obvious changes (~16.5 mA m^{-2}) as the impact force increases from 10 to 50 N, and the voltage increases very slightly from ~197 to 280 V. These results suggest that the FENG with one cycle (~0.5 s duration) of field emission reach the equivalent maximum efficiency of CE model controlled by contact force ≥ 50N. The transferred charge density only shows a very slight enhancement trend (**Figure S5C**, from ~134 to ~156 μC m^{-2}) as the force increase from 10 to 50 N. This further confirms that the 0.5 s FE equals the maximum active contact area under strong impact force in CE system. **Figure S6A and S6B** demonstrate the voltage and current density of the FENG operated at different contact frequencies, under conditions of 50 N impact force and 5 mm spacer distance. The current density increases gradually from ~6.0 to ~23.1 mA m^{-2} with the increase of contact frequency from 1 to 9 Hz, while the corresponding voltage increases from ~126 to ~332 V. Both current density and voltage increase with contact frequency are mainly contributed by faster charges induction and transfer under higher contact frequency. However, the transferred charge density drops slightly (**Figure S6C**, from ~164 to ~130 μC m^{-2}) with increasing frequency from 1 to 9 Hz, possibly owing to the decrease of contact time.

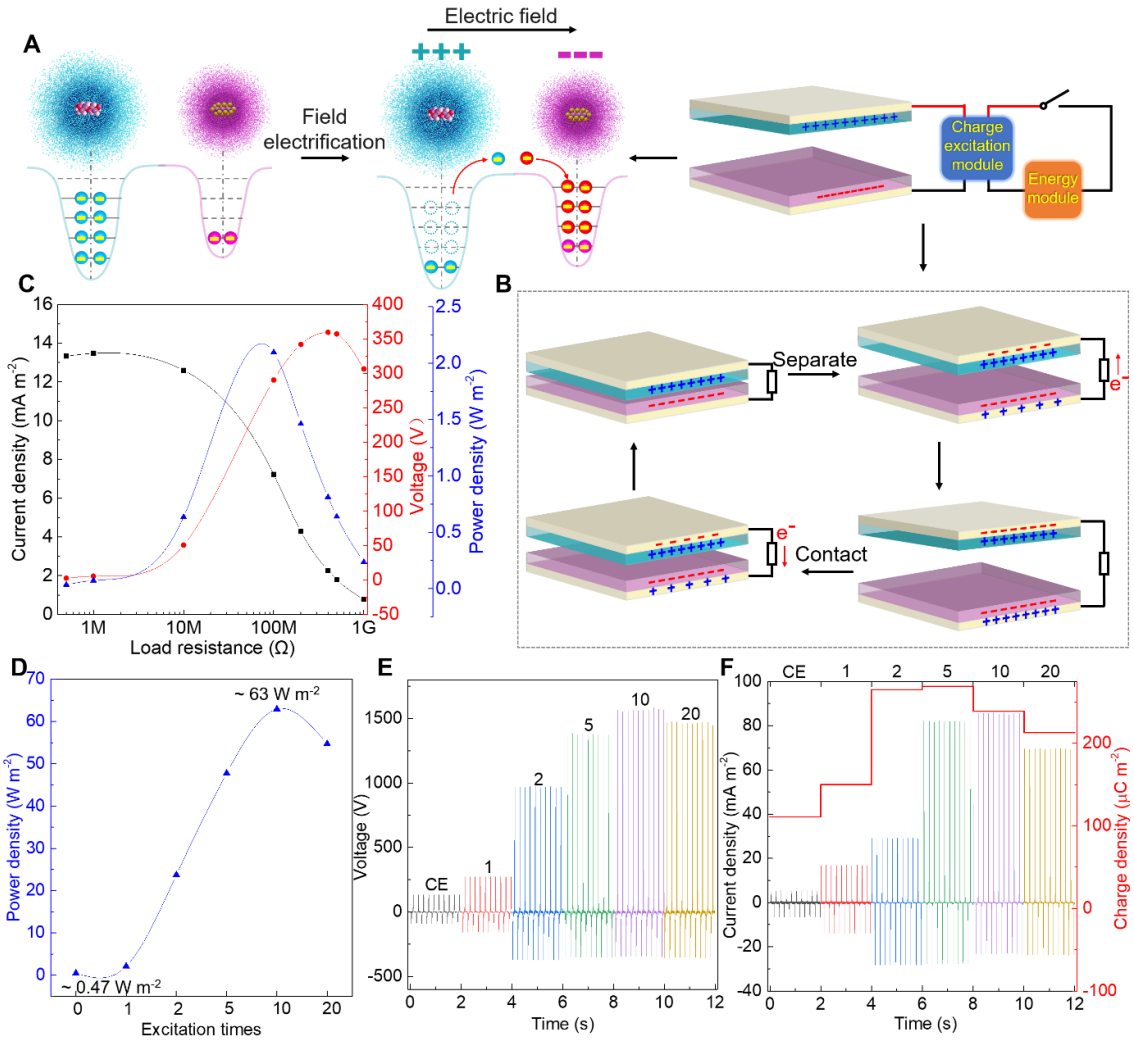

Figure 6.2.2 (A) The selection of a polar molecule PEO (cyan color) and a nonpolar molecule PTFE (pink color) as the experimental subjects, (B) the dielectric polarization of PEO and PTFE dielectrics with the excitation of a strong electric field, and the charges (gray color) transferred away through conductors. The contact-separation process of PEO/PTFE FENG under an impact force of 50 N, a frequency of 5 Hz and a spacer distance of 5 mm, (C) current density, voltage and power density of FENG with one times excitation under different external load, (D) power density of the FENG with different times of excitation, (E) output voltage, (F) short-circuit current density and charge density (colorful line on top) of the FENG with different charge excitation times, every exciting time with excitation duration is around 0.5 s.

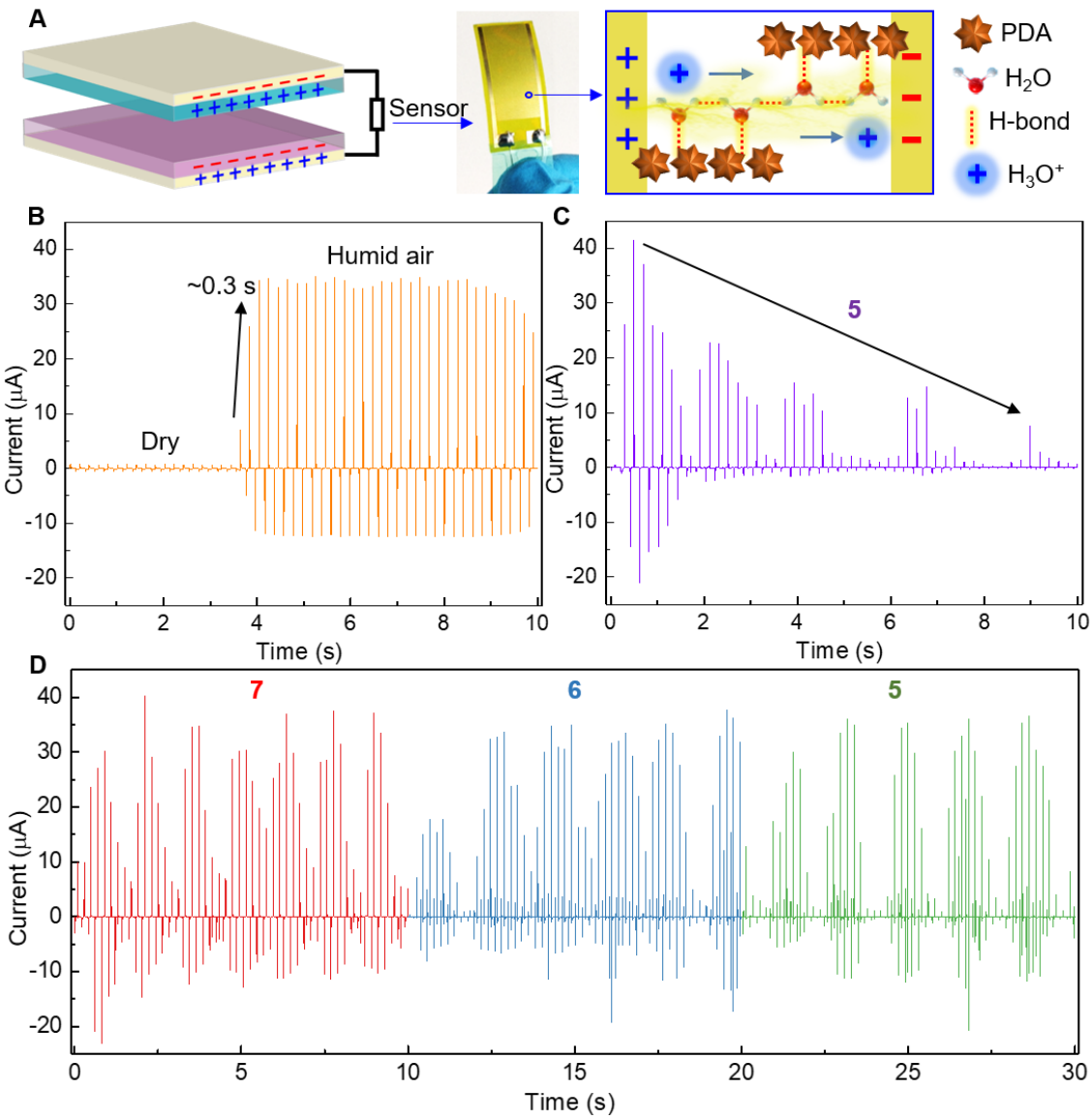

Figure 6.2.3 (A) Schematic illustration of self-powered humidity sensor. (B, C and D) Humidity flow sensing from the self-powered sensing device.

To realize practical applications of nanogenerator (*e.g.*, self-powered devices), stability and durability are critical. The PEO/PTFE FENG was activated one cycle via the field emission system and tested via the picoammeter. The current density and voltage of the FENG with ~27000 cycles were obtained at a contact frequency of 5 Hz, an impact force of 50 N and a spacer distance of 5 mm. Although the current density has a little attenuation in continuous operation of ~27000 cycles (**Figure S5D**, <10%), no obvious decay of the voltage can be

observed (**FigureS5E**). This suggests that FE is an irreversible process, thus the FENG presents stable and durable electric output. In addition to stability, the FE system reveals superb universality for different dielectrics. It was then applied to PA6/PTFE, PVA/PTFE and Paper/PTFE TENGs. As shown in **Figure S7**, the PA6/PTFE, PVA/PTFE and Paper/PTFE FENGs display much higher current density (~32.3, ~20.1, and ~5.5 mA m^{-2}) and voltage (~231, ~234, and ~112 V) than those of non-excited TENGs (J_{SC} ~5.0, ~7.1, and ~3.7 mA m^{-2} and voltage ~96, ~102, and ~68 V). Thus, the FE system is universal for various triboelectric materials.

A humidity sensor, designed using PDA (the adhesive proteins existed in mussels) was connected in series with the FENG to realize a self-power sensing device (**Figure 6.2.3**). The PDA formed a film via the interfacial polymerization process. According to the previous works (*38, 39*), hydrophilic groups in the film (*e.g.,* −OH, $-NH_2$) can immediately "capture" water molecules through dynamical hydrogen bond (H-bond) interactions, showing significantly high sensitivity to moisture monitoring. The H-bond allows the sensor to "release" water molecules with high speed at low relevant humidity for fast response and repeatable utilization. Since the humidity of the exhaled air is higher than the inhaled (ambient) air, it is possible to record individual respiration by monitoring changes in the relevant humidity values (*40*). The current significantly enhanced from ~0.7 to ~35 μA (50-fold) when weak humid air was introduced during expiration (**Figure S8A**), indicating that the FENG-powered humidity sensor is effective and sensitive in circumstances where weak moisture signal may change frequently. **Figure 6.2.3B** implies that the response time is around 0.3 s to reach a stable output. Based on the fast response and high sensitivity, this self-powered humidity sensor can be employed in wearable devices for human respiration real-time monitoring. The currents of one slow respiration and two light breaths were recorded (**Figure S8B**), revealing electrical changes with the humidity change during breathing. The current trends to decline as the humid air on the sensor surface decreases with reduction of the exhalation (**Figure 6.2.3C**), which indicates that the self-powered humidity sensor is a powerful and sensitive non-invasive tool to real-time monitor human respiration. **Figure 6.2.3D** displays current

changes for different breathing cycles (7, 6 and 5 cycles) over 10 s. For the respiration of 7 cycles in 10 s, the current changes were well recorded, confirming a fast response rate of this breathing sensor.

The calculations were carried out using the Gaussian 09 package (*41*). The structures were energy-minimized without symmetry constraints using the B3LYP method with the def2-SVP basis set (*42, 43*). The electric field (EF) direction from PEO ($-OCH_2CH_2-$ chain) to PTFE ($-CF_2CF_2-$ chain) is defined as positive EF, while the opposite direction is called the negative EF. The structure and ESP distributions were calculated and directly demonstrated in **Figure 6.2.4A and 6.2.4B**. The strong positive EF induced electrification causes that the electron transfers from PEO to PTFE side, so the surface of PEO is mostly positive (blue), while most of surface of PTFE side is negative (red). Oppositely, negative EF leads to a mostly negative surface of PEO (red) and a mainly positive surface of PTFE (blue) due to the reverse electron transfer. KPFM images show an obvious shift in the surface potential of the PEO (from 1.52 to 1.50 to 1.47 V) and PTFE (from -13.0 to -3.6 to 4.3 V) samples under positive, none and negative EF, which further confirms this phenomena (**Figure 6.2.4C**). These results provide detailed proof of why the FENG electrical outputs can enhance with the assistance of the proposed charge excitation system.

From the highest occupied molecular orbital (HOMO) and lowest unoccupied molecular orbital (LUMO) of PEO/PTFE model in **Figure S9A**, the LUMO orbital is mainly distributed on the PTFE surface, and HOMO orbital distributed on the PEO surface. It indicates that PEO is easier to lose electrons, while PTFE is easier to gain electrons. Therefore, during contact, the electron is transfer from PEO to PTFE. The Mulliken charges are linked to the molecule's electronic structure (*44*). The Mulliken charges with hydrogens summed into heavy atoms are shown in **Figure S9B, S9C and S10**. In **Figure S9B**, all carbon atoms in PEO except for C_{22} are positive, and the whole PEO chain loses 0.091 electron under positive EF. And only C_{10}, C_{25} and C_{28} in PEO are positive and the whole chain obtains 0.062 electron

from PTFE chain under negative EF. The corresponding Mulliken charges distribution are shown in **Figure S9**.

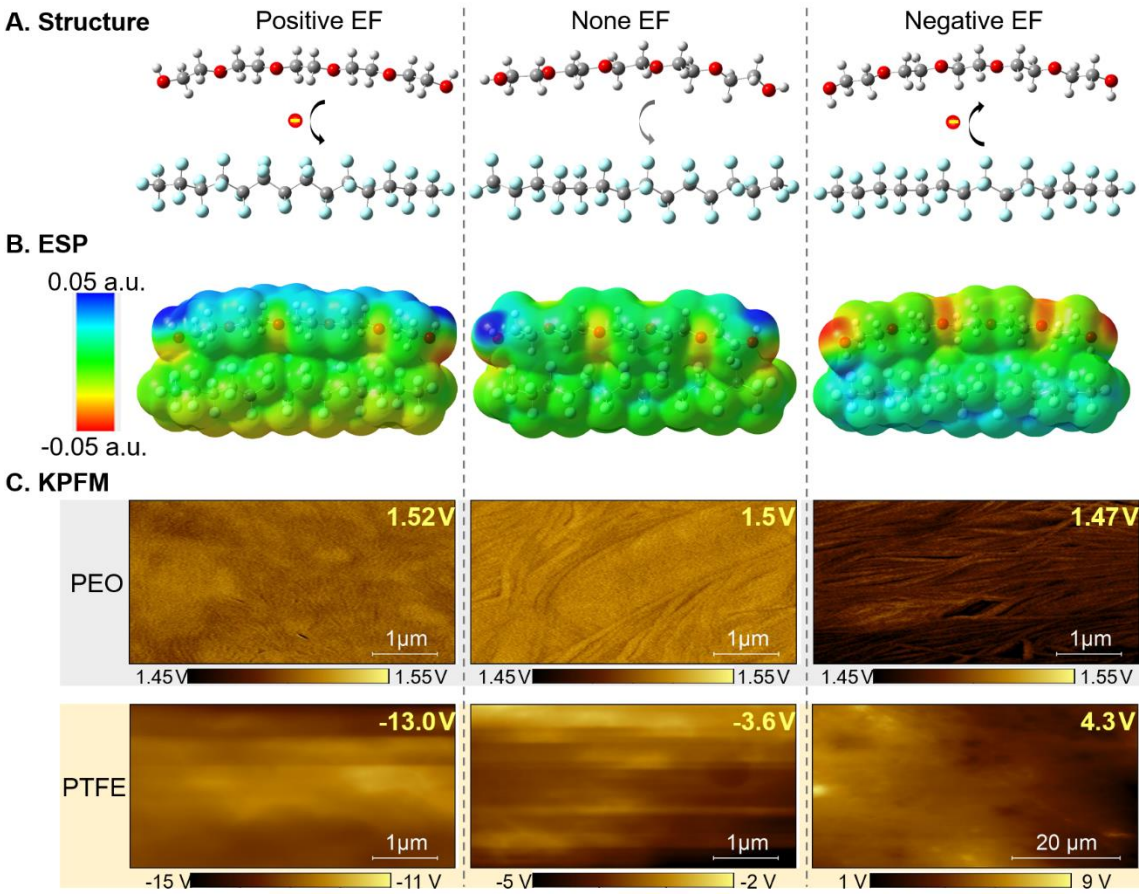

Figure 6.2.4 (A) Structure, (B) ESP and (C) KPFM surface potential distributions of PEO and PTFE under positive, none and negative EF.

6.2.4 Summary

We constructed a novel self-powered field electrification nanogenerator (FENG) with outstanding electrical output. The electric field emission can tune the output of FENG. As an example, the output characteristics of PEO/PTFE FENG increases with increasing excitation cycles and reaches maximums at 5 to 10 cycles excitation with power density ~63 W m^{-2} (~134-fold enhancement), voltage ~1580 V (~11.4-fold enhancement), current density ~86.0 mA m^{-2} (~16.9-fold), and charge density ~269 μC m^{-2} (~2.4-fold), while the reversed electric field can decrease the electrical output. Correspondingly, ESP and KPFM images illuminated

the proposed FENG's enhanced electron transferring and potential distributions, respectively, which agree with the electrical output results. In addition, the FE is an irreversible process, which makes it possible to retain the net charges on the surface of dielectrics after the excitation with the electric field. Therefore, the as-designed FE module is a powerful and universal strategy to realize higher electrical output than typical CE process. As the practical applications of FENG, a humidity sensor has been successfully applied to fabricate a self-powered, sensitive (50-fold difference of current using the FENG after 0.5 s field emission) and fast response (0.3 s) sensor to monitor human respiration in real-time. My work demonstrates the potential of FENG to enhance the performance output of different types of TENGs and as a flexible and sustainable power source for wearable electronics

References

1. Y. Lee, S. H. Cha, Y. W. Kim, D. Choi, J. Y. Sun, Transparent and attachable ionic communicators based on self-cleanable triboelectric nanogenerators. *Nat. Commun.* **9**, 1804 (2018).
2. Q. Wu, W. Chen, D. W. K. Ng, R. Schober, Spectral and energy-efficient wireless powered IoT networks: NOMA or TDMA? *IEEE T. Veh. Technol.* **67**, 6663-6667 (2018).
3. D. Liu, X. Yin, H. Guo, L. Zhou, X. Li, C. Zhang, J. Wang, Z. L. Wang, A constant current triboelectric nanogenerator arising from electrostatic breakdown. *Sci. Adv.* **5**, eaav6437 (2019).
4. R. Cao, X. Pu, X. Du, W. Yang, J. Wang, H. Guo, S. Zhao, Z. Yuan, C. Zhang, C. Li, Z. L. Wang, Screen-printed washable electronic textiles as self-powered touch/gesture tribo-sensors for intelligent human-machine interaction. *ACS Nano* **12**, 5190-5196 (2018).
5. K. Dong, Z. Wu, J. Deng, A. C. Wang, H. Zou, C. Chen, D. Hu, B. Gu, B. Sun, Z. L. Wang, A Stretchable yarn embedded triboelectric nanogenerator as electronic skin for biomechanical energy harvesting and multifunctional pressure sensing. *Adv. Mater.* **30**, e1804944 (2018).

6. Z. L. Wang, On Maxwell's displacement current for energy and sensors: the origin of nanogenerators. *Mater. Today* **20**, 74-82 (2017).
7. W. Yin, Y. Xie, J. Long, P. Zhao, J. Chen, J. Luo, X. Wang, S. Dong, A self-power-transmission and non-contact-reception keyboard based on a novel resonant triboelectric nanogenerator (R-TENG). *Nano Energy* **50**, 16-24 (2018).
8. Y. Xie, J. Long, P. Zhao, J. Chen, J. Luo, Z. Zhang, K. Li, Y. Han, X. Hao, Z. Qu, M. Lu, W. Yin, A self-powered radio frequency (RF) transmission system based on the combination of triboelectric nanogenerator (TENG) and piezoelectric element for disaster rescue/relief. *Nano Energy* **54**, 331-340 (2018).
9. C. Zhang, J. Chen, W. Xuan, S. Huang, B. You, W. Li, L. Sun, H. Jin, X. Wang, S. Dong, J. Luo, A. J. Flewitt, Z. L. Wang, Conjunction of triboelectric nanogenerator with induction coils as wireless power sources and self-powered wireless sensors. *Nat. Commun.* **11**, 58 (2020).
10. X. Peng, K. Dong, C. Ye, Y. Jiang, S. Zhai, R. Cheng, D. Liu, X. Gao, J. Wang, Z. L. Wang, A breathable, biodegradable, antibacterial, and self-powered electronic skin based on all-nanofiber triboelectric nanogenerators. *Sci. Adv.* **6**, eaba9624 (2020).
11. X. Pu, H. Guo, J. Chen, X. Wang, Y. Xi, C. Hu, Z. L. Wang, Eye motion triggered self-powered mechnosensational communication system using triboelectric nanogenerator. *Sci. Adv.* **3**, e1700694 (2017).
12. J. Wang, S. Li, F. Yi, Y. Zi, J. Lin, X. Wang, Y. Xu, Z. L. Wang, Sustainably powering wearable electronics solely by biomechanical energy. *Nat. Commun.* **7**, 12744 (2016).
13. Q. Shi, T. He, C. Lee, More than energy harvesting – Combining triboelectric nanogenerator and flexible electronics technology for enabling novel micro-/nano-systems. *Nano Energy* **57**, 851-871 (2019).
14. M. Lu, W. Yin, A. Peyton, Z. Qu, X. Meng, Y. Xie, P. Zhao, J. Luo, Q. Zhao, Y. Tao, T. Zhou, Z. Zhang, A model for the triboelectric nanogenerator with inductive load and its energy boost potential. *Nano Energy* **63**, (2019).
15. W. Xu, H. Zheng, Y. Liu, X. Zhou, C. Zhang, Y. Song, X. Deng, M. Leung, Z. Yang, R. X. Xu, Z. L. Wang, X. C. Zeng, Z. Wang, A droplet-based electricity generator

with high instantaneous power density. *Nature* **578**, 392-396 (2020).

16. B. Chen, Y. Yang, Z. L. Wang, Scavenging wind energy by triboelectric nanogenerators. *Adv. Energy Mater.* **8**, (2018).
17. Q. Zheng, Y. Zou, Y. Zhang, Z. Liu, B. Shi, X. Wang, Y. Jin, H. Ouyang, Z. Li, Z. L. Wang, Biodegradable triboelectric nanogenerator as a life-time designed implantable power source. *Sci. Adv.* **2**, e1501478 (2016).
18. L. Shi, S. Dong, P. Ding, J. Chen, S. Liu, S. Huang, H. Xu, U. Farooq, S. Zhang, S. Li, J. Luo, Carbon electrodes enable flat surface PDMS and PA6 triboelectric nanogenerators to achieve significantly enhanced triboelectric performance. *Nano Energy* **55**, 548-557 (2019).
19. P. Ding, J. Chen, U. Farooq, P. Zhao, N. Soin, L. Yu, H. Jin, X. Wang, S. Dong, J. Luo, Realizing the potential of polyethylene oxide as new positive tribo-material: Over 40 W/m2 high power flat surface triboelectric nanogenerators. *Nano Energy* **46**, 63-72 (2018).
20. H. Zou, L. Guo, H. Xue, Y. Zhang, X. Shen, X. Liu, P. Wang, X. He, G. Dai, P. Jiang, H. Zheng, B. Zhang, C. Xu, Z. L. Wang, Quantifying and understanding the triboelectric series of inorganic non-metallic materials. *Nat. Commun.* **11**, 2093 (2020).
21. S. H. Shin, Y. E. Bae, H. K. Moon, J. Kim, S. H. Choi, Y. Kim, H. J. Yoon, M. H. Lee, J. Nah, Formation of triboelectric series via atomic-level surface functionalization for triboelectric energy harvesting. *ACS Nano* **11**, 6131-6138 (2017).
22. H. Y. Li, L. Su, S. Y. Kuang, C. F. Pan, G. Zhu, Z. L. Wang, Significant enhancement of triboelectric charge density by fluorinated surface modification in nanoscale for converting mechanical energy. *Adv. Funct. Mater.* **25**, 5691-5697 (2015).
23. P. Zhao, N. Soin, K. Prashanthi, J. Chen, S. Dong, E. Zhou, Z. Zhu, A. A. Narasimulu, C. D. Montemagno, L. Yu, J. Luo, Emulsion electrospinning of polytetrafluoroethylene (PTFE) nanofibrous membranes for high-performance triboelectric nanogenerators. *ACS Appl. Mater. Interfaces* **10**, 5880-5891 (2018).

24. S. Wang, Y. Xie, S. Niu, L. Lin, C. Liu, Y. S. Zhou, Z. L. Wang, Maximum surface charge density for triboelectric nanogenerators achieved by ionized-air injection: methodology and theoretical understanding. *Adv. Mater.* **26**, 6720-6728 (2014).

25. L. Xu, T. Z. Bu, X. D. Yang, C. Zhang, Z. L. Wang, Ultrahigh charge density realized by charge pumping at ambient conditions for triboelectric nanogenerators. *Nano Energy* **49**, 625-633 (2018).

26. J. Wang, C. Wu, Y. Dai, Z. Zhao, A. Wang, T. Zhang, Z. L. Wang, Achieving ultrahigh triboelectric charge density for efficient energy harvesting. *Nat. Commun.* **8**, 88 (2017).

27. T. Zhou, L. Zhang, F. Xue, W. Tang, C. Zhang, Z. L. Wang, Multilayered electret films based triboelectric nanogenerator. *Nano Research* **9**, 1442-1451 (2016).

28. J. Nie, X. Chen, Z. L. Wang, Electrically responsive materials and devices directly driven by the high voltage of triboelectric nanogenerators. *Adv. Funct. Mater.* **29**, (2018).

29. W. Liu, Z. Wang, G. Wang, G. Liu, J. Chen, X. Pu, Y. Xi, X. Wang, H. Guo, C. Hu, Z. L. Wang, Integrated charge excitation triboelectric nanogenerator. *Nat. Commun.* **10**, 1426 (2019).

30. A. C. Wang, B. Zhang, C. Xu, H. Zou, Z. Lin, Z. L. Wang, Unraveling temperature-dependent contact electrification between sliding-mode triboelectric pairs. *Adv. Funct. Mater.* **30**, (2020).

31. S. Lin, L. Xu, L. Zhu, X. Chen, Z. L. Wang, Electron transfer in nanoscale contact electrification: photon excitation effect. *Adv. Mater.* **31**, e1901418 (2019).

32. C. Xu, Y. Zi, A. C. Wang, H. Zou, Y. Dai, X. He, P. Wang, Y. C. Wang, P. Feng, D. Li, Z. L. Wang, Networks of high performance triboelectric nanogenerators based on liquid-solid interface contact electrification for harvesting low-frequency blue energy. *Adv. Mater.* **30**, e1706790 (2018).

33. X. Li, J. Tao, X. Wang, J. Zhu, C. Pan, Z. L. Wang, Networks of high performance triboelectric nanogenerators based on liquid-solid interface contact electrification for harvesting low-frequency blue energy. *Adv. Energy Mater.* **8**, (2018).

34. R. Rahemi, D. Li, Variation in electron work function with temperature and its effect on the Young's modulus of metals. *Scr. Mater.* **99**, 41-44 (2015).

35. R. Strayer, W. Mackie, L. Swanson, Work function measurements by the field emission retarding potential method. *Surf. Sci.* **34**, 225-248 (1973).

36. K. L. Aplin, B. J. Kent, W. Song, C. Castelli, Field emission performance of multiwalled carbon nanotubes for a low-power spacecraft neutraliser. *Acta Astronaut.* **64**, 875-881 (2009).

37. H. Baytekin, A. Patashinski, M. Branicki, B. Baytekin, S. Soh, B. A. Grzybowski, The mosaic of surface charge in contact electrification. *Science* **333**, 308-312 (2011).

38. L. Chen, Y. Huang, L. Song, W. Yin, L. Hou, X. Liu, T. Chen, Biofriendly and regenerable emotional monitor from interfacial ultrathin 2D PDA/AuNPs cross-linking films. *ACS Appl. Mater. Interfaces* **11**, 36259-36269 (2019).

39. J. He, P. Xiao, J. Shi, Y. Liang, W. Lu, Y. Chen, W. Wang, P. Théato, S.-W. Kuo, T. Chen, High performance humidity fluctuation sensor for wearable devices via a bioinspired atomic-precise tunable graphene-polymer heterogeneous sensing junction. *Chem. Mater.* **30**, 4343-4354 (2018).

40. U. Mogera, A. A. Sagade, S. J. George, G. U. Kulkarni, Ultrafast response humidity sensor using supramolecular nanofibre and its application in monitoring breath humidity and flow. *Sci. Rep.* **4**, 4103 (2014).

41. M. Frisch, G. Trucks, H. B. Schlegel, G. E. Scuseria, M. A. Robb, J. R. Cheeseman, G. Scalmani, V. Barone, B. Mennucci, G. Petersson, gaussian 09, Revision d. 01, Gaussian. *Inc., Wallingford CT* **201**, (2009).

42. P. J. Stephens, F. J. Devlin, C. F. Chabalowski, M. J. Frisch, Ab initio calculation of vibrational absorption and circular dichroism spectra using density functional force fields. *J. phys. chem.* **98**, 11623-11627 (1994).

43. F. Weigend, R. Ahlrichs, Balanced basis sets of split valence, triple zeta valence and quadruple zeta valence quality for H to Rn: Design and assessment of accuracy. *Phys. Chem. Chem. Phys.* **7**, 3297-3305 (2005).

44. P. Govindasamy, S. Gunasekaran, S. Srinivasan, Molecular geometry,

conformational, vibrational spectroscopic, molecular orbital and Mulliken charge analysis of 2-acetoxybenzoic acid. *Spectrochim. Acta A Mol. Biomol. Spectrosc.* **130**, 329-336 (2014).

Supplementary Information

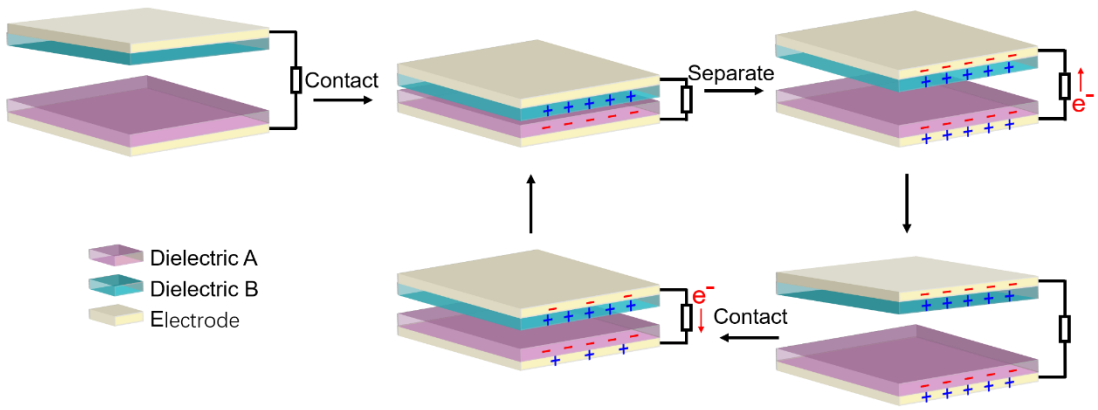

Figure S1. Working mechanism of a contact-separation TENG.

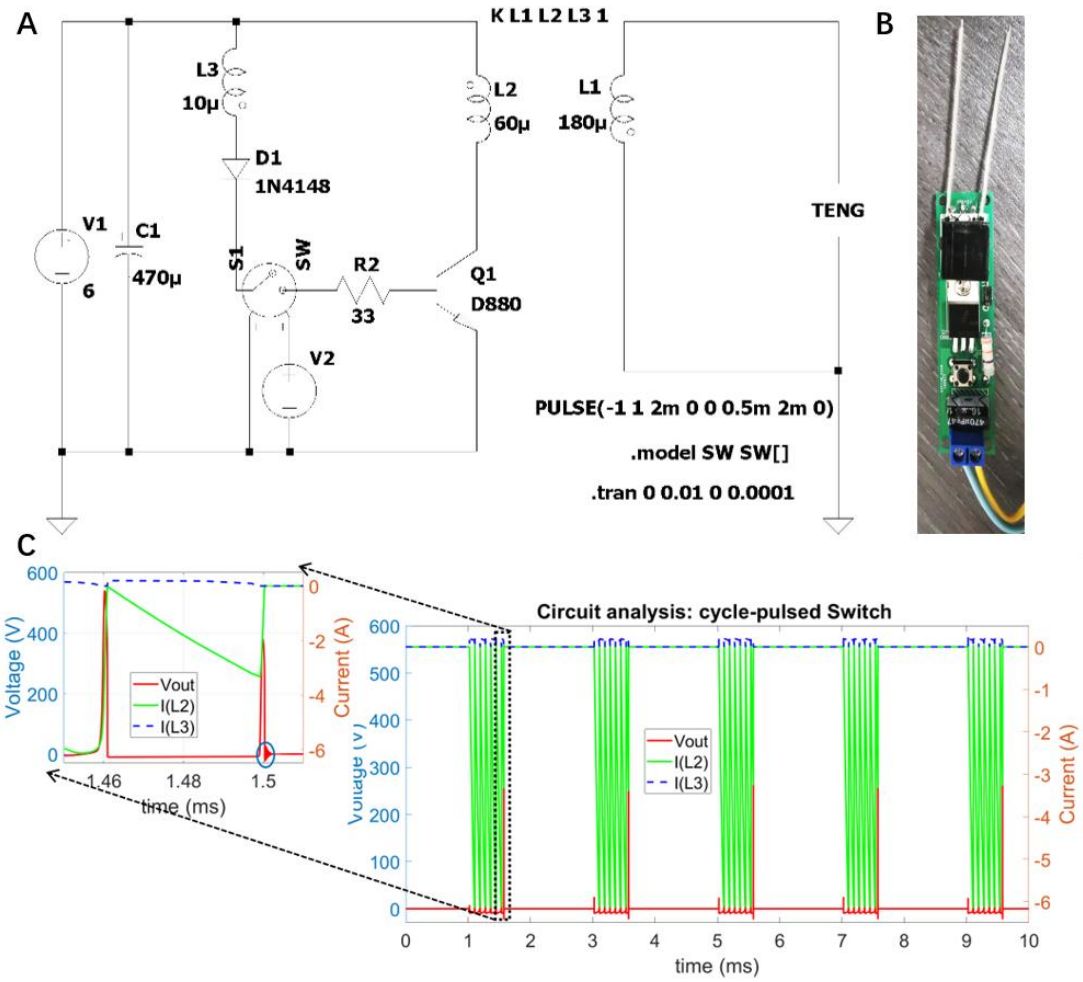

Figure S2. (A) The schematic diagram of the charge excitation system, (B) the manufactured charge excitation system with PCB, (C) the circuit analysis with a cycle-pulsed switch.

Figure S2A depicts a schematic diagram of the charge excitation system, in which the whole system is powered by an energy management module which can supply a 6V DC output (detailed introduction are shown in our previous work). Regarding the charge excitation system, there are two steps for this circuit to generate a high voltage output to nanogenerators:

1) the first step is with the transistor being turned on. A current drawn from the power source flows to the base of the transistor, resulting that the transistor switch is turned on, and the current goes to the primary winding coil of the transformer (L2). The current flow generates a magnetic field in which the energy is constrained in the core. Since the winding coils of L1 and L2 have a reverse phase, only a small part of energy is coupled to the secondary winding coil L1.
2) the second step is with the transistor being turned off. There is a voltage induced into the feedback winding coil L3, leading that the current flowing in L3 decreases gradually until the transistor switch is turned off. At the moment of transistor being turned off, the magnetic field collapses, and the energy is transferred to the secondary winding coil L2 to generate a high voltage output.

Once again, the current flows to the base of the transistor to turn it on and the cycle repeats; such cycle can be seemed as a self-oscillating system. The manufactured charge excitation system is shown in **Figure S2B**.

LTspice is used to model and analyze the circuit, with a cycle-pulsed switch to model the situation with a mechanical switch being pressed periodically. The switch starts to work from 1ms, with a switch-on duration of 0.5 ms and a switch-off duration of 1.5 ms. **Figure S2C** presents the output performance of the charge excitation system; from which the output voltage of the secondary winding coil L1 (Vout), the current flowing in the primary winding coil L2 (I(L2)) and the current flowing in the feedback winding coil L3 (I(L3)) are presented. The self-oscillating process starts from 1ms (the moment of the switch being turned on) and one cycle of the self-oscillation lasts 0.084 ms (**Figure S2A**) which means the frequency of

the self-oscillation is ～12 kHz. Taking the cycle from 1ms to 1.084ms of the self-oscillation as an example, I(L3) increases at first as the current draws from the power source, and the amplitude of I(L2) increases gradually since the transistor is turned on. Vout decreases from 0 V to about -8.7 V, which means a small part of energy is transferred from L2 to L1 since the polarity between L2 and L1 are opposite. Along by the coupling between L2 and L3, I(L3) decreases gradually until it is not large enough to turn on the transistor. Then the amplitude of I(L2) decreases since there is no current flowing through the transistor. At the same time, Vout increases immediately due to most of the energy stored in L2 being transferred to L1. Until now, one cycle of the self-oscillating process is done, and it repeats with a frequency of ~ 12 kHz. Based on the self-oscillation, a high voltage pulse (~ 540 V) is output to the load, which is nanogenerators in this work with a durations ~ 0.002 ms. With a high voltage output applied to tribo-layers, we can have a strong electric field E_{out} between them, aiming to improve the electron transfer efficiency, i.e., the output performance of nanogenerator.

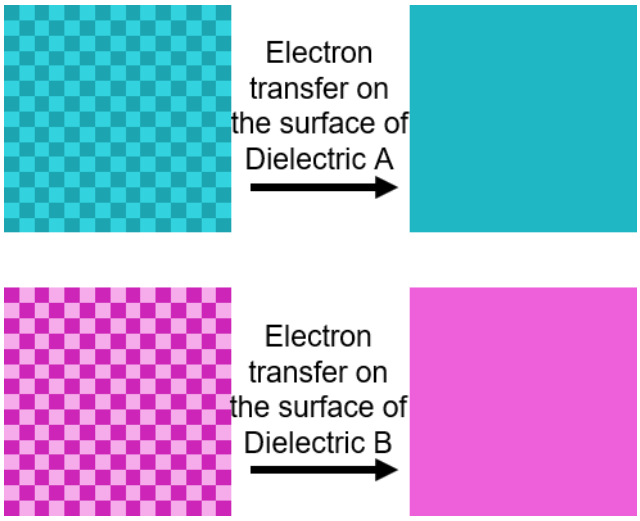

Figure S3. Electron transfer on the surface of dielectric A and B to realize uniform surface charging.

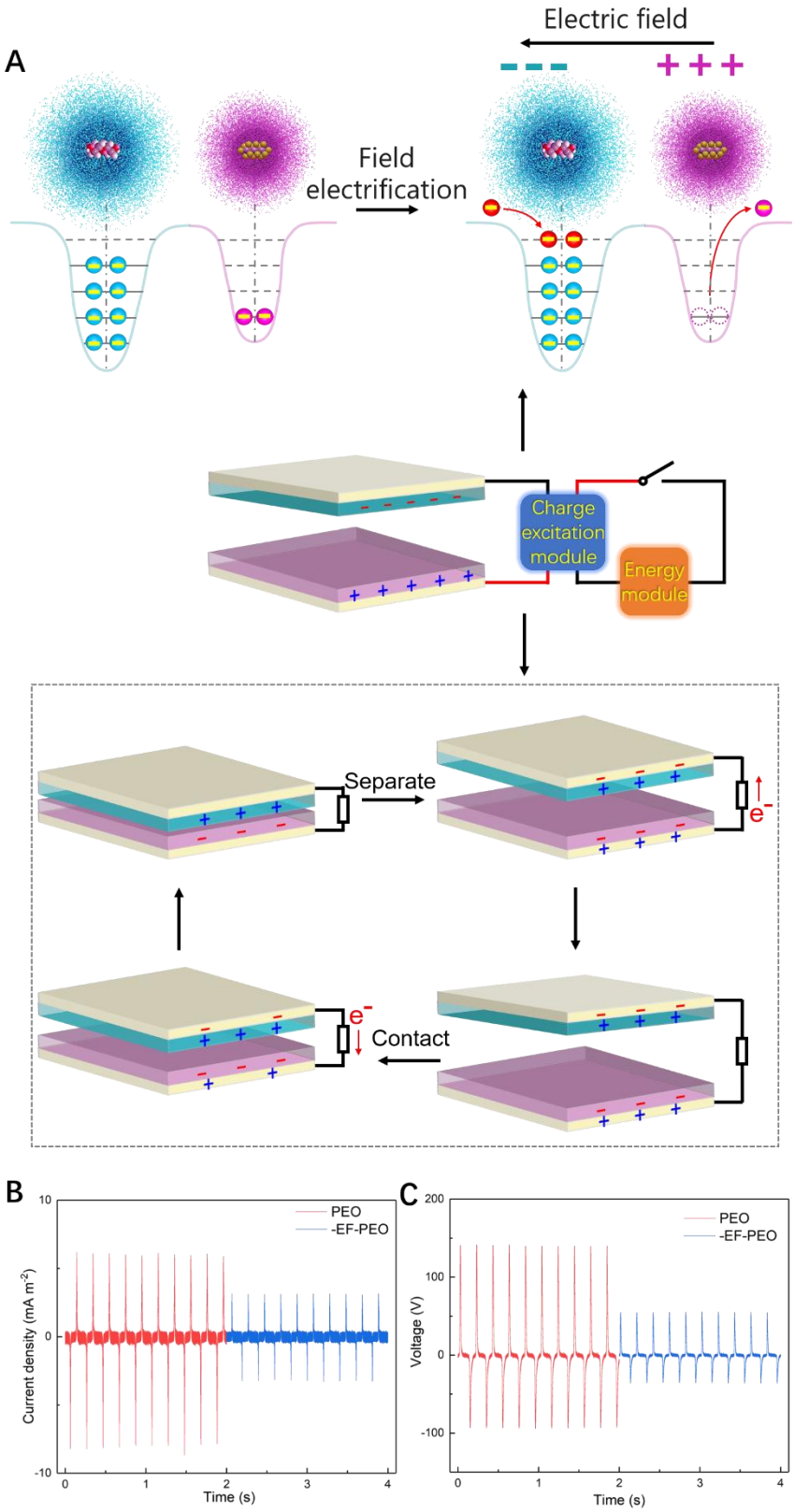

Figure S4. (A) Working mechanism of a contact-separation TENG after excitation of an opposite electric field. (B) short-circuit current density and (C) Output voltage of PEO/PTFE TENGs effected by negative electric field in the opposite direction.

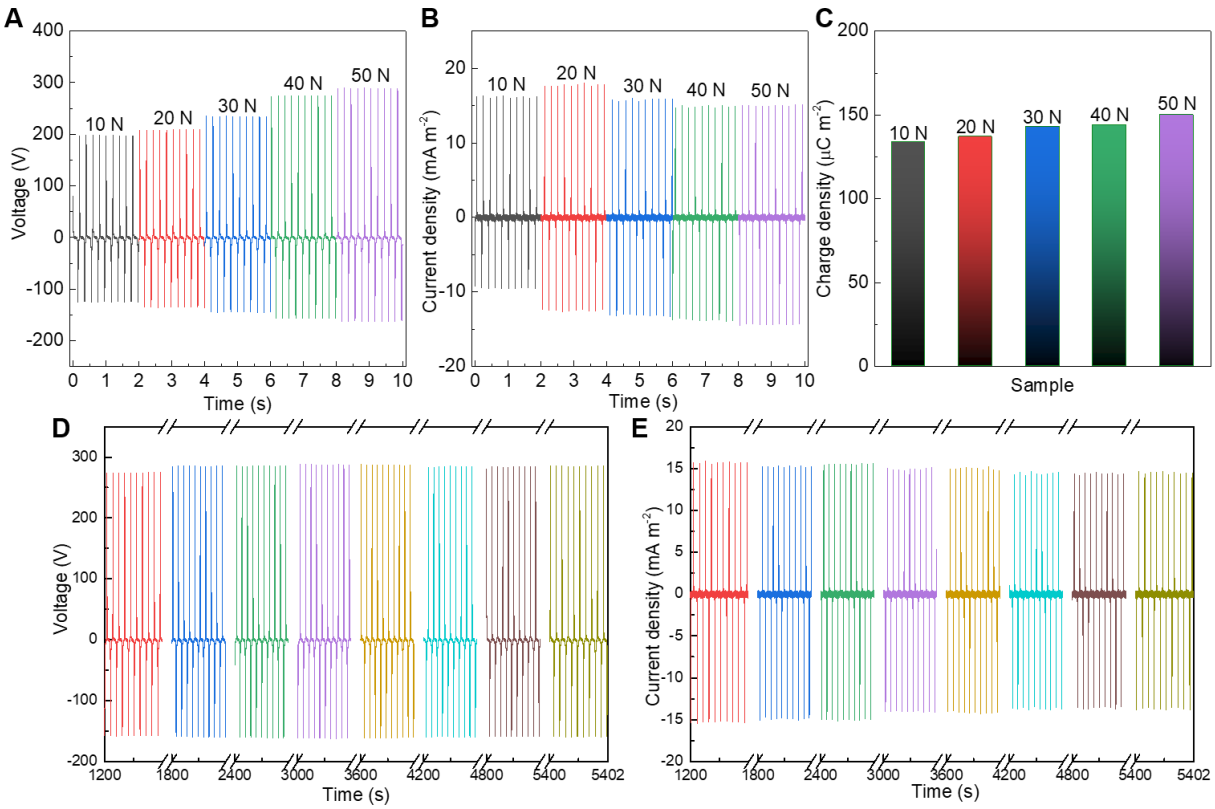

Figure S5. (A) Output voltage, (B) current density and (C) charge density of the PEO/PTFE FENG under different contact forces from 10 to 50 N. (D) Output voltage and (E) current density of the PEO/PTFE FENG for 27000 cycles at a contact frequency of 5 Hz.

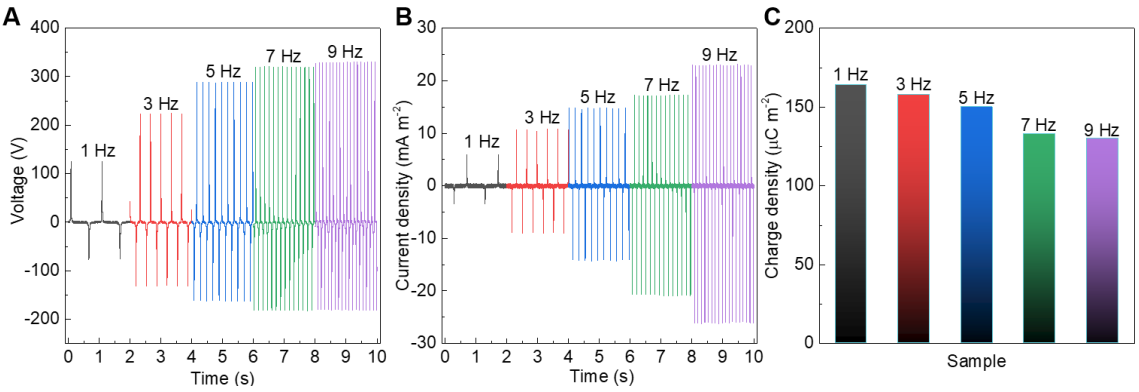

Figure S6. (A) Output voltage, (B) current density and (C) charge density of the PEO/PTFE FENG under different contact frequencies from 1 to 9 Hz.

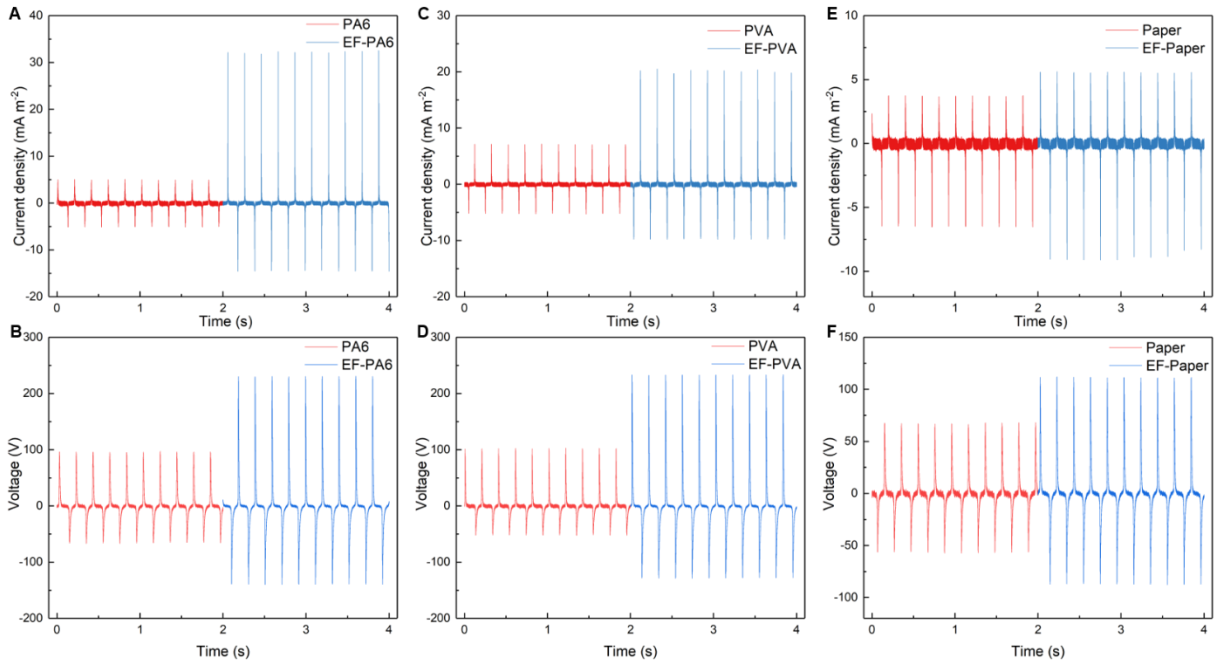

Figure S7. Short-circuit current density and output voltage of the (A, B) PA6/PTFE, (C, D) PVA/PTFE and (E, F) Paper/PTFE TENGs at contact frequency of 5 Hz and forces of 50 N.

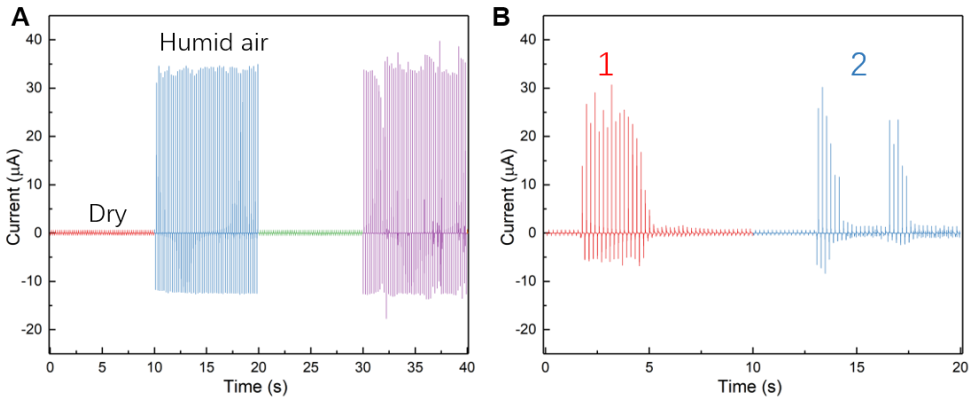

Figure S8. (A and B) Humidity flow sensing from the self-powered sensing device.

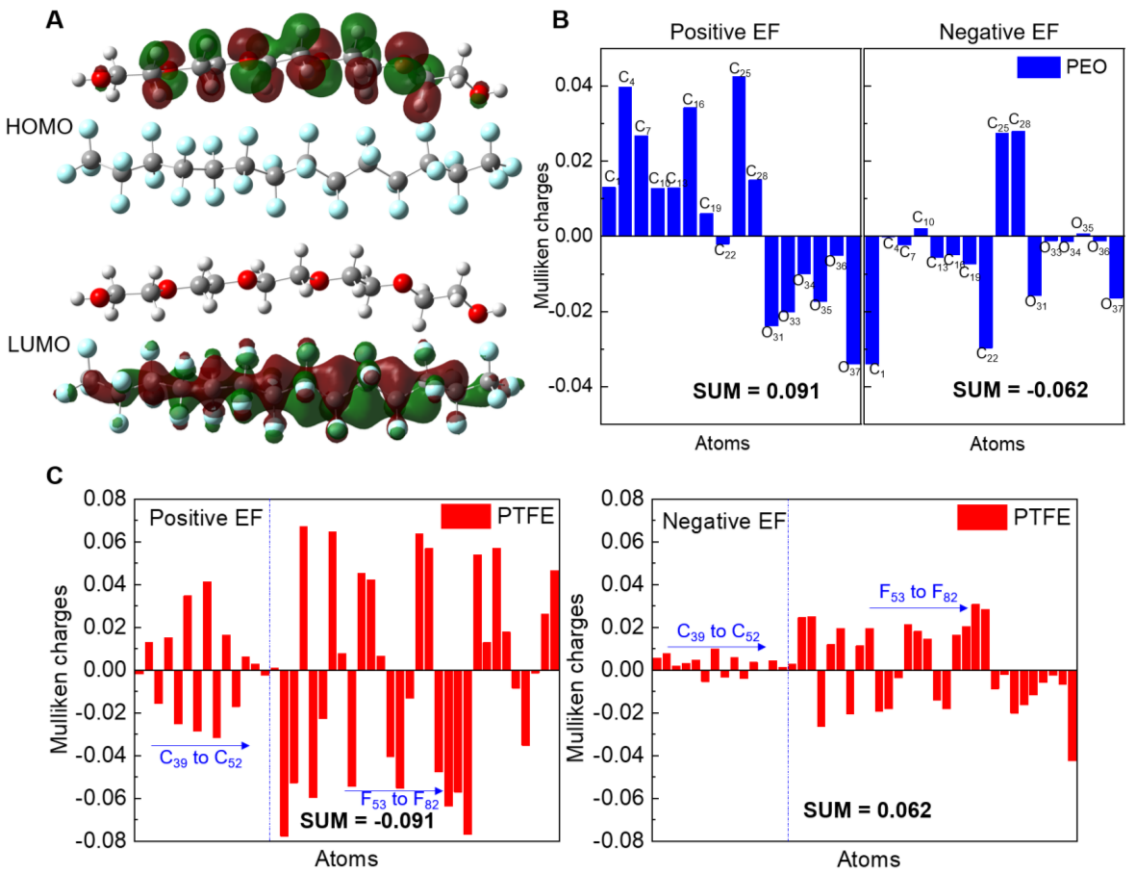

Figure S9. (A) Molecular orbitals and (B, C) Mulliken charge of PEO (-OCH_2CH_2- chain) and PTFE (-CF_2CF_2-chain) under positive and negative EF.

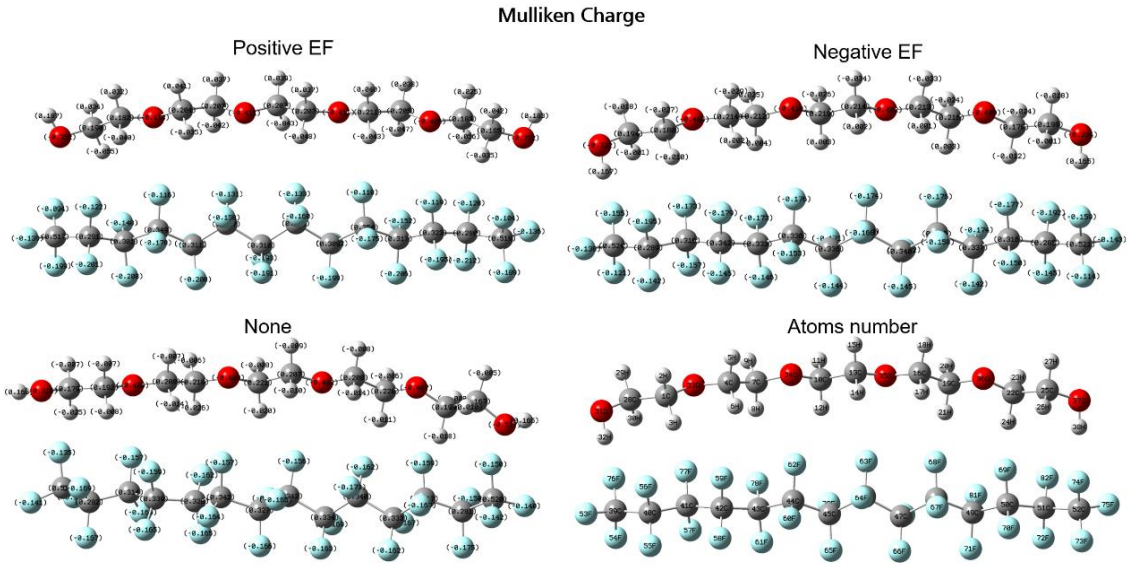

Figure S10. Mulliken charge under positive, negative and none EF, and atoms number of PEO/PTFE model.

Chapter 7 MXene-Coated Textile-based Self-Powered Sensor Array for Visualizing Touch Sense in 2D Image

Abstract

Human skin has different tactile receptors, which can sense the intensity of external stimuli at various locations. I propose a flexible multi-channel sensing system that can imitate tactile receptors to study the source and intensity of stimulus information. The system consists of a customized multi-channel EM instrument, a LabVIEW-based GUI and an innovative material MXene-coated textile. The 64-bit conformal sensor array with capacitive sensing function can realize real-time, multipoint and quantitative detection, and intuitively visualize touch perception in 2D imaging. Moreover, a TENG structure was designed on the sensor array, to construct self-powered sensor array. The findings should make an important contribution to the development of haptic devices, intelligent prostheses and intelligent robots.

7.1 Introduction

The human skin somatosensory system has many external stimulus receptors to uniquely perceive the spatial distribution of contact and strain on the skin.[1] Wearable electronics that imitate the body's somatosensory functions are expected to play an essential role in the fields of tactile devices, rehabilitation training sensing systems, prostheses, gesture recognition, and artificial robots.[2-7] Common rigid wearable electronics on the market have apparent shortcomings, especially low sensitivity, weak accuracy and poor user experience. Developing a sensing system that meets the requirements of high sensitivity, ultra-fast response, repeatability and large working range is still a challenge.[8-10] Regarding the research on wearable flexible sensors, most of them focus on developing new high-performance sensing materials. Many sensing materials have been found to have superior characteristics and many potential applications,[11-14] but some of them have never seen real commercial use (out of the lab onto the market) due to the inherent problems associated with weak interface adhesion in service, too expensive or difficult to manufacture, *etc.*.

Generally, there are three types of conductive sensing materials: polymers, metals, and two-dimensional (2D) materials. The most conductive polymer, PEDOT (single crystal conductivity as high as 8797 S/cm), can achieve strong adhesion to flexible substrates by cross-linking PSS.[15-17] However, the conductivity of PEDOT is affected by the growth of its particular crystal phase and concentration of insulative PSS.[18] Its low conductivity in the actual use process cannot meet the demand. A polymer-assisted metal deposition (PAMD) strategy was developed to obtain highly viscous and conductive metal materials.[19-22] However, due to the inherent rigid nature of metal materials, it is easy to form crack during stretching or bending, thus affecting the stability of the flexible electronics. Conductive 2D materials (such as graphene and MXene) have shown great potential in flexible sensing applications due to their unique ultra-thin layer structure, high surface area to volume ratio, and excellent electromechanical properties. For example, single-layer graphene has a conductivity of up to 10^8 S/cm due to its zero bandgap structure,[23,24] but high quality single-

layer graphene is difficult to mass-produce. On the other hand, the real conductivity of solution-processed graphene that can be mass-produced is largely decreased due to its structural defects.[25-27] What's worse, the preparation of graphene-based conductive solution requires the addition of stabilizer, resulting in lower conductivity. MXene, ($Ti_3C_2T_x$) is metallic, showing a better conductivity (20000 S/cm) than other solution-processed materials, including graphene.[28-30] Besides, It can form a stable colloidal solution without additives and show high electrical conductivity after drying.[31] However, the easy oxidation of MXene due to its hydrophilic propety is a challenge.

In this work, a stable MXene sensing material was mass produced via a simple and low-cost chemical engineering process. The prepared MXene, which has high conductivity and hydrophilicity, is coated on woven textiles to produce 8×8 sensor arrays for wearable electronics. The hydrophilic groups (hydroxyl, oxygen-based groups) of MXene is used to form hydrogen bonding interaction with the hydrophilic textile substrate, to achieve chemical adhesion and increase the hydrophobicity of the prepared sensor (remaining fluorine terminal functional group) to prevent oxidation. The-designed sensor array realizes outstanding performance, including high sensitivity, fast response, stability and durability (>6 months). A customized multi-channel EM instrument was developed to carry out 64 measurements simultaneously in real-time from the sensor array. The sensor array successfully imitates the human body's tactile sense, including stimulus source, stimulus sites, stimulus times and strain 2D imaging. Furthermore, a demonstrator is developed, integrating triboelectric nanogenerator (TENG) on the sensor array, hence enabling self-powered 2D imaging sensing.

7.2 Experimental Section

Materials

MXene was obtained from Nanoplexus Ltd. Ammonium PTFE films (~0.03 mm thickness) for fabricating tribo-negative layers were obtained from the College Hardware, China. Polyamide 6 (PA6) was purchased from Rhodia Ltd. The charge injection on PTFE films was carried out using a commercial antistatic gun (Zerostat 3, Milty).

Preparation of MXene-coated textile

50 wt% MXene water-based solution was prepared as the "conductive clay". The Woven fabric was attached 9 tapes with 2 mm width to create 8 stripes with 5 mm width. The conductive clay was brushed on the patterned surface to construct the MXene-coated stripe textile.

Preparation of MXene-based TENG

20 wt% PA6 solution was prepared in formic acid by gently stirring at 70 ℃ for 3 h. Then the above solution was spin-coated on conductive MXene-coated textile at a rotation speed of 500 rpm for 5 s, followed by 1000 rpm for 15 s. The synthesized PA6 film was acted as the tribo-positive layers. The tribo-negative layer was produced by attaching a PTFE thin film.

Characterization and measurement

The two layers were assembled into vertical contact-separate mode dielectric-dielectric nanogenerators. Electrical output performance of TENG was evaluated by a dynamic fatigue tester system (Popwil Model YPS-1) with controllable working parameters including contact force, frequency and separation distance. A picoammeter (Keysight B2981A) were connected in serial to test the short-circuit current. In a typical test, the electrode of the PA6-coated side was connected to the positive lead of the oscilloscope and picoammeter, while the PTFE side electrode was grounded.

SEM and EDX were carried out by a JSM-IT500A scanning microscope. The thickness of MXene single layer was characterized by atomic force microscope (AFM, Dimension 3100). X-ray computed tomography (XCT) was performed using a Zeiss VersaXRM520. Imaging

was performed at 60 keV with 100 ms exposure time, taking 1601 projections 180° around the sample.

7.3 Results and Discussion

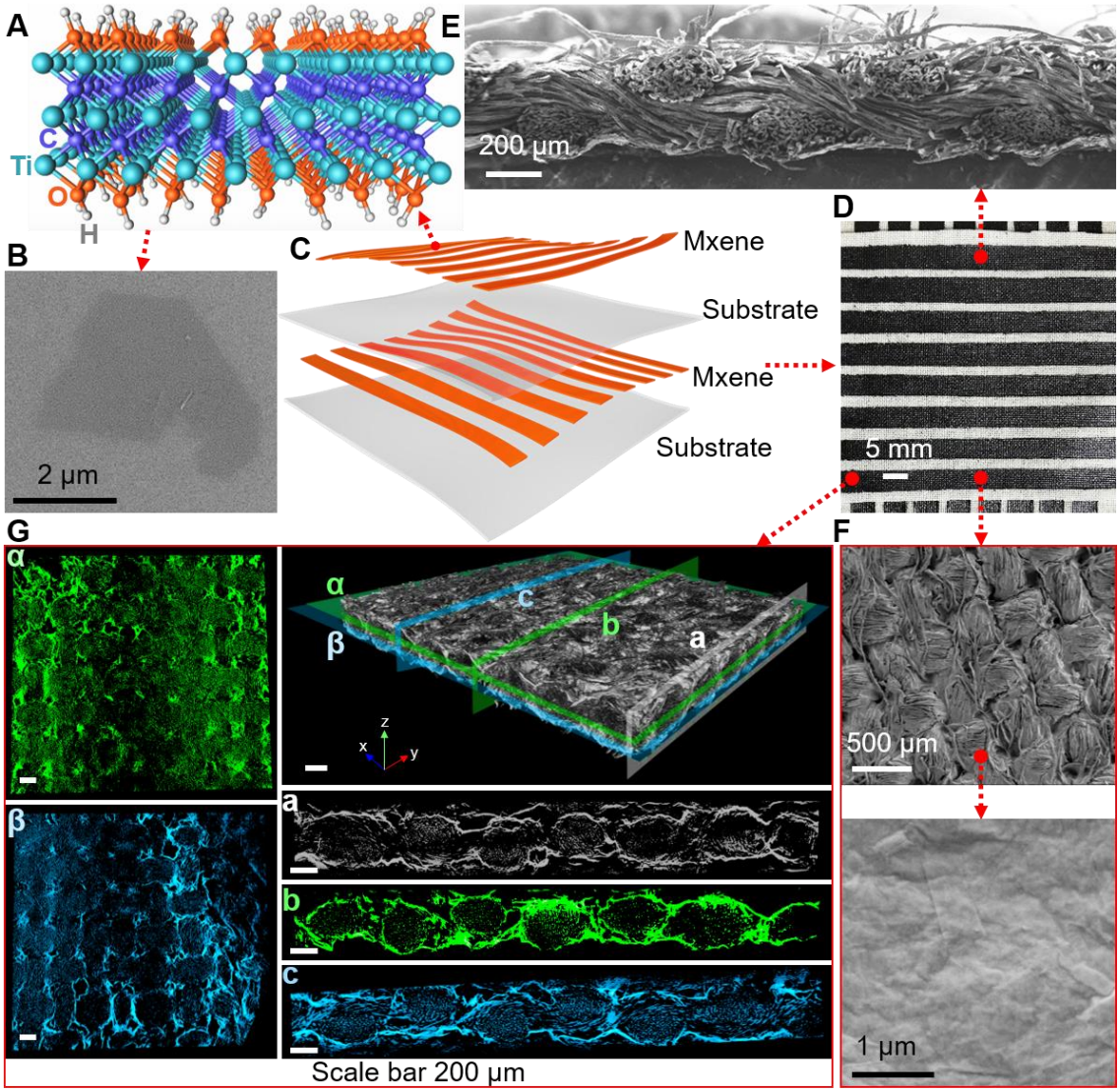

Figure 7.1 Microstructural investigation of MXene-coated textile. (A) Molecular structural of MXene. (B) SEM image of a single MXene nanosheet. (C) The sensor array based on two cross-stacked MXene-coated fabrics. (D) Photo of MXene-coated textile-based sensor array. (E) SEM images of MXene cross-sectional structure. (F) SEM of MXene-coated textile. (G) XCT images of the MXene. The 3D reconstruction of MXene within the MXene-coated fabrics sample; a-c is the cross-sectional structure perpendicular to the fabric plane direction; α-β is the cross-sectional structure parallel to the fabric plane direction.

The molecular of the sensing material, MXene, is shown in **Figure 7.1A**, which is a 3D porous $Ti_3C_2T_x$, where T_x is terminal hydrophilic groups. The mapping images (**Figure S1**) and XPS analysis (**Figure S2**) confirms the existence of C, O, Ti and F elements. **Figure 7.1B** displays the nanosheet structure of one MXene unit. AFM image (**Figure S3**) indicates that one nanosheet is ~2.4 nm, which composes of several atoms thickness. Hence, the sensing material's thickness can be precisely tuned. The MXene was coated onto the surface of textile substrate (**Figure 7.1C and 7.1D**). SEM cross-sectional image (**Figure 7.1E**) and surface microstructure (**Figure 7.1F**) demonstrate the uniform and dense coating of MXene on the surface of textile. The overall thickness is ~400 μm. The enlarged coating surface covers uniform nanosheets to realize high conductivity. The morphology and 3D homogeneity of MXene-coated textile is characterized by XCT (**Figure 7.1G**). The reconstruction analysis demonstrates MXene coatings is ~12 um thickness. From the vertical (a, b, c) and parallel (α-β) cross-section images, it can be clearly seen that the MXene has uniformly modified the whole structure of textile, so the conductivity of the coated textile is excellent. **Figure S5** shows a great conductivity and bending stability of MXene-coated textile. The resistance can be reduced to 1 Ohm/cm.

The sensor working system consists of three parts: a customized multi-channel EM instrument, a LabVIEW-based graphical user interface (GUI) and the sensor array constructed by MXene-coated textile. The demonstration setup is shown in the left of **Figure 7.2A**. During the demonstration, the multi-channel EM instrument generated a sinusoidal excitation signal to excite different sensing pairs in turn. Due to the presence of objects in the sensing area, the capacitance coupling between each sensing pair will change in the sensor array. These changes were measured and processed by the multi-channel EM instrument, and transmitted to the host PC and displayed in the GUI in real-time. The GUI is capable of observing the capacitance change between each sensing pair, providing location, geometry and size information of the test object(s). In addition, the measurement could be saved and processed to form 2D images and provide intuitive visual observations of the test objects. Design details will be introduced in the following sections.

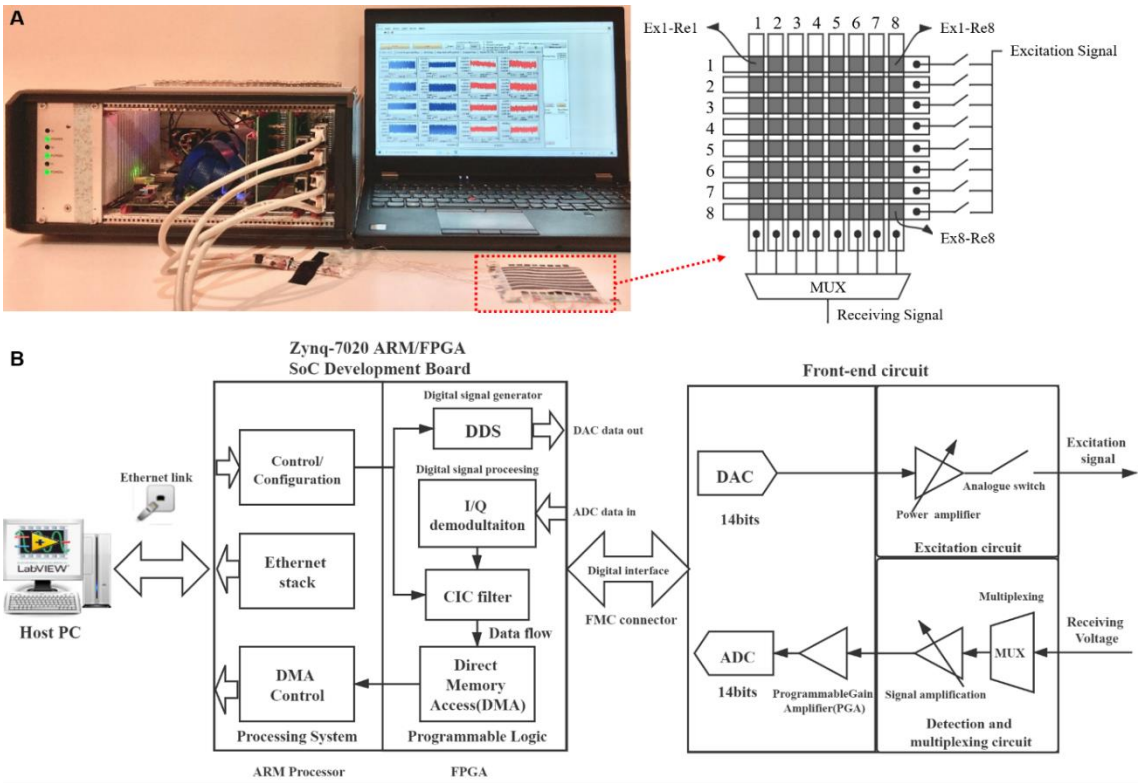

Figure 7.2 (A) Demonstration setups and diagram of sensor array. (B) System architecture of the multi-channel EM instrument.

The sensor array includes 8 excitation elements and 8 receiving elements, where each element is a stripe of MXene coating layer. The excitation elements are parallel to each other and vertical to the receiving elements. The area where the excitation elements overlap with the receiving elements forms a grid with 64 sensing points. The capacitance change within each sensing point can be obtained by the induced voltage from the receiving elements. During the demonstration, the excitation elements are excited in turns. At each excitation element, 8 induced voltages can be measured and multiplexed, illustrated in the right of **Figure 7.2A**. Thus, there are 64 measurements in each data frame (*e.g.*, Ex 1-Re 1, Ex 1- Re 2,…, Ex 1- Re 8, Ex 2- Re 1, Ex 2- Re 2,…, Ex 2- Re 8,…, Ex 8- Re 8).

The architecture of the multi-channel EM instrument is updated from our previous work[32] and shown in **Figure 7.2B**. It mainly consists of Zynq-7020 SoC and AD/DA circuits and front-end circuits. The Zynq-7020 SoC comprises two parts: A Processing System (PS) based

on an ARM dual Cortex-9 processor and a Xilinx 7-series FPGA which is also called Programmable Logic (PL). The PL section is preferable for implementing high-speed logic, arithmetic and dataflow subsystems, while the PS section supports software routines and operating systems. In the proposed application, the PL section is mainly responsible for generating sinusoidal excitation signal, implement in-phase and quadrature (IQ) demodulation for received signal and cascaded-integrator-comb (CIC) filters, while the PS section is in charge of all the data transfer process. The data transfer between the PL section and PS section is accomplished by a Direct Memory Access (DMA) controller. The PS section communicates with the host PC via an Ethernet stack module to send the data, control the process and configure parameters. The front-end circuits are devised for signal conditioning, signal amplification and multiplexing. It consists of an excitation circuit, detection circuits and multiplexing circuits for multi-channel measurement. The AD/DA circuits implement analogue and digital signal conversion as well as Programmable Gain Amplifier (PGA) gain control. Up to 8 channels are available in the hardware which is capable of providing 64 measurements from the sensor array in a single data frame.

With the help of measurement hardware, I can use the MXene-based sensor array to simulate the real human touch sense for mechanical stimuli at different positions and at different times (**Figure 7.3 and Figure S6 – S12**). When I contact different places on the surface of the sensor array, I can obtain 64 real parts of induced voltage (**Figure S7 and S8**), respectively. **Figure 7.3** shows five representative curves selected from 64 measurement results in Figure S7 and S8, to distinguish 12 different contact positions (a –l). Similarly, three representative curves were chosen from 64 measurement results in **Figure S10 and S11**, to differentiate five increased contact times (0.34 s, 1.64 s, 3.51 s, 5.02 s and 9.0 s).

The sensor array was then used to imitate human somatosensory function in response to different mechanical stimuli, including a 0.8 g metal disc, a 2 g glass plate, a 26 g triangular plug, a 120 g tomato and different fingers contact (**Figure 7.4**). The 64 measurements obtained from the multi-channel EM instrument were analysed via Matlab to form a 2D imaging.

Figure 7.4A suggests that the heavier the object, the greater the induced voltage output. **Figure 7.4B** demonstrates the 2D images can excellently reflect different fingers' contact places. When the sensor array was integrated into a smart glove, the sensor array system can visualize touch sense in 2D images. As shown in the right of **Figure 7.4B**, when I contact the sensor array on the surface of the smart glove, I can get a 2D image with the exact position and quantitative induced voltage changes according to the contact force.

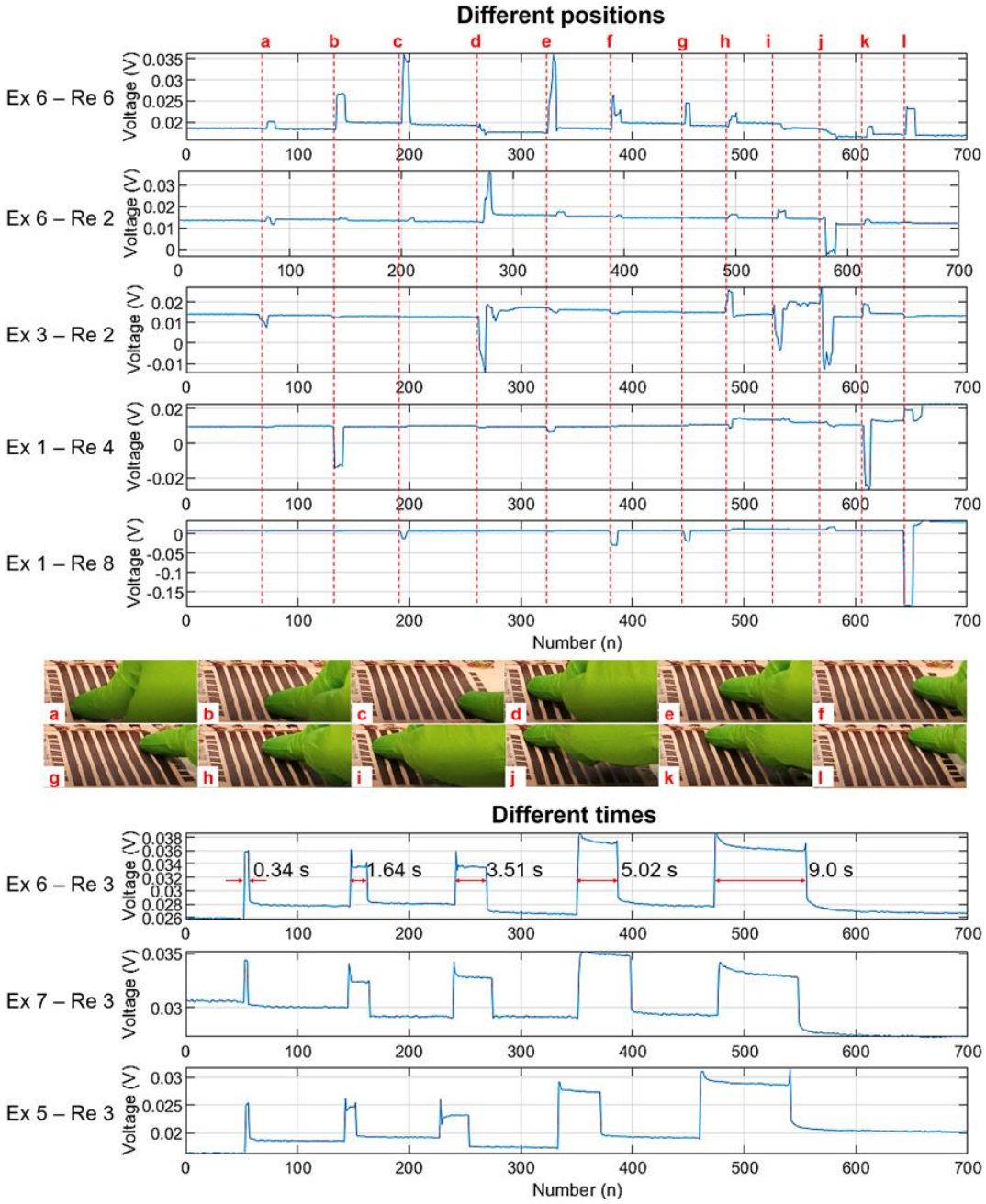

Figure 7.3 Real-time monitoring of MXene-based sensor array with different contact positions and different contact times.

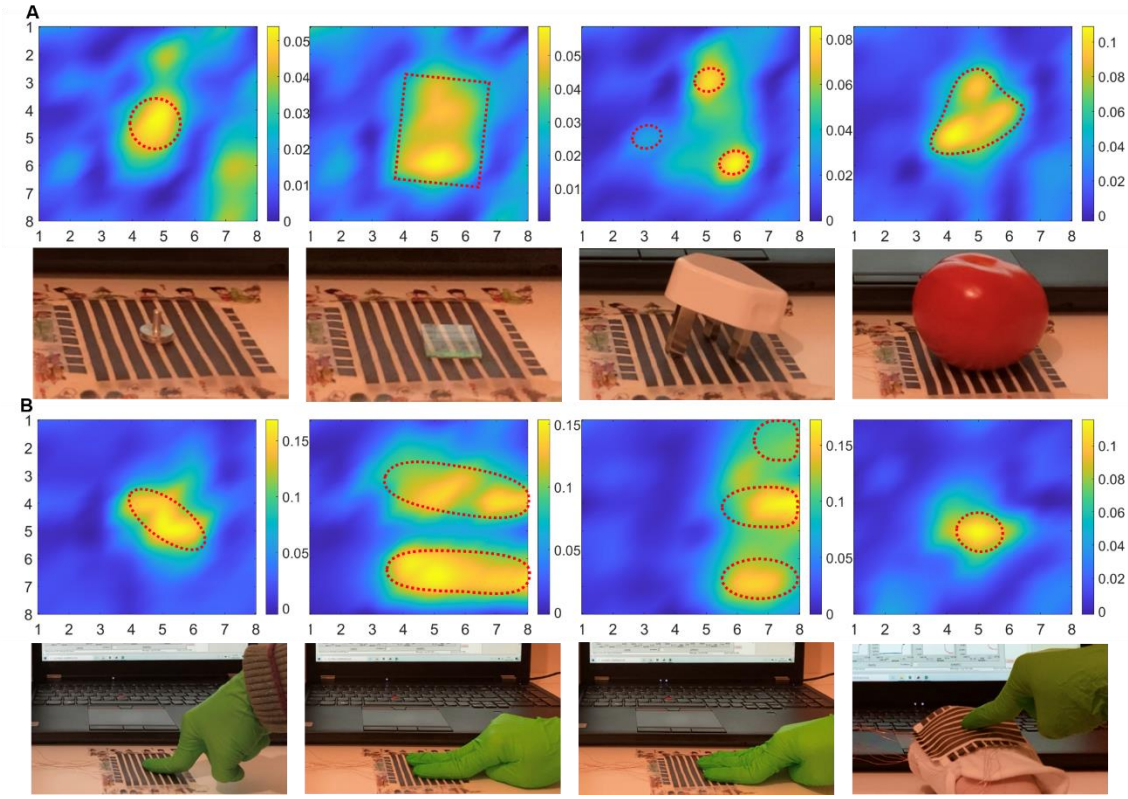

Figure 7.4 (A) Complex strain 2D imaging and real photos under various multiple stress.

The MXene coatings can be used as two electrodes of triboelectric nanogenerator (TENG). The positive and negative tribo-layers for storage of electrical charges are polyamide (PA6) and polytetrafluoroethylene (PTFE), respectively. When two surfaces are brought into contact (**Figure 7.5A**) and then separated (**Figure 7.5B**), a weak current will be transferred from PA6-side MXene-electrode to PTFE-side MXene-electrode via an external circuit. In this way, the 64-bit sensor array can collect signals without a bulky power supply, forming a self-powered sensor array. Two mechanical objects with square (**Figure 7.5C- E**) and spherical (**Figure 7.5F-H**) external forces were constructed to test the performance of the self-powered sensor array. More force induces higher current output. The current 2D image indicates a prominent stress range similar to the mechanical object I place. Such a self-powered sensor array helps us construct an all-flexible, energy-saving and weight-light wearable device to real-time monitor the various stress changes in daily activities.

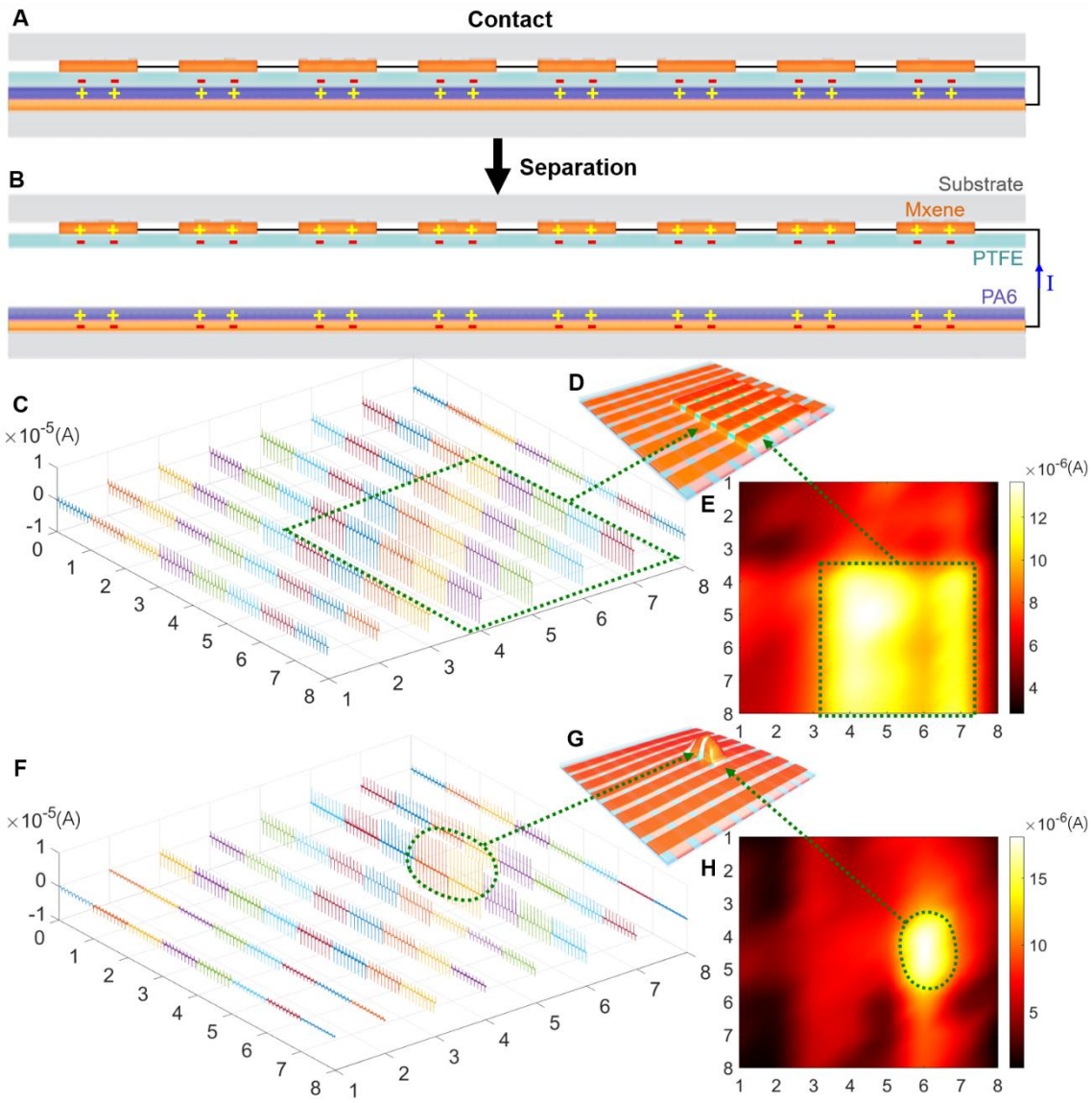

Figure 7.5 64-bit self-powered sensor array at (A) Contact and (B) separation states. Current output, mechanical model and current 2D image with square (C, D and E) and spherical (F, G and H) external forces.

7.4 Summary

A sensor array detection system was designed by connecting a customized multi-channel EM instrument, a LabVIEW-based GUI and a novel flexible sensing material MXene-coated textile. The morphology of MXene coating was characterized by SEM and XCT, which shows 3D homogeneity of a $Ti_3C_2T_x$ film with ~ 12 μm thickness. The hydrogen bonding between hydrophilic groups (hydroxyl, oxygen-based groups) of T_x and hydroxyl of cotton

enables the robust adhesion between the MXene and the cotton textile substrate. The rest fluorine group of T_x increased the hydrophobicity of the MXene-coated textile to prevent oxidation. The sensor array can realize quantitative detection at different positions and at different times with fast response and high sensitivity. 2D image visualization of touch sense achieves intuitive detection of multipoint and various sources of mechanical stimuli. Moreover, the MXene coatings was used as the two electrodes of TENG to construct self-powered sensor array in 2D imaging. This interdisciplinary research has bridged multi-channel instrumentation/measurements with novel 2D material sciences and applications in haptic devices, prostheses and smart gloves for the disabled to realize self-powered, real-time, multipoint, and quantitative detection.

References

1 Wang, M. *et al.* Artificial skin perception. *Adv. Mater.* **33**, e2003014, (2021).

2 Yu, X. *et al.* Skin-integrated wireless haptic interfaces for virtual and augmented reality. *Nature* **575**, 473-479, (2019).

3 You, I. *et al.* Artificial multimodal receptors based on ion relaxation dynamics. *Science* **370**, 961-965, (2020).

4 Ji, B. *et al.* Bio-inspired hybrid dielectric for capacitive and triboelectric tactile sensors with high sensitivity and ultrawide linearity range. *Adv. Mater.* **33**, e2100859, (2021).

5 Ma, Z. *et al.* Permeable superelastic liquid-metal fibre mat enables biocompatible and monolithic stretchable electronics. *Nat. Mater.* **20**, 859-868, (2021).

6 Wang, M. *et al.* Gesture recognition using a bioinspired learning architecture that integrates visual data with somatosensory data from stretchable sensors. *Nat. Electron.* **3**, 563-570, (2020).

7 Moin, A. *et al.* A wearable biosensing system with in-sensor adaptive machine learning for hand gesture recognition. *Nat. Electron.* **4**, 54-63, (2020).

8 Amjadi, M., Kyung, K.-U., Park, I. & Sitti, M. Stretchable, skin-mountable, and wearable strain sensors and their potential applications: a review. *Adv. Funct. Mater.*

26, 1678-1698, (2016).

9 Xie, M. *et al.* Flexible multifunctional sensors for wearable and robotic applications. *Adv. Mater. Technol.* **4**, (2019).

10 Jayathilaka, W. *et al.* Significance of nanomaterials in wearables: a review on wearable actuators and sensors. *Adv. Mater.* **31**, e1805921, (2019).

11 Trung, T. Q. & Lee, N. E. Flexible and stretchable physical sensor integrated platforms for wearable human-activity monitoringand personal healthcare. *Adv. Mater.* **28**, 4338-4372, (2016).

12 Khan, Y., Ostfeld, A. E., Lochner, C. M., Pierre, A. & Arias, A. C. Monitoring of vital signs with flexible and wearable medical devices. *Adv. Mater.* **28**, 4373-4395, (2016).

13 Zang, Y., Zhang, F., Di, C.-a. & Zhu, D. Advances of flexible pressure sensors toward artificial intelligence and health care applications. *Mater. Horiz.* **2**, 140-156, (2015).

14 Cai, P. *et al.* Biomechano-Interactive Materials and Interfaces. *Adv. Mater.* **30**, e1800572, (2018).

15 Cho, B. *et al.* Single-crystal poly(3,4-ethylenedioxythiophene) nanowires with ultrahigh conductivity. *Nano Lett.* **14**, 3321-3327, (2014).

16 Wang, X. *et al.* High electrical conductivity and carrier mobility in oCVD PEDOT thin films by engineered crystallization and acid treatment. *Sci. Adv.* **4**, eaat5780, (2018).

17 Worfolk, B. J. *et al.* Ultrahigh electrical conductivity in solution-sheared polymeric transparent films. *Proc. Natl. Acad. Sci. U. S. A.* **112**, 14138-14143, (2015).

18 Chen, H.-W. & Li, C. PEDOT: Fundamentals and its nanocomposites for energy storage. *Chin. J. Polym. Sci.* **38**, 435-448, (2019).

19 Chen, L. *et al.* Textile-based capacitive sensor for physical rehabilitation via surface topological modification. *ACS Nano* **14**, 8191-8201, (2020).

20 Chen, L. *et al.* Whole system design of a wearable magnetic induction sensor for physical rehabilitation. *Adv. Intell. Syst.* **1**, (2019).

21 Yu, Y. *et al.* Photoreactive and metal-platable copolymer inks for high-throughput, room-temperature printing of flexible metal electrodes for thin-film electronics. *Adv.*

Mater. **28**, 4926-4934, (2016).

22 Li, P., Zhang, Y. & Zheng, Z. Polymer-assisted metal deposition (PAMD) for flexible and wearable electronics: principle, materials, printing, and devices. *Adv. Mater.* **31**, e1902987, (2019).

23 Cao, M.-S., Wang, X.-X., Cao, W.-Q. & Yuan, J. Ultrathin graphene: electrical properties and highly efficient electromagnetic interference shielding. *J. Mater. Chem. C* **3**, 6589-6599, (2015).

24 Cooper, D. R. *et al.* Experimental review of graphene. *ISRN Condens. Matter Phys.* **2012**, 1-56, (2012).

25 Parvez, K. *et al.* Electrochemically exfoliated graphene as solution-processable, highly conductive electrodes for organic electronics. *ACS Nano* **7**, 3598-3606, (2013).

26 Paton, K. R. *et al.* Scalable production of large quantities of defect-free few-layer graphene by shear exfoliation in liquids. *Nat. Mater.* **13**, 624-630, (2014).

27 Lin, S. *et al.* Ultrathin nitrogen-doping graphene films for flexible and stretchable EMI shielding materials. *J. Mater. Sci.* **54**, 7165-7179, (2019).

28 Mathis, T. S. *et al.* Modified MAX phase synthesis for environmentally stable and highly conductive Ti_3C_2 MXene. *ACS Nano* **15**, 6420-6429, (2021).

29 Anasori, B., Lukatskaya, M. R. & Gogotsi, Y. 2D metal carbides and nitrides (MXenes) for energy storage. *Nat. Rev. Mater.* **2**, (2017).

30 Lipatov, A. *et al.* High electrical conductivity and breakdown current density of individual monolayer Ti3C2T MXene flakes. *Matter* **4**, 1413-1427, (2021).

31 Yang, W. *et al.* 3D Printing of freestanding MXene architectures for current-collector-free supercapacitors. *Adv. Mater.* **31**, e1902725, (2019).

32 Chen, Z. *et al.* A novel hybrid serial/parallel multi-frequency measurement method for impedance analysis in eddy current testing. *Rev. Sci. Instrum.* **91**, 024703, (2020).

Supplementary Information

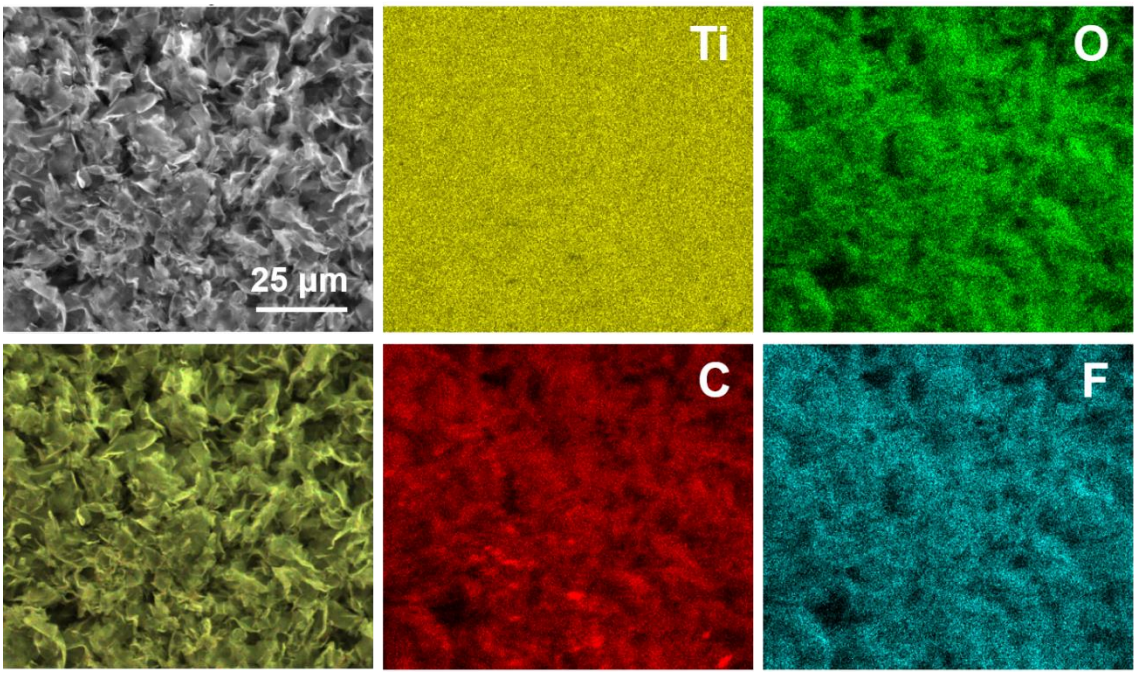

Figure S1 SEM and Mapping image of MXene microstructure.

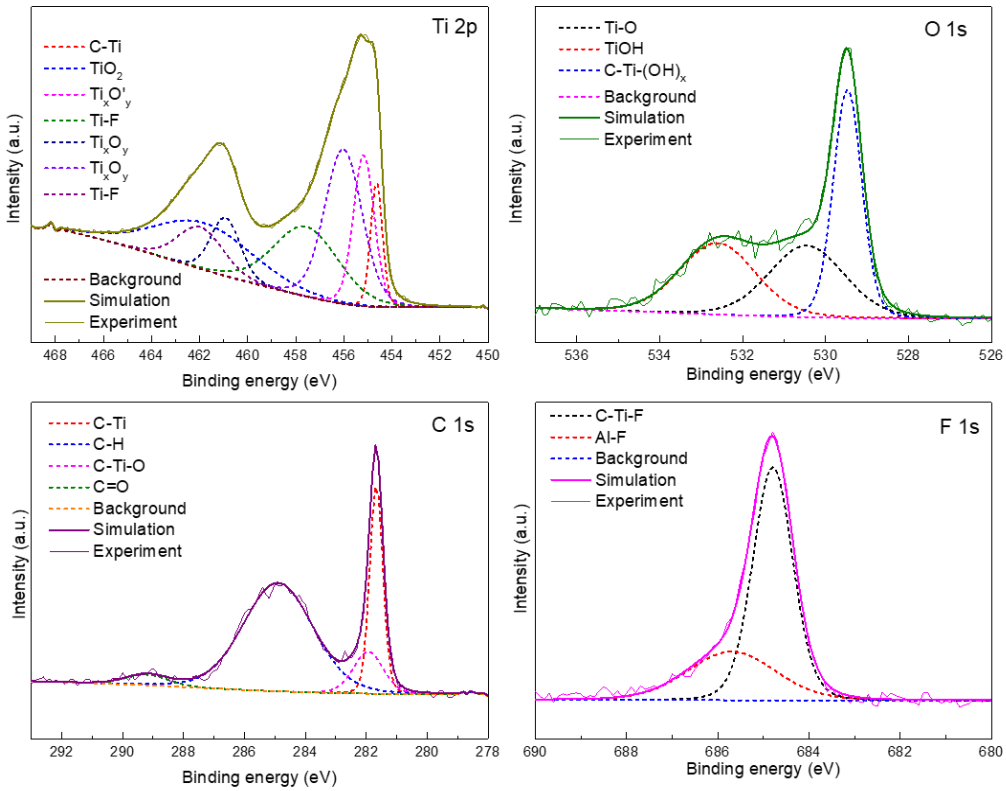

Figure S2 XPS of MXene coatings.

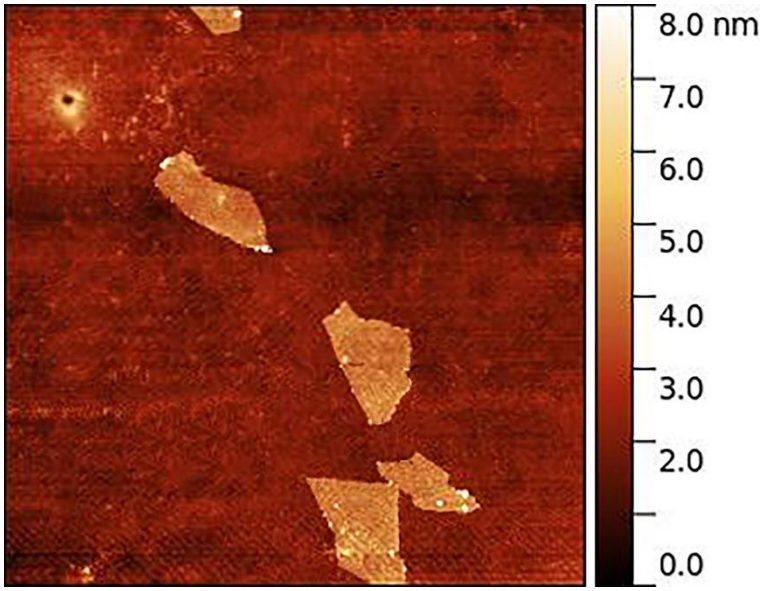

Figure S3 AFM image of MXene nanoflakes within 1-3 nm thickness.

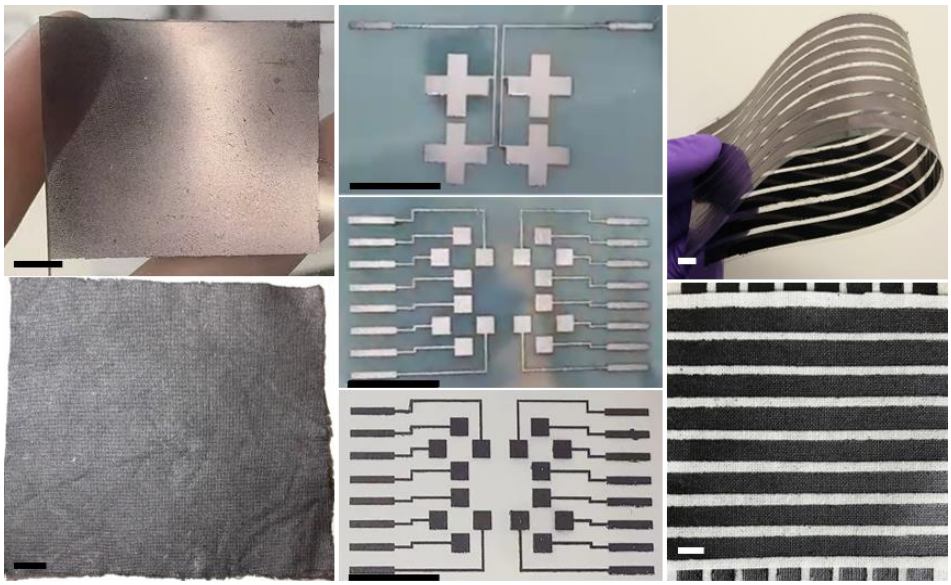

Figure S4 MXene coatings on different substrates, such as PDMS, cotton textile, PET and paper.

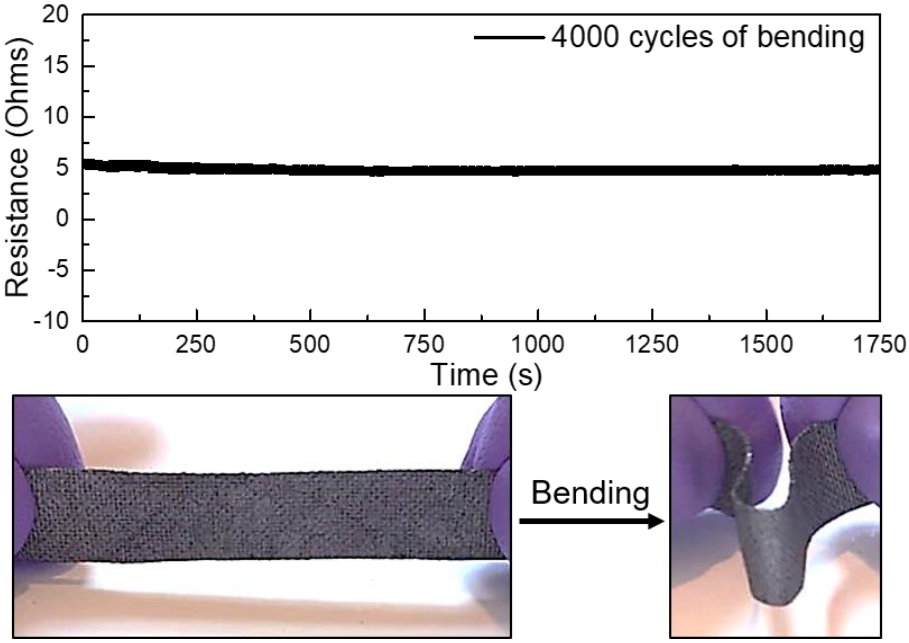

Figure S5 Bendability and stability of MXene-coated textile.

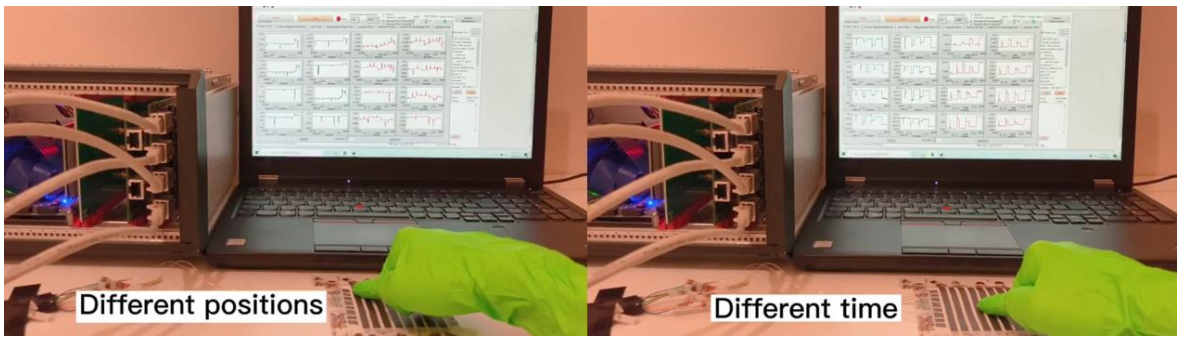

Figure S6 Working photos during real-time monitoring of MXene-based sensor array with different contact position and different contact time.

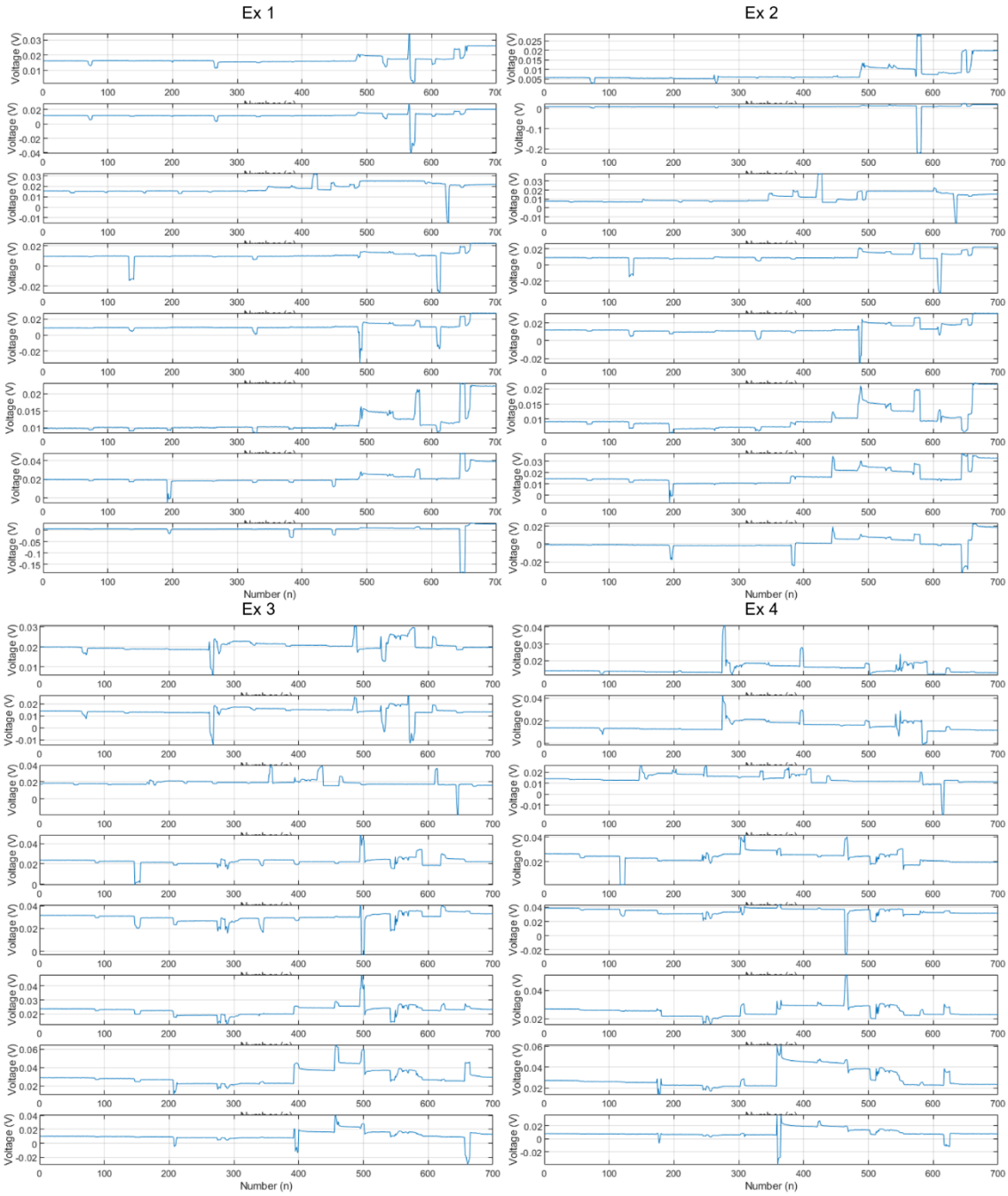

Figure S7 Real-time monitoring of real part of induced voltage of MXene-based sensor array with different contact positions (Ex1 - Ex4).

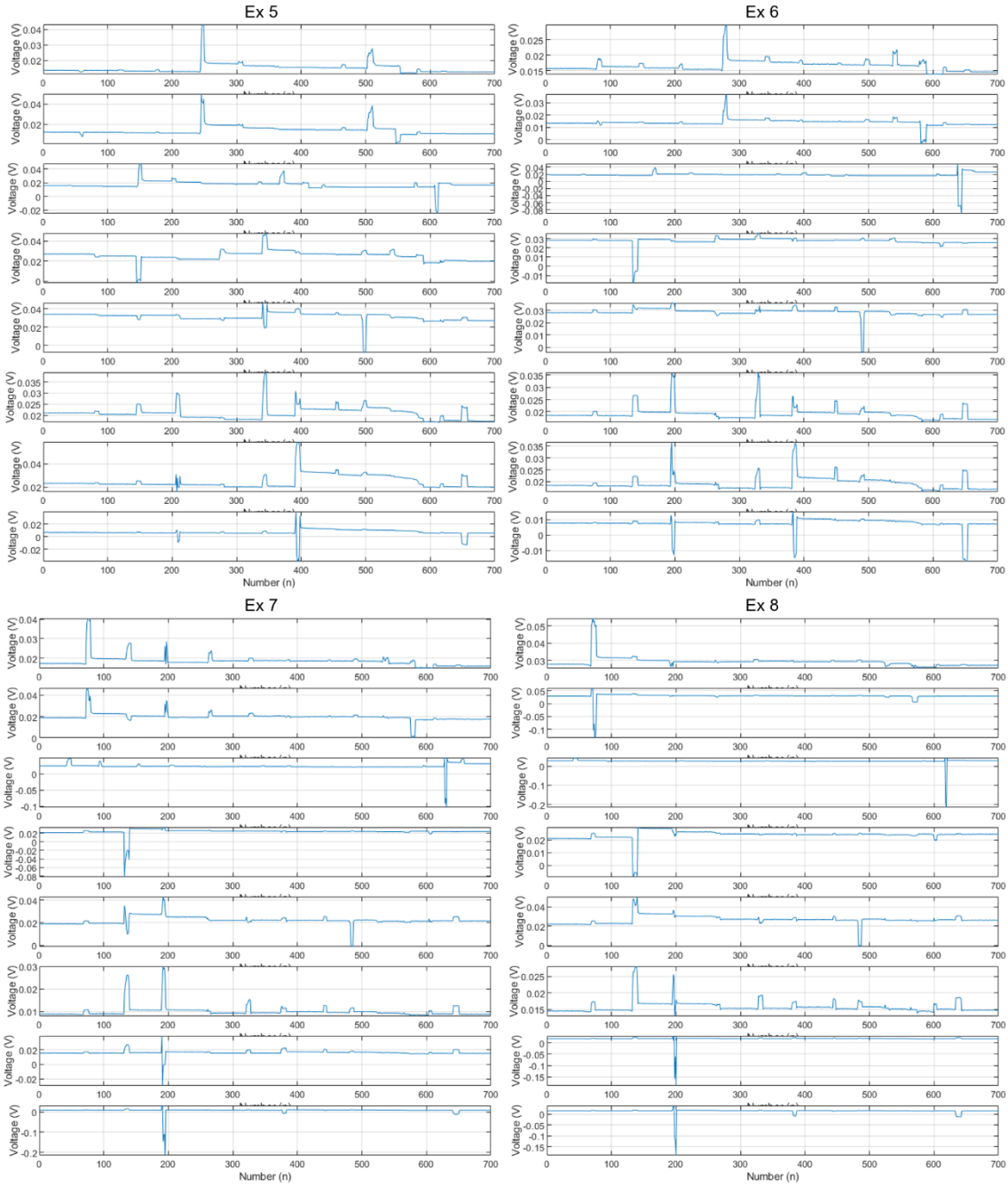

Figure S8 Real-time monitoring of real part of induced voltage of MXene-based sensor array with different contact positions (Ex5 - Ex8).

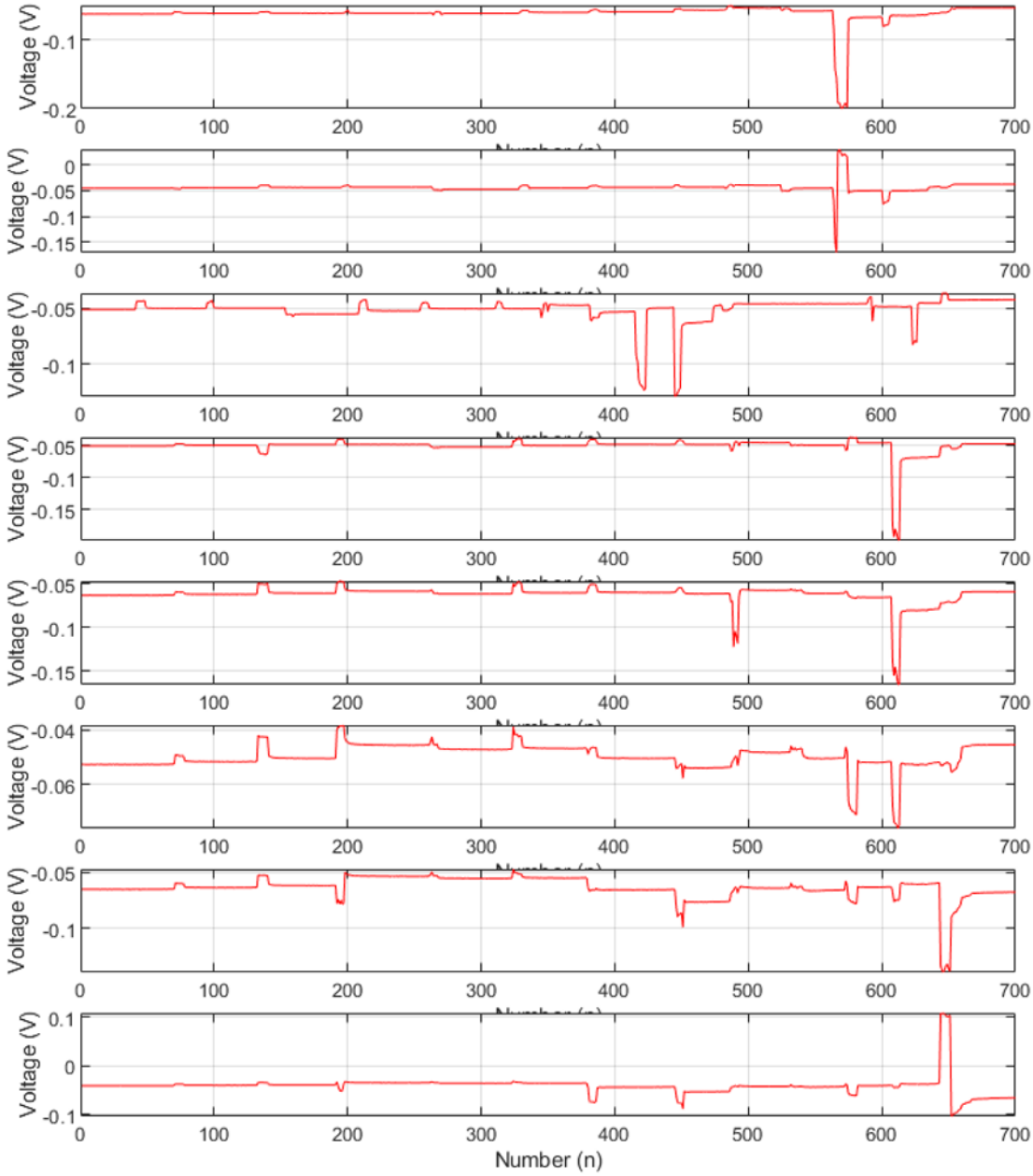

Figure S9 Real-time monitoring of imaginary part of induced voltage of MXene-based sensor array with different contact positions. The imaginary parts of induced voltage are similar under Ex1 - Ex8, so Re1 –Re8 of one of the excitation is listed.

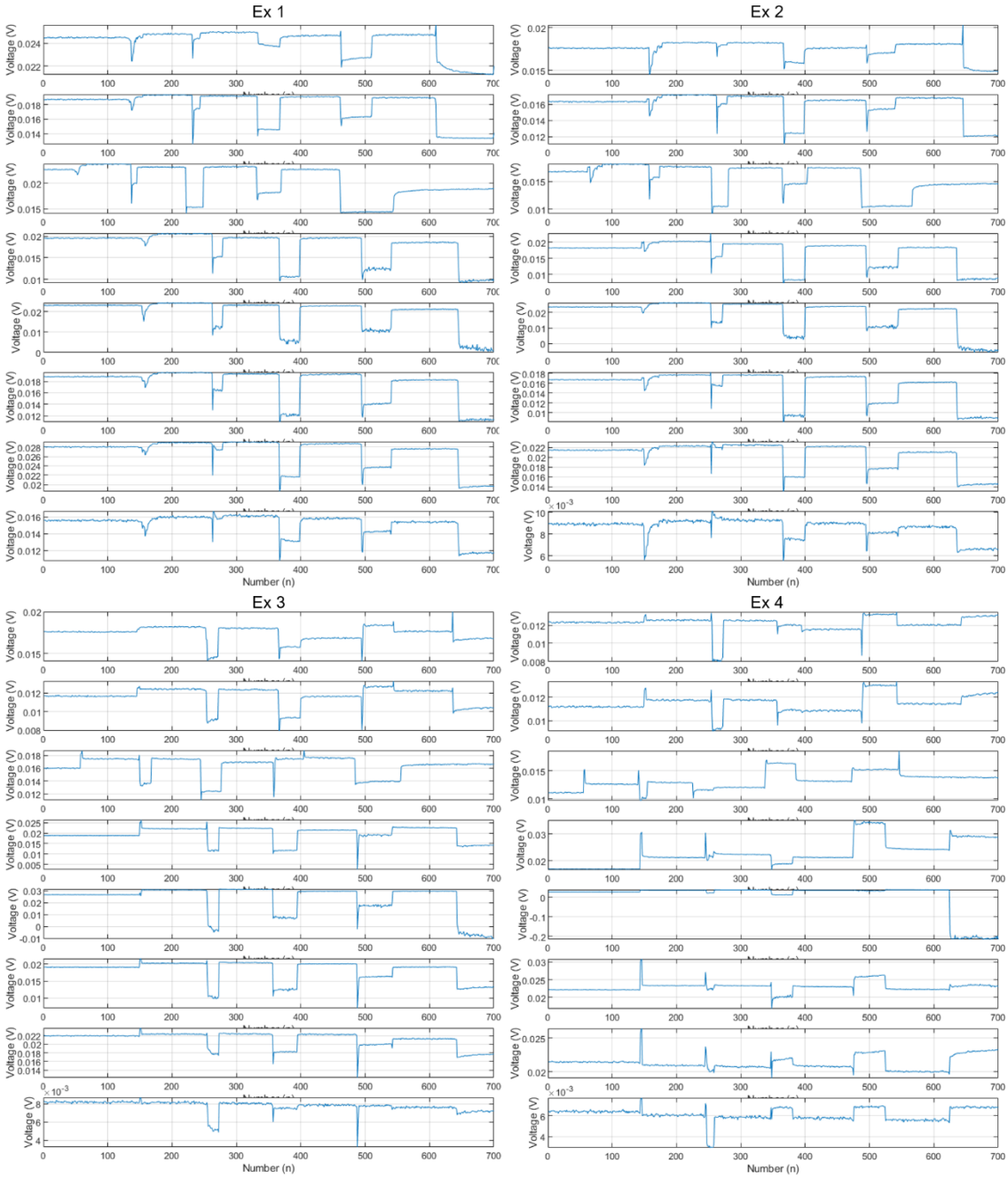

Figure S10 Real-time monitoring of real part of induced voltage of MXene-based sensor array with different contact times (Ex1 - Ex4).

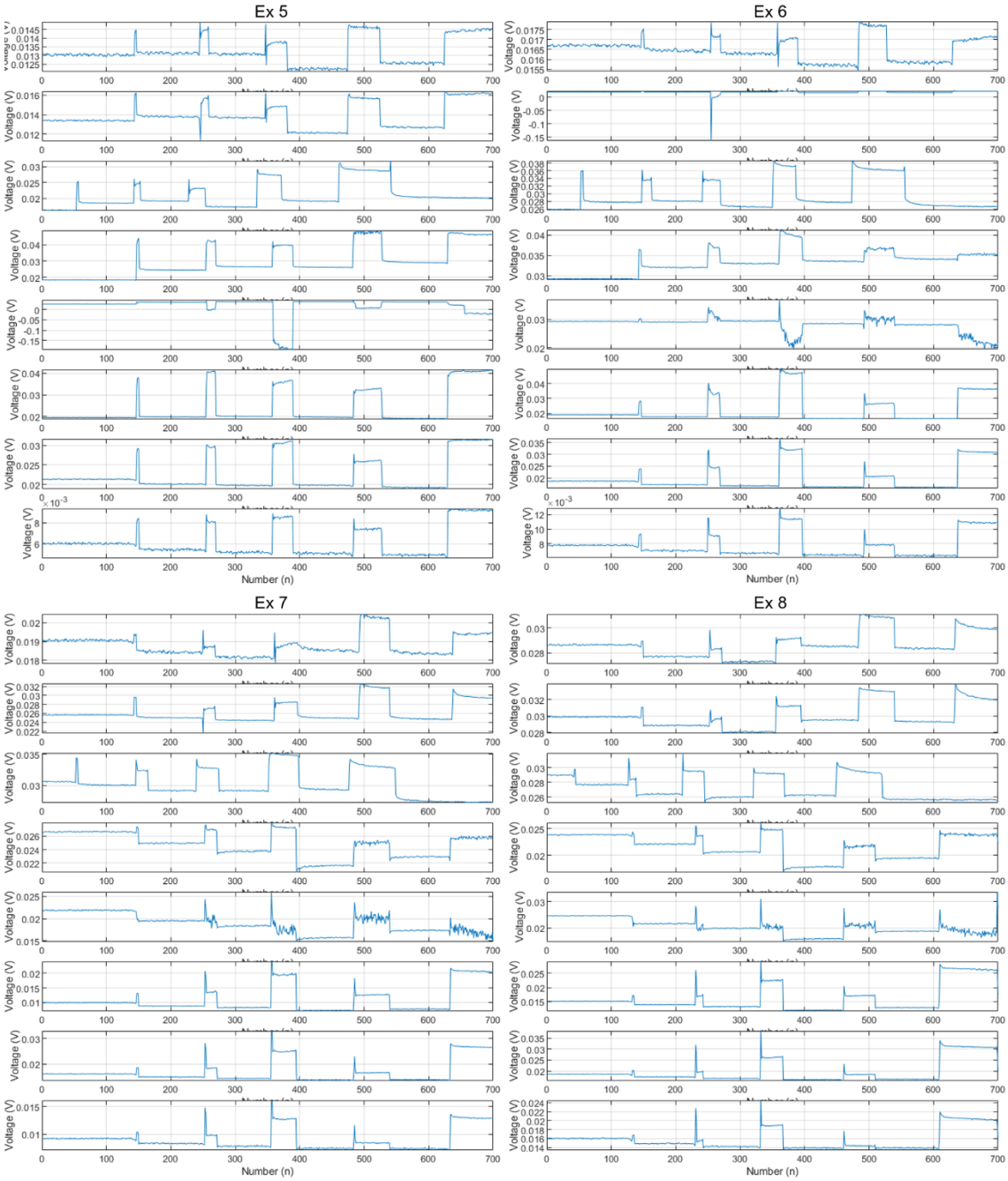

Figure S11 Real-time monitoring of real part of induced voltage of MXene-based sensor array with different contact times (Ex5 - Ex8).

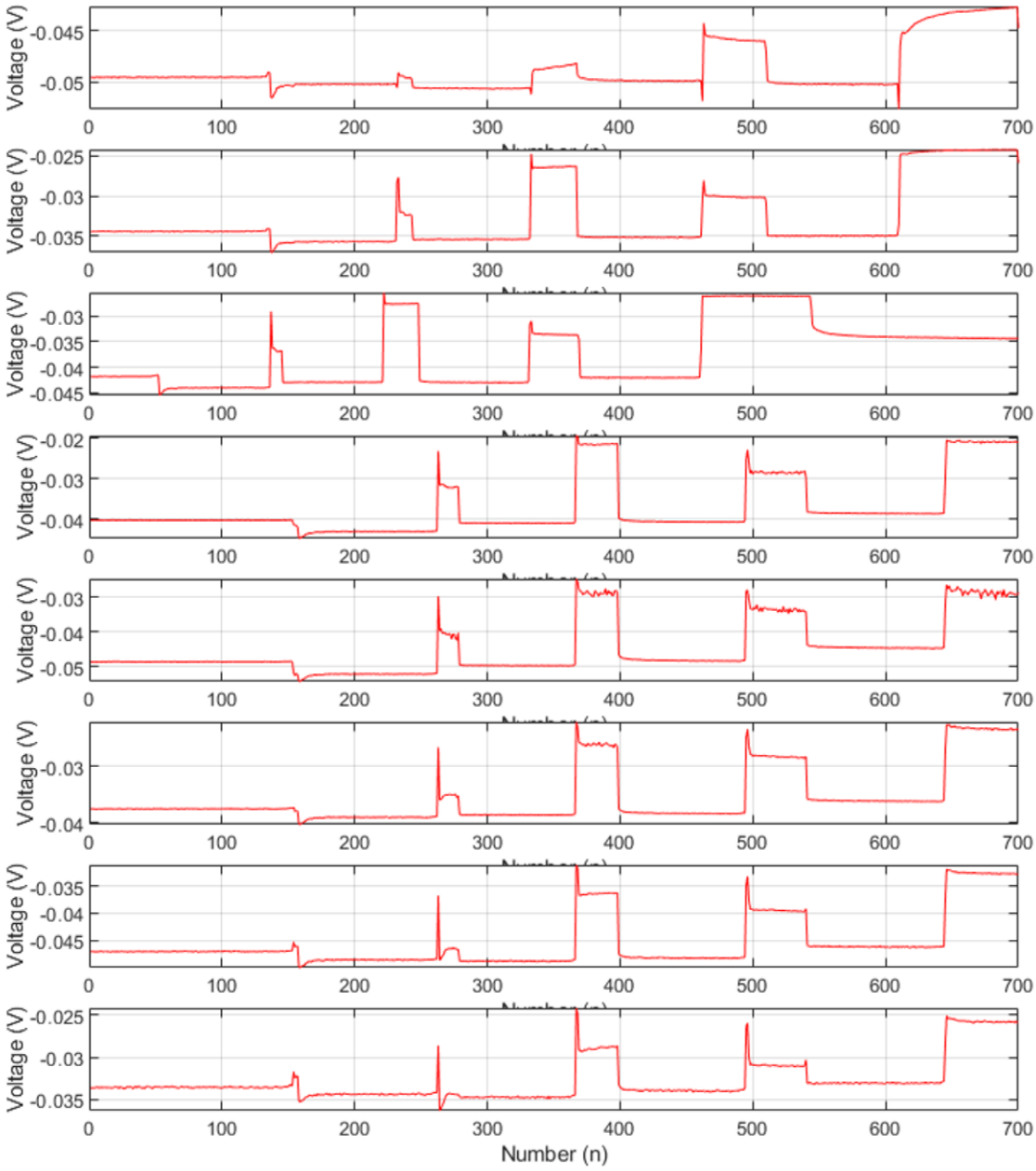

Figure S12 Real-time monitoring of imaginary part of induced voltage of MXene-based sensor array with different contact times. The imaginary parts of induced voltage are similar under Ex1 - Ex8, so Re1 –Re8 of one of the excitation is listed.

Chapter 8 Conclusions and Future Works

8.1 Conclusions

This thesis investigates three different sensors, and expands sensors to three kinds of functions, wireless, self-power and sensor array. Different sensing materials were successfully prepared, including metal nanomaterials (*e.g.,* nickel-coated textile, copper-coated textile), and 2D materials (*e.g.,* graphene, BN, MoS_2 and MXene). Different sensing materials can achieve different sensing capacities, such as flexibility, high sensitivity, stability, durability and rapid responsiveness. Then I designed wearable sensors based on above sensing materials to real-time monitor the signals of different human physiological activities, such as joints bending, running, speaking, blinking, and breathing with cough, fever, runny and stuffy nose. The electrical signals output were analyzed through experimental and theoretical results. For practical application, I developed wireless, sensor arrays and self-powered sensing technology for applications in human healthcare.

8.1.1 Fabrication of wearable sensors

Three developed sensors consist of two physical sensors (capacitance and inductance senor) and one chemical sensor (RC parallel circuit-based sensor). The physical sensors were applied to real-time monitor human motions during rehabilitation training. Moreover, the chemical sensor, to the individual's biomarkers (moisture) of instantaneous and continuous detection, can provide deeper personal health monitoring and medical diagnosis at the molecular level (symptoms of COVID-19 and flu). The sensing mechanism (signal analysis) and performance (*e.g.,* stability, durability and washability) have been systematically studied.

Capacitance sensor

A novel topological modification method was developed to achieve robust interaction between the active layer (copper or nickel) and the substrate (cotton fabric) through thread-

hole topology and bond topology. The prepared textile-based capacitive sensor shows outstanding stability and durability. The sensor was used to monitor physical rehabilitation training in real-time, such as breathing, speaking, blinking, head motions and joint motions.

This work was published in ACS Nano (2020, 14, 8191).

The article is cited by 35 pubilications. (Accessed on: 10/24/2021) The following are some examples of feedback: (1) The facile scale-up process obtained 3D-shaped fabrics with good air permeability, compression, and moisture transmission, have been demonstrated as a great achievement for developing next-gener-ation large-scale wearable sensors and soft robotics (Adv. Electron. Mater. 2021, 2100578); (2) Capacitive sensors have high response repeatability, small signal drift, long term cycle stability, and low energy consumption, but they are susceptible to external field interference, relatively low sensitivity, and limited sensing range (Materials 2021, 14, 6073); (3) Fiber surface modification is a successful chemical treatment in improving the adhesion and conductivity of the conductive fabric (Small 2021, 2102903); (4) The microstructure, distance and angles between the two conductive fabrics could cause changes in the capacitance, resulting in further improvement of the sensitivity of the capacitive sensor (J. Mater. Chem. A, 2020, 8, 25499).

Inductance sensor

A whole system design was proposed to prepare an inductance sensor for monitoring joints bending activities. During material preparation, robust chemical interaction between the nickel coatings and the substrate is achieved by PDA-assisted ELD process. Apart from the sensing material preparation, sensor assembly optimization, capture of sensing data, theoretical analysis, and final sensor performance characterization were all taken into account in this study.

This work was published in Adv. Intell. Syst. (2019, 1, 1900037) as the Cover Paper.

The article is cited by 24 pubilications. (Accessed on: 10/24/2021) An example of feedback is as following: Tactile sensors play an important role in medical science (*e.g.,* physical rehabilitation) where the sensors as a kind of wearable devices monitor human's health by detecting joint bending degree (IEEE Sens. J. 2021, 21, 2757).

RC parallel circuit-based sensor

Using pyrene-assisted ultrasonic exfoliation technique, a water-based h-BN was initially employed as a wireless humidity sensor for monitoring nose breathing with COVID-19 and flu symptoms. Impedance output is a dual function of resistance and capacitance, according to the comprehensive electrical signal analysis.

8.1.2 Functionalization of wearable sensor

To apply wearable sensors to real life, we must consider the power supply and signal processing. I proposed two methods to construct a high-performance flexible power supply to provide the power source for the developed wearable sensors. Besides, a wireless transmission system has been successfully used to receive the electrical signal in real-time using an APP of a smartphone instead of large test equipment, simplified the user interface for sensor testing. Furthermore, the sensor array was developed in a cheap and simple way to achieve multipoint detection.

Self-power system

TENG's performance as a flexible power source was improved using two methods. The first is LMNF-based TENG, which achieves full contact of two surfaces and thereby triples the charge density. The second is FENG's design, which has a maximum 134-fold increase in output power density. Then a humidity sensor was added to provide a self-powered sensor for human health monitoring.

Wireless transmission

The h-BN-based humidity sensor was easily coupled to a wireless transmission module to make the wearable sensor more practical. The new code has been developed for the system to receive the signal using an APP of a smartphone from the external wearable humidity sensor.

Sensor array

MXene, a novel 2D material, was utilized to make conductive fabric with a striped pattern that may be used as a self-powered capacitive sensor array. In 2D imaging, the sensor array can do multi-point and quantitative detection, as well as intuitively visualize touch perception.

8.2 Perspectives and Future Work

Although wearable sensors have made significant progress in human health monitoring and disease diagnosis, there are still many challenges. For my future work, I will focus on three research points for the development of wearable sensors:

1. Signal analysis for understanding the meaning of the health monitoring curve. Although several successful examples of signal analysis have been proposed in this thesis, it is not nearly enough to support all kinds of wearable sensing signals. The understanding of different wearable signals is still very inadequate.
2. More wireless transmission research. This is because the current Bluetooth-based wireless transmission system is power-consumption and rigid structure.
3. Expanding the sensor array detection system to more useful wearable applications.
4. Developing chemical sensors to provide deeper individual health monitoring and medical diagnosis at the molecular level.

Signal analysis

Electronic signal analysis for the practical application of wearable sensors is an urgent problem to be discussed and solved. In this thesis, the development of an h-BN-based humidity sensor is a successful example of electronic signal analysis. However, due to the lack of interdisciplinary knowledge among researchers, there is still little work related to signal analysis. My future work will take this as the focus of my research to further develop wearable sensors.

Figure 8.1 demonstrates a model of a sensor array that possibly mimics real human touch senses, including strain, temperature and humidity. By this sensor array, multipoint stresses with different directions are possibly detected, like the touch sense to various places of human skin. Through the electronic signal analysis, T and RH are dual functions of conductivity (σ) and permittivity (ε), and S is a dual function of an arc length (r_{dA}) and angle (θ). The arc is attributed to the direction of the electric field between the two conductors.

Capacitance is a function of r_{dA} and θ, r_{dA} changes to distance and relative area.

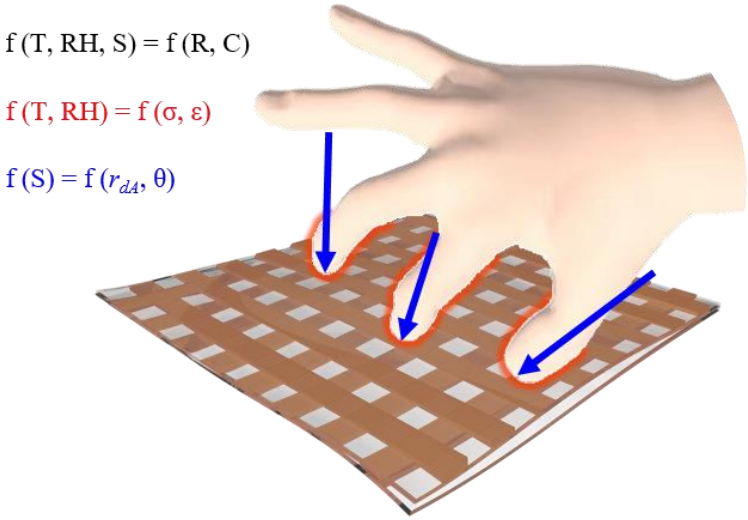

Figure 8.1 A sensor array to mimic real human touch senses, including strain (S), temperature (T) and relative humidity (RH).

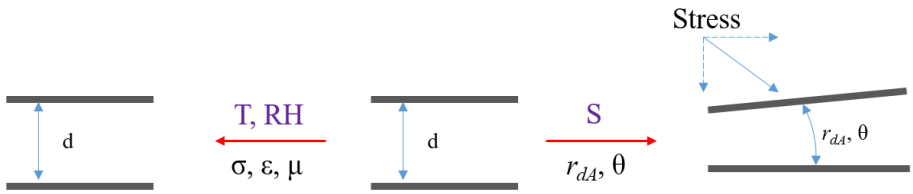

Figure 8.2 The analysis of a sensor unit with the changes of T, RH and S.

Figure 8.2 is the analysis of a sensor unit with the changes of T, RH and S. If the sensor array is placed on the surface of a human hand or artificial hand, mechanical deformation will occur under external stimulation. It is not simply a change in the distance because stress has a direction and can be divided into pressure, shear, and perhaps torsion. So deformation is a combination of tension, shear, and torsion that causes changes in the area, distance, and angle. Therefore, the strain will change the resistance and capacitance, simulated with r_{dA} and θ. In addition, external stimuli have different temperatures and humidity. It also affects the output of the signal, but it is often ignored in most research work. To improve the stability of the measurement and completely simulate the touch sense of human skin, I plan to combine the results of simulation and experiment to figure out how R_1 and C_1 are affected by temperature and humidity, R_2 and C_2 are affected by strain, and how total R and C affect the real and imaginary parts of impedance.

It would be easier if only to minimize signal interference to control the temperature or use filters. However, the use of signal analysis is more valuable. It can guide the development of wearable electronic products and is suitable for more practical applications, such as haptic devices, wearable medical sensors, prosthetics, robots and artificial skin. Some research works attempt to use both temperature and strain sensors, but actually, simplifying the structure of the sensor unit is very important. It is because when it mimics the sense of touch, especially for artificial limbs and artificial skin robots, there will be many sensor units integrated to respond to multiple stimuli.

The sensor units developed can be integrated into sensor arrays to simulate the thermal, humidity, and mechanical stimulation of human skin with complex deformations. I believe this work will lead to precise signal analysis to understand how wearable electronics or e-skin works. It will clearly show how strain, humidity and temperature stimuli affect the resistance and capacitance and then the signal output. It plays a significant role in developing useful wearable sensors, and is suitable for more practical applications.

Wireless transmission

Wearable sensing technology can only be realized with effective commercialization. It is impossible to buy professional equipment to detect health signals in daily life. Therefore, an affordable wireless sensing system is highly required. In the RC parallel circuit-based humidity sensor work, I have developed a wireless transmission through Bluetooth module to real-time record breathing signals using an APP of a smartphone. However, this wireless transmission system is still rigid. In the near future, I would like to develop a flexible wireless inductance sensor. The circuit diagram is shown in **Figure 8.3**. **Figure 8.4** shows an initial visual demo, where the L_1 changes with the distance and bending angles. A LED can visually detect the changed L_1 through mutual inductance. LED with L_2 is away from L_1, or L_1 is at bending status, decreasing mutual-inductance and thus the LED off.

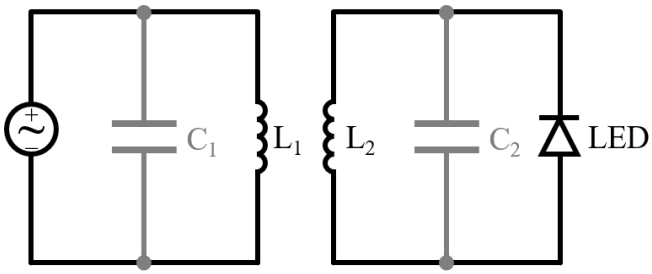

Figure 8.3 Circuit diagram of RLC Parallel-based wireless transmission.

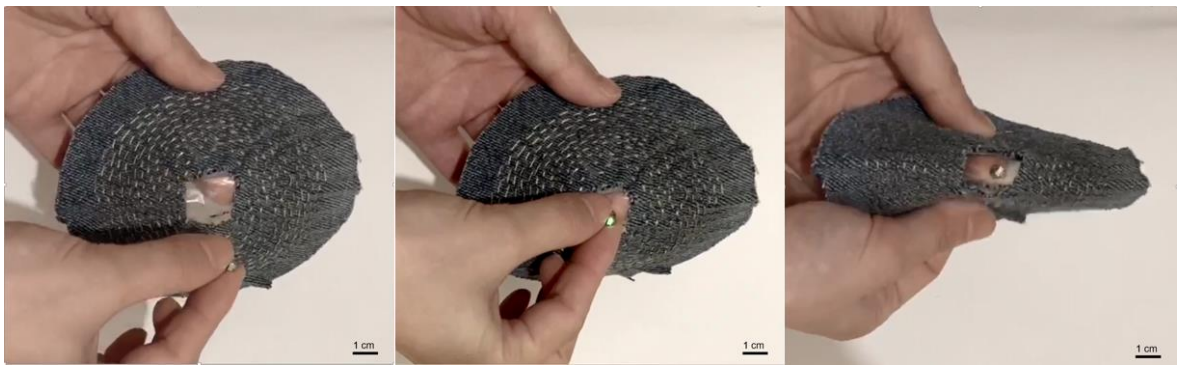

Figure 8.4 RLC Parallel-based wireless transmission visual demo.

Integration

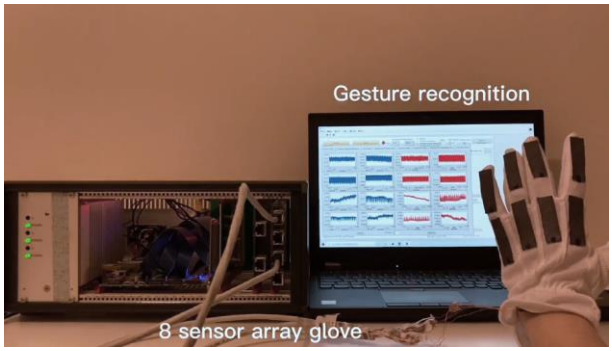

Figure 8.5 Experiment setups of 8 sensor array.

We believe the sensor array detection system can be expanded to many other wearable sensors. I have done some preliminary experiments. I used a robot hand to wear the smart glove to mimic human hand uniform motion process and record the signal in real time (**Figure 8.5**). At different excitation and different receiving channels, the signal outputs are different (**Figure 8.6**). For instance, when the index finger bending, induced voltage

obviously decreased at Ex7-Re6, while slightly increases at Ex8-Re3. And when all fingers back to the stretched state, the voltages of all excitation channels back to the same value with the initial state. In this case, I can real-time monitor hand movement activities and recognize different hand gestures. Besides, I repeated more than 3000 cycles of robot index hand bending activities, and listed the last 1250 cycles in **Figure 8.7**. The signal output is repeated very well, which suggests that the sensor is relatively stable and durable.

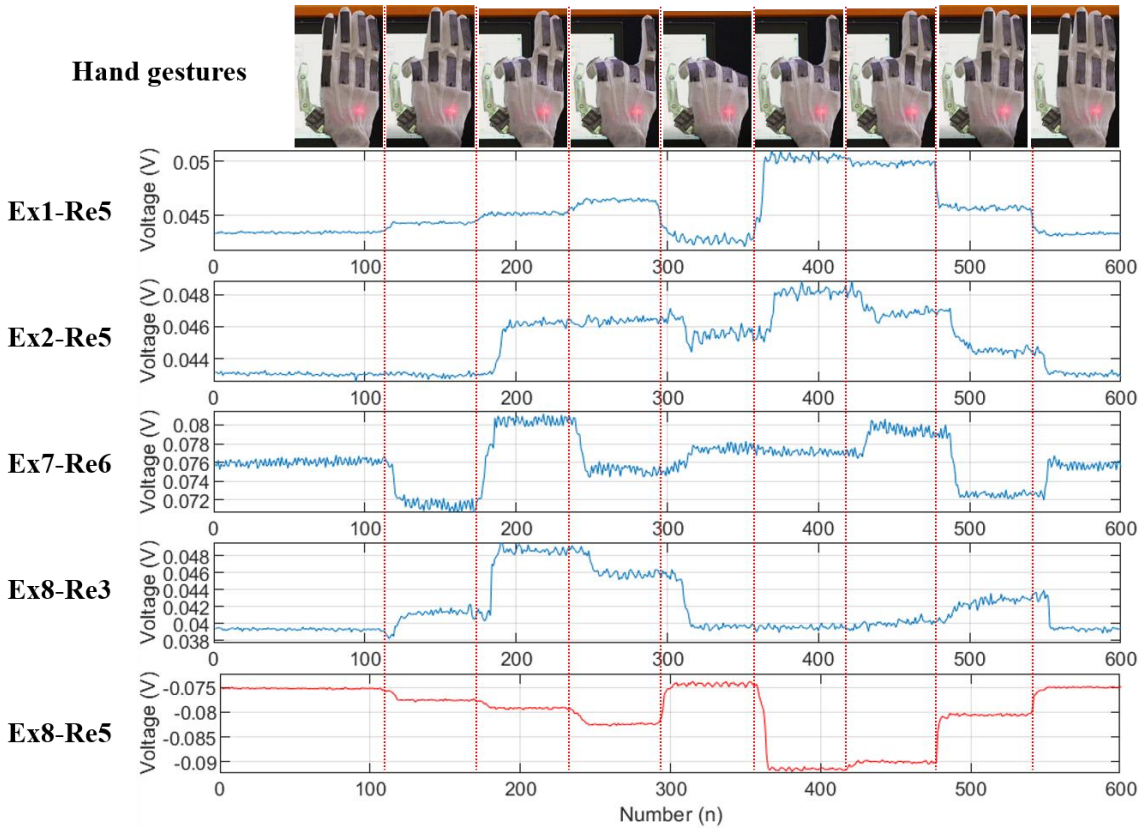

Figure 8.6 Robot hand gestures recognition of 8 sensor array.

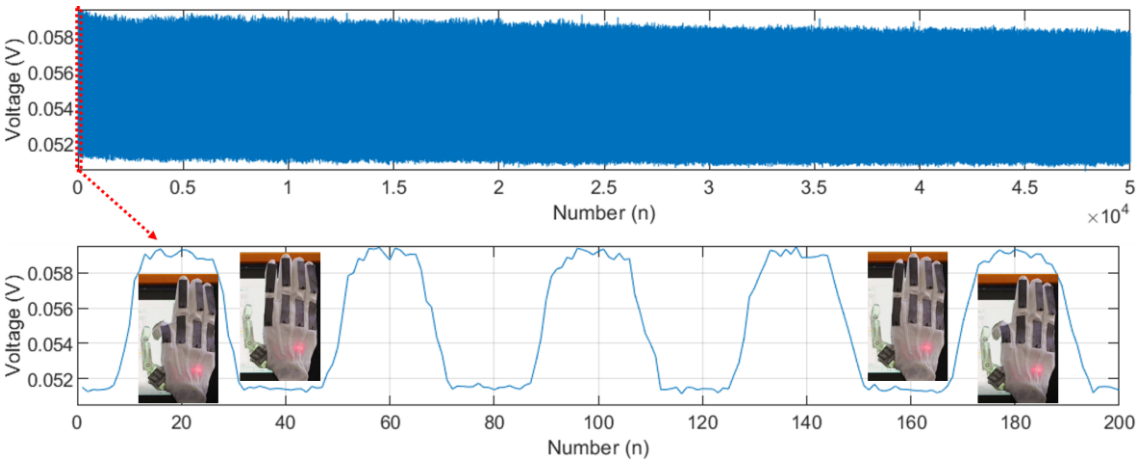

Figure 8.7 Stability test of 8 sensor array (Ex7-Re3).

Chemical sensor development

Most of the wearable sensors I developed are physical sensors. Physical sensors have been developed to effectively monitor different human health signals such as body motions, temperature, blood pressure and heart rate. To go beyond state of the art, chemical sensors that monitor individuals' biomarkers are needed because they would be able to provide deeper personal health monitoring and medical diagnosis at the molecular level. However, highly sensitive and reliable sensors for biomarkers monitoring are challenging due to the low concentration and dynamical change of biomarkers in the human body. In this thesis, I have developed a humidity sensor to detect moisture changes from nose breathing.

Actually, wearable chemical biosensors never reach their full potential, due to a lack of continuous and rapid monitoring of trace and variable biomarkers. Gao et al. integrated a flexible sensor and a PET-based circuit to achieve stable in-situ monitoring of multiple sweat analytes, including glucose, lactate, K^+ and Na^+. (Chem. Soc. Rev., 2019, 48, 1465 and Nature, 2016, 529, 7587) However, it is necessary to monitor the skin temperature simultaneously to calibrate the signal, which will affect the sensor's sensitivity and accuracy. Grzybowki et al. developed a sensor based on functionalized gold nanoparticles, which sense various environmental changes, such as humidity, gas, and various metal cations (Nat. Nanotechnol., 2016, 11, 603). However, the selectivity and sensitivity of this sensor are inherently limited by the material, which fails to detect biomarkers with extremely low concentrations and dynamic changes in body fluids. In the near future, I will continuously develop chemical sensors with excellent performance and study the sensing mechanism using instrument characterization and theoretical analysis of molecular dynamics.